IL
NUOVO CIMENTO
ORGANO DELLA SOCIETÀ ITALIANA DI FISICA
SOTTO GLI AUSPICI DEL CONSIGLIO NAZIONALE DELLE RICERCHE

VOL. XIV, N. 2 *Serie decima* 16 Ottobre 1959

Relaxation of Dislocations in Copper.

P. G. BORDONI, M. NUOVO and L. VERDINI

Istituto Nazionale di Ultracustica « O. M. Corbino » - Roma

(ricevuto il 22 Dicembre 1958)

Summary. — Frequency and attenuation of standing waves have been measured in polycrystalline copper in the frequency range between 1.8 kHz and 6.5 MHz as a function of temperature from 60 °K to 300 °K. Owing to the wide frequency range, the activation energy W and the limiting frequency ω_A associated with the attenuation peak due to dislocations have been evaluated with considerable accuracy. The values obtained ($W = 0.122$ eV (molecule)$^{-1}$, $\omega_A = 23.9 \cdot 10^{11}$ s^{-1}) agree satisfactorily with those computed according to the theories given by SEEGER, DONTH and PFAFF. The shape of the attenuation *vs.* temperature curves shows that the spectrum of relaxation frequencies is a bell-shaped line with its maximum at $\omega = \omega_m$; each frequency of the spectrum is associated with the value of W given above. The height of the attenuation peaks has been compared with the total relaxation exhibited by the frequency *vs.* temperature curves. Below 100 kHz the results agree with the theory of relaxation effects with a continuous spectrum. At higher frequencies the polycrystalline structure gives rise to an attenuation larger than the values that could be expected from the frequency relaxation measurements. The effects of heat treatments have also been investigated, showing that the attenuation and the frequency relaxation are both reduced by treatments whose temperature does not exceed 500 °K, whilst ω_A is slightly increased. Treatments at higher temperatures give rise to comparatively large changes in attenuation and frequency, which do not seem directly related to the pre-existing dislocations. These changes are reversible and can be cancelled by a suitable amount of cold work.

3177

1. – Introduction.

Much interest has been shown recently in the low temperature relaxation effect due to dislocations which was first reported by one of us, some years ago, and which has proved a very sensitive test for the study of the properties of dislocations in metals.

Measurements have been made on aluminum by HUTCHINSON, HUTTON and FILMER, and by EINSPRUCH and TRUELL; the same effect was experimentally investigated on copper by NIBLETT and WILKS, by THOMPSON and HOLMES, by CASWELL and by PARÉ; measurements on lead, quartz and magnesium were also made by some of the previous authors and by BOEMMEL, MASON and WARNER [1].

The first attempt to give a model for the motion of dislocations, to which the effect is related, was made by MASON assuming that a dislocation line between two pinning points could be displaced from its potential well by thermal agitation, and that the small stress applied would make the potential well asymmetrical giving rise to a macroscopic anelastic strain, thus producing a relaxation effect. This model lays perhaps too much emphasis on the effect of the impurity content, and was discussed by WEERTMAN and by SEEGER. More recently it has been suggested by SEEGER that the dislocations are confined to certain crystallographic directions by the PEIERLS stress, and may form pair of kinks under the combined action of thermal fluctuations and applied elastic stress. The same theory has been improved by SEEGER, DONTH and PFAFF, who have shown that the relation between the relaxation frequency and the temperature does not require any special hypothesis, but may be derived from the theory of stochastic processes.

Notwithstanding the large amount of experimental data and theoretical treatments which are presently available, some basic questions concerning the relaxation effect due to dislocations are still unanswered. From the first measurements it was evident that the position of the attenuation maximum on the temperature scale was a function of the frequency of vibration. Later measurements confirmed this result, without giving any satisfactory information on the relation between frequency and temperature, as they were made on materials with a different impurity content, or they covered a very narrow frequency range. In fact, the attempts which have been made to relate the temperature of maximum damping with the vibration frequency by means of an exponential function, have given rather scattered values for the fundamental parameters.

---

[1] For a bibliography see: P. G. BORDONI: *Proc. I.C.A. Congress*, 101 (1956); P. G. BORDONI and M. NUOVO: *Effect of crystal dislocations upon vibrations* (Contribution to the Palais de la Science of the Exp. Univ. Bruxelles).

3178

It is also evident from all the measurements available that the attenuation peak is not due to a single relaxation frequency, but must be associated with a rather wide relaxation spectrum. However no attempt has been made to evaluate this spectrum, whose model is obviously of fundamental importance for any theory of the motion of dislocations.

The present work was essentially undertaken in order to obtain more systematic information on the above basic features of the relaxation effect. In addition to them the effects of heat treatments have also been investigated together with the frequency dependence of the temperature of the small peak first noticed by NIBLETT and WILKS.

Measurements were made on polycrystalline copper; no special care was taken in order to obtain a very pure material, as previous investigations have proved that this is not a very essential requirement. However all the samples had the same impurity content and the same mechanical history. Moreover some recent improvements of the experimental technique made it possible to investigate the effect *on the same sample* in a frequency range wider than three decades, eliminating in this way any accidental cause of error due to slight changes in the properties of the material. In addition to the attenuation measurements the frequency has been also determined and these data have proved quite essential for the interpretation of some results.

2. – Experimental method.

A resonance technique was used as in a previous investigation [2], two different apparatus being employed for the measurements in the acoustic or low ultrasonic range (1 kHz ÷ 100 kHz) and in the high ultrasonic range (100 kHz ÷ 10 MHz) respectively.

In the first type of measurements the flexural vibrations of a circular plate free at its edge were excited and the resonant frequencies of its lowest modes were measured together with the resonant coefficient Q or the logarithmic decrement d.

According to the theory of the elastic vibrations of a thin plate, the frequency $f_{m,n}$ of the vibration mode with m nodal circles and n nodal diameters is related to the geometrical and elastic parameters by the formula [3]

$$f_{m,n} = \alpha_{m,n} \frac{h}{a^2} \sqrt{\frac{E}{\varrho(1-\sigma^2)}}, \tag{1}$$

[2] P. G. BORDONI: *Journ. Acoust. Soc. Amer.*, **26**, 495 (1954); *Ric. Scient.*, **23**, 1193 (1953).

[3] See for instance: LORD RAYLEIGH: *The Theory of Sound*, **1**, nn. 221, 218, 2nd ed. (London, 1937), ch. X, pp. 359, 366; H. LAMB: *The Dynamical Theory of Sound*, 2nd ed. (London, 1925), ch. V, n. 56, pp. 154, 157; S. TIMOSHENKO: *Vibration Problems in Engineering*, 3rd ed. (New York, 1928), ch. IV, n. 56, pp. 316, 317.

where h = thickness of the plate; a = radius; E = Young's modulus; ϱ = density; σ = Poisson's ratio; $\alpha_{m,n}$ = eigenvalues given by Table I.

TABLE I. – *Eigenvalues $\alpha_{m,n}$ for the first flexural vibration modes of a circular free plate with m nodal circles and n nodal diameters.*

m	$n=0$	$n=1$	$n=2$	$n=3$
0	—	—	0.2412	0.5619
1	0.4170	0.9428	1.619	2.431
2	1.770	2.750	—	—

For the first two symmetrical modes ($n=0$) the radii of the nodal circles are given by

$$r_{1,0} = 0.678a\,; \qquad \begin{cases} r'_{2,0} = 0.392a \\ r''_{2,0} = 0.842a \end{cases} . \tag{2}$$

By means of the equation (1) and of the values of E, ϱ, and σ given by the literature, the size of a vibrating plate can be chosen in such a way that its resonances cover a given frequency range. The same equation could also be employed to compute the Young's modulus from the measured values of $f_{m,n}$. However the value obtained in this way would be less accurate than the modulus computed from measurements on extensional vibrations owing to the larger effect of finite thickness on flexural vibrations. It may also be observed that the frequencies of the modes of vibration have a more fundamental meaning than the macroscopic elastic moduli, according to the statistical theory of solids. For these reasons in the following the measured values of $f_{m,n}$ will be systematically considered in the place of Young's modulus.

As in any other type of vibrations the anelastic damping can be evaluated through the ratio of the energy ΔU dissipated in half a cycle to the total vibration energy U by means of the equation:

$$\frac{\Delta U}{U} = 2\pi Q^{-1} = d\,. \tag{3}$$

The driving force was supplied by the electrostatic pressure between the plate and a small electrode facing one of its bases; the same electrode, connected to a high frequency resonant circuit, was employed to mesure the amplitude

of the vibrations. A detailed description of the apparatus will be found in previous papers [4].

In order to avoid any appreciable change of resonant frequency and damping due to external causes, the vibrating plate was supported by three needle points located in small holes on a nodal circle (Fig. 1). Additional damping due to air was also avoided by keeping the vibrating plate into an evacuated container; the pressure inside the container could be reduced to less than 10^{-3} mm Hg.

The distance between the electrode and the plate was controlled by turning through a vacuum seal a thin rod fastened to the latter. The same rod, insulated from the metallic container, was also employed as an electrical connection.

In the second type of measurements the specimen used was the same, but the vibrations excited were longitudinal instead of flexural. The resonant frequency f_p of the longitudinal mode having two antinodal planes on the bases of the plate and p nodal planes between them, is given by the very simple equation

$$f_p = \frac{h}{2p}\sqrt{\frac{\lambda + 2\mu}{\varrho}}, \tag{4}$$

where λ, μ = elastic constants of Lamé.

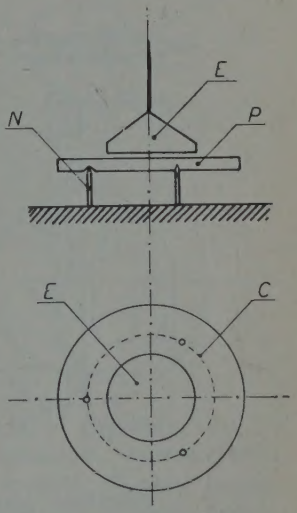

Fig. 1. – Vibrating plate P in its lowest symmetrical mode ($m=1$, $n=0$) supported by three needle points N on the nodal circle C. E: electrode.

Recent measurements have shown that (4) is very accurate provided d is not too small [5]. The anelastic damping can be evaluated by means of the equation (3), as for flexural vibrations.

The driving force was supplied by the electrostatic pressure between the plate and a small electrode insulated from one of its bases by a thin sheet of mica. A second electrode is insulated in the same way from the other basis and is connected to a tuned capacitive detector [6] to measure the amplitude of vibrations (Fig. 2).

---

[4] P. G. Bordoni: *Nuovo Cimento*, **4**, 177 (1947); *Ric. Scient.*, **18**, 103 (1948); P. G. Bordoni and M. Nuovo: *Acustica*, **4**, 184 (1954); *Ric. Scient.*, **24**, 560 (1954); *Acustica*, **7**, 1 (1957); *Ric. Scient.*, **27**, 695 (1957).

[5] See the last two papers quoted in footnote [4].

[6] P. G. Bordoni and M. Nuovo: *Acustica*, **8**, 351 (1958).

The vibrating plate is clamped by a broken flat ring in the middle plane between its bases. This type of clamping seems to have no appreciable effect upon vibrations as the damping at room temperature has almost the same value for the modes corresponding to odd values of p, when the middle plane is a nodal plane, and for the modes corresponding to even values of p, when the same plane is an antinodal one. This is possibly due to the fact that the driving electrode has a smaller diameter than the plate; thus the vibration amplitude at the edge of the plate is much smaller than at its center.

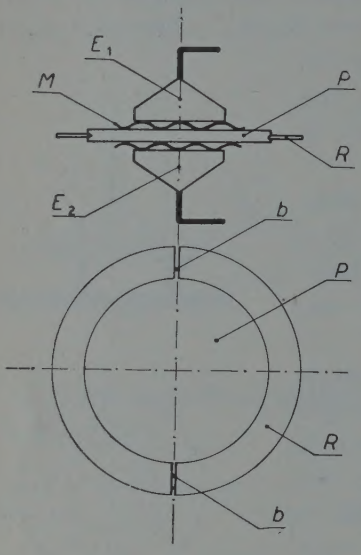

Fig. 2. – Vibrating plate P in longitudinal (thickness) modes. E_1 driving electrode; E_2 measuring electrode; M insulating layer of mica; R clamping ring, broken at b, b.

The mechanical contact between the electrodes and the vibrating system is always very poor owing to the small currugations of the insulating layer of mica, as it has been shown in previous papers ([7]). Therefore the perturbations due to the electrodes upon the values of f_p and Q are negligible when the vibrating system is very stiff, as it is the case with a plate vibrating in its longitudinal modes. In fact no changes have been found in resonance or damping when the pressure of the electrodes upon the plate was altered.

The resonant frequencies were measured in the range from 1 kHz to 100 kHz by means of a quartz-controlled cycle counter, with an accuracy of $10^{-4}(\pm 0.5)$ Hz. From 100 kHz to 10 MHz the frequency was compared with a known multiple of a standard frequency supplied by a quartz oscillator. The difference between the two frequencies was given by a direct-reading frequency meter, whose calibration was checked immediately before every measurement. In this way the accuracy obtained was of the same order as in the lower frequency range.

The anelastic damping was evaluated either through the bandwidth of the resonance curve measured by Q, or through the logarithmic decrement d for free vibrations. In some cases, when it was possible to employ both methods, the values obtained were checked by means of equation (3) and a satisfactory agreement was found.

To measure the temperature of the plate without perturbing its flexural vibrations, two of the needle points of Fig. 1 were respectively made of iron

([7]) See the second and third paper quoted in footnote ([4]).

and constantan, employing the plate itself as thermocouple joint. The e.m.f. was measured by a sensitive potentiometer and this was found to be the most satisfactory way to avoid systematic differences between the measurements made when the plate is cooling or heating.

The same *broken* thermocouple T_1 was also employed with the apparatus for longitudinal vibrations; in this case the iron and constantan wires were placed in two small holes near the plate edge.

The evacuated container was placed in a cryostat, which could be gradually cooled by boiling small amounts of liquid nitrogen; (Fig. 3). To allow the plate to reach the cryostat temperature, the pressure inside the container was kept between 100 mm Hg and 500 mm Hg. The temperature changes could however be stopped by reducing the pressure below 10^{-2} mm Hg, and the measurements were made in a thermal equilibrium condition. A second thermocouple T_2 and a copper resistance thermometer O were employed to measure the temperature inside the cryostat.

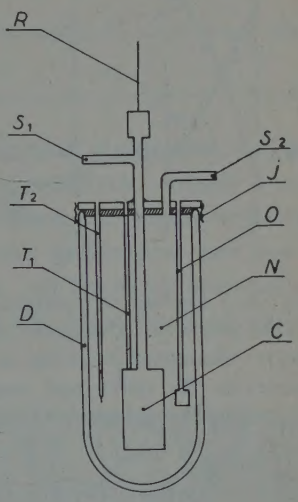

Fig. 3. – Apparatus for low temperature measurements. D cryostat; T_1 plate thermocouple; T_2 cryostat thermocouple; S_1 tube for the evacuation of the container; R control rod for electrode spacing and electrical connections; S_2 tube for the evacuation of the cryostat; J air-tight joint; O resistance thermometer; N liquid nitrogen; C container.

When the boiling point of nitrogen was reached and the cryostat was almost filled with liquid, the vapor pressure was reduced by means of a rotary pump, and further cooling was obtained until what remained of the liquid was completely frozen. During the last process the e.m.f. of the thermocouple T_2 and the resistance of the thermometer O were recorded as a function of time (Fig. 4).

The region where they don't change with time corresponds to the melting point of pure nitrogen. Owing to the presence of oxygen dissolved from the atmosphere, somewhat lower temperatures can be reached, their values being measured by comparison with the resistance thermometer.

Measurements were also made when the plate was heating inside the cryostat, the process of melting and boiling the oxygen-nitrogen mixture being suitably accelerated by pumping small amounts of warm air inside the cryostat. The rate of temperature change of the plate was controlled as before by means of the pressure inside the container.

The boiling points of oxygen and nitrogen and the melting point of the latter have been employed to calibrate the resistance thermometer and the

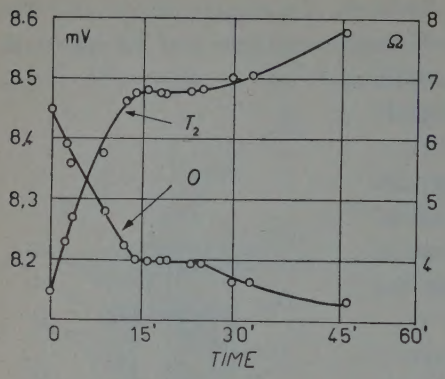

Fig. 4. – Boiling of nitrogen under reduced pressure. Abscissae: time. Ordinates: electromotive force of the thermocouple T_2 (left) and resistance of the thermometer O (right).

thermocouples. Fig. 5 shows that the measured values of resistance are on the same straight line with the points computed from the resistivity data given by literature ([8]) and from the room temperature value of resistance. This proves that the boiling point of nitrogen and the temperature at which solidification begins are not affected by the presence of a small amount of dissolved oxygen. No difference has been found between the e.m.f. of the thermocouples T_1 and T_2 when the lower part of the container is removed, and they are immersed in the same bath. The experimental points are very near to the literature data ([9]), the difference being probably due to the chemical composition of constantan. When the literature values are altered by a constant factor of 0.9955 they fit perfectly

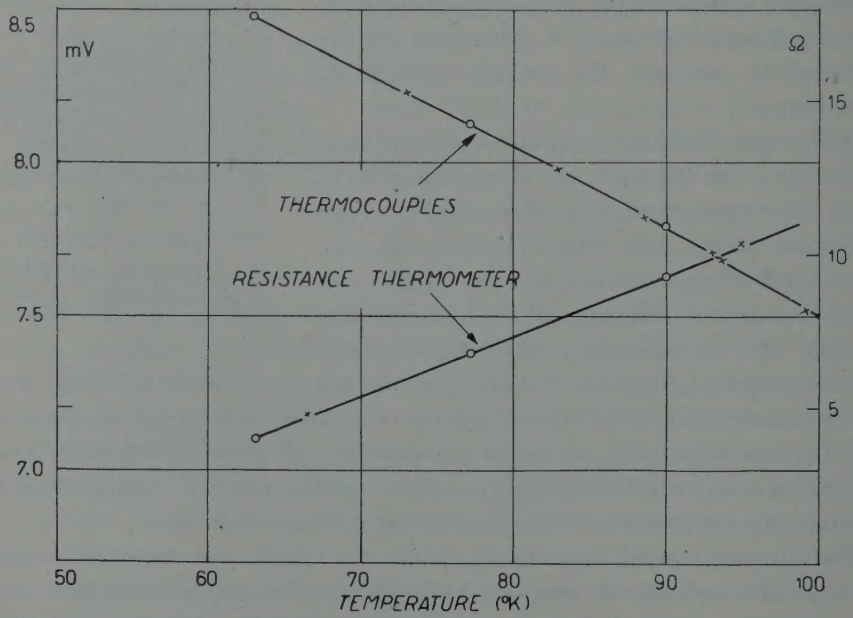

Fig. 5. – Low temperature calibration of the resistance thermometer and of the thermocouples. ○: experimental points; ✦: literature data (altered by a factor 0.9955 for the thermocouples).

([8]) C. HODGMAN: *Handb. of Chem. and Phys.*, 30th ed. (Cleveland, 1948), p. 1954.
([9]) See the paper quoted in footnote ([8]), p. 1979.

3184

with the experimental points as is shown by Fig. 5. The e.m.f. computed in this way were therefore taken as calibration values for the thermocouples.

3. – Results.

Measurements have been made on a group of six circular plates and a rectangular rod, machined out of the same sheet of electrolytic copper containing 0.12% lead with traces of iron and zinc ([10]). The main characteristics of the samples are listed in Table II together with the mechanical and heat treatments that they have undergone *after* machining. All the annealing treatments were made in vacuum, with the exception of the treatments of plate n. 4 at 411 °K which were made in air.

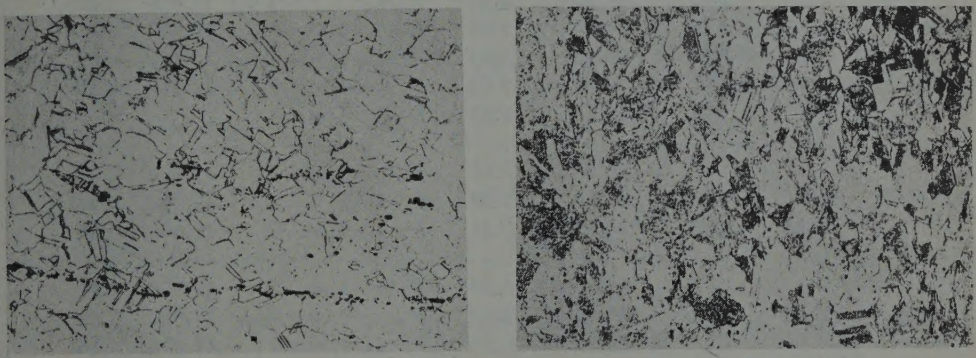

a) *b*)

Fig. 6. – Grain structure of the samples after machining (×150): *a*) parallel to the sheet plane; *b*) normal to the sheet plane.

The grain structure of the samples after machining is shown in Fig. 6. Owing to the cross rolling which the material has undergone after casting to be flattened into a sheet, the average grain size changes with direction. Parallel to the sheet plane it is about $6 \cdot 10^{-2}$ mm, whilst in a normal direction it may be estimated to one half of the above value.

The resonant frequency and damping have been measured as a function of temperature between 60 °K and 300 °K for different vibration modes of the rod n. 1 and of the plates n. 1*b*, 2, 4, 5 after machining. The data obtained cover the whole frequency range between 1.8 kHz and 6.5 MHz as it is shown by Table III.

([10]) The authors wish to thank Prof. M. BACCAREDDA, Director of the Laboratory of Industrial Chemistry of the University of Pisa, where the analysis was made.

3185

TABLE II. – *Main characteristics of the samples.*

Sample	Mechanical and heat treatments		Size		Vibration mode	Frequency (kHz)	Q^{-1}
	Time (h)	Temperature (°K)	Diameter (mm)	Thickness (mm)	F = flexural L = longitudinal m = nodal circles n = nodal diameters l = nodal lines p = nodal planes	at 293 °K	
Plate 1*a*	—	—	46.92	4.75	F, $m=1$, $n=0$	13.218	$38\cdot10^{-5}$
	—	—	46.92	4.75	F, $m=1$, $n=2$	48.090	—
Plate 1*b*	—	—	36.10	4.75	F, $m=1$, $n=0$	21.698	37
	—	—	36.10	4.75	F, $m=1$, $n=1$	43.834	50
	1h 00′	873	36.10	4.75	F, $m=1$, $n=0$	22.350	160
Plate 2	—	—	36.35	2.67	F, $m=1$, $n=0$	12.956	36
	5h 00′	419	36.35	2.67	F, $m=1$, $n=0$	—	—
	2h 30′	449	36.35	2.67	F, $m=1$, $n=0$	12.998	21
	6h 00′	516	36.35	2.67	F, $m=1$, $n=0$	13.250	166
	cold worked		36.35	2.63	F, $m=1$, $n=0$	12.892	26
	0h 30′	582	36.35	2.63	F, $m=1$, $n=0$	12.918	13
	1h 00′	873	36.35	2.63	F, $m=1$, $n=0$	—	—
Plate 3	—	—	36.05	2.62	F, $m=1$, $n=0$	12.820	36
	2h 00′	498	36.05	2.62	F, $m=1$, $n=0$	12.860	18
	2h 00′	515	36.05	2.62	F, $m=1$, $n=0$	12.950	50
Plate 4	—	—	36.20	2.60	F, $m=1$, $n=0$	12.700	45
	16h 00′	411	36.20	2.60	F, $m=1$, $n=0$	12.762	18
	35h 00′	411	36.20	2.60	F, $m=1$, $n=0$	12.764	16
	cold worked		36.20	2.60	F, $m=1$, $n=0$	12.764	17
	5h 00′	483	36.20	2.60	F, $m=1$, $n=0$	12.800	15
Plate 5 (*)	—	—	36.00	4.40	F, $m=0$, $n=2$	14.4	—
	—	—	36.00	4.40	L, $p=1$	536.7	74
	—	—	36.00	4.40	L, $p=2$	1067.2	68
	—	—	36.00	4.40	L, $p=5$	2658.8	66
	—	—	36.00	4.40	L, $p=10$	5314.5	146
	—	—	36.00	4.40	L, $p=12$	6370.2	184
Plate 6 (*)	—	—	36.05	4.97	F, $m=1$, $n=0$	23.947	38
	—	—	36.05	4.97	L, $p=4$	1878.2	70
	8h 00′	425	36.05	4.97	F, $m=1$, $n=0$	24.000	22
	8h 00′	425	36.05	4.97	L, $p=4$	1880.1	54
	1h 00′	873	36.05	4.97	F, $m=1$, $n=0$	24.592	161
	1h 00′	873	36.05	4.97	L, $p=4$	1910.4	148
Rod 1	—	—	49.95 · 9.95 · 1.21		F, $l=2$	1.811	58

(*) With ring.

3186

TABLE III. – *Frequency and damping as a function of temperature, after machining.*

Rod n. 1 $F, l=2$			Plate n. 4 $F, m=1, n=0$			Plate n. 2 $F, m=1, n=0$		
T (°K)	f (kHz)	Q^{-1}	T (°K)	f (kHz)	Q^{-1}	T (°K)	f (kHz)	Q^{-1}
63.5	1.899	$273 \cdot 10^{-5}$	71.0	13.220	$350 \cdot 10^{-5}$	63.5	13.524	$245 \cdot 10^{-5}$
67.0	.889	337	74.0	.206	378	65.5	.517	260
69.0	.885	368	74.5	.200	380	69.0	.500	296
71.0	.883	368	76.0	.190	415	71.5	—	326
72.0	.881	368	78.5	.180	423	74.7	—	357
76.0	.879	337	80.6	—	450	78.0	.444	372
79.0	.878	291	81.5	.174	—	81.5	.420	401
82.0	.876	216	83.2	—	456	84.0	.410	395
83.0	.875	205	84.0	.150	455	86.5	.404	388
88.0	.873	120	86.0	.140	445	90.0	.390	359
103.5	.867	58	89.5	.130	405	92.5	.380	314
117.0	.863	48	97.0	.090	334	97.0	.360	285
138.0	.856	43	110.0	.076	150	100.6	.344	240
211.0	.838	58	153.5	12.980	45.5	106.5	.330	188
290.0	.812	58	297.0	.692	45.5	113.5	.310	120
						121.5	.290	78
						129.5	.274	58
						291.5	12.960	36

3187

TABLE III (*continued*).

Plate n. 1*b*						Plate n. 5		
F, $m=1$, $n=0$			F, $m=1$, $n=1$			L, $p=1$		
T (°K)	f (kHz)	Q^{-1}	T (°K)	f (kHz)	Q^{-1}	T (°K)	f (kHz)	Q^{-1}
74.0	22.544	$346 \cdot 10^{-5}$	62.5	45.844	$207 \cdot 10^{-5}$	60.5	555.08	$115 \cdot 10^{-5}$
76.7	.524	373	64.0	.826	223	62.0	4.88	114
80.0	.496	417	66.5	.796	250	64.5	4.64	128
83.0	.470	435	69.0	.762	280	70.5	4.20	142
87.2	.435	410	71.5	.730	307	72.0	4.00	160
94.5	.398	366	75.0	.632	376	74.0	4.00	177
98.5		304	81.5	.546	457	77.0	3.66	188
106.0	.332	205	83.5	.526	457	81.0	3.00	217
111.0	.312	162	85.5	4.88	497	86.0	2.64	246
121.0	.277	99	87.5	.464	500	93.0	1.90	290
143.5	.200	50	96.5	4.00	462	95.0	1.70	293
175.5	.100	31	99.0	.268	406	97.0	1.50	298
209.5	21.986	31	118.5	.080	178	99.0	1.20	304
293.0	.698	37	139.0	44.916	98	103.0	0.86	298
			159.0	.790	54	109.5	550.00	294
			198.5	.518	49	112.5	—	283
			293	43.834	50	118.0	—	262
						120.0	—	248
						126.0	548.20	236
						128.5	7.60	217
						139.0	6.76	152
						145.0	6.60	132
						149.0	6.40	117
						159.5	6.00	98
						185.0	—	62
						200.0	3.58	57
						273.0	536.54	74

3183

TABLE III (*continued*).

Plate n. 5

L, $p=2$			L, $p=2$			L, $p=5$		
T (°K)	f (kHz)	Q^{-1}	T (°K)	f (kHz)	Q^{-1}	T (°K)	f (kHz)	Q^{-1}
63.5	1095.0	$91 \cdot 10^{-5}$	168.0	—	$98 \cdot 10^{-5}$	77.0	2727.00	$148.0 \cdot 10^{-5}$
68.5	4.40	102	173.0	—	94	88.5	2722.80	202
73.5	3.80	119	195.0	1078.26	78	94.5	0.40	221
77.0	3.60	132	208.0	6.60	78	99.0	2718.80	236
79.0	3.20	142	231.0	4.36	75	104.0	7.40	248
81.0	2.90	154	243.5	3.00	75	106.5	6.00	257
81.5	2.60	159	257.0	1.24	71	110.0	4.30	270
87.0	1.80	190	273.0	1069.30	60	115.5	1.60	274
90.5	1.64	214	296.0	1066.88	68	119.0	0.60	285
95.0	0.80	225				123.5	2709.20	281
98.0	0.40	243				128.0	8.00	268
100.5	1090.00	260				132	6.00	258
108.5	1088.72	287				134.5	5.20	252
110.0	8.56	285				137.0	4.00	244
112.0	8.28	289				140.0	3.00	237
115.0	7.72	282				143.0	2.60	222
117.0	7.50	277				146.0	1.2	207
119.0	7.10	267				148.0	0.6	207
121.0	6.88	260				152.0	2699.60	193
123.5	6.60	255				163.5	6.00	173
126.0	6.14	240				195.0	2686.80	110
129.0	5.80	225				210.5	2682.52	84
131.0	5.60	208				273.0	2664.30	63
136.5	4.90	184				296.0	2658.00	66
141.0	4.26	180						
151.0	3.00	136						

3189

TABLE III (*continued*).

Plate n. 5								
L, $p=10$			L, $p=12$			L, $p=12$		
T (°K)	f (kHz)	Q^{-1}	T (°K)	f (kHz)	Q^{-1}	T (°K)	f (kHz)	Q^{-1}
77.0	5447.20	$191 \cdot 10^{-5}$	66.5	6542.40	$202 \cdot 10^{-5}$	186.5	6488.00	$240 \cdot 10^{-5}$
98.0	5434.60	268	69.5	—	210	195.0	5440.80	229
101.0	2.60	273	71.5	—	208	212.0	6430.00	207
104.0	0.60	284	76.5	6536.80	212	214.0	6428.00	210
105.5	—	291	78.5	—	220	227.0	6422.00	202
107.5	5428.00	303	82.5	6532.00	226	237.0	—	197
112.0	4.00	317	88.0	—	237	247.0	6408.00	197
117.5	1.60	336	92.0	6523.20	244	255.0	—	199
121.0	5419.00	340	104.5	—	265	273.0	6387.00	203
127.0	5.20	354	108.0	—	277	296.0	—	184
131.0	1.00	339	109.0	—	279			
132.0	5409.60	344	114.0	6508.00	294			
136.5	6.80	322	117.0	3.00	298			
146.0	5400.00	312	123.0	6498.00	308			
149.0	5398.00	305	128.0	—	316			
152.5	6.00	297	131.0	—	317			
157.5	3.20	290	132.0	—	316			
164.5	5387.40	271	135.0	6490.00	310			
175.0	2.00	234	137.5	—	308			
193.0	5376.00	208	141.0	6481.00	306			
195.0	5370.00	184	145.0	—	294			
212.0	5360.80	156	148.0	—	294			
273.0	5325.80	139	153.0	6474.00	285			
290.0	5316.00	146	163.0	6466.00	266			
			169.0	—	263			
			173.5	6458.00	254			

3190

TABLE III (*continued*).

Plate n. 6					
F, $m=1$, $n=0$			L, $p=4$		
T (°K)	f (kHz)	Q^{-1}	T (°K)	f (kHz)	Q^{-1}
64.0	24.970	$201 \cdot 10^{-5}$	62.5	1928.5	$93.5 \cdot 10^{-5}$
64.5	.966	209	63.5	28.0	106
66.0	.954	232	65.2	27.4	109
68.5	.930	260	66.7	27.0	112
69.6	.920	285	76.0	25.2	130
72.5	.902	313	77.0	24.6	140
76.0	.866	366	84.5	23.4	183
79.5	.840	379	89.2	22.7	198
82.0	.822	379	91.5	22.0	218
84.0	.800	379	94.0	21.2	233
89.7	.758	366	97.5	20.2	260
96.2	.708	304	98.0	19.6	250
104.5	.653	224	99.5	19.8	260
112.5	.618	146	103.0	18.5	267
123.5	.574	73	106.5	18.0	286
144.3	.501	40	108.0	17.2	267
154.5	.462	37	116.0	14.8	302
166.2	.418	32.8	123.5	13.0	256
173.0	.388	32.8	132.0	10.0	230
181.3	.363	33	144.0	07.6	189
191.5	.328	33	155.0	05.4	147
199.5	.298	33	158.0	05.0	137
207.5	.265	37.5	163.0	04.0	123
216.5	.232	33	168.5	02.8	116
223.7	.206	25	179.0	00.4	105
229.7	.182	28	188.0	1899.2	100
235.7	.160	33	194.5	98.0	94.0
240.5	.142	37.5	201.0	96.4	94.2
249.7	.105	33	207.5	95.4	76.0
257.2	.080	34.5	216.0	93.8	79.6
263.0	.060	28.5	231.5	90.8	70.0
269.0	.034	33	237.0	89.6	70.0
275.7	.008	33	243.0	88.4	70.0
278.0	.002	33	245.0	88.0	69.5
281.0	23.994	33	293.8	78.0	69.5
282.5	.988	33	294.5	77.7	69.5
283.7	.982	33			
285.7	.977	33			
293.2	.951	37.5			

3191

All the damping *vs.* temperature curves exhibit a peak whose temperature increases with frequency from 72.0 °K for the rod vibrating at 1.882 kHz, up to 130 °K for the plate vibrating at 6.492 MHz (Fig. 7). When the

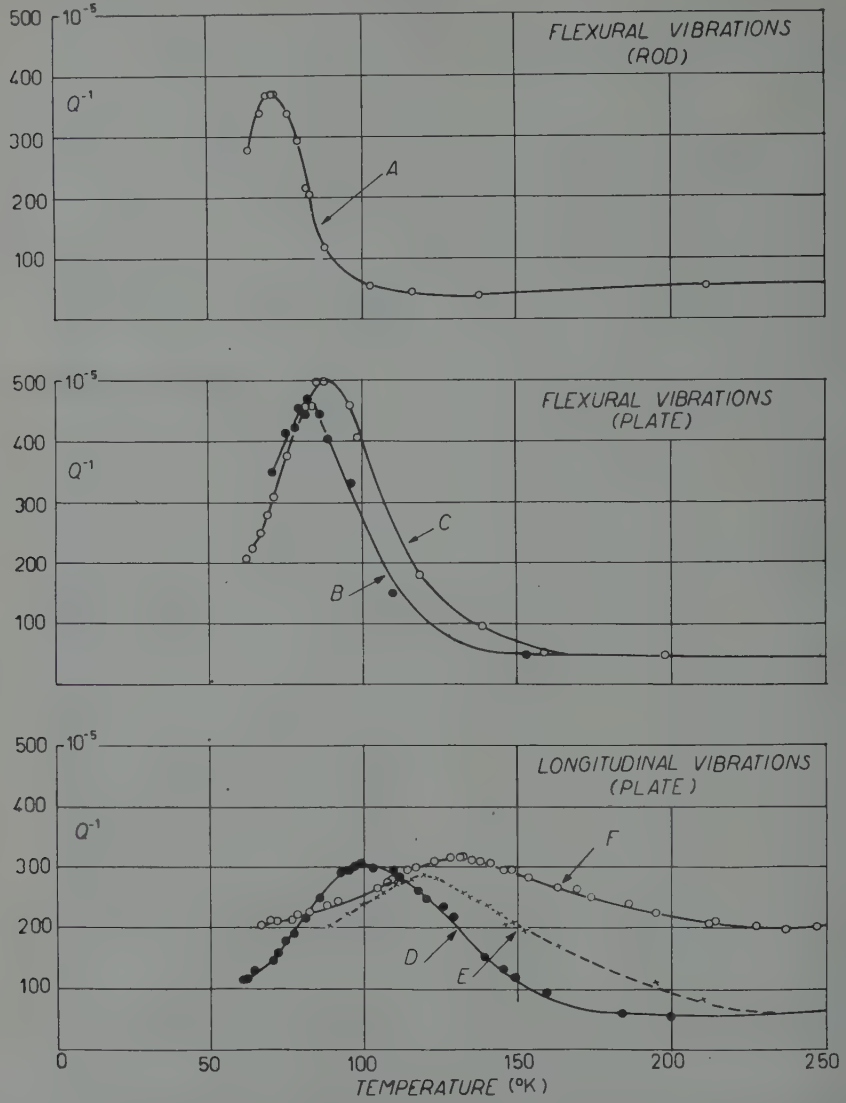

Fig. 7. – Damping as a function of temperature for different frequencies after machining. *A*) rod n. 1 (F, $l=2$); *B*) plate n. 2 (F, $m=1$, $n=0$); *C*) plate n. 1*b* (F, $m=1$, $n=1$); *D*) plate n. 5 (L, $p=1$); *E*) plate n. 5 (L, $p=5$); *F*) plate n. 5 (L, $p=12$).

frequency is raised the peak becomes broader; its height shows a general tendency to decrease with increasing frequency while the opposite tendency is exhibited by the value of damping at room temperature.

3192

In a single case it was possible to extend the measurements down to the boiling point of Helium ([11]) (Fig. 8). In addition to the main peak, a « bump » was found on the low-temperature side of the damping curve, a little below 40 °K. This bump is very similar to that noticed by CASWELL ([12]) in a much

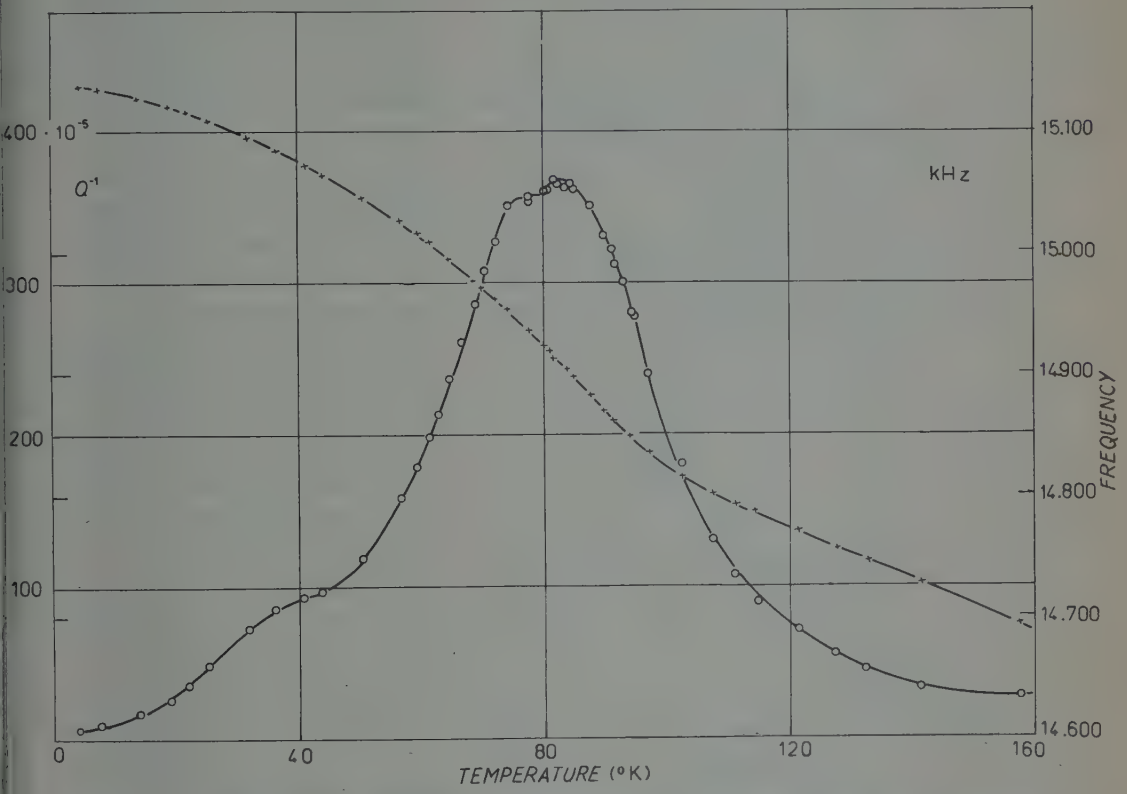

Fig. 8. – Damping and frequency as a function of temperature down to the boiling point of He. Plate n. 5 after machining (F, $m=0$, $n=2$).

purer material (99.992% Cu) for a vibration frequency of 40 kHz, and seems to be due to the same cause as the sharper peak first observed by NIBLETT and WILKS ([13]) in high purity oxygen-free copper (99.999% Cu) at about 32 °K, for a vibration frequency of 1.1 kHz.

([11]) The Authors express their gratitude to the Division of Pure Physics of the National Research Council of Canada for its kind cooperation in the measurements at low temperatures, and in the analysis of the grain structure reproduced in Fig. 6.

([12]) H. L. CASWELL: *Journ. Appl. Phys.*, **29**, 1210 (1958).

([13]) D. H. NIBLETT and J. WILKS: *Phil. Mag.*, **1**, 415 (1956); **2**, 1427 (1957).

The temperature at which the damping becomes maximum can be evaluated with good accuracy from the half-width points of the damping curve, taken at different heights (Fig. 9). This evaluation has been made not only for the experimental data listed in Table III, but also for some preliminary measurements on plates n. 1 and 2 and for the measurements on plate n. 5 given by the curves of Fig. 8. The results are listed in Table IV, together with the frequencies at which the maximum damping occurs.

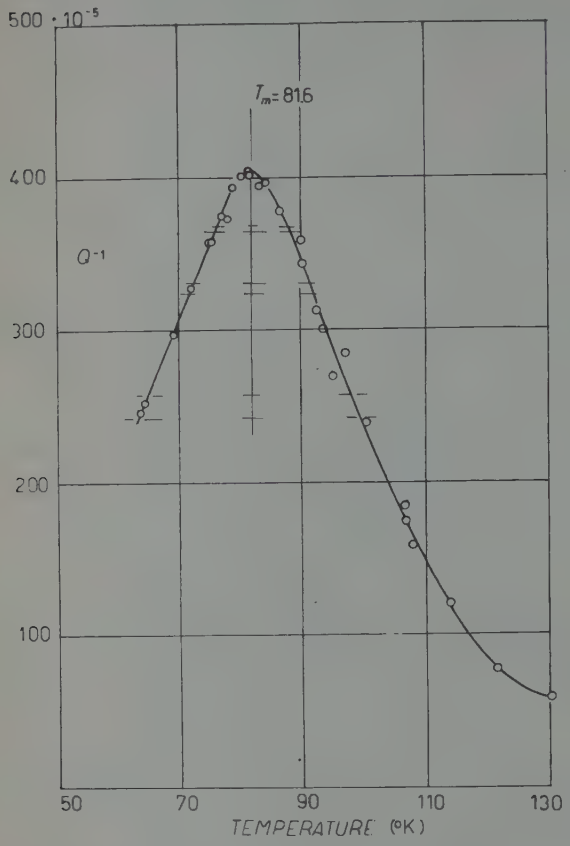

Fig. 9. – Evaluation of the temperature of maximum damping. Plate n. 2, after machining (F, $m=1$, $n=0$).

For the flexural vibrations, the frequency *vs.* temperature curve exhibits clearly an inflexion point at the temperature of maximum damping (Fig. 8), as it is required by the theory of relaxation effects.

To compare the frequency curves for different vibration modes, the same scale must obviously be chosen for the relative frequency changes. This may be done by dividing the frequency $f(T)$ at the temperature T by the value $f(273)$ measured for the same vibration mode at 273 °K, as it has been done in Fig. 10. All the frequency curves for flexural vibrations are very similar to the curve A, and their inflexion point is much more clearly shown than in the same curves for longitudinal vibrations, which are of the type B. It will also be noticed that the temperature coefficient of the frequency is larger for flexural vibrations than for the longitudinal ones. Near 273 °K the logarithmic derivative of a flexural frequency with respect to T is about $1.6 \cdot 10^{-4}(°K)^{-1}$, whilst for a longitudinal frequency its value is only $1.08 \cdot 10^{-4}\ (°K)^{-1}$.

A general reduction of damping in the whole temperature interval from 60 °K to 300 °K and a slight shift of the peak towards the low temperatures, are the effect of an annealing treatment at a temperature a little above 400 °K

(Fig. 11). To make the comparison between the effects of different heat treatments easier, the values of Q^{-1} measured on every plate have been divided by the value $Q_{m,0}^{-1}$ measured for the same plate at the peak of the damping curve, *before any heat treatment*. The same treatment raises the flexural frequency at room temperature without changing its value near the absolute zero. Thus the inflection of the frequency curve becomes less marked after annealing and the temperature coefficient near 273 °K is also reduced.

The same results are found when the annealing temperature is raised without exceeding 500 °K (Fig. 12, 13, curves *A*, *B*). Above this temperature the heat treatments have a quite different effect. As it is shown by Fig. 12 (curves *C*) a treatment of 1 hour at 515 °K increases the resonant frequency of flexural vibrations by a comparatively large amount. In the temperature interval between 60 °K and 300 °K the increase of frequency seems to be independent on the tempera-

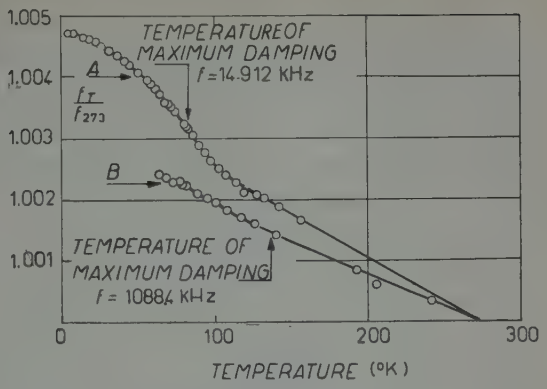

Fig. 10. – Temperature dependence of frequency. Plate n. 5: *A*) flexural vibration mode with $m=0$, $n=2$. *B*) longitudinal vibration mode, with $p=2$. Ordinates f_T/f_{273}.

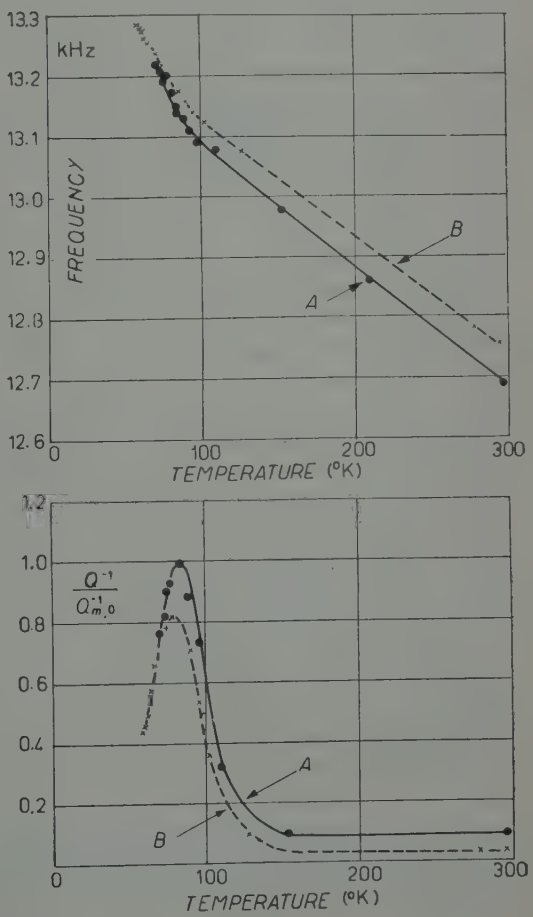

Fig. 11. – Effect of mechanical and heat treatments on resonant frequency and damping. Plate n. 4 flexural vibrations $m=1$, $n=0$. *A*) after machining; *B*) after 16 h at 411 °K.

ture, and the frequency curve after the treatment at 515 °K looks like the curve obtained before, shifted by a given amount into the direction of the frequency axis. Another difference between the treatment at 515 °K and those at lower temperatures is that the former increases the damping at room temperature giving raise to a broader and lower peak.

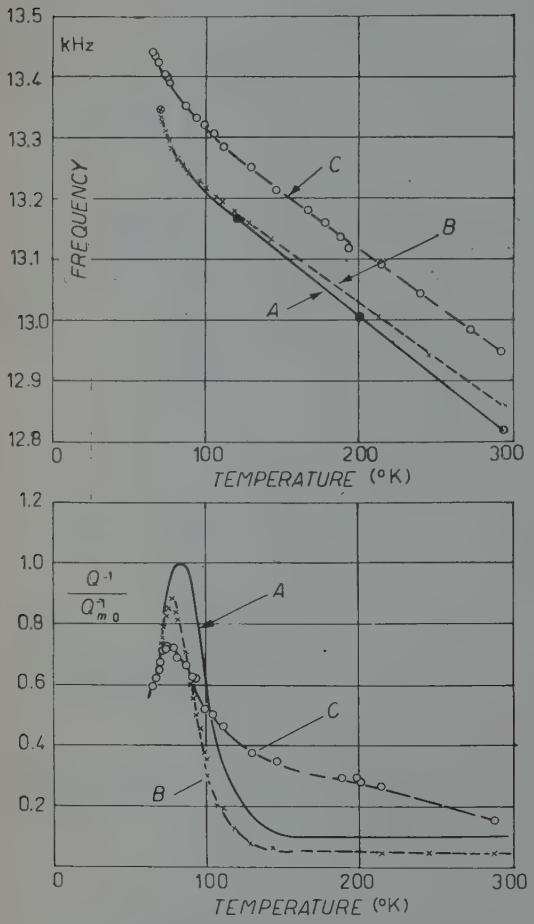

Fig. 12. – Effect of mechanical and heat treatments on resonant frequency and damping. Plate n. 3 flexural vibrations, $m=1$, $n=0$. *A*) after machining; *B*) after 2 h at 498 °K; *C*) after and additional treatment of 1 h at 515 °K.

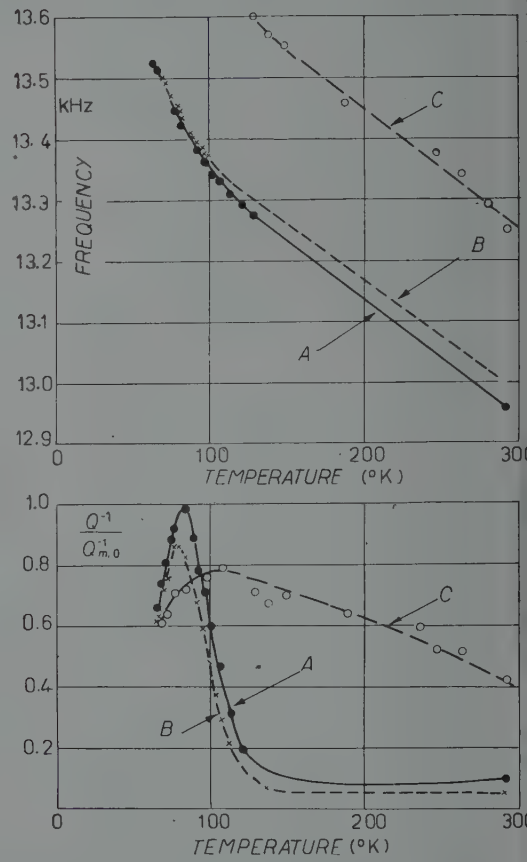

Fig. 13. – Effect of mechanical and heat treatments on resonant frequency and damping. Plate n. 2 flexural vibrations, $m=1$, $n=0$. *A*) after machining; *B*) after 5 h at 419 °K and 2.5 h at 449 °K; *C*) after an additional treatment of 6 h at 516 °K.

A longer treatment at the same temperature produces a larger permanent increase of the frequency and of Q^{-1}, while the damping curve becomes flatter (Fig. 13, curves *C*). After the material has been treated 1 hour at 873 °K

every trace of the damping peak has been cancelled, and no inflexion point is shown by the frequency curve (Fig. 14, curves B).

Another effect of the high temperature heat treatments is to make the elastic and anelastic behaviour of the plate very sensitive to the vibration amplitude X, even for very small values of the strain ([14]). In Fig. 15 the relative changes of frequency and the ratio of Q^{-1} to its limiting value for vanishing strain are given as a functions of the strain component e_{xx}, computed at the center of one basis and normally to the plate axis. In every case the frequency was found to be a decreasing function of strain, whilst Q^{-1} increases with e_{xx}. When the strain is of the order of 10^{-7}, the changes of f are hardly measurable in the machined material because they are smaller than 10^{-4}. Damping is of course more sensitive to the vibration amplitude, its variations being of the order of 10^{-1}. After 1 hour at 873 °K the changes in frequency for the same values of the strain are about twenty times larger and Q^{-1} becomes almost double of the limiting value for vanishing strain.

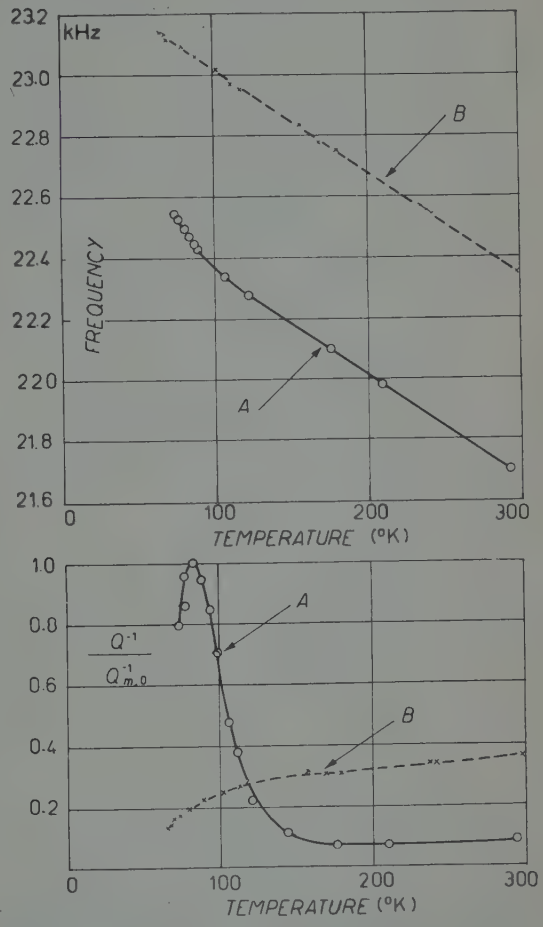

Fig. 14. – Effect of mechanical and heat treatments on resonant frequency and damping. Plate n. 1*b*, flexural vibrations, $m=1$, $n=0$. A) after machining; B) after 1 h at 873 °K.

After a high temperature treatment a peak can be reintroduced into the damping curve by means of cold work. Fig. 16 shows the effect of a permanent strain of $1.5 \cdot 10^{-2}$ parallel to the axis of the plate n. 2,

([14]) The amplitude X is proportional to the output voltage of the vibration detector and to its sensitivity. The measurement of X is illustrated in the first paper quoted in footnote ([4]).

which had been previously kept 1 hour at 873 °K. The height of the peak is about one third of that originally measured on the same plate after machining

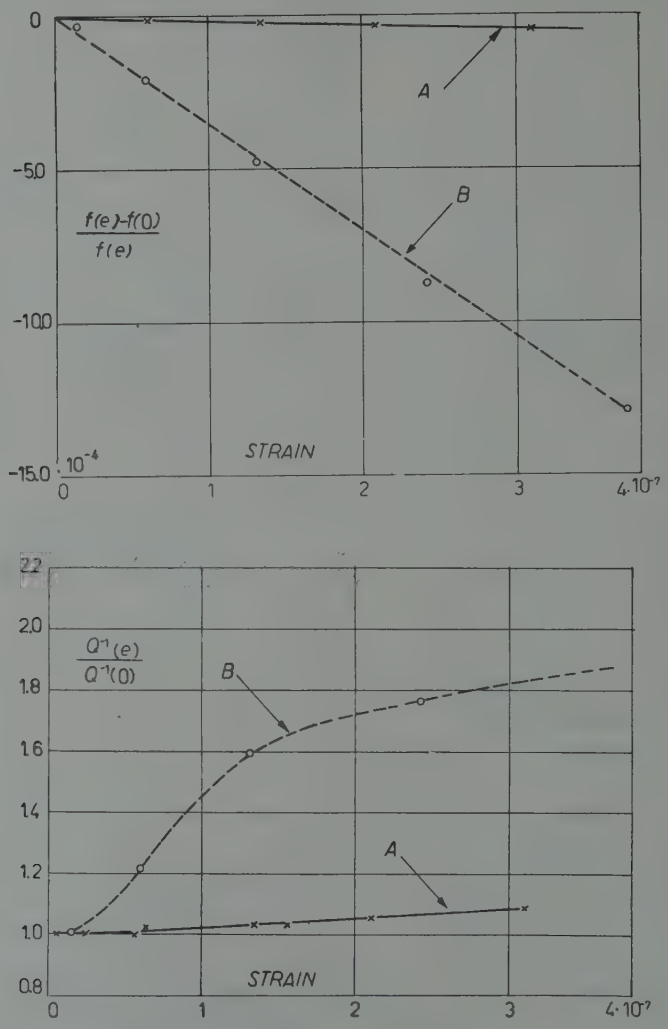

Fig. 15. – Dependance of the resonant frequency and damping at 294 °K upon the strain component e_{xx} computed at the center of one basis and normally to the plate axis; $f(e)$, $Q^{-1}(e)$: values measured when the strain amplitude is e; $f(0)$, $Q^{-1}(0)$: limiting values for vanishing strain. Flexural vibrations of plate n. 1*b* ($m=1$, $n=0$); *A*) after machining; *B*) after 1 h at 873 °K.

(Fig. 13) and its temperature is somewhat lower. The frequency (corrected for the change in thickness) takes values very near the original ones, and a

slight inflexion is found at the temperature of maximum damping. It may be added that the amplitude dependence of frequency and damping is greatly reduced by cold work, and the measurements of $f(e)$ and $Q^{-1}(e)$ on the strained material are very similar to those represented by the curves A of Fig. 15.

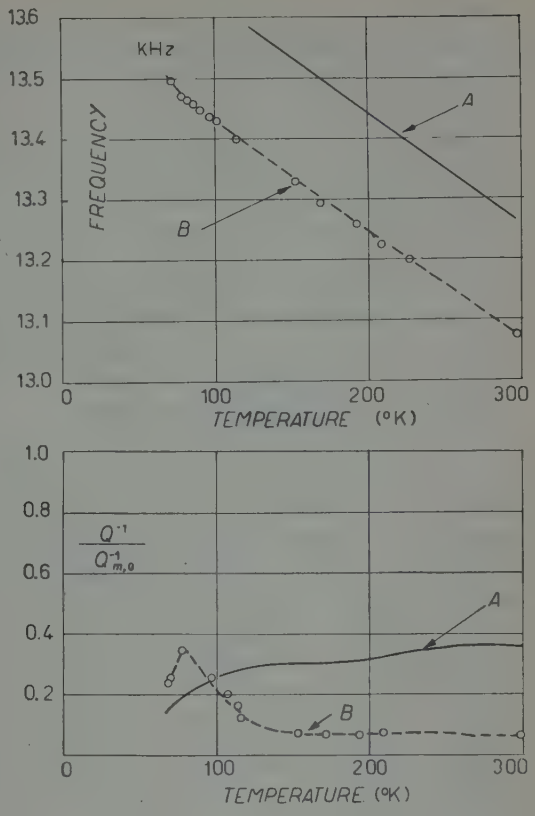

Fig. 16. – Effect of cold work upon frequency and damping. Plate n. 2, flexural vibrations ($m=1$, $n=0$). A) after 1 h at 873 °K; B) after a permanent strain of $1.5 \cdot 10^{-2}$ parallel to the plate axis. The values of frequency have been corrected for the change in thickness.

4. – Discussion.

4·1. *Activation energy.* – The values of frequency and temperature at which the maximum damping occurs (after machining and before any heat treatment) are given in Table IV. If the logarithm of frequency f is plotted against the inverse of temperature, the experimental points are placed, with good accuracy, on the same straight line. This shows that the peak of the damping curve is associated with a characteristic relaxation frequency ω which depends exponentially upon the temperature [15]

$$\omega = \omega_A \exp\left[-\frac{W}{kT}\right]. \tag{5}$$

[15] The term «frequency of a dislocation» is commonly employed, but it must be remembered that it has only a statistical meaning. From the classical standpoint it means only the inverse of a characteristic time. The maximum damping occurs when the product of ω by the vibration period equals unity.

Moreover the two parameters ω_A and W have the same value for the flexural vibrations of plates and for their longitudinal vibrations, as the points of Fig. 17 are placed on the *same* line. In fact for each type of vibration the distance between the experimental points is large enough to show an eventual difference in the slope or position of the straight lines drawn separately through the points belonging to each type of vibration.

TABLE IV. – *Frequency dependence of the temperature of maximum damping.*

Vibrating system	Vibration mode F = flexural L = longitudinal m = nodal circles n = nodal diameters l = nodal lines p = nodal planes	Frequency f (kHz)	Temperature T (°K)	$k \ln f$ (eV · molecule^{-1} · degree^{-1})	T^{-1} (°K^{-1})
Rod n. 1	F, $l=2$	1.882	72.0	$0.0649 \cdot 10^{-2}$	$1.390 \cdot 10^{-2}$
Plate n. 4	F, $m=1$, $n=0$	13.160	82.5	0.0816	1.212
Plate n. 2	F, $m=1$, $n=0$	13.418	81.6	0.0818	1.226
Plate n. 2 (*)	F, $m=1$, $n=0$	13.418	82.0	0.0818	1.220
Plate n. 1a (*)	F, $m=1$, $n=0$	13.716	82.4	0.0820	1.214
Plate n. 5 (**)	F, $m=0$, $n=2$	14.912	80.5	0.0827	1.242
Plate n. 1b	F, $m=1$, $n=0$	22.470	84.5	0.0862	1.183
Plate n. 6 (**)	F, $m=1$, $n=0$	24.805	84.0	0.0871	1.190
Plate n. 1b	F, $m=1$, $n=1$	45.470	89.0	0.0923	1.124
Plate n. 1a (*)	F, $m=1$, $n=2$	49.880	86.9	0.0931	1.151
Plate n. 1a (*)	F, $m=1$, $n=2$	49.880	88.0	0.0931	1.136
Plate n. 5 (**)	L, $p=1$	550.9	102.5	0.1138	0.9757
Plate n. 5 (**)	L, $p=2$	1088.4	111.5	0.1196	0.8969
Plate n. 6 (**)	L, $p=4$	1916.0	114.0	0.1245	0.877
Plate n. 5 (**)	L, $p=5$	2711.0	119.7	0.1275	0.835
Plate n. 5 (**)	L, $p=10$	5415.2	126.0	0.1334	0.794
Plate n. 5 (**)	L, $p=12$	6492.0	130.0	0.1350	0.769

(*) Temperature measured with « unbroken » thermocouple in a hole of the vibrating plate; from data not listed in Table III.
(**) With ring.

When the natural logarithm of frequency is multiplied by the constant k, as it was done in Fig. 17, the slope of the line gives directly the value of the activation energy W. Owing to the very wide frequency range on which measurements were made (from 1.882 kHz to 6.492 MHz) to which corresponds an interval from 72.0 °K to 130 °K for the temperature of maximum damping, the activation energy W may be computed from Fig. 17 with an error smaller than $\pm 4\%$

(6) $$W = (0.122 \pm 0.005) \text{ eV (molecule)}^{-1} .$$

3200

The intercept of the straight line with the frequency axis gives the value of $k \ln f = k \ln (\omega_A/2\pi)$ for vanishing T^{-1}. The factor ω_A of equation (5) has then the value

$$\omega_A = 23.9\,(1.8)^{\pm 1} \cdot 10^{11}\ \mathrm{s}^{-1}\,. \tag{7}$$

The factor $(1.8)^{\pm 1}$ is due to the uncertainty in the slope and the position of the straight line. The theory of dislocation damping developed by SEEGER [16]

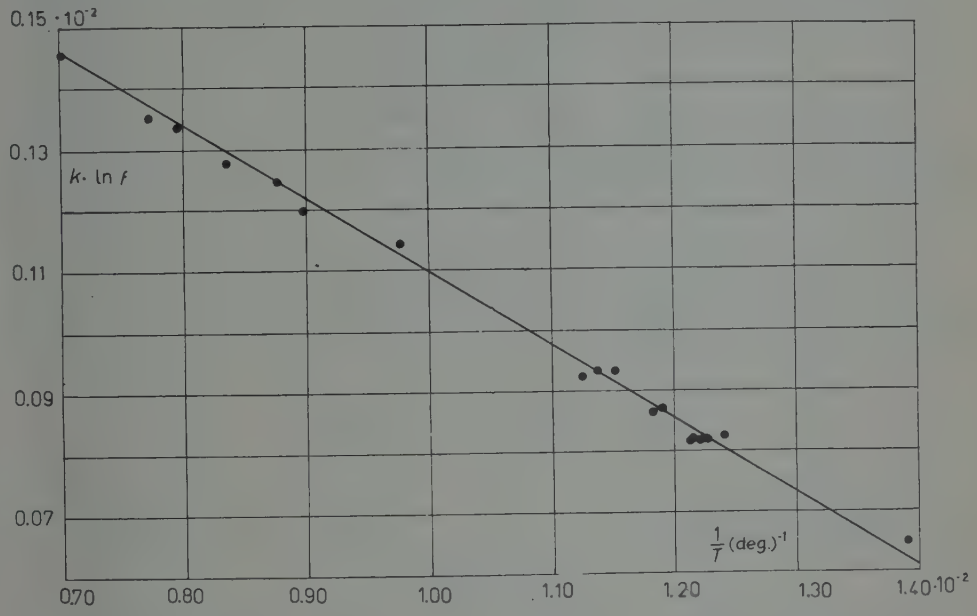

Fig. 17. – Frequency dependence of the temperature of maximum damping for the machined material. Activation energy: $W = 0.122$ eV (molecule)$^{-1}$; $\omega_A = 23.9 \cdot 10^{11}$ s^{-1}.

gives W and ω_A in terms of one unknown parameter, the Peierls stress τ_p^0 [17] by means of the following equations,

$$W = \frac{7b^3}{\pi^3}\,\mu \sqrt{\frac{\tau_p^0}{\mu}}\,, \tag{8}$$

$$\omega_A = \frac{\sqrt{10 \cdot \pi}}{b}\, v_s \sqrt{\frac{\tau_p^0}{\mu}}\,, \tag{9}$$

---

[16] A. SEEGER: *Phil. Mag.*, **1**, 651 (1956). See also W. P. MASON: *Physical Acoustics and the Properties of Solids*, 1st ed. (New York, 1958), pp. 266, 271.

[17] The parameter τ_p^0 is the stress required to force the dislocation over the steepest part of the Peierls potential.

where: b = distance between the closest atoms in the glide direction of the dislocation $= 2.5512 \cdot 10^{-8}$ cm for copper; μ = second Lamé constant or shear modulus $= 4.6 \cdot 10^{11}$ dynes cm^{-2} for copper; v_s = shear velocity in the glide plane $= 2.27 \cdot 10^5$ cm$\cdot$s^{-1} for copper ([18]).

The best way to check this theory with the experimental data is to use the value of W, which is known with a fairly good accuracy from Fig. 17, to compute the ratio τ_p^0/μ by means of equation (8), and to insert this value in to equation (9) to find the limiting frequency ω_A. The values obtained are

$$\tau_p^0/\mu = 4.18 \cdot 10^{-4}, \tag{10}$$

$$\omega_A = 12.5 \cdot 10^{11}\ \text{s}^{-1}. \tag{11}$$

The limiting frequency ω_A calculated in this way can be considered in a good agreement with the experimental value given by (7) if one takes in account the peculiar assumptions of the Seeger's theory ([16]). Moreover the ratio τ_p^0/μ is very near the upper limit found by COTTRELL ([19]), which is $3.6 \cdot 10^{-4}$.

A different calculation of the temperature dependence of the relaxation frequency has been recently given by SEEGER, DONTH and PFAFF ([20]). According to the theory of stochastic processes ω and T must satisfy the equation:

$$\ln \omega = F_1(r, \alpha) + \ln \frac{2\pi B}{T} + \ln T. \tag{12}$$

The function F_1 is given by a graph, and the dimensionless variables r and α are defined by:

$$r = \frac{2W_k}{kT}, \tag{13}$$

$$\alpha = 1 - \frac{\pi}{8} \frac{\tau}{\tau_p^0}, \tag{14}$$

where: W_K is the energy of a kink of the dislocation and does not depend upon T; τ is the shearing stress acting upon the dislocation.

The parameter B contained in (12) has the physical dimensions of a frequency, and is given by

$$B = \frac{\pi^2 k}{6b^4} \sqrt{\frac{1}{\varrho\mu}} \cdot T, \tag{15}$$

where ϱ = density = 8.94 g cm^{-3} for copper.

([18]) See footnote ([16]).

([19]) A. H. COTTRELL: *Dislocation and Plastic Flow in Crystals*, 1st ed. (Oxford, 1953), pp. 62, 64.

([20]) A. SEEGER, H. DONTH and F. PFAFF: *Discussions Faraday Society*, **23**, 19 (1957).

Then the ratio B/T depends only upon the physical properties of the material; for copper

$$\frac{B}{T} = 2.66 \cdot 10^{8}\ \mathrm{s^{-1} \cdot deg^{-1}}. \tag{15'}$$

If the values of T and ω corresponding to an attenuation peak are known, the equations (12) and (15') give the value of $F_1(r, \alpha)$. Since the measurements were all done at low strain amplitudes ($\tau < \tau_p^0$), equation (14) reduces to $\alpha \approx 1$ and the graph of the function F_1 gives the value of r corresponding to the experimental data. The relaxation frequency may be computed for any temperature by means of equations (12) and (13). This has been done choosing a central point on the experimental curve of Fig. 17 ($T^{-1} = 1.050 \cdot 10^{-2}$; $k \ln f = k \ln (\omega/2\pi) = 0.103 \cdot 10^{-2}$ eV$\cdot$(molecule$\cdot$degree)$^{-1}$) to compute F_1 and r for $\alpha = 1$ and $\alpha = 0.9$, and the results are shown in Fig. 18. The agreement

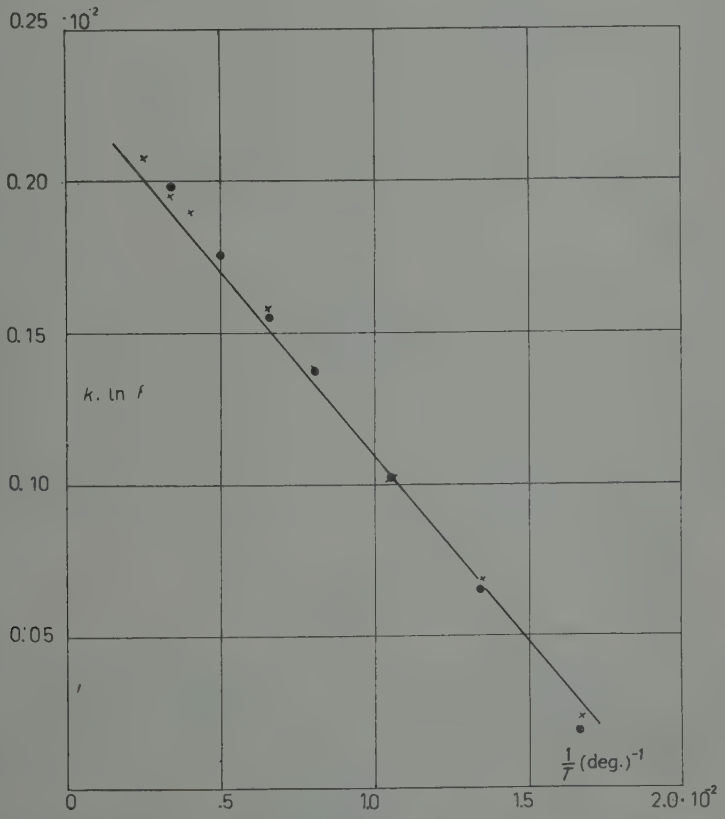

Fig. 18. – Comparison between experiment and the theory of Seeger, Donth and Pfaff. ● computed values for $\alpha = 1$; × computed values for $\alpha = 0.9$. Heavy line: average of experimental data.

between the experimental data and the calculation is satisfactory; however the theoretical points lie on a line somewhat steeper than the one found experimentally. A slight correction of the values taken by the function F_1 seems therefore to be needed to obtain a complete agreement between the theory and the experiment.

Since the value of r is known for a given temperature, the energy W_k of a kink may be computed according to the equation (13) and from it the ratio τ_p^0/μ is derived by means of the relation:

$$\frac{\tau_p^0}{\mu} = \frac{2\pi^3}{3\sqrt{3}} \cdot \frac{W_k^2}{\mu^2 b^6} = \frac{\pi^3}{6\sqrt{3}} \frac{r^2 k^2 T^2}{\mu^2 b^6} . \tag{16}$$

From the experimental data this value is found to be:

$$\frac{\tau_p^0}{\mu} = 4.72 \cdot 10^{-4} , \tag{16'}$$

and is quite near to that given by equation (10).

The same theory gives the number per unit volume of dislocation loops (of average length L) contributing to the relaxation process, as a function of maximum damping Q_m^{-1}. Taking $Q_m^{-1} = 425 \cdot 10^{-5}$ (cf. Table III):

$$L^3 N_0 \approx 24 \cdot Q_m^{-1} \approx 0.1 , \tag{17}$$

which for an average loop length of $4.5 \cdot 10^{-5}$ cm gives a density $N_0 = 10^{12}$ cm^{-3}.

4·2. *Relaxation spectrum.* – If the relaxation effect were due to the sum of many elementary effects associated with the single dislocations and having all the same values of the parameters W and ω_A, the experimental curves would coincide with those derived by the Zener theory for a single relaxation time ([21]). According to this theory the ratio of Q^{-1} to its maximum value Q_m^{-1} depends only upon the ratio:

$$\overline{y} = \frac{Q^{-1}}{Q_m^{-1}} = \operatorname{sech}\left(\ln \frac{\omega}{\omega_m}\right), \tag{18}$$

where ω_m is the characteristic relaxation frequency for maximum damping. Taking for ω the expression given by (5), a normalized expression is obtained for all the relaxation effects associated with given values of ω_A and W,

$$\overline{y} = \frac{Q^{-1}}{Q_m^{-1}} = \operatorname{sech} \frac{W}{k}\left(\frac{1}{T_m} - \frac{1}{T}\right), \tag{19}$$

([21]) C. ZENER: *Elasticity and Anelasticity of Metals*, 1st ed. (Chicago, 1948), pp. 46, 47.

where T_m is the temperature corresponding to the maximum damping and is related to ω_m and to ω_A by

$$\omega_m = \omega_A \exp\left[-\frac{W}{kT_m}\right]. \tag{20}$$

Taking for W the value given by (6) the experimental values of Q^{-1}/Q_m^{-1} have been compared with the curve given by (19) (Fig. 19). The comparison has been made for every type of vibration and for very different frequencies; curve A gives the values measured for the flexural vibrations of the rod n. 1 ($f = 1.882$ kHz); curve B those obtained for the plate n. 2, vibrating with a single nodal circle ($f = 13.418$ kHz); curve C those obtained for plate n. 5 vibrating longitudinally with two nodal planes ($f = 1.088$ MHz). In every case the experimental curves are much broader than the theoretical curve Z for a single relaxation time.

Since the hypothesis of a single relaxation time must necessarily be rejected, the two simplest assumptions that can be made are:

a) all the elementary relaxation effects have the same value for ω_A, but different activation energies W;

b) all the elementary relaxation effects have the same activation energy W, but different values for ω_A.

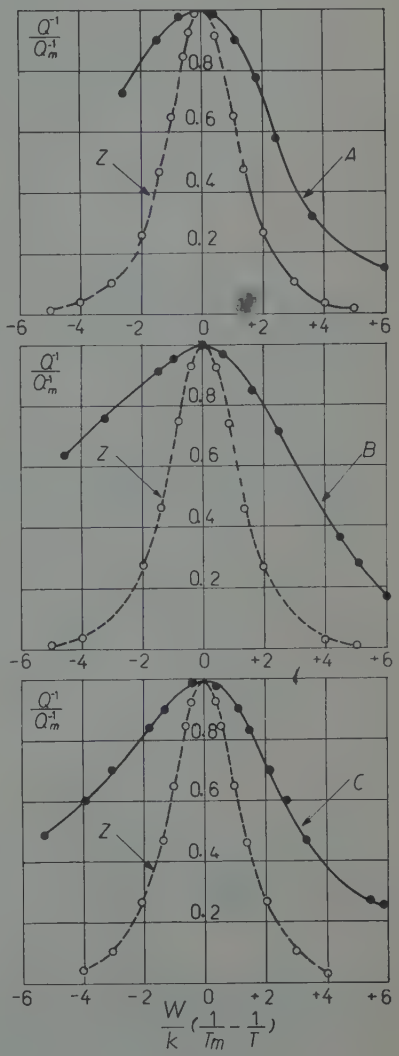

Fig. 19. – Comparison between the experimental data and the theory for a single relaxation time. Abscissae $(W/k)\,(1/T_m - 1/T)$; ordinates Q^{-1}/Q_m^{-1}. Curve A, measurements on rod n. 1; $(F, l=2)$ curve B, measurements on plate n. 2 $(F, m=1, n=0)$; curve C, measurements on plate n. 5 $(L, p=2)$ curve Z, computed values for a single relaxation time [equation (19)].

According to the first hypothesis, if S is the total relaxation strength [22] and $\varrho(W)$ the relaxation strength density with respect to the activation energy, then the relaxation strength of all the dislocations with an activation energy between W and $W+\mathrm{d}W$ is $\mathrm{d}S=\varrho(W)\cdot\mathrm{d}W$. Owing to the exponential relation between ω and W, a constant density with respect to the energy corresponds to a constant density with respect to $\ln\omega$ for a fixed value of the temperature. When the width of the energy spectrum is $2\Delta W$, the ratio r^2 of the maximum frequency ω_2 of the spectrum to the minimum frequency ω_1 is given by

$$r^2=\frac{\omega_2}{\omega_1}=\exp\left[\frac{2\Delta W}{kT}\right], \tag{21}$$

and decreases with increasing temperature. If the center of the energy spectrum is denoted by $\overline{W}$ and the corresponding frequency by $\overline{\omega}$, then the value of Q^{-1} is given as a function of temperature by

$$Q^{-1}=\frac{S}{2\Delta W}\,kT\,\mathrm{arctg}\left[\overline{y}\cdot\sinh\frac{\Delta W}{kT}\right], \tag{22}$$

where $\overline{y}$ is the damping function for a single relaxation frequency given by (18), (19) and (20), where $\overline{\omega}$ and $\overline{W}$ take the place of ω and W.

To compare the damping computed by means of (22) with the experimental results, the values given by (6) and (7) were taken as good approximation for $\overline{W}$ and ω_A, and ΔW was chosen in order to make the theoretical curve as near as possible to the damping measured on plate n. 2 at about 13 kHz. The same values of $\overline{W}$, ω_A and ΔW have been employed to compute the damping measured for longitudinal vibrations on plate n. 5 at about 1 MHz. Fig. 20 shows that for the high frequency vibrations the computed curve is much narrower than the experimental one, and therefore the hypothesis *a*) does not seem to agree with the experimental data.

A more satisfactory result is obtained from the hypothesis *b*), with a constant logarithmic density. In this case, the ratio r^2 of the maximum frequency of the spectrum ω_2 to the minimum frequency ω_1 does not depend

---

[22] The relaxation strenght S is defined as the difference between the unrelaxed and relaxed elastic moduli M_U and M_R, divided by their geometric mean. Owing to the smallness of S the following relations hold with good approximation:

$$S=\frac{M_U-M_R}{\sqrt{M_U M_R}}\simeq\frac{M_U-M_R}{M_U}\simeq\frac{M_U-M_R}{M_R}.$$

For the derivation of the following formulae on relaxation spectra, see: P. G. BORDONI: *Thermally activated relaxation effects with continuous spectra* (in press).

3206

upon temperature, and Q^{-1} is given by

$$Q^{-1} = \frac{S}{2\eta} \operatorname{arctg}\left[\overline{y} \cdot \sinh \eta\right], \tag{23}$$

where $\omega_m = \sqrt{\omega_1 \omega_2}$, $\eta = \ln r$, and $\overline{y}$ has the same meaning as in (22).

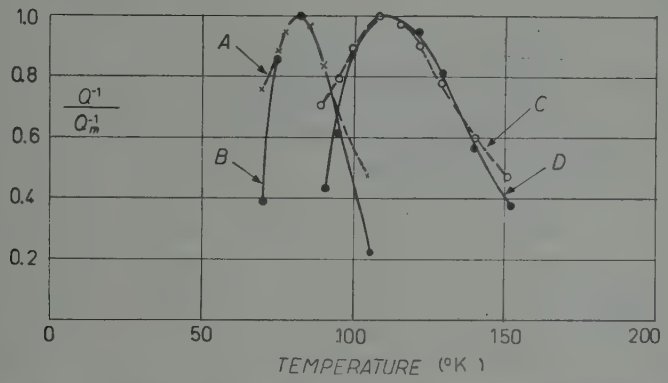

Fig. 20. – Comparison between experiment and theory for a relaxation spectrum with W variable and ω_A constant. Curves A, C: measurements on plate n. 2 at 13 kHz and on plate n. 5 at 1 MHz; curves B, D: computed for the same plates, according to (22) with the values of W and ω_A given by (6) and (7) and $\Delta W = 0.019$ eV (molecule)$^{-1}$.

Fig. 21 shows that it is possible to choose a value for the bandwidth ($r = 15$, $\eta = 2.70$) which makes the theoretical curves agree fairly well with the experimental ones both at low and high frequency. Obviously the agreement

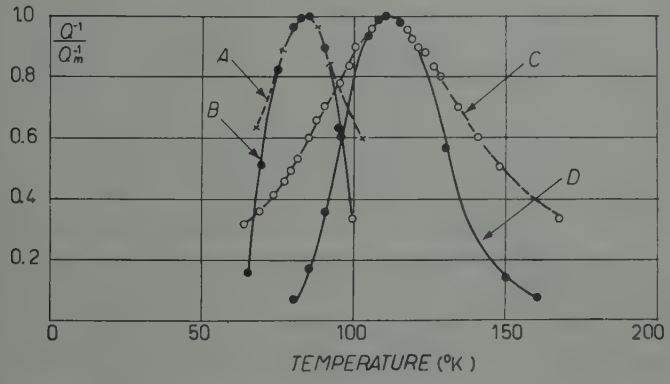

Fig. 21. – Comparison between experiment and theory for a relaxation spectrum with W constant and ω_A variable. Curves A, C, are the same as in Fig. 20; curves B, D, have been computed according to (23) with $\eta = 2.70$.

3307

is limited to the values of Q^{-1} near the maximum; in fact the lower values of the damping are considerably affected by the shape of the relaxation spectrum, which is only roughly represented by a constant density. Moreover the effect of other causes of damping different from the relaxation of dislocations is more severely felt when the damping due to the latter cause is small, so that no satisfactory agreement between theory and experiment can be expected at a distance from the peak.

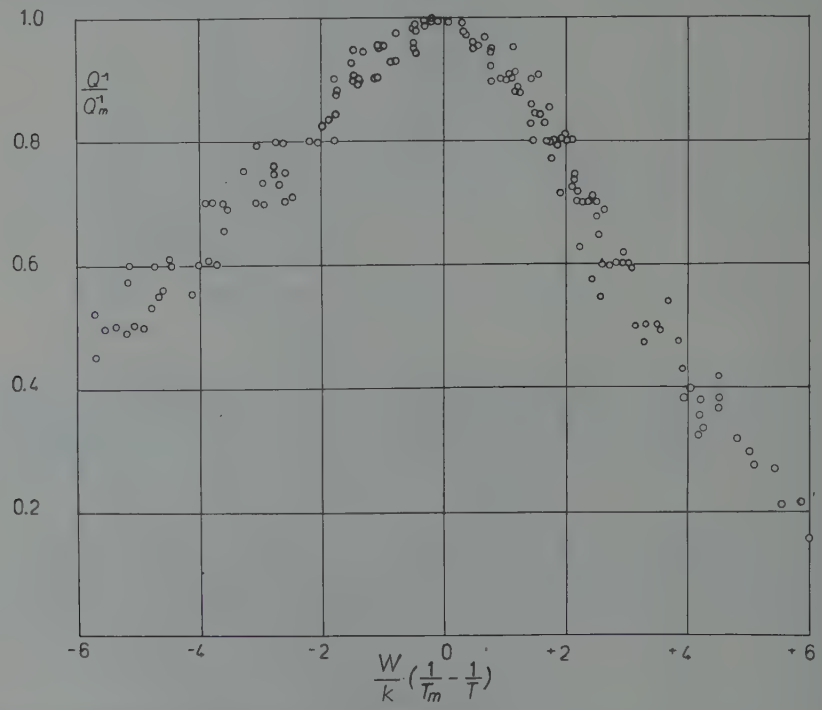

Fig. 22. - Comparison between all the measurements of Table III plotted as a function of the variable $(W/k)(1/T_m - 1/T)$; ordinates: Q^{-1}/Q_m^{-1}.

It must be observed that, according to the assumption *b*) for a given frequency spectrum, the ratio between Q^{-1} and its maximum value Q_m^{-1} depends only upon the variable $(W/k)(1/T_m - 1/T)$ as in the case of a single relaxation time. In Fig. 22 all the experimental data listed in Table III have been plotted as a function of this variable. To make the measurements at high frequency comparable with the other ones, the value of damping at room temperature has been reduced to the common value of $60 \cdot 10^{-5}$. The agreement between the different measurements is quite satisfactory, considering the wide range of frequencies covered (from 1.8 kHz to 6.4 MHz; see Table II). The main difference between the average experimental curve and the damping

3208

computed by means of (23), is that the former is markedly asymmetrical with respect to its maximum, with the low-temperature branch higher than the other one. The asymmetry cannot be due to the presence of an additional attenuation produced by thermoelastic effect; in fact this kind of attenuation decreases with temperature and any correction for this type of damping would make the curves still more asymmetrical. The difference between the values of damping for points whose abscissae differ only in sign is found to be a linear function, which increases as $(W/k)(1/T_m - 1/T)$ becomes more negative. It seems therefore probable that the asymmetry of the damping curve is mainly due to the Niblett and Wilks maximum, whose peak is out of the range covered by Fig. 22 for all the frequencies considered.

To get some additional information about the shape of the relaxation spectrum related to the main peak, the average curve drawn through the points of Fig. 22 has been corrected for the effects of the secondary maximum. The curve obtained (Fig. 23*a*) is quite well represented by the function

$$(24) \qquad \frac{Q^{-1}}{Q_m^{-1}} = \operatorname{sech}\left[\alpha \frac{W}{k}\left(\frac{1}{T_m} - \frac{1}{T}\right)\right],$$

with $\alpha = 0.39$. According to the theory given by Fuoss and Kirkwood [23] the relax-

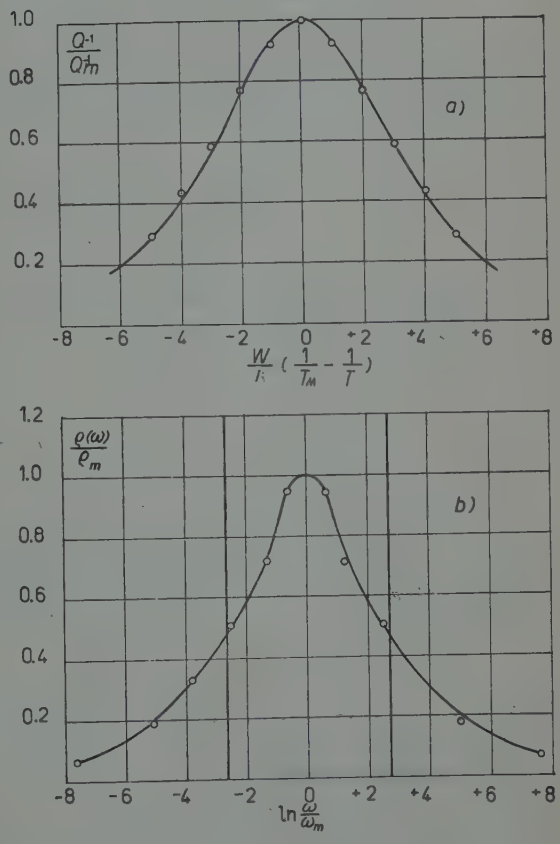

Fig. 23. – *a*) Comparison between the average values of attenuation obtained from Fig. 22 and corrected for the Niblett and Wilks maximum (circles) and the attenuation curve computed for a Fuoss and Kirkwood spectrum ($\alpha = 0.392$; heavy line). Abscissae: values of $(W/k)(1/T_m - 1/T)$; ordinates: Q^{-1}/Q_m^{-1}. *b*) Fuoss and Kirkwood spectrum for $\alpha = 0.392$ and a rectangular spectrum having the same total relaxation strength. Abscissae: $\ln(\omega/\omega_m)$; ordinates: ratio of the spectrum density to its maximum value.

[23] R. M. Fuoss and J. G. Kirkwood: *Journ. Chem. Phys.*, **63**, 385 (1941).

ation spectrum is then given by:

$$\varrho(\omega) = \frac{2S}{\pi} \frac{\cos(\alpha\pi/2)\cdot\cosh(\alpha\cdot\ln(\omega_m/\omega))}{\cos^2(\alpha\pi/2) + \sinh^2(\alpha\cdot\ln(\omega_m/\omega))}. \tag{25}$$

In Fig. 23*b*, the spectrum given by (25) for $\alpha = 0.39$ is compared with the rectangular spectrum having the bandwidth $\eta = 2.70$ and the same total relaxation strength.

4·3. *Modulus relaxation strength and maximum damping.* – In the very simple case of a rectangular spectrum the vibration frequency f can be obtained as a function of the variable $(W/k)(1/T_m - 1/T)$ and of the « relaxed » frequency f_R, corresponding to an instantaneous motion of the dislocations:

$$\frac{f - f_R}{f_R} = \frac{S}{2}\left\{\frac{1}{2} + \frac{1}{4\eta}\ln\left[\frac{\cosh[r - (W/k)(1/T_m - 1/T)]}{\cosh[\eta + (W/k)(1/T_m - 1/T)]}\right]\right\}. \tag{26}$$

It will be noticed that the limiting value of $(f/f_R - 1)$ for vanishing T, is independent of the width of the spectrum and equals $S/2$, whilst the maximum damping depends upon the width of the spectrum, and is given by

$$Q_m^{-1} = \frac{S}{2}\frac{\operatorname{arctg}(\sinh\eta)}{\eta} = 0.535\cdot\frac{S}{2}, \tag{27}$$

according to (23). The derivative of the frequency with respect to the variable $\xi = (W/k)(1/\overline{T}_m - 1/T)$ computed for $T = \overline{T}_m$, is inversely proportional to the width of the rectangular spectrum

$$\frac{1}{f_R}\left[\frac{\partial f}{\partial \xi}\right]_{\xi=0} = -\frac{S}{2}\frac{\operatorname{tgh}\eta}{2\eta} \approx -\frac{S}{2}\cdot\frac{1}{2\eta} = -0.185\frac{S}{2}. \tag{28}$$

For the Fuoss and Kirkwood spectrum the analogous of (26) and (28) cannot be obtained in closed form; however it is easily proved that the limiting value of $(f/f_R - 1)$ when T vanishes is still $S/2$, whilst the maximum damping depends upon the spectrum width, as in the rectangular case, and is given by

$$Q_m^{-1} = \alpha\frac{S}{2} = 0.392\frac{S}{2}. \tag{29}$$

The frequency derivative with respect to ξ can be obtained from a diagram; its value for $T = \overline{T}_m$ and $\alpha = 0.392$ is

$$\frac{1}{f_R}\left[\frac{\partial f}{\partial \xi}\right]_{\xi=0} = -0.138\frac{S}{2}. \tag{30}$$

The values of $(f/f_R - 1)$ can be obtained from the experimental data subtracting from the measured frequency at the temperature T, the frequency computed with a linear extrapolation from room temperature measurements [24]. The results of this computation are shown in Fig. 24 together with the damping

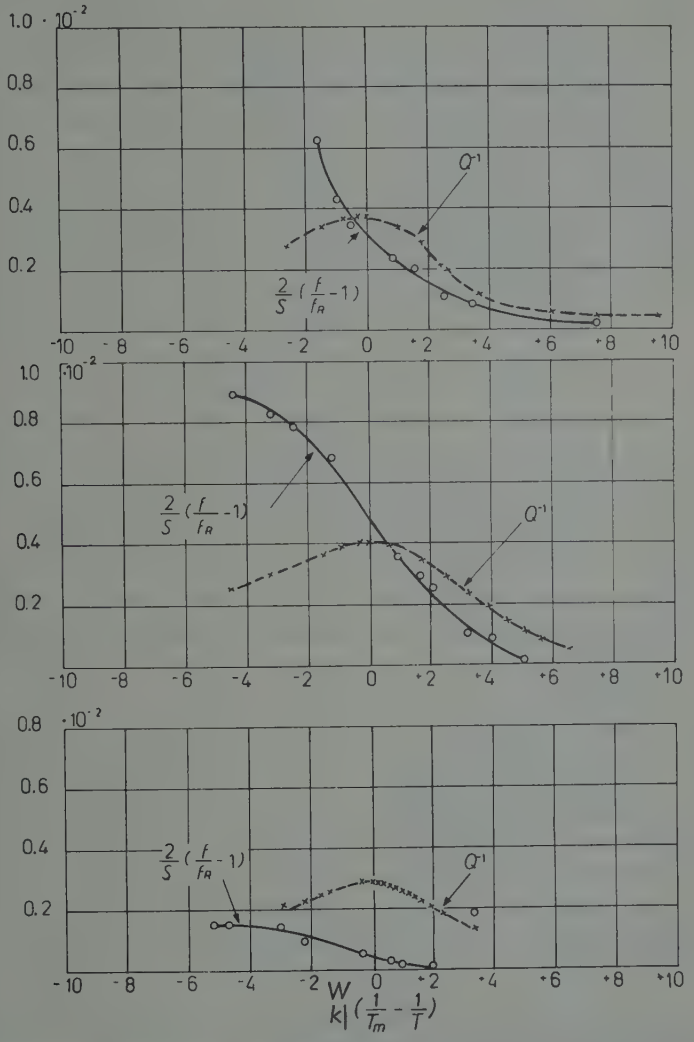

Fig. 24. – Frequency relaxation and attenuation for different frequencies. Abscissae: $(W/k)(1/T_m - 1/T)$; ordinates: Q^{-1} and $(f/f_R - 1)$. Upper curves rod n. 1 (1.8 kHz); middle curves, plate n. 2 (13 kHz); lower curves, plate n. 5 (1 MHz).

---

[24] The values of $(f/f_R - 1)$ obtained in this way are always smaller than the real ones, owing to the curvature of the frequency *vs.* temperature curve for the material free from dislocations, which is neglected in the present computation. However the error is quite small for the considered temperature interval.

curves, plotted in the same scale for comparison purposes. For the flexural vibrations of rods and plates the ratio between the maximum damping and the total relaxation is near 0.4 and agrees better with the value given by (29) than with the value computed according to (27), as it could be expected from the previous discussion on the shape of the spectrum. No similar agreement is however found for the high frequency measurements. In this case the total relaxation of the frequency is about one fifth of the one measured for flexural vibrations, whilst the maximum damping has almost the same value.

It is not difficult to explain the strong reduction found in the total relaxation, observing that the motion of dislocations changes the shape of the solid, rather than its volume. If we assume that the compressibility modulus $\lambda+\frac{2}{3}\mu$ is not affected by the motion of dislocations, the following relation is found between the relaxation strength $S^{(l)}$ for longitudinal vibrations and the corresponding value $S^{(e)}$ for the flexural or extensional ones:

$$S^{(l)} = 2S^{(e)} \frac{[c^{(t)}]^4}{[c^{(e)}]^2 \cdot [c^{(l)}]^2}, \tag{31}$$

where $c^{(t)}$, $c^{(e)}$, $c^{(l)}$, are the velocities for torsional, extensional and longitudinal waves. Taking for them the values given by the literature ($c^{(t)} = 2\,260$ m s^{-1}, and in the same units $c^{(e)} = 3\,580$ and $c^{(l)} = 4\,600$), the relaxation of longitudinal velocity or frequency is found to be 0.19 of that for flexural and extensional vibrations, in satisfactory agreement with the experimental results.

It must still be explained why the maximum damping is little affected by the type of vibrations, and may even take values larger than $S/2$, in apparent contradiction with the theory of relaxation. To this purpose it must be remembered that measurements were made on a polycrystalline material, whose average grain size, according to Fig. 6, is of the order of 10^{-2} of the wavelength when the vibrations are in the megacycle range. Owing to the large anisotropy of copper crystals and to the random orientation of grains, the stress is then not entirely of longitudinal type, but may be considered as the sum of a purely longitudinal stress and of a more complex stress changing from grain to grain. The latter stress does not correspond to any appreciable macroscopic force, because of the randomness of the grain orientation, and therefore has no influence upon the vibration frequency. On the contrary, the elastic energy associated with the same stress is not negligible in comparison with the energy associated with the longitudinal part, and must be taken into account when the total energy dissipation is evaluated. This fact explains why Q_m^{-1} which can be larger than the value which could correspond to a purely longitudinal stress.

In Fig. 25 *a* the esperimental value of $(f/f_R - 1)$ measured on plate n. 2 at about 13 kHz (curve *A*) are compared with those computed by means of

(26) for a rectangular spectrum. If the same bandwidth is taken as for the attenuation curve ($\eta = 2.70$, curve B), the agreement with the experimental data is rather poor; moreover the slopes of the theoretical and experimental curves are not the same at the inflexion point. Hence according to (28) the value chosen for η cannot be the right one. If a larger bandwidth is taken in order to have the same slope as the experimental curve ($\eta = 3.5$, curve C) the agreement in somewhat better, but the attenuation curve becomes too wide in comparison with the experimental data.

A more satisfactory result is found when the same curve A is compared with the theoretical relaxation curve for a Fuoss and Kirkwood spectrum, as it is done in Fig. 25 b (curve D). Taking for α the value which is found to fit best with the attenuation measurements ($\alpha = 0.392$) (see Fig. 23 a) the general agreement is quite satisfactory, and the slope of the two curves at the inflexion point is exactly the same, as is required by (30).

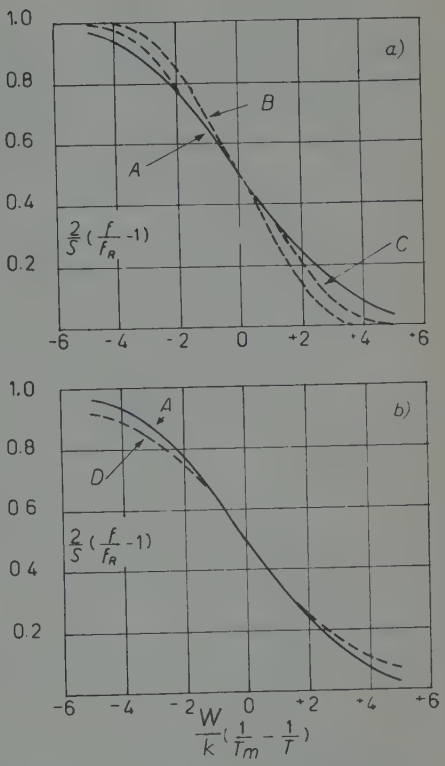

Fig. 25. – Comparison between the experimental relaxation of frequency measured on plate n. 2 (13 kHz) (curve A) with the theoretical curves for a rectangular spectrum (B, $\eta = 2.70$; C, $\eta = 3.5$) and for a Fuoss and Kirkwood spectrum (D, $\alpha = 0.392$). Abscissae $(W/k)(1/T_m - 1/T)$; ordinates $(2/S)(f/f_R - 1)$.

4·4. *Niblett and Wilks peak.* – The small maximum which was first noticed a little above 30 °K by NIBLETT and WILKS, is clearly exhibited as a « bump » by the curve which gives the attenuation values down to the liquid Helium temperature (Fig. 8). The secondary maximum can be separated from the main one, computing the hyperbolic cosine of the ratio Q_m^{-1}/Q^{-1} and plotting it as a function of $(W/k)(1/T_m^{-1} - 1/T^{-1})$. According to the previous remarks on the shape of the relaxation spectrum, the curves obtained in this way are straight lines near the main maximum and on the high temperature side, where the effects of the secondary maximum are little felt. The low temperature peak can be isolated taking the difference between the straight line obtained by extrapolation of the values near the main maximum, and the

actual curve. The hyperbolic secant of these values multiplied by Q_m^{-1} gives the attenuation due to the Niblett and Wilks peak. The curves of Fig. 26 which show that the temperature of maximum damping increases with the

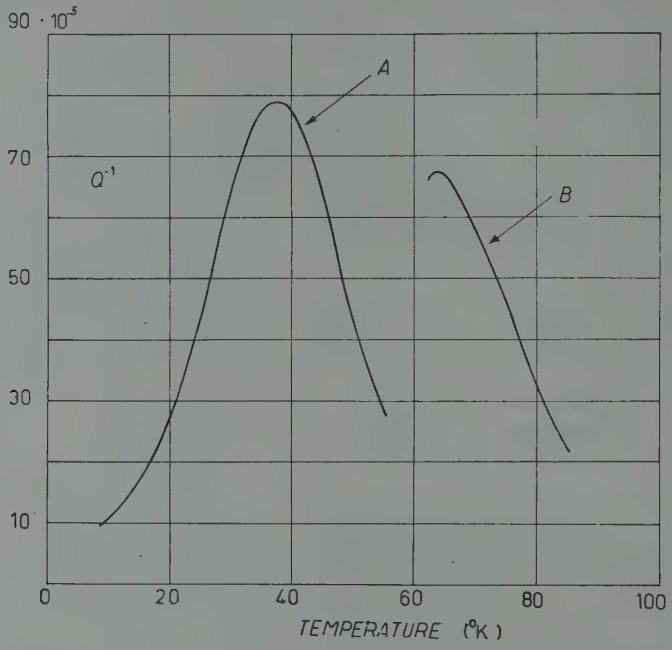

Fig. 26. – Niblett and Wilks peak. Curve A, plate n. 5 (F, $m=0$, $n=2$) frequency 15 kHz; curve B, plate n. 6 L, $p=4$, frequency 1.915 MHz.

vibration frequency as for the main peak, have been obtained in this way. The same computations have been made for other measurements (Table V) and the frequencies have been plotted in a logarithmic scale against $\overline{T}_m^{-1}$ (Fig. 27).

TABLE V. – *Frequency dependence of the temperature of the Niblett and Wilks peak.*

Vibrating system	Vibration mode	Frequency (kHz)	Temperature T (°K)	$k \ln f$ (eV · molecule^{-1} · degree^{-1})	T^{-1} (°K^{-1})
Plate n. 5	flexural $m=0$, $n=2$	15.087	37.5	$0.0828 \cdot 10^{-2}$	$2.67 \cdot 10^{-2}$
Plate n. 5	longitudinal $p=1$	551.00	55.5	0.114	1.80
Plate n. 6	longitudinal $p=4$	1915.0	64.0	0.126	1.56
Plate n. 5	longitudinal $p=12$	6492.0	69.5	0.135	1.44

The experimental points are placed on the same straight line, together with the points obtained for the same peak by NIBLETT and WILKS, CASWELL

and PARÉ ([25]). The activation energy computed from the slope of the line has the value

$$W' = 0.041 \text{ eV (molecule)}^{-1} \tag{32}$$

and is therefore about one third of the activation energy found for the main maximum. This low value of W' is consistent with the fact that the relaxation frequency associated with the Niblett and Wilks peak must necessarily

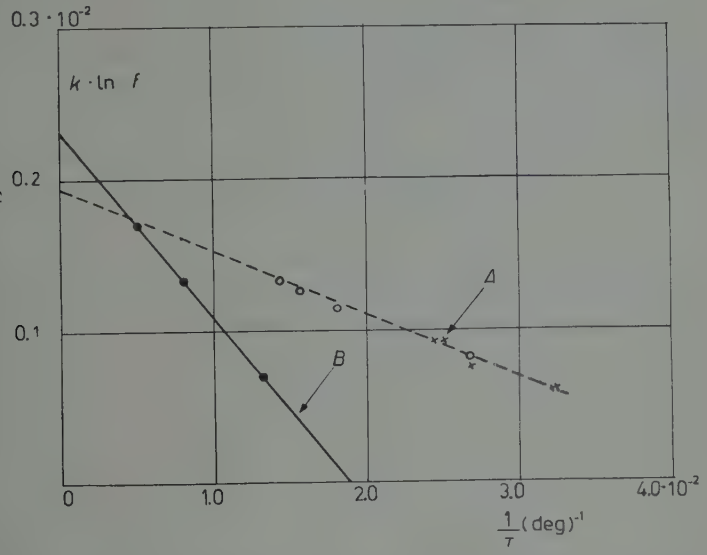

Fig. 27. – Frequency dependence of the temperature of maximum damping. Curve A, Niblett and Wilks peak. Activation energy 0.041 eV $(\text{mol})^{-1}$; $\omega_A = 6.10^9$. ∘ data of Table V; × values obtained by Niblett and Wilks, Caswell and Paré. Curve B, main relaxation peak (see Fig. 17).

be lower than the upper frequency limit due to the periodic structure of copper crystals. At the melting point ($T^{-1} = 0.7 \cdot 10^{-3}$) the value of $k \ln f$ cannot exceed $0.27 \cdot 10^{-2}$ eV (molecule · degree)$^{-1}$. This gives for the activation energy of the smaller peak an upper limit of 0.065 eV $(\text{molecule})^{-1}$ which shows that the value given by (32) is a reasonable one. It may be added that the shape of the curves of Fig. 26 is also consistent with the value found for W'. In fact both of them are somewhat broader than the curve for a single relaxation

([25]) V. PARÉ: *Experimental and Theoretical Study of Low Temperature Internal Friction in Copper*. Cornell University, Department of Engineering Physics, Technical Report n. 4 (July 1958).

time, plotted as a function of temperature according to the value of W' given by (33). This seems to point out that even the Niblett and Wilks maximum is associated with a relaxation spectrum, whose bandwidth seems to be of the same order as that found for the main maximum. It will also be noticed that at room temperature the relaxation frequencies associated with the two peaks have almost the same value, owing to the difference of their activation energies (Fig. 27).

4·5. *Heat treatments.* – The heat treatments may be broadly divided in two classes, according to their effect upon dislocations.

When the temperature of the treatment does not exceed 500 °K, the total number of dislocations is reduced or they become less active in the relaxation process. This is proved not only by the general lowering of the attenuation curve, but also by the reduction of frequency relaxation (Fig. 11, 12, 13). No other permanent change is undergone by the material and the limiting value of the frequency at very low temperatures does not vary. The dislocations more easily removed seem to be those associated with the lowest values of relaxation frequency; in fact, after the treatment the average frequency of the spectrum is higher, as is shown by the decrease of the temperature of maximum damping. The change in the value of $(T_m^{-1} - T^{-1})$ is of the order of $0.3 \cdot 10^{-2}$ °K^{-1}, which corresponds to an increase of the frequencies of the spectrum by a factor 1.5 according to the value found for the activation energy.

When the temperature of the treatment is considerably higher than 500 °K, the dislocations are entirely cancelled, the damping at the temperature of the maximum takes a value much lower than before the treatment and no trace of relaxation is found in the frequency curves (Fig. 14).

In addition to this effect, which is quite clearly understood, the material undergoes also a more complex permanent change of its elastic and anelastic behaviour. The frequency is raised by an amount independent of the temperature and almost proportional to the temperature coefficient of the frequency itself; at the same time the room temperature damping takes a much larger value than before the treatment and the material becomes very sensitive to non-linear effects and to handling (Fig. 15). In previous investigations only the changes in damping have been considered. These could be referred to the formation of new dislocations, and in this way also non-linear effects are explained. However the above hypothesis does not give any reason for the considerable rise in frequency, which must also be related in some way to dislocations as it may be cancelled by cold work like the increase in damping or the non-linear effects (Fig. 16).

3216

5. - Conclusion.

The temperature of the peak in the attenuation *vs.* temperature curve due to dislocations is related to the vibration frequency by an Arrhenius equation. The activation energy and the limiting value for the relaxation frequency when T increases, have the same value for flexural and longitudinal vibrations. Owing to the wide frequency range covered by the measurements the above parameters have been determined with remarkable accuracy. Their values agree satisfactorily with those computed by means of the theory given by SEEGER. The lack of agreement noticed in this respect by NIBLETT and WILKS, CASWELL and PARÉ is due to the fact that they derived the activation energy and the limiting frequency from the comparison of experimental data for different materials, or from measurements over a narrow frequency range, obtaining therefore values which were not accurate enough.

With respect to the more recent theory given by SEEGER, DONTH and PFAFF, it must be remarked that the experimental data seem to follow *exactly* an Arrhenius equation, in the temperature interval from 72 °K to 130 °K, whilst the theory gives a somewhat different law. However theory and experiment could be easily reconciled, within the limits of the experimental accuracy, by a slight change of some parameters involved in the theory.

The two values of the Peierls stress computed from the experimental data by means of the above theories, are quite close to each other and agree with the value found by COTTRELL on very different grounds.

The attenuation peak is not due to a single relaxation time but to a continuous spectrum, which seems to be of the type studied by FUOSS and KIRKWOOD, with a constant value of the activation energy for all the relaxation frequencies and a bell-shaped distribution of the limiting frequencies around a central value. This spectrum explains not only the shape of the curves which give the attenuation and the vibration frequency as a function of the temperature, but also the relation between the total frequency relaxation and the maximum damping for flexural vibrations.

When the vibrations are of longitudinal type, the total relaxation of frequency is found to be smaller than the maximum value of attenuation. This result, which seems to contradict the theory of relaxation effects, is due to the grain structure of the metal which gives rise to a stress distribution more complex than a purely longitudinal stress.

The small peak found by NIBLETT and WILKS is associated with an activation energy having a value which is about one third of the activation energy for the main maximum. This small value is consistent with the upper limitations for the vibration frequencies due to the periodic structure of crystals and with the shape of the attenuation *vs.* temperature curves.

The effect of heat treatment is only that of reducing the number of dislocations or their contribution to the anelastic strain, provided the temperature of the treatment does not exceed 500 °K. This effect is more pronounced for the dislocations having low relaxation frequencies; the relaxation spectrum is therefore displaced towards the high frequencies after the treatment.

When the temperature exceeds 500 °K the material undergoes also a permanent change of its elastic and anelastic behaviour, which does not seem to be directly related to any relaxation effect.

The comparison of the above results with those obtained by other experimenters on copper having a different impurity content and on single crystals, shows that the relaxation effect due to dislocations is not very sensitive to the impurity content or to the grain structure, but seems to be more directly related to the basic properties of the crystal lattice and to the interatomic bonds.

RIASSUNTO

Si sono misurati la frequenza e la dissipazione di onde elastiche nel rame policristallino fra 1.8 kHz e 6.5 MHz in funzione della temperatura nel campo da 60 °K a 300 °K. Si è potuto così calcolare con considerevole precisione, sia l'energia di attivazione W, sia la frequenza limite ω_A, associate al massimo di assorbimento provocato dalle dislocazioni. I valori ottenuti ($W = 0.122$ eV (molecole)$^{-1}$; $\omega_A = 23.9 \cdot 10^{11}$ s^{-1}) concordano in modo soddisfacente con quelli calcolati con la teoria di Seeger, Donth e Pfaff. La forma delle curve attenuazione-temperatura mostra che lo spettro delle frequenze di rilassamento è rappresentabile con una curva a campana che ha il suo massimo per il valore $\omega = \omega_m$ e che ciascuna frequenza dello spettro è associata con il medesimo valore dell'energia di attivazione sopra riportato. I valori massimi della dissipazione sono stati confrontati con il rilassamento totale che si osserva nelle curve frequenza-temperatura. Per le vibrazioni di frequenza al disotto di 100 kHz i risultati concordano con la teoria degli effetti di rilassamento aventi uno spettro continuo. A frequenze più elevate, la struttura policristallina del materiale dà invece origine ad una dissipazione maggiore di quella che corrisponderebbe ai valori del rilassamento. Sono stati anche studiati gli effetti provocati da trattamenti termici diversi e si è visto che, se durante il trattamento la temperatura non supera i 500 °K, si ottiene una riduzione degli effetti di rilassamento e, contemporaneamente, ω_A aumenta leggermente. Se durante il trattamento si raggiungono temperature più elevate, si provocano, nel rame policristallino, variazioni relativamente grandi della dissipazione e della frequenza delle onde elastiche, le quali sembrano non essere legate direttamente alle dislocazioni preesistenti. Queste variazioni possono essere cancellate con un opportuno incrudimento del materiale.

IL NUOVO CIMENTO Vol. XIV, N. 2 16 Ottobre 1959

The Interaction of K^--Mesons with Photographic Emulsion Nuclei.

Part II.

The Emission of Hyperons from K^--Interactions at Rest.

(K^--Collaboration)

B. Bhowmik (*), D. Evans, D. Falla, F. Hassan, A. A. Kamal (**), K. K. Nagpaul (***) and D. J. J. Prowse

H. H. Wills Physical Laboratory - University of Bristol

M. René

Laboratoire de Physique Nucléaire - Université Libre de Bruxelles

G. Alexander (****), R. H. W. Johnston and C. O'Ceallaigh

School of Cosmic Physics, Institute for Advanced Studies - Dublin

D. Keefe

University College - Dublin

E. H. S. Burhop, D. H. Davis, R. C. Kumar, W. B. Lasich M. A. Shaukat (****) and F. R. Stannard

Physics Department, University College - London

M. Bacchella (†), A. Bonetti, C. Dilworth, G. Occhialini and L. Scarsi

Istituto di Scienze Fisiche dell'Università - Milano

Istituto Nazionale di Fisica Nucleare - Sezione di Milano

M. Grilli, L. Guerriero, L. von Lindern (§), M. Merlin (×) and A. Salandin

Istituto di Fisica dell'Università - Padova

Istituto Nazionale di Fisica Nucleare - Sezione di Milano

(ricevuto il 28 Febbraio 1959 e licenziato dagli Autori il 15 Ottobre 1959)

(*) Now at the University of Delhi, India.

(**) Now at the University of Hyderabad, India.

(***) On leave of absence from the University of Pa njab, (in Part I, *Nuovo Cimento*, **13**, 690 (1959), it was mistakenly written Panjab, Pakistan).

(****) Now at Rehowoth, Israel.

(*****) Now at the Institute for Advanced Studies, Dublin.

(§) Now at C.I.S.E., Milano.

(†) Now at Max-Planck-Institute, München.

(×) Now at the Istituto di Fisica dell'Università, Bari.

Summary. — The emission of Σ-hyperons from 3037 K^- capture stars at rest in nuclear emulsion has been studied. The identification of the hyperons is discussed. Charged Σ-hyperons are emitted from $(17.6 \pm 1.0)\%$ of all K^--stars while $(9.6 \pm 0.6)\%$ of them lead to the emission of both Σ-hyperons and π-mesons. The Σ^-/Σ^+ ratio for all stars is 0.86 ± 0.12 while for stars in which a π-meson is also emitted it is 0.45 ± 0.10. The difference between this latter value and the markedly different value (2.0) obtained for K^--interactions at rest in a hydrogen bubble chamber is attributed to the Fermi motion of nucleons in the nucleus, and a dependence of the relative K^- transition amplitudes on the energy of relative motion of the K^--meson and nucleon. The branching ratio, R, of the number of Σ^+ decays to π^+ and proton respectively is 1.23 ± 0.27. The stable prong distribution of the stars in which a hyperon is emitted, as well as the energy distribution of the Σ-hyperons at emission has been studied. About 16% of all identified charged Σ-hyperons had an emission energy above 60 MeV, and had to be attributed to multi-nucleon interactions of the K^--meson. It is estimated that the proportion of all multi-nucleon primary capture processes may be as high as $(30 \div 40)\%$. The interaction of a K^--meson with a pair of neutrons seems to occur rarely, if at all. From the fraction of Σ^+ emitting stars which also emit a π^--meson it is concluded that only about 10% of the π^--mesons fail to escape from the nucleus in which capture occurs. This could be understood if K^--capture occurs predominantly in the peripheral region of the nucleus. From a similar study of Σ^- emitting stars it is found however that the proportion of π^+ or π^0-mesons, or both, that are absorbed in the nucleus is much higher. Estimates are made of the mean free path in nuclear matter of Σ-hyperons and π^0-mesons. Most of the one-nucleon interactions leading to Σ-hyperon production take place with protons and the transition amplitudes corresponding to the $T=1$ state of isotopic spin is smaller than the $T=0$ transition amplitude.

Introduction.

Part I [1] of this series of papers was concerned with the emission of π-mesons and stable particles from 3035 K^--meson capture stars at rest. We now present the results on the hyperons created in such interactions. The paper is divided into sections, the first of which explains the nomenclature used throughout to describe the different types of event. The second and third sections are devoted to an account of the difficulties involved in estimating the correct numbers of hyperons emitted, and the manner in which these problems of identification have been treated is outlined. Section **4** presents a summary of the corrected numbers of hyperons so obtained, and the relative frequencies of the various interactions and decays of Σ-particles.

[1] K^- Collaboration: *Nuovo Cimento*, **13**, 690 (1959).

Sections **5** and **6** give the data concerning the energy spectra of the hyperons, and the characteristics of the K^--stars from which such particles are emitted.

The final sections of the paper are devoted to questions of interpretation. These include the estimation of the importance of K^--interactions with 2 nucleons compared with those with one nucleon, and the probabilities that the secondary π-mesons produced will fail to escape from the nucleus. An attempt is made to estimate the numbers of the various primary K^--interaction processes among the capture stars studied and to account for the values of the absorption probabilities derived.

1. – The nomenclature used to describe decays and interactions of hyperons.

As discussed in I, all the prongs with $g^* > 2.5$ from K^--interactions were followed to rest or to a point where they decayed or interacted in flight or left the stack. The prongs were identified as due to stable particles, π-mesons, Σ-hyperons or hyperfragments by studying their ends for evidence of decay or interaction.

The heavy unstable particles emitted from K^--interactions are Σ^+, Σ^-, Σ^0 and Λ^0-hyperons and hyperfragments. Σ^0 and Λ^0-hyperons are difficult to identify in emulsion investigations of this kind. A few cases have been found of a Λ^0-hyperon associated with a K^--star but generally the emission of neutral particles goes unobserved.

Charged Σ-hyperons may decay in one of the processes

$$\Sigma^+ \to p + \pi^0 , \qquad \Sigma^+ \to n + \pi^+ , \qquad \Sigma^- \to n + \pi^- .$$

The nomenclature adopted for specifying the different types of decay events is summarized in Table I. The sign of the charge of Σ-hyperons decaying in

TABLE I. – *Summary of nomenclature.*

Term	Description
$R\Sigma_p^+$	$\Sigma^+ \to p + \pi^0$ at rest
$F\Sigma_p^+$	$\Sigma^+ \to p + \pi^0$ in flight
$R\Sigma_\pi^+$	$\Sigma^+ \to \pi^+ + n$ at rest
$F\Sigma_\pi^\pm$	$\Sigma^\pm \to \pi^\pm + n$ in flight
$R\Sigma_\sigma^-$	Σ^- capture stars at rest
$R\Sigma_\rho^-$	Σ^- giving rise to ρ ends
$F\Sigma_{out}^\pm$	$\Sigma^\pm$ leaving the stack (*)
$F\Sigma_{inter}^\pm$	$\Sigma^\pm$ interaction in flight

(*) These have not been identified but their number is estimated in a later section.

flight into a charged π-meson has not generally been determined but Σ-hyperons that undergo decay at rest to a charged π-meson have been assumed to be Σ^+.

2. – The identification of hyperons.

The identification of Σ-hyperons is not always straightforward and considerable care has to be taken in making allowance for observational losses.

The emitted π-meson sometimes escapes detection in the case of $R\Sigma_\pi^+$ and $F\Sigma_\pi^\pm$ decay type. For $R\Sigma_p^+$ decays the identification is facilitated by the unique range of the decay proton so that the loss factor would be expected to be small, but, under certain circumstances, $F\Sigma_p^+$ decays can be mistaken for proton scatters or for $R\Sigma_\sigma^-$ interactions which result in only one prong being emitted. The identification of $R\Sigma^-$ also presents difficulty since a large proportion of them produce no visible star at the end of their range.

Owing to the increased difficulty in identifying Σ-hyperon decays or interactions when either the primary or secondary is dipping steeply it might be expected that observational losses would increase in such cases. The distributions of angles of dip of the identified hyperons and of their secondaries were accordingly investigated and it was found that while the secondaries were isotropically emitted, the number of steeply dipping primary tracks was smaller than expected. Owing to the rather poor statistics it is difficult to estimate the magnitude of the correction for this loss or to say precisely at what dip angle it became important. It was definitely in evidence for angles of dip greater than 60° and not apparent for dip angles less than 30°. To have taken a dip angle cut-off as low as 30° would have meant a serious reduction of the number of events on which this investigation is based. As a compromise therefore a cut-off angle of 45° was employed on the primary Σ-hyperon tracks and only Σ-hyperons with a smaller dip angle than this were considered in estimating the total number of Σ-hyperons emerging from K^--stars. The number of events so obtained has then to be multiplied by a factor of 1.4 to allow for Σ-hyperons emitted with angles of dip between 45° and 90°. No dip angle cut-off was applied for secondary tracks.

Even when a dip cut-off of this kind is employed, however, many difficulties of identification remain and these are dealt with below.

2·1. *$R\Sigma_\pi^+$ and $F\Sigma_\pi^\pm$.* – The decay points of these hyperons should be uniformly distributed in depth throughout the emulsion. In fact, there is some falling-off in the density of the decay points near the interfaces of the emulsion, indicating that some decay π-mesons escaped detection. The effects of observational losses of π-mesons are discussed in detail below.

In addition to the loss of hyperons due to the π-meson escaping observation there might also be confusion in certain events between the interpretation of an $F\Sigma_\pi^\pm$ which decays close to the end of its range and an $R\Sigma_\pi^+$. From the distribution of residual ranges of the decay points of $F\Sigma_\pi^\pm$ it can be estimated that about 10 cases of a decay in flight occurring in the last 200 μm of the range of the Σ-hyperon have been mistakenly classed as being at rest. The details of this estimation are set out in Appendix I.

2·2. $R\Sigma_p^+$. – These events can be identified because, apart from straggling, the proton secondary is expected to have a unique range. However, a number of $R\Sigma_\sigma^-$ hyperons produce 1-prong capture stars and if these have a range between 1500 and 1800 μm they could be mistaken for $R\Sigma_p^+$ events. Fig. 1 shows the range distribution of single prongs coming from the ends of tracks of Σ-hyperons that have been brought to rest. Interpolating from the number of these prongs with range less than 1500 μm or greater than 1800 μm it is seen that the number that would be expected with range between 1500 and 1800 μm is 2. Actually the number observed is 61, so that the number of $R\Sigma_p^+$ events is estimated to be 59 and it is concluded that the error in this estimate as a result or $R\Sigma^-$-contamination is small.

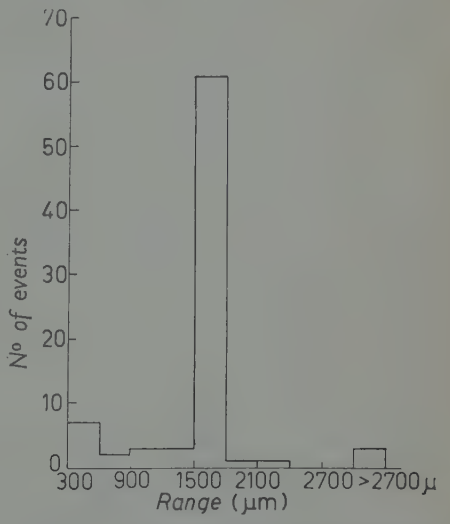

Fig. 1. – Length of prong in one-prong Σ^- capture stars or $R\Sigma_p^+$ decays.

2·3. $F\Sigma_p^+$. – We consider first those $F\Sigma_p^+$-events which are considered to have a residual range > 200 μm and are, in general, clearly seen to be in flight.

If the proton is emitted in the forward direction in the C.M.S., the event is easily observed owing to the change in grain density provided that the secondary does not dip steeply. There is, however, the possibility that such an event is due to the interaction of a $\Sigma^\pm$-hyperon in flight producing one fast proton. For this reason all events have been checked to see that the energy of the proton, the angle of decay in the laboratory system, and the estimated energy of the hyperon are consistent with the kinematics of $F\Sigma_p^+$ decay. Since interactions in flight are much less frequent, events which were consistent with $F\Sigma_p^+$-decay have been classified as such.

On the other hand, if the proton is emitted in the backwards hemisphere of the C.M.S. the position may be less clear. For a certain range of angles

the proton is emitted in the laboratory system with approximately the same velocity, and hence the same grain density, as the parent hyperon. An event of this kind is indistinguishable from the scattering of a proton. A histogram showing the distribution of the C.M.S. decay angle for the definitely identified $F\Sigma_p^+$ might then be expected to have more events in which the proton is emitted in the forward than in the backward direction. Fig. 2-*a* shows such an asymmetry, contrasting with Fig. 2-*b* which gives the corresponding distribution for $R\Sigma_p^+$. If the doubtful $F\Sigma_p^+$ which could also be interpreted as the scattering of a proton are included, the deficiency is partly compensated. To introduce these doubtful events, however, would lead to considerable uncertainty. It is more satisfactory to consider only the $F\Sigma_p^+$ emitted in the forward direction to obtain the energy spectrum. Assuming an isotropic distribution in C.M. decay angle (*) we later double this number of events to obtain the total number of $F\Sigma_p^+$.

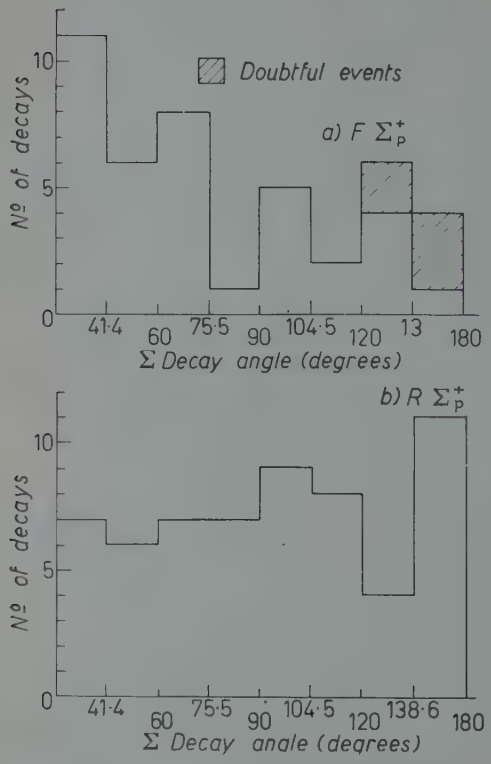

Fig. 2. – Distribution of C.M. angle of decay for Σ-hyperons decaying to protons.

For Σ^+-hyperons decaying with residual range < 200 μm, it follows from the kinematics of the decay, that the proton must have a range > 200 μm so that for such events there is no confusion with proton scattering. This is because the length of the prong would imply that at the point of scattering the proton had a residual range > 200 μm. It would, thus, be expected to have been seen to be in flight. However, when the residual range is < 200 μm, it is not always possible to say with certainty whether the Σ-hyperon had come to rest or not. It is expected, therefore, that there might be some confusion with $R\Sigma_a^-$ in which only 1 prong is emitted.

(*) This procedure is adopted on the basis of the symmetry found for $R\Sigma_p^+$. It cannot be excluded that a real asymmetry in $F\Sigma_p^+$ exists, due to longitudinal polarization of the Σ-hyperon at production, but our sample is neither clean enough nor large enough to be sure.

3221

The importance of the effect can be gauged by estimating the numbers of $F\Sigma_p^+$-decays expected to occur with residual range $< 200\ \mu$m. The time taken for a Σ-hyperon to traverse the last 200 μm of track is $0.96 \cdot 10^{-11}$ s. There are 38 $R\Sigma_p^+$-decays in the accepted solid angle so that we have observed Σ^+-hyperons which subsequently decay to a proton for $38 \cdot 0.96 \cdot 10^{-11}$ s $= 36 \cdot 10^{-11}$ s during their final 200 μm of track. Taking $8 \cdot 10^{-11}$ s as the lifetime of a Σ^+-hyperon, about 4 events in this category would be expected. There are in fact 5 such definitely identified decay events.

2·4. $R\Sigma^-$. – The basic interaction between a Σ^--hyperon and a nucleon giving rise to a Σ^--star is believed to be one of the following:

$$\Sigma^- + p \to \Lambda^0 + n\,,$$

$$\Sigma^- + p \to \Sigma^0 + n\,.$$

The excitation in the second case is so small that it would be expected to give only zero-prong stars, while even in the first case an appreciable number of zero prong stars would be expected. Such $R\Sigma_\rho^-$ endings cannot be distinguished from proton endings.

There is an added difficulty in that when a Σ^--star consists of a single prong of length $< 200\ \mu$m it is impossible to say with certainty that the event is not simply a proton scatter, for, as was explained in Section 2·1, a heavy track $< 200\ \mu$m from the end of its range can appear to be at rest. An estimate of the correction factor to be applied to the observed number of $R\Sigma_\sigma^-$ to take account of the $R\Sigma_\rho^-$ and the Σ^- giving rise to one short prong can be made if one has a knowledge of the prong distribution of Σ^--stars.

Such a distribution can be obtained by making a study of interactions of K-mesons with the hydrogen in the emulsion to give $K^- + H \to \Sigma^- + \pi^+$. When the interaction takes place at rest, such events can be readily identified since they consist of a Σ-hyperon and π-meson emitted collinearly, the Σ^--particle having a unique range $\sim 700\ \mu$m. Thus, if an event is obtained consisting of a collinear π meson and a baryon prong, the baryon having this characteristic range, it is known to be a Σ^--hyperon whether it produces a star or not. In cases where the interaction takes place in flight, evidence for identification of the heavy prong as a Σ^--particle is very strong from the coplanarity and dynamics of the event. A prong distribution for Σ^--stars can, therefore, be made unambiguously, though the statistics are, at present, poor. The collaboration has 20 events of this type of which 11 were found in the G-5 stack and 9 in a later stack of K-5 emulsion, and when other published events [2]

(2) D. J. Prowse: collected by private communication.

are added there are 63 altogether. These are shown in Fig. 3. In a sample of five events consisting of one prong only, two were such that the length of the secondary track was < 200 μm.

From Fig. 3 the ratio of the total number of $R\Sigma^-$ to the number of $R\Sigma_\sigma^- = 2.5$, while the ratio of all $R\Sigma^-$ to those $R\Sigma_\sigma^-$ excluding the ones emitting a single prong of range < 200 μm $= 3.0 \pm 0.8$. This is the value adopted in the present work. It is supported by the less direct evidence given in Appendix II.

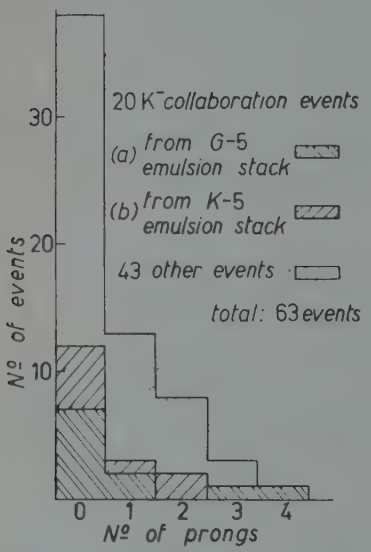

Fig. 3. – Prong distributions of Σ^- stars where the Σ^- hyperon originates from a $K^- + H \rightarrow \Sigma^- + \pi^+$ interaction. (The 43 other events were collected by D. J. Prowse from a number of other collaborations).

Finally, it must be mentioned that there are some cases that could be interpreted as either an $R\Sigma_\sigma^-$ or a hyperfragment, when the range of the primary is too short for accurate measurements, *viz.* < 100 μm. It is possible that some events classified as hyperfragments are actually Σ^- (see I, Section **5**·4).

An upper limit can be obtained to the number of those short-range Σ-hyperons which are accompanied by a π-meson from the parent K-star. Of the K-stars emitting solely a π-meson and a short heavy track, the latter subsequently producing a secondary star, there are six that have a visible energy release less than the maximum permissible for Σ-hyperon production. If all these six short tracks are assumed to be produced by Σ^--hyperons, one would expect two additional hyperons from K-stars that emit stable prongs as well as the Σ-hyperons and π-meson, (see I, Section **5**·3-*b*) making an upper limit of eight in all. It is not possible to use similar arguments for events in which no π-meson accompanies the unstable baryon from the parent star. However, the energy spectrum of Σ^--hyperons given in Fig. 8-*c* makes it appear unlikely that there could be as many as 10 more short Σ^--hyperons in all in the energy range from 0 to 5 MeV. In the present work, owing to the apparent smallness of the correction and to the difficulty of estimating it, it has been ignored.

2·5. $\Sigma^\pm$ *interactions in flight.* – In following out the prongs from K-capture stars a total track length of 12 metres of proton track has been observed and a total of 16 interactions in flight producing stars of one or more branches recorded. The number of proton interactions expected in this length is of the same order. However, three of the interactions appear to give rise to an energy

release greater than the kinetic energy of the incoming particle (assuming it to be a proton) and have thus to be interpreted as $\Sigma^{\pm}$-hyperon interactions in flight.

2·6. $F\Sigma^{\pm}_{out}$. – 15% of baryons with energy between 60 and 90 MeV leave the stack before coming to rest. With energy greater than 90 MeV the proportion rises to 40%. These particles will contain a number of hyperons, and an attempt has been made to estimate the magnitude of this loss.

The method used depends upon the use of an observation time computed from the ionization-range data supplied for each track escaping, to form a summation probability for the number of hyperons which survive to leave the stack without identification. Details are given in Appendix III.

It is concluded that of the 76 baryons leaving the stack there are probably about 2 Σ^+ and 6 Σ^--hyperons. Since the escape of particles is predominantly through the end plates the loss is greatest among the more steeply dipping tracks.

3. – The effect of the observational loss of π-mesons on the classification of hyperons.

It is known (see I, Section 3·5) that a substantial proportion of π-mesons from K-stars in the present stack escape detection. The analysis of K-interactions in a new stack in which the π-mesons can be more readily detected owing to the greater freedom from background and the higher grain density of tracks of relativistic particles, suggests that it is necessary to multiply the number of π-mesons from K-stars observed in the present work by a loss factor of about 1.3 to obtain the actual number of π-mesons emitted [3]. Evidence presented in I suggests that this loss is mainly confined to π-mesons of energy greater than 60 MeV. If all the observed losses were of such high energy mesons the corresponding loss factor for these mesons would be about 1.8.

In Table II the observed hyperons are classified according to whether or not they were accompanied by a π-meson from the primary K-star. To allow for observational losses of π-mesons a certain number of events have to be transferred from the « Σ without π » category to the « $\Sigma+\pi$ » category. It appears however that the observational loss factor that must be applied for this purpose is much smaller than the value of 1.3 deduced for all K-stars. The mean energy of mesons from stars from which Σ-hyperons are emitted

---

[3] M. C. Amerighi, M. Beniston, A. Bonetti, D. H. Davis, M. Di Corato, C. C. Dilworth, D. Ferreira, E. Frota-Pessoa, W. B. Lasich, N. N. Raina, M. René, J. Sacton and A. E. Sichirollo: *Nuovo Cimento*, **12**, 91 (1959).

is less than that from other stars (see I, Table VIII) so that a smaller observational loss is expected. Further, an additional re-scan was made of these stars and this resulted in the detection of some π-mesons that had previously been missed. On the basis of the result of this re-scan and of the depth distribution of observed π-mesons, assuming losses to occur predominantly at the top and bottom of the emulsion, a loss factor of 1.1 has been taken for π-mesons from stars in which a Σ-hyperon is emitted.

TABLE II. – *Summary of corrected numbers of all Σ-hyperons.*

Type of event	$\Sigma+\pi$				Σ without π				All Σ's Corrected Assuming π observational loss factors set out in text
	Observed		Corrected (*,*)		Observed		Corrected		
	All dip angles	Dip angles less than 45°	(*a*) Ignoring π observational losses	(*b*) Assuming π observational losses	All dip angles	Dip angles less than 45°	(*a*) Ignoring π observational losses	(*b*) Assuming π observational loss factors set out in text	
$F\Sigma^{\pm}_{\pi}$	34	30	49	63	45	41	64	70	133
$F\Sigma^{+}_{\text{inter}}$	1	—	1	1	3	—	3	3	4
$R\Sigma^{+}_{p}$	44	—	44	48	15	—	15	11	59
$R\Sigma^{+}_{\pi}$	52	36	43	59	21	11	8	15	74
$F\Sigma^{+}_{p}$	23	19 (*)	39	43	15	14 (**)	25	21	64
$F\Sigma^{+}_{\pi}$	—	—	38	53	—	—	25	26	79
$F\Sigma^{+}_{\text{inter}}$	—	—	1	1	—	—	1	1	2
$F\Sigma^{+}_{\text{lost}}$	—	—	0	0	—	—	2	2	2
Total Σ^{+}	—	—	165±20	204±24	—	—	76±15	76±15	280±28
$R\Sigma^{-}_{\sigma}$	25	19	25	27	38	26	38	36	63
$R\Sigma^{-}_{\rho}$	—	—	50	54	—	—	76	72	126
$F\Sigma^{-}_{\pi}$	—	—	11	10	—	—	39	44	54
$F\Sigma^{-}_{\text{inter}}$	—	—	0	0	—	—	2	2	2
$F\Sigma^{-}_{\text{lost}}$	—	—	0	0	—	—	6	6	6
Total Σ^{-}	—	—	86±20	91±21	—	—	161±32	160±32	251±38
Total of all Σ	179	—	253±24	295±29	137	—	237±35	236±35	531±47

(*) Including 14 in forward direction in C.M. system.

(**) Including 9 in forward direction in C.M. system.

(*,*) The values shown in Part I, Table XXI, are somewhat different from these (see also Table XI in the following), since there no dip angle cut-off was applied to the observed Σ-hyperons, and the correction for π-meson loss was that given by the depth distribution of π-mesons [smaller than that given by the π/K^{-} ratio of AMERIGHI *et al.* (3)].

Loss of decay π-mesons from $R\Sigma_\pi^+$ and $F\Sigma_\pi^\pm$ events is to be expected, but the correction to be applied to obtain the true numbers of such events is difficult to estimate. Since the decay π-mesons will have energies above 60 MeV, it might be thought at first that an observational loss factor of 1.8 would be appropriate. On the other hand there is a strong reason for suspecting that the sudden stopping of a baryon track in flight might be associated with the emission of a π-meson so that such endings have been scrutinised for an especially long time. A considerably lower value of the observational loss factor might therefore be expected to apply to $F\Sigma_\pi^\pm$ events. An upper limit to the π-observational loss factor applicable to $F\Sigma_\pi^\pm$ events can be estimated since, if the decay π-meson escapes observation, the event will appear to be a baryon stopping in flight. In our sample in which 79 $F\Sigma_\pi^\pm$ events have been observed, 18 such stops in flight have been found. If all these stops in flight were to be attributed to loss of π-mesons from $F\Sigma_\pi^\pm$ decays the corresponding loss factor would be 1.23. A few cases of proton stops in flight would be expected in our sample, however, and there may well be some genuine cases of Σ-hyperons stopping in flight. An observational loss factor of 1.2 has been applied to $F\Sigma_\pi^\pm$ events in calculating the numbers given in Table II. When a single baryon prong comes from a K-star from which a π-meson has also been detected, there is a high probability that the baryon is a Σ-hyperon (see I, Table IV). Such baryon prong endings were therefore scrutinised for a longer time than it was practicable to devote to all prongs so that a lower observational loss factor should be applicable. Greater losses are to be expected however in stars in which a π-meson is accompanied by several baryon prongs. These comprise only about 20% of all « $\pi+\Sigma$ » events. A loss factor of 1.2 has been applied to all $R\Sigma_\pi^+$ events in which a π-meson accompanies the hyperon from the primary K-star to obtain the figures given in Table II, but there is clearly considerable uncertainty in this estimate.

The ends of baryon prongs from K-stars from which no π-meson has been observed have not been examined with any special care and it appears likely that observational losses may have been considerable in such cases. The loss factor of 1.8 has therefore been assumed for such events in obtaining the figures given in Table II. This figure is based on the fact that the observational loss correction factor of π-mesons from K^--stars is 1.3 and the energy of the π-mesons from $R\Sigma_\pi^+$ events is much larger than the mean energy of π-mesons from K^--capture stars.

4. – The corrected numbers of hyperons.

In Table II are collected the numbers of hyperons after the corrections described in the previous section have been applied. The actual numbers of observed events originally classified under each category are also given. The

hyperons are further classified according to whether or not they were emitted together with a π-meson from the primary K^--star. The errors quoted in the Table are statistical errors.

In view of the uncertainty about the size of the appropriate π-meson observational loss factors the corrected numbers of hyperons given in Table II have been calculated

a) assuming no π-loss;

b) assuming the following values of the π-observational loss factor (see Section **3**):

i) For loss of π-mesons emitted together with a Σ-hyperon from the primary K^--star 1.1

ii) For loss of π-mesons from $F\Sigma_\pi^\pm$ events 1.2

iii) For loss of π-mesons from $R\Sigma_\pi^+$ events when the hyperon is accompanied by a π-meson from the primary K^--star . 1.2

iv) For loss of π-mesons from $R\Sigma_\pi^+$ events when the hyperon is not accompanied by a π-meson from the primary K^--star 1.8

There are comparatively few events in this last category so that the numbers in Table II are not very sensitive to it.

The number of $F\Sigma_\pi^+$ events has been estimated by multiplying the number of $F\Sigma_p^+$ events by the branching ratio, R, between the two decay modes of the Σ^+-hyperon. Its value is sensitive to the correction factor for observational loss of π-mesons. Since this correction factor is smaller and less uncertain for hyperons accompanied by a π-meson from the primary K^--star, only such events have been used in deriving the value of R. Among these stars are estimated to be 53 $R\Sigma_p^+$ and 65 $R\Sigma_\pi^+$ events so that

$$R = \frac{\text{no. of } \Sigma^+ \to \pi^+ + n}{\text{no. of } \Sigma^+ \to \pi^0 + p} = \frac{65}{53} = 1.23 \pm 0.27 ,$$

where the error stated is statistical error only. Uncertainty in the true value of R arises both from uncertainty in the π-meson observational loss factor and in the magnitude of the correction for misclassification of some 5 $F\Sigma_\pi^\pm$ events as $R\Sigma_\pi^+$ (*).

If no correction had been made for π-meson observational loss the ratio R would have been reduced to 0.98 while if the correction for the contami-

(*) The 10 events referred to in Sect. **2.1** have been divided equally among K stars with and without a π, as the number of $F\Sigma_\pi^\pm$ is almost equal for each class.

nation of $R\Sigma_\pi^+$ by $F\Sigma_\pi^\pm$ events had not been made, R would have been increased to 1.38.

Removing the $F\Sigma_\pi^+$ events from the general class $F\Sigma_\pi^\pm$, the remainder are attributed to $F\Sigma_\pi^-$. The details of this procedure together with the application of corrections for observational loss are set out in Table III.

TABLE III. – *Estimation of the numbers of* $F\Sigma_\pi^+$ *and* $F\Sigma_\pi^-$.

	$\Sigma+\pi$	Σ without π	All Σ's
No. of $F\Sigma_\pi^\pm$ of dip $< 45°$	30	41	71
No. corrected for loss of decay π ($\times 1.2$)	36	49	85
No. corrected for confusion with $R\Sigma_\pi^+$ (add 10 events)	41	54	95
No. corrected for all dips ($\times 1.4$)	57	76	133
No. corrected for loss of π in K-star ($\Sigma+\pi$ events $\times 1.1$)	63	70	133
No. of $F\Sigma_p^+$	43	21	64
Estimated no. of $F\Sigma_\pi^+$ using $R = 1.23$	53	26	79
Estimated no. of $F\Sigma_\pi^-$ (*i.e.*, $F\Sigma_\pi^\pm - F\Sigma_\pi^+$)	10	44	54

An alternative method of estimating the numbers of Σ^+ and Σ^--hyperons contained in this class is obtained by following the accompanying π-meson from the K-stars. As was pointed out in Part I, charge exchange effects are so small that it can be inferred that the Σ-hyperon has opposite charge from that of the π-meson. It has, in fact, been possible to follow only 13 π-mesons from this type of event, of which 7 were negative and 6 positive. This would indicate that the 60 $\Sigma^\pm$ hyperons should be divided up as 32 Σ^+ and 28 Σ^-. This procedure seems to favour, therefore, a higher number of Σ^--hyperons than was obtained by the first method described, but the difference is not statistically significant. As this second method is not applicable for events in which the hyperon is emitted without a π-meson, the first estimate based on the numbers of $F\Sigma_p^+$ and the branching ratio R is used throughout.

It may be noted that the corrected number of $R\Sigma_\pi^-$ without an accompanying π-meson in the K-star is less than the number of observed events. This is partly because some of the decays actually occur in flight close to the end of the range of the hyperon (Section 2·1) and partly because the π-meson from the K-star has sometimes not been observed. For these reasons a few events may have been wrongly classified initially. The latter cause also accounts for the observed number of $R\Sigma_p^+$ without an accompanying π-meson being apparently larger than the corrected number.

3231

Table IV gives a summary of the numbers of Σ-hyperons of energy greater than 60 MeV classified in the same way as in Table II. Table V summarizes the results on the proportion of stars emitting charged Σ-hyperons and on the

TABLE IV. – *Summary of corrected numbers of* $\Sigma^{\pm}$ *hyperons* > 60 MeV.

Type of event	$\Sigma + \pi$		Σ without π		All Σ's
	Observed (all dip angles)	Corrected	Observed (all dip angles)	Corrected	Corrected
$F\Sigma^{\pm}_{\pi}$	1	1	32	45	46
$F\Sigma^{\pm}_{\text{inter}}$	0	0	2	2	2
$R\Sigma^{+}_{\rho}$	0	0	1	1	1
$R\Sigma^{+}_{\pi}$	0	0	2	3	3
$F\Sigma^{+}_{\rho}$	1	1	7	17	18
$F\Sigma^{+}_{\pi}$	—	1	—	21	22
$F\Sigma^{+}_{\text{inter}}$	—	0	—	1	1
$F\Sigma^{+}_{\text{lost}}$	—	0	—	2	2
Total Σ^{+}	—	2	—	45	47
$R\Sigma^{-}_{\sigma}$	0	0	5	5	5
$R\Sigma^{-}_{\rho}$	—	0	—	10	10
$F\Sigma^{-}_{\pi}$	—	0	—	24	24
$F\Sigma^{-}_{\text{inter}}$	—	0	—	1	1
$F\Sigma^{-}_{\text{lost}}$	—	0	—	6	6
Total Σ^{-}	—	0	—	46	46
Total all Σ	2 (*)	2	49	91	93

(*) These two hyperons had a dip angle greater than 45°, and an estimated kinetic energy just over 60 MeV. The errors in energy determination are such that their true energy may be less. These two cases are not referred to in the discussion of Sect. 7.

Σ^{+} branching ratio deduced from the present investigation. The errors quoted in the figures given in the Table are statistical errors but estimates are made of how these results are affected by the assumed value of the π-meson observation loss correction, by the uncertainty in the knowledge of the true ratio of $R\Sigma^{-}_{\rho}$ events, and by the statistical uncertainty in the true value of R.

It is seen that the uncertainties in the π-meson observational loss factor affect mainly the value of the branching ratio, R, but have much less influence on the other values quoted in Table V.

3232

TABLE V (*).

	Best estimate from present work	Value obtained assuming no π-meson observational loss	Range of values consistent with possible range of $R\Sigma_{\rho}^{-}/R\Sigma^{-}$ ratio	Range of values consistent with possible statistical uncertainty in R
$R = \frac{\text{no. of } \Sigma^{+} \to \pi^{+} + n}{\text{no. of } \Sigma^{+} \to \pi^{0} + p}$	1.23 ±0.27 (1.38)	0.98 (1.14)	—	—
Proportion of stars emitting charged Σ hyperons	0.176±0.010 (0.175)	0.161 (0.160)	0.160÷0.192	—
Proportion of stars emitting Σ hyperons with accompanying π-meson	0.096±0.006 (0.097)	0.084 (0.086)	0.089÷0.103	—
Proportion of stars emitting charged Σ hyperons of energy greater than 60 MeV	0.029±0.003 (0.029)	0.026 (0.026)	0.028÷0.030	—
Σ^{-}/Σ^{+} ratio for all K^{-} stars	0.86 ±0.12 (0.77)	1.00 (0.85)	0.69 ±1.04	0.72÷1.00
Σ/Σ^{+} ratio for hyperons of energy greater than 60 MeV	1.02 ±0.19 (0.86)	0.98 (0.80)	0.75 ÷0.83	0.65÷0.95
Σ^{-}/Σ^{+} ratio for K^{-} stars emitting a π-meson	0.45 ±0.10 (0.38)	0.51 (0.43)	0.34 ÷0.56	0.38÷0.53

(*) The values given in brackets in columns (2) and (3) are those that would be obtained if no transfer of events from the $R\Sigma_{\pi}^{\pm}$ to the $F\Sigma_{\pi}^{\pm}$ category had been made to correct for $F\Sigma_{\pi}^{\pm}$ decays mistakenly classed as $R\Sigma_{\pi}^{\pm}$.

5. – The energy spectra of emitted hyperons.

The $R\Sigma_{\rho}^{+}$ events are perhaps the easiest of all to distinguish on account of the characteristic range (~ 1.7 mm) of the decay proton. There was no evidence of loss of steeply dipping tracks for these events and the unique range made practicable the distinction between decays at rest and in flight

3233

without ambiguity. For this reason the energy histogram of Fig. 4 includes Σ^+-hyperons of all dip angles, identified by their $R\Sigma_p^+$ ending. Those hyperons accompanied by a π-meson in the K-star are shown cross-hatched.

Owing to the difficulties of identification introduced when the hyperon dips steeply in the emulsion, all the remaining energy spectra are based solely on events where the dip angle is $< 45°$.

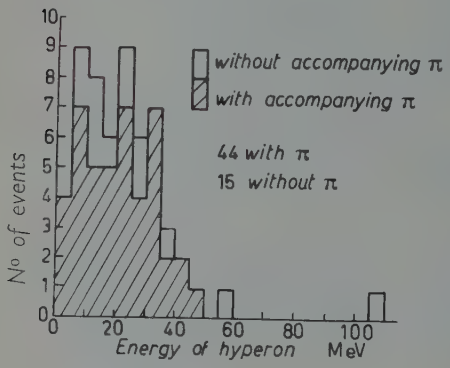

Fig. 4. – Energy spectrum of Σ^+ hyperons that decay to a proton at rest. (All dip angles included).

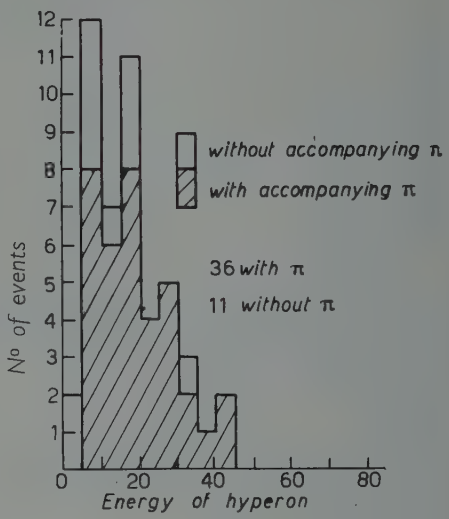

Fig. 5. – Energy spectrum of Σ^+ hyperons that decay to a π-meson at rest (dip angle of $\Sigma < 45°$).

Fig. 5 gives the distribution for $R\Sigma_\pi^+$ events. It was shown earlier that there was reason to expect about 10 events in this distribution which are in fact $F\Sigma_\pi^\pm$. As there is no method of distinguishing which of the events have been wrongly classified they are all included in Fig. 5.

Fig. 6-*a*, shows the spectrum of energies for definitely identified $F\Sigma_p^+$ of dip angle $< 45°$. A bias possibly exists in this hi-

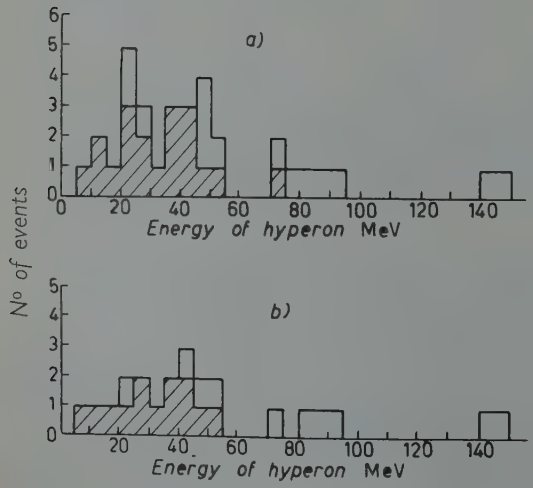

Fig. 6. – Energy spectrum of Σ^+ hyperons that decay to a proton in flight. *a*) All CMS decay angles. *b*) Forward decays in CMS only (dip angle of $\Sigma < 45°$).

stogram as some events in which the proton decays backwards in the C.M.S. are missed and this loss is correlated with the energy of the primary particle. Because of this Fig. 6-*b* is also given, being based on only those Σ-hyperons in which the proton decay is in the forward hemisphere in the C.M.S. Mention must be made of the effect of hyperons leaving the stack undetected. These are almost exclusively high-energy particles and would be expected to affect especially those categories in which the Σ-hyperon decays in flight. As was seen earlier, about 2 Σ^+-hyperons are expected to have been lost. This is not serious and so the histogram is considered to be almost free from bias.

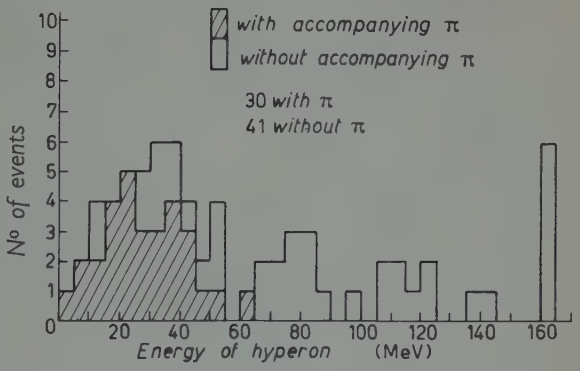

Fig. 7. – Energy spectrum of $\Sigma^{\pm}$ hyperons that decay to a π-meson in flight (dip angle of $\Sigma < 45°$).

Fig. 7 which shows the energy distribution of Σ-hyperons that decay to π-mesons of either sign in flight, might be expected to be more affected by hyperons that leave the stack. If all the Σ-hyperons leaving the stack had decayed in flight, it is expected that there would be about 6 $F\Sigma_{\pi}^{-}$ and 1 $F\Sigma_{\pi}^{+}$ to add to the number observed. These, however, will be predominantly steep hyperons, for most of the fast baryons not followed to rest had large angles of dip and left the stack through the end plates. It is concluded for this reason that, while a few events perhaps should

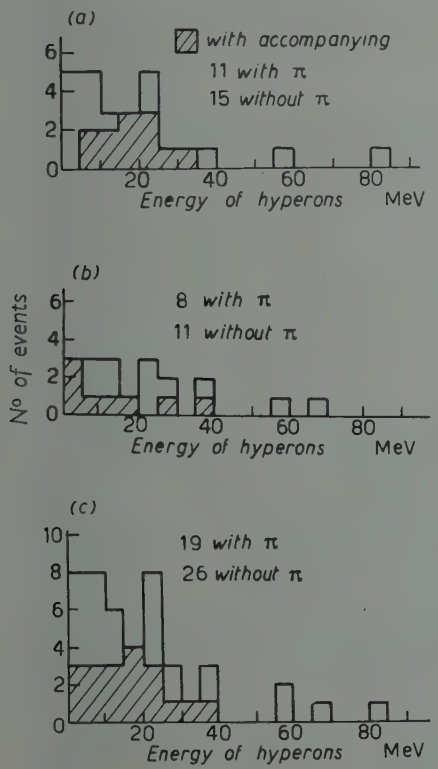

Fig. 8. – Energy spectrum of Σ^- hyperons that come to rest (dip angle of $\Sigma < 45°$). *a*) Σ^- hyperons producing a star with more than one prong. *b*) Σ^- hyperons producing 1 prong only of length greater than 200 μm. *c*) *a*) and *b*) combined.

be added at the high energy end of the spectrum, Fig. 7 is not greatly different from the true shape of the distribution.

Fig. 8 gives the energy distribution of Σ-hyperons which subsequently come to rest to produce stars. Fig. 8-*a* shows the spectrum of those which produce a star of more than 1 prong, while Fig. 8-*b* contains Σ^--hyperons which give rise to 1-prong stars with the prong length greater than 200 μm. These distributions are seen to be essentially the same, as would be expected, and so Fig. 8-*c* combines them both into one histogram. There are, however, two possible sources of bias. One concerns the high-energy tail of the spectrum where perhaps some events have been undetected because the hyperons leave the stack. This effect is expected to be small, amounting to not more than one or two events. At the low energy end, ambiguity sometimes exists between low energy Σ^--hyperons and hyperfragments of short range, so that the number of events in the interval 0 to 5 MeV is rather uncertain (see Section 2·4).

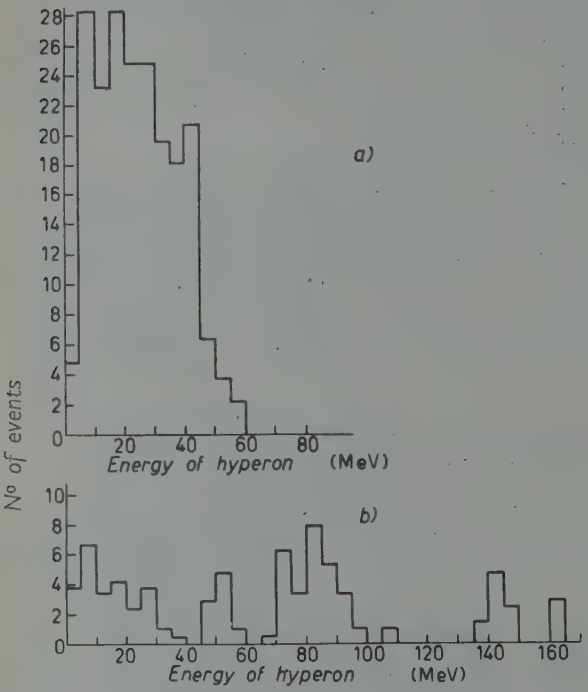

Fig. 9. – Energy spectrum of all Σ^- hyperons. *a*) Σ hyperons accompanied by π-meson (203 events — corrected number of Σ hyperons less one interaction in flight). *b*) Σ hyperons not accompanied by π-meson (73 events — corrected number less one interaction in flight and two lost from stack).

Figs. 9 and 10 show the energy distribution of all Σ^+ and Σ^--hyperons respectively both when accompanied and when not accompanied by a π-meson from the K-star. These are obtained by normalizing the histograms for the various types of event to the appropriate corrected numbers in Table II. The normalized histograms are then added to give the composite ones. Events of type $F\Sigma_\pi^+$ were assumed to have the same distribution as $F\Sigma_p^+$, and their contribution was subtracted from the $F\Sigma_\pi^\pm$ distribution to obtain that of $F\Sigma_\pi^-$.

Finally, Fig. 11-*a*,*b* combines Figs. 9-*a*,*b* and 10-*a*,*b* to give the energy spectrum of all charged Σ-hyperons.

It will be noticed that the energy spectra of the Σ-hyperons depend mar-

3236

kedly upon whether there is an accompanying π-meson or not. The spectra of both Σ^+- and Σ^--hyperons display this feature. This is attributable to the fact that a Σ-hyperon emitted without a π-meson could have arisen either from a one-nucleon interaction of the K-meson in which the π-meson has been absorbed or from a 2-nucleon interaction. This second process generally produces more energetic Σ-hyperons and gives rise to the high energy tails in Figs. 9-*b* and 10-*b*. The 2-nucleon interactions of K-mesons are discussed further in Section **7**.

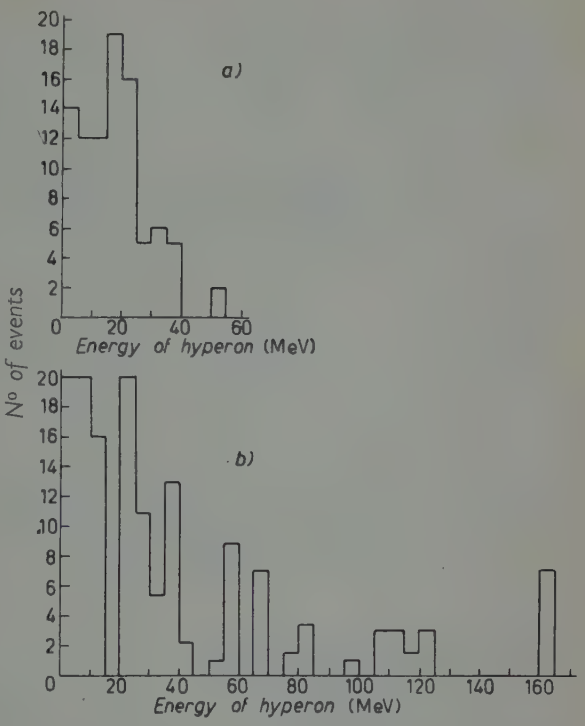

Fig. 10. – Energy spectrum of all Σ hyperons. *a*) Σ hyperons accompanied by π-meson (91 events). *b*) Σ hyperons without accompanying π-meson (152 events) (corrected number of Σ^- hyperons less 2 interactions in flight and 6 estimated lost from stack).

Secondly for hyperons accompanied by π mesons there is a difference between the spectra for Σ^+- and Σ^--hyperons. This is due to the presence of the Coulomb potential, V_c, which has the effect of reducing the kinetic energy of the Σ^- and increasing that of the Σ^+.

If in Fig. 11-*a*, the ordinate axis is displaced 15 MeV to the right the distribution becomes very similar to Fig. 11-*b*. This is consistent with a Coulomb potential well of depth about 7 MeV. It has been suggested by CAPPS [4] that Σ^+-hyperons of energy less than 7 MeV must arise mainly from interactions in light nuclei and he estimated that on his model of the K^--interaction process in a nucleus, about 10 % of all Σ^+-hyperons from light nuclei should have energy less than 7 MeV. Indeed, no fewer than 18 Σ^+-hyperons were observed to be emitted with an energy of 7 MeV or less, *i.e.*, about 10 % of all identified Σ^+-hyperons. If Capps' estimate is reasonable this would suggest that a very substantial pro-

(4) R. H. CAPPS: *Phys. Rev.*, **107**, 239 (1957).

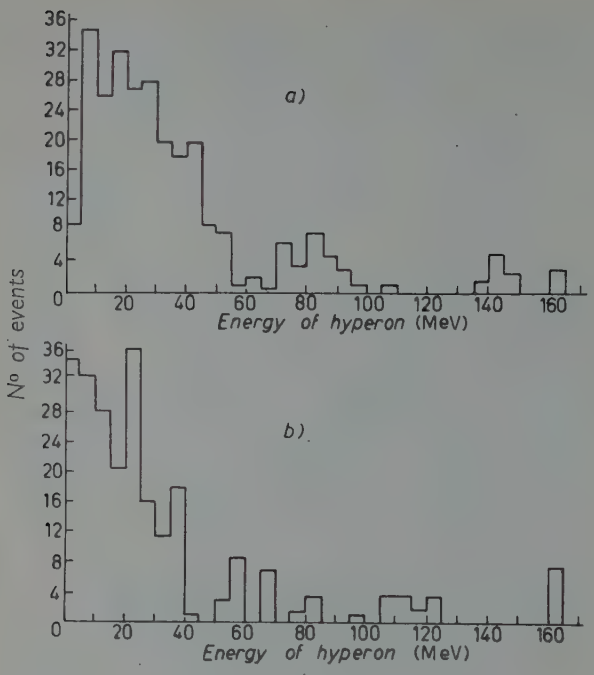

portion of all K^--captures must occur on light nuclei. Alternatively, if, as seems indicated by other considerations (Section **10**), the K^--capture occurs predominantly on the periphery of the nucleus, the Coulomb barrier would be much less effective in inhibiting the emission of low energy Σ^+-hyperons from heavy nuclei.

Fig. 11. – *a*) Energy spectrum of all Σ^+ hyperons. *b*) Energy spectrum of all Σ^- hyperons.

6. – The characteristics of the K^--stars emitting Σ-hyperons.

Tables VI and VIII (Section **7**) give the prong distributions of K-stars from which Σ-hyperons of either sign have been emitted. These distributions are compiled in the same manner as the composite histograms for the energy spectra of the Σ-hyperons (Figs. 9-11). The distributions associated with Σ-hyperons undergoing different types of decay and interaction are each separately normalized to the corrected number of events in Table II. These are then added to get the complete distribution. This procedure is necessary since the characteristics of the K-star depend upon the energy of the hyperon emitted and the higher energy hyperons have more chance of decaying in flight than those of lower energy. It has been seen earlier that the efficiency of detection of the different types of event varies greatly. For this reason it is essential that the individual distribution associated with each specific type of event should be correctly normalized before compounding them to obtain the final distribution.

The types of star are divided according to whether the Σ-hyperon had an energy less than or greater than 60 MeV. This is because Σ-hyperons of energy above 60 MeV are only produced in multi-nucleon K^--interaction processes while Σ-hyperons of energy less than 60 MeV are mainly produced in K^--inter-

actions with a single nucleon, although multi-nucleon interactions may also contribute.

TABLE VI. – *Stable prong distributions of* K *stars emitting* Σ *hyperons* (*). (Energy of hyperon ⩽ 60 MeV) (numbers of hyperons normalized to agree with Tables II, column (*b*), and IV and Figs. 9 and 10)

No. of stable prongs / Type of events	0	1	2	3	4	5
	No. of events					
Σ^+-hyperon emitted with π-meson	165	24	8	6	0	0
Σ^--hyperon emitted with π-meson	74	12	0	0	5	0
Σ^+-hyperon (energy <60 MeV) emitted without π-meson	17	7	3	3	1	0
Σ^--hyperon (energy <60 MeV) emitted without π-meson	20	22	18	26	25	3

(*) The distribution in these table includes $F\Sigma^{\pm}_{\pi}$ events for which the sign identification is not certain. These have been divided between Σ^+ and Σ^- in the proportions estimated in Tables II and IV.

The distributions for stars in which either Σ^+- or Σ^--hyperons are emitted with energy less than 60 MeV and without accompanying π-mesons undoubtedly also contain some events in which a charged π-meson has been emitted but has escaped detection. Evidence for this is seen in the prong distribution. It is a striking feature of the « $\Sigma+\pi$ » events that a large proportion (about 80%) are without other stable prongs. A large proportion of the events in which a Σ^+-hyperon of energy less than 60 MeV is emitted without accompanying charged π-meson also have no other stable prongs, as would be expected if there is a contamination of « $\Sigma^+ + \pi^-$ » events in which the π^- has been lost. The effect is less marked in the case of stars emitting a Σ^--hyperon because there are fewer « $\Sigma^- + \pi^+$ » events.

The distribution of total visible energy release in stable prongs accompanying hyperon emission is given in Table VII the events being classified in the same categories as in Table VI. In compiling Table VII an allowance of 8 MeV binding energy has been added for each stable prong.

TABLE VII. – *Total visible energy release in stable prongs of* K^- *stars emitting* Σ^+ *and* Σ^-*-hyperons* (*) (Energy of hyperon $\leqslant$60 MeV).
(numbers of hyperons normalized to agree with Tables II and IV and Figs. 9 and 10).

Total visible energy release (MeV) / Type of event	0 ÷ 10	10 ÷ ÷20	20 ÷ ÷30	30 ÷ ÷40	40 ÷ ÷60	60 ÷ ÷80	80 ÷ ÷100	100 ÷ ÷120	120 ÷ ÷140	140 ÷ ÷180
	No. of events									
Σ^+ hyperon (emitted with π-meson)	172 (168) (**)	13	14	4	0	0	1	—	—	—
Σ^- hyperon (emitted with π-meson)	77 (74)	6	0	3	5	0	0	—	—	—
Σ^+ hyperon (energy < 60 MeV) emitted without π-meson	17 (17)	4	2	2	2	3	0	1	—	—
Σ^- hyperon (energy < 60 MeV) emitted without π-meson	26 (20)	8	1	13	9	16	15	9	4	15

(*) The numbers in brackets refer to the number of zero prong events.
(**) The distribution in these table includes $F\Sigma\frac{+}{\pi}$ events for which the sign identification is not certain. These have been divided between Σ^+ and Σ^- in the proportions estimated in Tables II and IV.

7. – K^- interactions with two or more nucleons.

Some 47 cases of the emission of fast hyperons (kinetic energy > 60 MeV) were observed among the 316 hyperons identified (*i.e.*, about 16% of all hyperons identified had an energy above 60 MeV). Since there is a sharp cut-off near 60 MeV in the energy spectrum of Σ-hyperons accompanying π-mesons, these fast hyperons have to be attributed to processes in which no π-meson is produced. The possible processes, involving two nucleons are set out below:

(i) $K^- + p + p \rightarrow \Sigma^+ + n$

(ii) $K^- + p + p \rightarrow \Sigma^0 + p$

(iii) $K^- + p + p \rightarrow \Lambda^0 + p$

(iv) $K^- + n + p \rightarrow \Sigma^- + p$

(v) $K^- + n + p \rightarrow \Sigma^0 + n$

(vi) $K^- + n + p \rightarrow \Lambda^0 + n$

(vii) $K^- + n + n \rightarrow \Sigma^- + n$

Further processes involving more than two nucleons are also possible.

Ten high energy Σ-hyperons have been identified as Σ^+, five as Σ^- and 34 have not had their signs identified. Two of these interacted in flight producing an exothermic energy release while the rest decayed, $(\Sigma^{\pm} \to \pi)$ in flight.

The ten identified high energy Σ^+ include 1 $R\Sigma_p^+$, 2 $R\Sigma_\pi^+$ and 7 $F\Sigma_p^+$. The corrected number of $F\Sigma_p^+$ is 17 (*) and assuming the branching ratio R to be 1.23 the number of $F\Sigma_\pi^+$ is 21. The estimated number of Σ^+-hyperons leaving the stack or interacting in flight is 4 and the total corrected number of Σ^+-hyperons of energy greater than 60 MeV becomes 45 ± 17.

On correcting for observation loss of high energy Σ^--hyperons the number of $R\Sigma^-$ becomes 15, of $F\Sigma_\pi^-$ 24, while 7 events in all are estimated to leave the stack or interact in flight. This gives for the total number of Σ^--hyperons of energy greater than 60 MeV, 46 ± 14.

If none of the Σ-hyperons of energy less than 60 MeV were attributed to multi-nucleon processes the percentage of all charged hyperons produced in such processes would be $(16 \pm 6)\%$ for Σ^+ and $(18 \pm 5)\%$ for Σ^-. If all the observed charged hyperons of energy less than 60 MeV and emitted without accompanying π-mesons were attributed to multi-nucleon processes, upper limits of $(27 \pm 8)\%$ of all Σ^+ and $(64 \pm 10)\%$ of all Σ^- would be obtained.

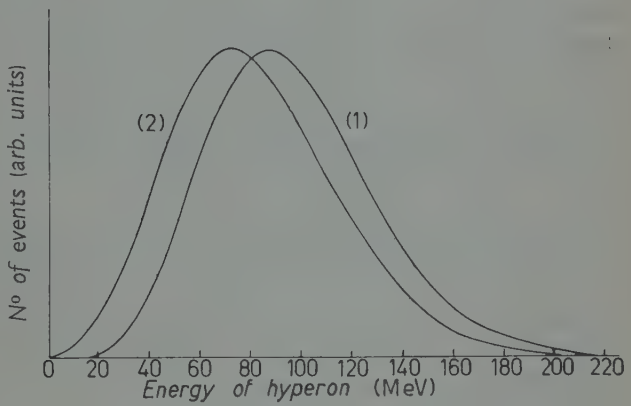

Fig. 12. – Energy spectrum of hyperons from two-nucleon processes.

1) Σ^+ from $K^- + p + p \to \Sigma^+ + n$;
2) Σ^- from $K^- + p + n \to \Sigma^- + p$.

A better estimate of the numbers of charged hyperons from two nucleon processes, emitted with energy less than 60 MeV can be obtained from a consideration of their expected energy distribution.

In Fig. 12 the expected energy distributions of Σ^+ and Σ^--hyperons from two-nucleon processes have been calculated for the momentum distribution

(*) Of the $7\,F\Sigma_p^+$ referred to, all had dip angles less than 45° and 6 were emitted in the forward direction in the CMS. Assuming therefore isotropy in dip and in C.M. decay direction the corrected number of $F\Sigma_p^+$ decays $= 6 \times 1.4 \times 2 = 17$.

of nucleons in the nucleus:

$$N(p)\,\mathrm{d}p = N_0 p^2 \exp\left[-p^2/\alpha^2\right]\mathrm{d}p\,, \tag{1}$$

with $\alpha = 160$ MeV/c, $V_\Sigma = -15$ MeV, $V_K = -15$ MeV, and assuming the sum of the binding energy of the two nucleons involved and the residual excitation of the final nucleus to be 40 MeV (*). These curves suggest that about 13% of all Σ^+-hyperons and 26% of all Σ^--hyperons from two nucleon processes should be emitted with energy less than 60 MeV. Assuming then that the multi-nucleon processes involve two nucleons only, the estimate of the total number of Σ's emitted in such processes becomes 52 for Σ^+ (*i.e.*, 19% of all Σ^+) and 62 for Σ^- (*i.e.*, 25% of all Σ^-). Fig. 12 has been calculated assuming the hyperons do not lose energy in collisions in escaping from the nucleus. In I (Sections 5·2.1) the conclusion that little, if any, such energy loss took place, was reached for Σ-hyperons produced in association with π-mesons. It does not necessarily follow for the faster hyperons produced in multi-nucleon processes. Comparison of Fig. 12 with the energy distributions given in Figs. 9-*b* and 10-*b* should give information on this point but unfortunately the statistics are not yet sufficiently good to enable very definite conclusions to be drawn. Any such collision loss would shift the maxima of the curves of Fig. 12 toward lower energies and thus increase the present estimate of the total number of two-nucleon processes so that the figures given should be regarded in the nature of lower limits. In these calculations it has also been assumed that the absorption probability of the Σ-hyperons does not depend on their energy. This assumption is open to serious question. If, as in the case of π-mesons the absorption cross-section increases at high energies, the numbers of hyperons of energy less than 60 MeV will have been underestimated further.

To obtain the total number of primary processes giving rise to the production of Σ^+ and Σ^--hyperons it is necessary to allow for the probability of absorption of the fast hyperons before emerging from the nucleus in which they have been produced. If the absorption probability can be taken to be the same as for the slower hyperons produced in one-nucleon interactions (~ 0.5) the total number of primary processes (i) and (iv) in the stars we investigated comes out to be about 100 for each. Insufficient is known about the Σ interaction with nucleons to permit an assessment of the validity of this assumption. In the case of π-mesons the cross-section for absorption in nuclear matter is believed to increase practically linearly with momentum

(*) There are many uncertainties in this calculation. For instance V_Σ is not known to better than within ± 10 MeV (see I), while it is not certain what value should be taken for V_K for low energy K-mesons.

over a wide range of energy (FRANK, GAMMEL, WATSON) (5). If the Σ-hyperon absorption cross-section behaves in the same way the estimates of the numbers of two-nucleon processes would be substantially increased.

Assuming charge independence, a further 100 Σ^0-hyperons would be expected, and the total number of two nucleon processes leading to Σ-hyperon production in the stars we have measured would come out to be about 300 *i.e.*, to about 10% of all the K^- interactions investigated. This is probably a considerable underestimate. It would be increased if any appreciable energy loss of Σ-hyperons occurred in escaping from the nucleus since this would increase the proportion emitted with energy less than 60 MeV. It would be increased further if the Σ absorption probability increases with energy.

Some estimate of the relative importance of the various possible two-nucleon processes (i)–(vii) may be obtained from a study of the stars accompanying fast hyperon emission. Table VIII gives details of such stars accompanying definitely identified fast Σ-hyperons.

In this Table the numbers in brackets give the number of stars that contained a stable prong corresponding to the emission of a baryon of energy greater than 30 MeV.

The occurrence of reaction (1) is established by the observation of Σ^+-hyperons which, neglecting charge exchange, can only arise from this source. It is seen from Table VIII that among the 10 identified high energy Σ^+-hyperons, 5 had no accompanying stable prongs from the primary K star. This indi-

TABLE VIII. – *Stable prong distribution of stars emitting fast hyperons* (> 60 MeV).

No. of prongs	0	1	2	3	4	5
Σ^+	5	2	1 (1)	1 (1)	1	0
$\Sigma^\pm$	4	8 (5)	8 (4)	3 (2)	5 (2)	1
Σ^-	0	3 (1)	0	1	1 (1)	0

cates that the neutron in reaction (1) has about a 50% probability of escaping from the nucleus without giving rise to other charged particles. All the 5 definitely identified Σ^--hyperons are accompanied by prongs from the K-star. Further, for the $\Sigma^\pm$-events, only about one seventh are unaccompanied by other prongs. Since about half these hyperons are Σ^+, it appears that few of the fast Σ^--hyperons can be unaccompanied by other prongs on emission from the K-star.

This suggests that processes (vii) occurs comparatively rarely, if at all, and that the greater part of the Σ^--hyperons are produced in process (iv), accompanied by a fast proton.

(5) R. M. FRANK, J. L. GAMMEL and K. M. WATSON: *Phys. Rev.*, **101**, 891 (1956).

3243

Assuming charge independence, expressions can be calculated for the relative transition rates for the processes (i)–(vii) in terms of three complex amplitudes (see Appendix III). To determine these uniquely, five independent pieces of information would be needed. If it can be assumed that process (vii) is very rare, as our data would suggest, some simple relations follow, *viz.*

$$N_2 = \tfrac{1}{2}N_1\,, \qquad N_5 = \tfrac{1}{2}N_4\,,$$

where N_1 is the transition rate for process (1), etc. In this case the number of primary processes (ii) and (v) would each come to be about 50.

There is no basis for estimating the number of two-nucleon processes leading to Λ^0-hyperon production in processes (iii) and (vi). The maximum energy of fast protons that are produced in a two-nucleon process in association with a Σ-hyperon is about 190 MeV and a few protons of energy greater than this have been observed. These might be attributable to a Λ^0 production process, but it is also energetically possible to produce such fast protons as a result of the absorption of fast π-mesons by pairs of nucleons. What can be said with confidence from the present work is that the proportion of all K^--interactions with more than one nucleon in emulsion nuclei is not negligible. It is unlikely to be less than 15% of the total number of K^--meson captures and could be considerably larger.

8. – The absorption probabilities for π-mesons in the nuclei in which they are produced.

The single nucleon interactions of K^--mesons which result in the production of π-mesons are

(viii) $\quad K^- + p \to \Sigma^+ + \pi^-$

(ix) $\quad K^- + p \to \Sigma^- + \pi^+$

(x) $\quad K^- + p \to \Sigma^0 + \pi^0$

(xi) $\quad K^- + n \to \Sigma^- + \pi^0$

(xii) $\quad K^- + n \to \Sigma^0 + \pi^-$

(xiii) $\quad K^- + p \to \Lambda^0 + \pi^0$

(xiv) $\quad K^- + n \to \Lambda^0 + \pi^-$

We confine ourselves to interactions in which a Σ^+ or Σ^--hyperon has been emitted, and of these consider a further subdivision according to whether or not, in addition, a charged π-meson has also been emitted. If a π-meson

emerges from the nucleus it is defined as being non-interacting, even though, in these circumstances, it may have undergone an inelastic collision within the nucleus.

In this Section we estimate the absorption probability, $p(\pi)$ of the π-mesons produced in one of the reactions (viii)–(xii). We do this by comparing the number of cases in which a Σ-hyperon of either sign is emitted with and without an accompanying π-meson. In this way we shall obtain an estimate for the absorption probability of the π-mesons produced in stars in which a Σ-hyperon is emitted. The chance of emission of a Σ-hyperon is greater if its initial direction of motion is outwards from the nucleus. However, as noted in I, the accompanying π-meson will then most probably be moving into the nucleus and its chance of absorption will be correspondingly increased. It would be expected therefore that the estimated value $p(\pi)$ will be greater than the average value $p_0(\pi)$ for all π-mesons, irrespective of whether or not the Σ-hyperon, produced together with them, escapes. It is this latter absorption probability, $p_0(\pi)$, which is needed in the calculation of the total number of π-mesons produced in primary processes so that an attempt will be made to estimate it later.

The estimates $p(\pi)$, $p_0(\pi)$ made in this way are not applicable to the faster π-mesons from reactions (xiii), (xiv), accompanying Λ^0 formation. Since the emission of a Λ^0-hyperon can only rarely be detected using the emulsion method, it is not possible to obtain an estimate of the appropriate absorption probability, $p_0^{\Lambda}(\pi)$.

Since the values of $p(\pi^-)$ and $p(\pi^+)$ are obtained from the study of stars in which a charged Σ is emitted, they refer to primary K^--interactions with protons. If the seat of the interaction with neutrons is different from that with protons, it would not be legitimate to assume the same absorption probabilities to be applicable in this case.

8·1. *The π^- absorption probability.* – Only in reaction (viii) may a Σ^+ hyperon be produced in a single-nucleon interaction. This makes it possible to estimate $p(\pi^-)$ with relatively little ambiguity.

The total observed number of identified Σ^+-hyperons of energy less than 60 MeV is 159 and of these, 41 have no identified accompanying π-meson. If all Σ^+-hyperons were supposed to originate from reaction (viii) these figures would imply an absorption probability,

$$p(\pi^-) = \frac{41}{159} = 0.26 \pm 0.04 .$$

The value is certainly an overestimate since some of the 41 events will be due to multi-nucleon processes (of type i) in which the Σ^+-hyperon is

emitted with energy less than 60 MeV. Others will be events in which the π^--meson has been emitted but has escaped detection. On the other hand some $R\Sigma^+_{\pi}$ and $F\Sigma^-_{\pi}$ decays will have been missed through non-observation of the decay π-meson.

After allowing for these and other losses or misclassifications, and taking account of the $F\Sigma^-_{\pi}$ events, it is estimated (see Tables II and IV) that in our sample the total number of Σ^+-hyperons of energy less than 60 MeV emitted was 233, and 31 of these had no associated π meson. Further, it has been estimated (Section **7**) that 7 of these latter arose from multi-nucleon processes, thus leading to a more realistic estimate of

$$p(\pi^-) = \frac{31 - 7}{235 - 7} = 0.10 \pm 0.03 \, .$$

The actual uncertainty is larger than the statistical error quoted. There are three sources of uncertainty, two of which will tend to lower and the third to raise $p(\pi^-)$. The correction for multi-nucleon processes may be too low. If it were doubled, $p(\pi^-)$ would be reduced to 0.07. The observational loss of π-mesons from K^- stars may be underestimated, In Table II it has been taken as 10%. If it were doubled, $p(\pi^-)$ would be reduced to 0.03.

On the other hand observational losses will be greater for $R\Sigma^+_{\pi}$ decays when no π meson accompanies the hyperon from the K-star. Allowance has already been made for this in Table II where loss factors of 1.2 and 1.8 have been assumed in the two cases. This differential loss may have been underestimated. Even if the two loss-factors had been taken as 1.2 and 3.0 respectively, $p(\pi^-)$ would only have been increased to 0.16.

It has already been pointed out (see Section **6**) that the distribution of stable prongs from stars in which a Σ^+-hyperon is emitted without an accompanying π-meson provides *a priori* evidence for observational loss of emitted π-mesons. After correction has been made for observational loss and multi-nucleon production this prong distribution should be characteristic of π^--meson absorption stars, so that it is of interest to compare it with that for stars produced by incident π-mesons.

The main results with which comparison can be made are those of BERNARDINI and LÉVY ([6]) and of FERRARI *et al.* ([7]), which refer to π^--mesons of energy 35 to 90 MeV and 120 MeV respectively. Some recent work of MAJOR ([8])

([6]) G. BERNARDINI and F. LÉVY: *Phys. Rev.*, **84**, 610 (1952).

([7]) G. FERRARI, L. FERRETTI, R. GESSAROLI, E. MANARESI, E. PEDRETTI, G. PUPPI, G. QUARENI, A. RANZI, A. STANGHELLINI and S. STANTIC: *Suppl. Nuovo Cimento*, **4**, 914 (1956).

([8]) J. V. MAJOR: private communication.

3216

gives significant results for 86 MeV π^--mesons. The relevant data in our case are those of BERNARDINI and LÉVY ([6]) based on 104 events, and of MAJOR ([8]) based on 379. In Table IX are given the prong distributions found by these authors and also that of the 41 events we have found in which an identified Σ^+-hyperon of energy less than 60 MeV is emitted without an accompanying π-meson. The figures are expressed as percentages. The abnormally high number of zero-prong stars in the K^--stack events is evident, and this is in agreement with the view that there is a contamination of « $\Sigma^+ + \pi^-$ » stars in which the π-meson has escaped detection. Also Table VIII suggests that approximately half the multi-nucleon events contained in this sample will contribute to the zero-prong category. The « K-stack corrected » distribution is that obtained after allowance for π-meson observational loss and multi-nucleon contamination. It is consistent with that expected for π^- capture stars.

TABLE IX. – *Stable prong distribution of π^- absorption stars* (figures are in percentages).

	0	1	2	3	4	5	6
K^- stack	55	22	10	10	3	0	0
BERNARDINI and LÉVY	12	36	26	20	4	2	0
MAJOR	26	23	24	16	8	3	0
K-stack corrected	35	30	20	15	0	0	0

It is concluded that the value of $p(\pi^-)$, the absorption probability of π^- mesons produced in association with Σ^+-hyperons is surprisingly small. Making reasonable assumptions about the size of the various observational losses its value can hardly exceed 0.16 ± 0.03 and could be as low as 0.07 ± 0.03. Estimates of $p_0(\pi^-)$, the absorption probability applicable for all π^--mesons produced in reactions (viii) and (xii), are made in Section **10** for different assumptions about the mean free path for the absorption of Σ-hyperons in nuclear matter. It appears that $p_0(\pi^-) \sim 0.75 p(\pi^-)$ so that $p_0(\pi^-)$ lies between 0.05 and 0.12.

8·2. *The absorption probabilities for π^+ and π^0-mesons.* – The production of a Σ^--hyperon may occur through either of the primary processes (ix) or (xi), accompanied by the production of a π^+ or π^0-meson respectively. The relative number of cases of emission of a Σ^--hyperon without accompanying π^+-meson or other prongs depends on the absorption probabilities, $p(\pi^+)$, $p(\pi^0)$ and ζ, the *a priori* probability that the Σ^--hyperon has been produced in reaction (xi).

Neglecting the mass difference of π^+ and π^0-mesons, the Σ^--hyperons produced in (ix) and (xi) might be expected to have the same energy spectra,

so that ζ is also the fraction of emergent Σ^--hyperons that were originally produced in reaction (xi). The analysis is naturally much more complicated than that leading to the estimate of $p(\pi^-)$, and it leads to two relations between $p(\pi^+)$, $p(\pi^0)$ and ζ.

There are 26 observed Σ^--hyperons (of energy less than 60 MeV and dip angle less than 45°) emitted without, and 19 emitted with, an identified accompanying charged π-meson (assumed to be a π^+-meson). Those without an accompanying π^+-meson are expected to be a mixture of events in which the π^+-meson was absorbed or escaped detection, a π^0-meson was created, or the K^--meson interacted with more than one nucleon. Table X shows the prong distribution of the stars from which the 26 definitely identified Σ^--hyperons were emitted; both the actual numbers of events and the percentages are given, the latter for comparison with the prong distribution of 115 π^+ absorption stars observed by BERNARDINI and LÉVY (6) and the 62 observed by SHAFI and PROWSE (9).

TABLE X. – *Stable prong distribution of stars in which a Σ^- hyperon is emitted (without π^+-meson), compared with the observed prong distribution of π^+ absorption stars.*

No. of prongs	0	1	2	3	4	5	6	7
	(1) K^- stars in which Σ^- emitted without identified π^+							
Actual number of stars (*)	5	6	2	7	5	1	0	0
Number expressed as a percentage	19	23	8	27	19	4	0	0
	(2) π^+ absorption stars							
Number expressed as a percentage								
1) BERNARDINI and LÉVY	0	9	28	27	16	13	5	2
2) SHAFI and PROWSE	5	10	18	25	16	13	13	—

(*) This prong distribution differs from that given in Table VI for stars emitting Σ^- hyperons without an accompanying π-meson. Only definitely identified Σ^- events are included here. The distribution in Table VI included a proportion of stars emitting a hyperon identified as $F\Sigma^{\pm}_{\pi}$ that could not be definitely identified as Σ^-.

A feature of the prong distribution of the stars from which a Σ-hyperon is emitted without identified $\pi^{\pm}$-meson (we call these category *A* stars) is the small number of cases (5 in 26) in which there are no other stable prongs.

(9) M. SHAFI and D. J. PROWSE: *Padua-Venice Conference Report* (1957), p. X-2.

By contrast, 17 of the 19 stars in which a π^+-meson accompanies the Σ^--hyperon category *B* stars) have no other stable prongs.

BERNARDINI and LÉVY found no cases of zero prong events among their π^+ absorption stars. In later work SHAFI and PROWSE [9] found 3 zero-prong events among some 62 interactions of π^+-mesons in which the meson failed to emerge. We conclude the number of zero prong stars due to π^+ absorption in our category *A* stars is 0 or 1. Some of the apparent category *A* stars must be attributed to category *B* stars in which the emitted π^+-meson has escaped detection. The estimate of this number of wrongly classified stars is 1 or 2, and they would be expected to be without other stable prongs.

As already pointed out, category *A* will also include stars in which a π^0 has been emitted. These would be expected to have a prong distribution similar to category *B*, *i.e.*, they will consist mainly of zero stable prong events. But there are only 5 such events among the category *A* stars and between 1 and 3 are already accounted for. We conclude that the number of cases of π^0 emission must be very small. We estimate between 2 and 4 such cases in the present sample. This allows for one case of π^0 absorption producing a zero prong star.

Some of the events in category *A* must be ascribed to multi-nucleon processes. In Section **7** it has been estimated that 16 of the 114 cases of emission of a Σ^--hyperon of energy less than 60 MeV without an accompanying π-meson are produced in multi-nucleon processes (*i.e.*, about one seventh of the total). In category *A*, therefore, 4 stars should be attributed to two-nucleon processes and these (see Section **7**) would all be expected to be accompanied by stable prongs. The remaining 16-19 events with stable prongs in category *A* must be ascribed to events in which a π^0 or π^+-meson is absorbed. The prong distribution agrees, within statistical error, with that found experimentally for π^+ absorption stars as does the proportion of stars in which a fast proton (> 30 MeV) is emitted; (53 % compared with 59 % for π^+ absorption stars). These measurements lead therefore to an estimate of a mean absorption probability, $p(\pi^+, \pi^0)$ for π^+ and π^0 mesons produced in stars in which a Σ^--hyperon is emitted of

$$\frac{16 \div 19}{26 + 19 - 3} = 0.38 \div 0.45 \ (\pm 0.12) .$$

8·3. *The separate π^+ and π^0 absorption probabilities and the number of cases of emission of Σ-hyperon and π-meson.* – We now attempt to separate the individual absorption probabilities $p(\pi^+)$, and $p(\pi^0)$. We define α as the fraction of Σ^--events in which a π^+-meson is emitted and have the relation

$$\alpha = (1 - \zeta)(1 - p(\pi^+)) = \frac{19 + (1 \text{ or } 2)}{26 + 19 - 4} \cong 0.5 . \tag{2}$$

Similarly we define β as the fraction of these events in which a π^0 is emitted and have

$$\beta = \zeta(1 - p(\pi^0)) = \frac{2 \div 4}{26 + 19 - 3} = 0.05 \div 0.1 \,. \tag{3}$$

The relationship between ζ, $p(\pi^+)$, $p(\pi^0)$ is shown in graphical form in Fig. 13. For $\alpha = 0.5$, $\beta = 0.05$, 0.1.

It is seen that if $p(\pi^+) = p(\pi^-)$ $(= 0.1)$ as would be expected on the basis of charge independence and equal numbers of protons and neutrons in the nucleus, $p(\pi^0)$ would have to be very large, lying between 0.75 and 1.0. At the same time ζ would be ~ 0.45. On the other hand a value $p(\pi^0) = 0.5$ would correspond to $p(\pi^+) = 0.38$ and $\zeta = 0.2$.

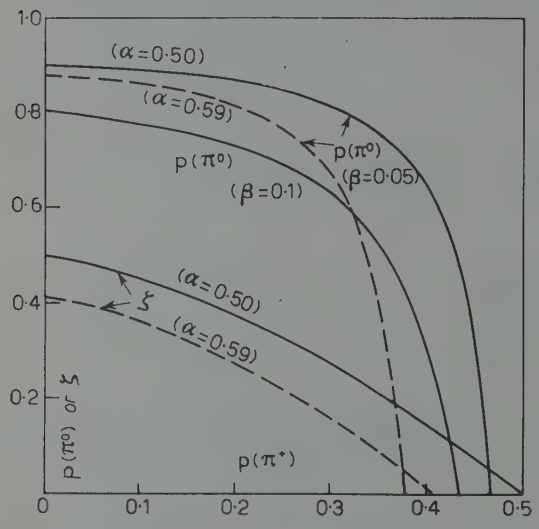

Fig. 13. – Dependence of $p(\pi^0)$ and ζ on $p(\pi^+)$.

The value of α depends on the estimate of the number of Σ^--hyperons of energy less than 60 MeV due to multi-nucleon reactions. The dotted curves show the effect of increasing the estimate of the number of such processes in our sample by a factor of 3. It is seen that $p(\pi^0)$ would still need to be very large if $p(\pi^+) = p(\pi^-)$. Even larger contributions from multi-nucleon processes cannot be completely excluded but this seems unlikely, because if the spectrum of the Σ^--hyperons is distorted so much, the Σ^+ spectrum might be expected to exhibit a similar distortion. There are insufficient observed Σ^+-hyperons of energy less than 60 MeV without accompanying π-mesons to permit such an interpretation.

The value of β is not well determined owing to the very small statistics involved but the present analysis strongly suggests the conclusion that either $p(\pi^+) \gg p(\pi^-)$, or $p(\pi^0)$ is extremely large. If the former is the case, reaction (xi) occurs much less frequently than reaction (ix) (*i.e.*, $\zeta \ll 0.5$). In the latter case however (xi) would be only slightly less probable than (ix).

Estimates made in Sect. **11** suggest once again that $p_0(\pi^+)$, the absorption probability applicable for all π^+-mesons, whether or not associated with an emitted Σ^--hyperon is about three quarters of $p(\pi^+)$.

The values of $p(\pi^0)$ and ζ can be obtained independently by using the estimate of the number of cases in which a Σ^0-hyperon is emitted from a K^- star together with a π^--meson (see I, Section 5·5.*d*.). This number was estimated to be 64 ± 20, before correction is made for π-meson observational loss at the centre of the K^--star. Results obtained using the K_5 stack ([3]) suggested this correction will be substantial for this class of event and might be expected to increase this number to about 90. The number of primary processes (xii) is thus

$$\frac{90}{\{1-p(\pi^-)\}\{1-p(\Sigma^0)\}},$$

and putting $p(\Sigma^0) \simeq 0.5$, $p(\pi^-) \simeq 0.1$ this becomes equal to 200. Assuming charge independence this will also be equal to the number of primary processes (xi).

We have seen that in a sample of events containing 19 cases of emission of an identified Σ^--hyperon together with a π^+-meson there are at most 4 cases of emission of an identified Σ^--hyperon and a π^0-meson. From Tables II and IV it is seen that the estimated total number of Σ^--hyperons emitted together with a π^+-meson is 91 so that there should be at most 19 cases in which a π^0-meson and Σ^--hyperon have been emitted and we have

$$19 = 200\{1-p(\Sigma^-)\}\{1-p(\pi^0)\}.$$

Putting $p(\Sigma^-) \simeq 0.5$ gives $p(\pi^0) \simeq 0.8 \pm 0.1$.

This suggests then that of the two alternative interpretations of Fig. 13 the one leading to a very high value of $p(\pi^0)$ is the more likely one. In this case, assuming $p(\pi^+) \simeq p(\pi^-) = 0.1$, $\zeta \simeq 0.45 \pm 0.05$. This conclusion is based on the estimate made in I of the number of « $\pi^- + \Sigma^0$ » events, which depends on the assumption that π^--mesons of energy less than 50 MeV emitted alone from K^--stars do not originate from « $\pi^- + \Lambda^0$ » type events.

But a value of $p(\pi^0)$ so large in comparison with that of $p(\pi^-)$ is so surprising that it seems worth while to examine the evidence on which these estimates are based. Some behaviour of this kind is to be expected from the figures given in Tables II and IV. The small number of « Σ^+ without π » events in which the Σ^+-hyperon has an energy less than 60 MeV makes the small value of $p(\pi^-)$ almost inevitable. On the other hand the correspondingly large number of « Σ^- without π » events suggests either a very large value of $p(\pi^+)$ or a considerable probability for the primary process (xi) in which a Σ^--hyperon and a π^0-meson are produced. A value of $p(\pi^+)$ many times greater than $p(\pi^-)$ would be very difficult to understand theoretically, so that one is led to assume a substantial probability for $(\Sigma^-\pi^0)$ production. However the prong distribution (Table X) of stars in which the Σ^- is emitted without accompanying charged π-meson, indicates that very few of the π^0-mesons can escape, leading

to the conclusion that $p(\pi^0) \gg p(\pi^-)$. It cannot be excluded, however, that this difference in prong distribution could arise from a difference in the relative frequencies of $(K^- + p)$ to $(K^- + n)$ interaction in the light and heavy nuclei of the emulsion.

The estimate of $p(\pi^0)$ depends on the assumed number of low energy Σ^- hyperons from two nucleon processes, which may possibily be underestimated. But it is not very sensitive to this number. The assumed number of low energy Σ^+-hyperons from such processes cannot be increased very much without causing the estimate of $p(\pi^-)$ to vanish altogether, so that if the large number of Σ^--hyperons without accompanying π-mesons were to be attributed to two nucleon processes it would be necessary to assume a difference in behaviour of Σ^+ and Σ^--hyperons in nuclear matter with respect to absorption and inelastic scattering. Such a difference would appear to be as difficult to accept theoretically as a marked difference between $p(\pi^-)$ and $p(\pi^+)$. The most probable interpretation of the data suggests therefore a value of $p(\pi^0)$ much greater than either $p(\pi^+)$ or $p(\pi^-)$.

9. – The number of primary K capture processes.

In this section we discuss the conclusions that can be drawn about the results presented both in the present paper and also in Part I. The numbers of different types of event are listed below (Table XI).

TABLE XI (*).

	Numbers uncorrected for π-meson observational loss	Numbers corrected for π-meson observational loss	As in II, but expressed as a percentage
	I	II	III
Total number of K^- capture events	3024	3024	100
$\pi^- + \Sigma^+$ emissions	165 ± 20	204 ± 24	6.7 ± 0.8
$\pi^+ + \Sigma^-$ emissions	86 ± 20	91 ± 21	3.0 ± 0.7
$\pi^- + \Sigma^0$ emissions	64 ± 20	93 ± 29	3.1 ± 1.0
$\pi^- + \Lambda^0$ emissions	277 ± 40	388 ± 58	12.8 ± 1.9
π^- + double star	46 ± 7	67 ± 10	2.2 ± 0.3
$\pi^- + \Sigma^0, \Sigma^+$ (Σ absorbed)	186 ± 26	274 ± 37	9.1 ± 1.2
$\pi^+ + \Sigma^-$ (Σ absorbed)	65 ± 20	95 ± 29	3.1 ± 1.0
Σ^+ (without charged π)	76 ± 15	76 ± 15	2.5 ± 0.5
Σ^- (without charged π)	161 ± 32	161 ± 32	5.3 ± 1.1

(*) For a comparison with the figures shown in Part I, Table XXI, see note to Table II, Sect. 3.

The first column of Table XI gives the numbers uncorrected for π-meson observational losses. The second column gives these numbers corrected for such losses, assuming the true fraction of K^--stars that emit a π-meson to be 0.40 ([3]). (We refer to this quantity henceforth as the π/K ratio). In making this correction it is assumed that the same observational loss correction factor has to be used for all stars from which no identified Σ-hyperon was emitted. Probably a larger correction should have been applied to the « $\pi^- + \Lambda^0$ » events in view of the larger π meson energy in these cases. The third column gives the numbers in column 2 expressed as a percentage.

To obtain the proportion of different types of primary processes it is necessary to make use of the absorption probabilities derived. There is some ambiguity about the values to be used for some of these however. The relative numbers of the different processes also depend on the value taken for the true proportion of K^--stars emitting a π-meson. Estimates of the proportion of different primary processes have therefore been made using two different sets of values for these quantities. The results of these calculations are set out in Table XII.

TABLE XII.

Type of primary process	Percentage of all primary processes	
	I	II
(viii) $K^- + p \to \Sigma^+ + \pi^-$	13.5 ± 1.6	13.5 ± 1.6
(ix) $K^- + p \to \Sigma^- + \pi^+$	6.3 ± 1.5	7.5 ± 1.7
(x) $K^- + p \to \Sigma^0 + \pi^0$	7.4 ± 2.7	8.0 ± 2.8
(xi) $K^- + n \to \Sigma^- + \pi^0$	6.6 ± 2.0	6.6 ± 2.4
(xii) $K^- + n \to \Sigma^0 + \pi^-$	6.6 ± 2.0	6.6 ± 2.4
(xiii) $K^- + p \to \Lambda^0 + \pi^0$	5.5 ± 0.8	7.6 ± 1.1
(xiv) $K^- + n \to \Lambda^0 + \pi^-$	14.2 ± 2.1	19.8 ± 2.9
Total	60.1 ± 4.8	69.6 ± 5.7
Fraction of all one-nucleon captures on neutrons	0.46	0.48
Fraction of all one-nucleon captures leading to Λ^0 production	0.33	0.39
Ratio $\lvert a_1\rvert^2/\lvert a_0\rvert^2$	0.21	0.24
Ratio $\lvert b_1\rvert^2/\lvert a_0\rvert^2$	0.24	0.33

The estimates given in column I of the Table have used observational loss factors based on a value of 0.4 for the π/K ratio and it has been assumed that the same value applies to all stars emitting a π^+-meson without any observed $\Sigma^\pm$-hyperon. The absorption probabilities employed were $p(\pi^-) = p(\pi^+) = 0.1$

3256

(this implies $p(\pi^0) \simeq 0.8$ but this was not used directly). $p^{\Lambda}(\pi^-) = 0.2$ for π-mesons from « $\pi^- + \Lambda^0$ » type events, $p(\Sigma^-) = p(\Sigma^+) = p(\Sigma^0) = 0.45$.

In column II the π/K ratio has been taken to be 0.44 but it has been assumed that, on account of their greater energy the observational loss factor applicable to π^--mesons from « $\pi^- + \Lambda^0$ » type events is 50% greater than that for other events in which a $\pi^{\pm}$-meson is emitted without accompanying charged Σ-hyperon. The same absorption probabilities for π mesons have been assumed as in I but the values $p(\Sigma^-) = 0.55$, $p(\Sigma^0) = 0.50$, $p(\Sigma^+) = 0.45$ have been used for the Σ-hyperon absorptions. These values which are entirely within the experimental accuracy of the determinations make some allowance for a possible trapping of some Σ-hyperons by the Coulomb field.

The numbers N_8, N_9, N_{12}, N_{14} of the processes (viii), (ix), (xii) and (xiv) have been obtained directly from the measurements. The numbers N_{10}, N_{11} of processes (x) and (xi) can then be obtained from the relations

$$N_{10} = \tfrac{1}{2}(N_8 + N_9 - N_{12}/r)\,, \qquad N_{11} = N_{12}\,, \qquad N_{13} = N_{14}/2r\,,$$

which are valid assuming charge independence, r being the ratio of the number of neutrons to the number of protons in the nucleus. The errors given in Table XII are statistical only and do not include the larger uncertainties in interpretation, or the errors in the estimate of the absorption probabilities.

The results of Table XII indicate that less than one half of the captures on a single nucleon take place on neutrons. When allowance is made for the neutron excess it is seen that the chance of K^- capture occurring on a neutron is about two-thirds of the chance of capture on a proton. Further, more than half the captures on neutrons lead to Λ^0 production.

These conclusions can be stated alternatively in terms of the transition amplitudes for the K^- capture process. The capture of K^--mesons on protons can occur either through a $T = 0$ or a $T = 1$ state of isotopic spin while the capture on neutrons occurs exclusively through the $T = 1$ state. Table XII gives values of the ratios

$$\frac{|a_1|^2}{|a_0|^2} \qquad \text{and} \qquad \frac{|b_1|^2}{|a_0|^2}\,,$$

where a_0 and a_1 are the respective transition amplitudes for the $T = 0$ and $T = 1$ isotopic spin states leading to Σ hyperon production and b_1 is the transition amplitude leading to Λ^0 production.

The single nucleon processes listed in Table XII account for 60% and 70% of the total number of K^--meson captures for the sets of values of absorption probabilities and π/K ratio used in calculating columns I and II. Evidently the remaining 30 to 40% of all K^- captures must take place on more than one

3364

nucleon. A lower limit of about 15% has been derived for the number of such processes from a study of the number of hyperons with kinetic energy greater than 60 MeV (Section 7). This estimate assumes that Σ-hyperons do not lose energy in collision before escaping from the nucleus in which they are produced and does not include allowance for direct Λ^0 production in multi-nucleon processes, such as (iii) and (vi) of Section 7. Further it uses values of $p(\Sigma)$ derived from a study of one nucleon interactions and does not allow for any possible increase in absorption probability for the faster hyperons produced in multi-nucleon interactions. In view of these considerations an estimate that from 30 to 40% of all K^- interactions take place through such processes is not unreasonable.

In Section 7 we have seen that the processes

(1) $$K^- + p + p \to \Sigma^+ + n \quad \text{and} \quad K^- + n + p \to \Sigma^- + p$$

occur with comparable frequency and have estimated a lower limit of 3% of all K^- captures by emulsion nuclei to occur through them. On the other hand the fact that no definite evidence has been obtained of the process

(vii) $$K^- + n + n \to \Sigma^- + n$$

suggests that it occurs rather rarely.

10. – Comparison with the results of investigations using hydrogen and deuterium bubble chambers.

Results are now available of experiments on K^- capture in a hydrogen bubble chamber for K^--mesons both at rest ([10]) and in flight ([11]) and in a deuterium bubble chamber for K^--mesons at rest ([12]). From the measurements in hydrogen the relative frequency of K^- capture processes on neutrons can be estimated if charge independence is assumed to apply. These estimates (expressed as percentages) are shown in Table XIII. From the measurements in deuterium the relative frequency of the neutron capture processes can be obtained directly provided it is assumed that the observed interactions are due to K^- capture by a single nucleon, the second nucleon playing the role

---

([10]) L. W. Alvarez, H. Bradner, P. Falk-Vairant, J. D. Gow, A. H. Rosenfeld, F. T. Solmitz and R. D. Tripp: *Nuovo Cimento*, 5, 1026 (1957).

([11]) Berkeley bubble chamber results, reported by M. F. Kaplon: *Geneva Conference Report* (1958), p. 176.

([12]) R. D. Tripp: *Geneva Conference Report* (1958), p. 185.

of a spectator only. Table XIII shows also the relative frequency of the one nucleon interactions deduced from the present work, taking the two sets of values of absorption probabilities and π/K ratio used in column I and II of Table XII.

TABLE XIII.

Interaction process	Hydrogen Bubble Chamber (K^- at rest)	Deuterium Bubble Chamber (K^- at rest)	Present emulsion work (*)	
			as in column I of Table XII	as in column II of Table XII
(viii) $K^- + p \to \Sigma^+ + \pi^-$	14.8 ± 1.5	21.6 ± 1.6	25.6 ± 3.0	21.5 ± 2.6
(ix) $K^- + p \to \Sigma^- + \pi^+$	29.5 ± 2.3	24.5 ± 1.7	11.9 ± 2.8	12.0 ± 2.7
(x) $K^- + p \to \Sigma^0 + \pi^0$	14.8	20.8 ± 1.4	14.1 ± 5.1	12.4 ± 4.5
(xi) $K^- + n \to \Sigma^- + \pi^0$	14.8	4.6 ± 0.8	9.1 ± 3.0	8.9 ± 2.9
(xii) $K^- + n \to \Sigma^0 + \pi^-$	14.8	4.6 ± 0.8	9.1 ± 3.0	8.9 ± 2.9
(xiii) $K^- + p \to \Lambda^0 + \pi^0$	3.7	8.0 ± 1.0	9.4 ± 1.3	12.1 ± 1.8
(xiv) $K^- + n \to \Lambda^0 + \pi^-$	7.4	16.0 ± 1.4	20.8 ± 3.2	24.2 ± 3.5
π^-/π^+ ratio (at production)	1.25 ± 1.0	1.25 ± 0.32	4.6 ± 0.9	4.5 ± 0.9
Σ^-/Σ^+ ratio (at production)	3.2 ± 1.3	1.38 ± 0.28	0.82 ± 0.24	0.97 ± 0.30
$\pi^+\Sigma^-/\pi^-\Sigma^+$ (at production)	2.0 ± 0.3	1.22 ± 0.24	0.47 ± 0.11	0.56 ± 0.13

(*) The emulsion data are reduced to represent the case of equal numbers of protons and neutrons in the nucleus, for comparison with the bubble chamber work.

There is a major disagreement between the results obtained in hydrogen and in emulsion nuclei for the ratio of the number of $\pi^+\Sigma^-$ events (interaction viii) to $\pi^-\Sigma^+$ events (interaction ix). The hydrogen bubble chamber results give a value of 2.0 for this ratio while the emulsion work gives a value of about 0.5. The emulsion results depend of course on the estimates of the absorption probabilities of the π-meson and Σ hyperon, but extreme assumptions about the values of these quantities which would just be consistent with the experimental data could not raise this ratio above 1.0. The differences obtained for the π^-/π^+ ratio and the Σ^-/Σ^+ ratio are related closely to the difference in the $\pi^+\Sigma^-/\pi^-\Sigma^+$ ratio.

These differences may be interpreted to mean that the transition amplitudes are velocity dependent. Recent hydrogen bubble chamber measurements of K^- interactions in flight have demonstrated such a velocity dependence ([10]). Evidence for such a variation has been presented by the Berne group ([13]) as a result of measurements of the interactions with emulsion nuclei

([13]) Y. EISENBERG, W. KOCH, E. LOHRMANN, E. NIKOLIĆ, M. SCHNEEBERGER and H. WINZELER: *Nuovo Cimento*, **9**, 745 (1958).

3256

of K^--mesons in flight. For K^--mesons of energy 86 MeV they estimated a π^-/π^+ ratio of 8, compared with 4.5 in the present work and 1.25 for K^--mesons at rest (deduced from the hydrogen bubble chamber work) and they found the Σ^-/Σ^+ ratio also varied with energy. For K^- capture at rest by emulsion nuclei, the Fermi motion of the nucleons means that the K^--nucleon interaction takes place under conditions in which the energy of relative motion may be 20 MeV.

Further evidence that the discrepancies may be explained in this way is provided by the observation that for interactions on free protons in emulsions the ratio $\pi^+\Sigma^-/\pi^-\Sigma^+$ is 1.4 ± 0.4, in much closer accord with the value deduced from the hydrogen bubble chamber work than the ratio 0.5 deduced for interactions with protons in emulsion nuclei. Also it is seen from Table XIII that in the deuterium bubble chamber the Σ^-/Σ^+ and $\pi^+\Sigma^-/\pi^-\Sigma^+$ ratios depart from the values obtained in hydrogen in the direction toward closer agreement with the results of the present investigation, as might be expected if the internal nucleon momentum is important in determining this ratio.

11. – The interpretation of the measurements in terms of the basic K^- capture mechanism.

The small value (~ 0.10) of the absorption probability $p(\pi^-)$ of π^--mesons formed as a result of the capture by bound protons of K^--mesons that have come to rest, strongly suggests that the capture occurs mainly near the periphery of the nucleus (*). The small number of stable prongs associated with events in which both π-mesons and Σ-hyperons are emitted suggests that inelastic scattering is not important in this class of event, lending further support to the idea that a substantial proportion of K^--interactions occurs near the nuclear surface. The process of the capture of K^--mesons by silver and bromine nuclei of the emulsion has been discussed by JONES [14]. He supposes K^--mesons, moving very slowly, are captured into a circular orbit of high quantum number to form a K-mesic atom. The K-meson cascades down to lower orbits. Nuclear capture occurs when the lifetime in a given orbit against such capture of the K^--meson becomes less than the lifetime against electromagnetic transition to a lower orbit. He estimates that for an « average » heavy nucleus in the emulsion for which $A = 94$, $Z = 41$, capture occurs from a $5\,g$ orbit. Considering only the Coulomb interaction between the K-meson and the nucleus, this orbit has a mean radius of approximately 6 fermis, while the mean nuclear radius is 5.5 fermis. Assuming the proton distribution found by the Stanford electron

(*) See contribution to KAPLON's Report, Geneva Conference (1958).

[14] P. B. JONES: *Phil. Mag.*, **3**, 33 (1958).

scattering experiments (RAVENHALL ([15])) *viz.*

$$\varrho(r) = \varrho_0 \left(1 + \exp\left[\frac{r - c}{\delta}\right]\right)^{-1}, \tag{4}$$

where for $Z = 41$, $A = 94$, $c = 4.7$ fermi, $\delta = 0.55$ fermi

$$\varrho_0 = 0.083\,7 \text{ (fermi)}^{-3}$$

and that the neutron and proton distributions have the same shape, Fig. 14 shows the distribution of distance from the nuclear centre for which K^- capture takes place in the case of capture in the $5\,g$ and $6\,h$ orbits of the K-mesic atom.

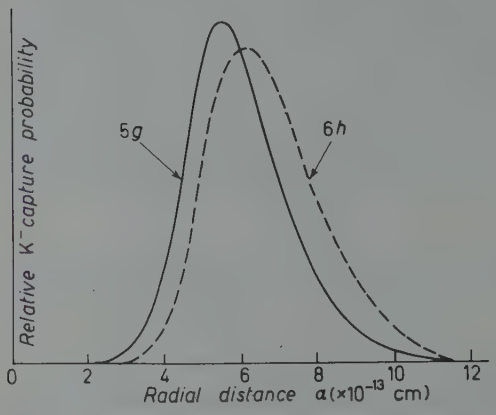

Fig. 14. – Radial distance at which K^- capture occurs from $5g$ and $6h$ Coulomb states of a K mesic atom (ordinates arbitrary).

The absorption of π-mesons in nuclear matter has been discussed by FRANK, GAMMEL and WATSON ([5]). On the basis of measurements on the absorption of π-mesons by deuterons they derive an expression for the absorption mean free path, λ, of π-mesons in nuclear matter which is in satisfactory agreement with the experimental data on the absorption of π-mesons by heavy nuclei.

Absorption probabilities for π-mesons produced at various distances from the centre of a heavy emulsion nucleus have been calculated using the absorption mean free path of FRANK, GAMMEL and WATSON. For a meson originating at a radius a, the mean absorption probability,

$$p_0(\pi) = 1 - \frac{1}{2}\int_0^{\pi} \sin\theta \exp\left[-\int_0^{\infty} \frac{\mathrm{d}l}{\lambda(r)}\right] \mathrm{d}\theta\,, \quad (*)$$

where $r^2 = a^2 + l^2 - 2al\cos\theta$.

([15]) D. G. RAVENHALL: *Rev. Mod. Phys.*, **30**, 430 (1958).

(*) Throughout this section it is assumed that the direction of motion of the π-meson (and therefore of the Σ-hyperon) is isotropically distributed. This may not be justified, since, if the capture occurs from an orbit of high angular momentum the momentum of the K^--meson before capture will be predominantly tangential and this might be expected to favour a tangential direction of emission of the π and Σ. Such an effect would make it easier to interpret the low value of $p(\pi^-)$ observed but would imply very large Σ and π^0 interaction cross-sections to account for the high values of $p(\Sigma^{\pm})$ and of $p(\pi^0)$.

3258

For an assumed mean π-meson energy of 55 MeV (see I, Table VIII)

$$\frac{1}{\lambda(r)} = \frac{0.021\,\Gamma_\pi}{\{1+\exp[(r-c)/\delta]\}} \text{ (fermi)}^{-1}, \tag{5}$$

where Γ_π is a factor that measures the relative cross-section for the absorption of a π-meson by a neutron-proton pair in the nucleus to the absorption by a free deuteron. The value of Γ_π depends on the constants in the expression for the nucleon distribution. It was estimated from the experimental data of CHEDESTER, ISAACS, SACHS and STEINBERGER and of R. L. MARTIN ([16]), on the absorption of π-mesons in nuclei of medium atomic number.

The method described by ROSSI ([17]) was used. Unfortunately, it is difficult to obtain an accurate estimate of λ, and therefore of Γ_π. A value of Γ_π about 10 is consistent with the measured cross-section.

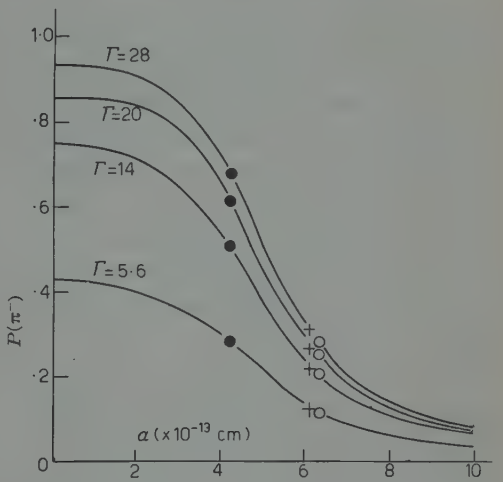

Fig. 15. – Mean $p_0(\pi^-)$ corresponding to K^- capture at distance « a » from centre of nucleus. 1) $\Gamma_\pi = 5.6$; 2) $\Gamma_\pi = 14$; 3) $\Gamma_\pi = 20$; 4) $\Gamma_\pi = 28$. • Mean $p(\pi^-)$ assuming uniform production throughout nucleus. + Mean $p(\pi^-)$ assuming capture from $5g$ Coulomb state. ○ Mean $p(\pi^-)$ assuming capture from $6h$ Coulomb state.

Fig. 15 illustrates the dependence of $p_0(\pi^-)$ on the radius of origin, a, for different values of Γ_π. Values are given for the equivalent radii of production for the following cases:

1) Uniform production throughout the nucleus (4.2 fermis).
2) Capture from the 5 g Coulomb state (6.1 fermis).
3) Capture from the 6 h Coulomb state (6.35 fermis).

The values of the π^+ absorption probability $p_0(\pi^+)$ can be obtained from the curves of Fig. 15 by adjusting Γ_π in the neutron to proton ratio. This will give values of $p_0(\pi^+)$ on the assumption of identical neutron and proton density distributions. It is seen from Fig. 15 that $p_0(\pi^+)/p_0(\pi^-)$ will certainly

([16]) C. CHEDESTER, P. ISAACS, A. SACHS and J. STEINBERGER: *Phys. Rev.*, **82**, 958 (1951); R. L. MARTIN: *Phys. Rev.*, **87**, 1052 (1952).

([17]) B. ROSSI: *High Energy Particles* (New York, 1952), p. 359.

3059

be less than 53/41, the assumed neutron to proton ratio, that is the two absorption probabilities will not be very different even in the heavy nuclei of the photographic plate.

It has already been pointed out (Section 8) that the measured values of absorption probabilities, $p(\pi)$, refer to a particular class of event, *viz.* one in which a Σ-hyperon is emitted, and will be different from the value $p_0(\pi)$, appertaining to all π-mesons produced as a result of processes (viii)–(xiii).

The effect of Σ^+ absorption on the measured π^- absorption probability is calculated in Appendix V. Assuming $\Gamma_{\pi^-} = 5.6$, and the analogous strength factor for the Σ-hyperon, $\Gamma_{\Sigma^+} = 28$, values of $p(\pi^-)$ and $p(\Sigma^+)$ can therefore be obtained in rough agreement with our measurements, although $p(\pi^-)$ is somewhat high (*) (see Table XV inAppendix V).

With such a model, however, there is no way of accounting for any large difference between $p(\pi^+)$ and $p(\pi^-)$, such as might be suggested by one interpretation of the data (see Section 8·2). Suggestions have sometimes been made, however, that the neutron radius of a nucleus should be larger than the proton radius (JOHNSON and TELLER [18]), and the question has not been settled conclusively. It was pointed out by JONES [14] that the capture of K^--mesons at rest might provide an effective tool for probing the composition of the outer fringe of the nucleus since the mesons spend a comparatively large proportion of their time in this region. Calculations have therefore been carried out of $p_0(\pi^+)$, $p_0(\pi^-)$, assuming the neutrons to have a density distribution of the same form as that found for protons, but with the constants, c, δ, 20% greater. It was not possible in this way, however, to obtain a ratio $p_0(\pi^+)/p_0(\pi^-)$ above about 1.4 so that it would be difficult to interpret any very large asymmetry between these quantities.

In Section 8·2 it was pointed out that the data on stars in which a Σ^- hyperon is emitted indicated either that $p_0(\pi^+) \gg p_0(\pi^-)$ or $p_0(\pi^0)$ is very large. The latter interpretation appeared more likely and the estimate of $p(\pi^0)$ obtained was $p_0(\pi^0) \sim 0.8 \pm 0.1$. The difficulty of accounting for any large difference in $p_0(\pi^+)$ and $p_0(\pi^-)$ clearly lends further support for this large value of $p(\pi^0)$. The small value of $p_0(\pi^-)$, however, requires for its interpretation that K^- capture at rest should occur predominantly on the nuclear surface.

It is difficult to understand how at the one time the K^- interaction process can be sufficiently peripheral to account for the low value of $p(\pi^-)$ while at the same time giving the large value of $p(\pi^0)$ that seems indicated.

(*) The calculations of this section have been carried out for a typical heavy emulsion nucleus. Since an appreciable (but unknown) fraction of captures is expected to occur on light emulsion nuclei and these should have smaller absorption probabilities, one would expect the calculated absorption probabilities on heavy nuclei to be somewhat larger than the average measured values.

([18]) M. H. JOHNSON and E. TELLER: *Phys. Rev.*, **93**, 357 (1954).

3210

The observed values of the Σ absorption probabilities, $p(\Sigma^-)$, $p(\Sigma^+)$, of about 0.5 would also indicate a mean free path for absorption in nuclear matter of about 1.5 fermis for the processes

(xv) $$\Sigma^+ + n \rightarrow \Lambda^0 + p\,,$$

(xvi) $$\Sigma^- + p \rightarrow \Lambda^0 + n\,.$$

The comparatively large proportion of two-nucleon processes (15 to 40%) suggests a high degree of correlation between pairs of nucleons, at least in the peripheral region of the nucleus in which capture seems to occur.

Measurements on the capture of K^--mesons from rest in the deuterium bubble chamber (TRIPP ([12])) suggest that less than one per cent of all K^- captures occur through processes of type (iv) and (v) involving two nucleons. Evidently pairs of nucleons are correlated in the nuclear periphery with a mean separation considerably smaller than is the case in the deuteron. It is not possible to say whether these clusters of nucleons are in pairs or in larger units.

The results of the Berne Group ([13]) have indicated a far smaller proportion of multi-nucleon processes following K^--mesons in interactions in flight with emulsion nuclei. In our results also, while the mean energy of the Σ-hyperons at emission was 32.5 MeV in the case of K^- interactions at rest, it was only 22 MeV for interactions in flight (see I, Section 4·2) suggesting again a much greater proportion of multi-nucleon interactions in the former case. Since interactions in flight would be expected to take place throughout the nuclear volume it would appear that clusters of nucleons occur more frequently on the nuclear surface than in the central regions of the nucleus (*).

12. – Conclusions.

1) The multi-nucleon K^- absorption processes account for between at least 15 and possibly as much as 40% of all interactions of K^--mesons at rest with emulsion nuclei. The two-nucleon process $K^- + n + n \rightarrow \Sigma^- + n$ occurs rarely compared with other such processes leading to Σ emission. The importance of multi-nucleon absorption processes suggests a high degree of correlation of pairs or clusters of nucleons on the nuclear surface.

(*) *Note added in proof.* - Recently WILDERMUTH developed the « cluster-model » of the nucleus, giving arguments in favour of the clustering of nucleons at the periphery of nuclei (K. WILDERMUTH and TH. KANELLOPOULOS: CERN, Theor. Division (1959)).

2) The relative probabilities of the processes resulting from the interaction of a K^--meson at rest with a single nucleon in the emulsion are not the same as the bubble chamber results on the capture of K^--mesons at rest in hydrogen, but they are closer to the results of K^- capture from rest in a deuterium bubble chamber. This is probably associated with the Fermi motion of nucleons in nuclei and is consistent with the velocity dependence of K^- capture transition amplitudes obtained in other experiments.

3) Most of the one-nucleon interactions leading to Σ-hyperon production take place with protons. The transition amplitude corresponding to the $T=1$ state of isotopic spin leading to Σ-hyperon production is smaller than the $T=0$ transition amplitude.

4) For π^--mesons produced in association with Σ^+-hyperons the absorption probability in emerging from the nucleus in which they are produced is about 0.10. This small absorption is consistent with K^- absorption on the nuclear periphery. There is some difficulty in accounting for the apparently large combined absorption probability of π^+ and π^0-mesons. The evidence favours the more likely assumption that the absorption probability of π^+-mesons is of the same order as that of π^--mesons, indicating a large absorption of the π^0-mesons.

5) The absorption probabilities of Σ^+ and Σ^--hyperons formed in association with charged π-mesons are approximately 0.5. This is consistent with an interaction mean free path of about 1.5 fermis for Σ-hyperons in nuclear matter.

* * *

We are greatly indebted to Drs. R. W. Birge and E. J. Lofgren of the Radiation Laboratory, University of California, for their care and attention in carrying out the exposure and to Dr. W. Barkas and his group who devised the K^--meson beam used; to Professor C. F. Powell who helped to initiate the present collaboration; to Professor G. Puppi and his collaborators at Bologna and to Dr. J. V. Major of Durham for making available to us, prior to publication, data on the absorption and inelastic scattering of π-mesons by emulsion nuclei; to Dr. L. Castillejo of the University of Birmingham, for many illuminating discussions of theoretical points. Acknowledgement is also made of a D.S.I.R. special development grant to University College London, of a D.S.I.R. Research Fellowship to F.R.S., of a D.S.I.R. Studentship to D.H.D., of an Egyptian Ministry of Education Scholarship to F.H., and of a British Council Colombo plan award to K.K.N.

We wish to thank also the many scanners and microscopists in all groups for their painstaking work.

Appendix I

The misclassification of $F\Sigma_\pi^\pm$ as $R\Sigma_\pi^+$.

The range of the Σ is divided into intervals such that the particle takes the same time, $0.5 \cdot 10^{-11}$ s to traverse each interval. From the number of hyperons estimated to have traversed these intervals, the distribution in residual range of $F\Sigma_\pi^\pm$ events can be evaluated, assuming appropriate values for the lifetimes of Σ^+ and Σ^-. In Fig. 16 the curve shows the expected distribution, taking $\tau_{\Sigma^+} = 8 \cdot 10^{-11}$ s, and $\tau_{\Sigma^-} = 17 \cdot 10^{-11}$ s (cfr. Part III). In constructing this curve the measurement errors in the estimate of the residual range have been « folded in ». The histogram gives the actual number of events classed as $F\Sigma_\pi^\pm$. The agreement is seen to be good above $1 \cdot 10^{-11}$ s. However, below this value, corresponding to a residual range of 200 μm, there seems to be a deficiency of events, *viz.* 4 instead of about 16, although this number cannot be estimated very accurately. It should be borne in mind that this number may be altered by assigning different values to τ_{Σ^+} and τ_{Σ^-} or if the estimate of the number of $R\Sigma_\rho^-$ events is in error.

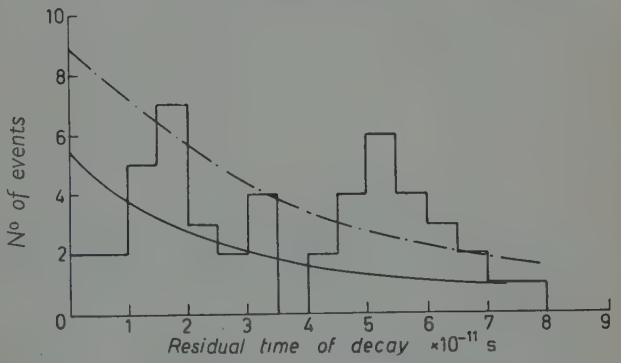

Fig. 16. – Distribution of residual time at decay for $F\Sigma_\pi^\pm$ (dip angle of $\Sigma < 45°$). The histogram gives the experimental distribution of residual times. — Expected contribution from $F\Sigma_\pi^-$. -·-·- Total expected number of $F\Sigma_\pi$ of both signs.

If a prong appears to be at rest and there is no π in the K-star, then, as has been pointed out above, a loss factor of 1.8 instead of 1.2 is applicable. This implies that some of the $\Sigma \to \pi$ decays have been missed altogether. This would account for about 2 of these « missing » events.

There remain about 10 events still unaccounted for, and we assume these have been ascribed wrongly to the $R\Sigma_\pi^+$ class. There is no method of distinguishing which events are the ones wrongly classified.

Appendix II

A method of determining the number of $R\Sigma_\rho^-$.

We consider a sample of stars which emit a π-meson together with one baryon which has not been identified as a hyperon.

Table XIV shows, for different energy ranges of the baryon (calculated on the assumption that it was a proton), the number of cases in which the angle between the π and baryon prong was greater or less than 90°, and the sign ratio of the accompanying π-mesons.

TABLE XIV.

Energy of baryon (MeV)	Ratio of number events in which the π-baryon angle is $> 90°$ to the number in which it is $< 90°$	Ratio of π^- to π^+ found
$0 \div 10$	$59 : 35 = 1.7 : 1$	$13 : 4 = 3.3 : 1$
$10 \div 30$	$65 : 26 = 2.5 : 1$	$13 : 10 = 1.3 : 1$
$30 \div 60$	$23 : 17 = 1.4 : 1$	$9 : 2 = 4.5 : 1$
$\geqslant 60$	$7 : 5 = 1.4 : 1$	$3 : 1 = 3.0 : 1$

In the energy range $(10 \div 30)$ MeV the number of cases in which the angle between the two prongs is large is abnormally high while the π^-/π^+ sign ratio is correspondingly low. This is exactly what would be expected if the sample of « protons » in this energy range contained a contamination of hyperons, predominantly negatively charged.

The total number of non-identified hyperons in this sample can be estimated using a method of analysis similar to one developed by the Göttingen [19] group and based on the distribution of the angle between the π-meson and the baryon. It is assumed first that the distribution should be symmetrical in the case of « π+proton » events but that for « $\pi+\Sigma$ » events it should lie predominantly between 90° and 180°. Any observed asymmetry has then to be attributed to the hyperon contamination. For the events in which the energy of the proton was between 10 MeV and 30 MeV, this would require 45 of the observed baryon prongs to be Σ-hyperons that have escaped identification. These will include not only Σ^- endings but also $R\Sigma_\pi$ decays in which the π has escaped observation and $F\Sigma_p$ decays in flight in which the proton was emitted backwards in the C.M.S.

If the stable prong is a proton produced by absorption its direction might be expected to be correlated with that of the Σ-hyperon producing it. This could lead to an asymmetry even in « π+1 stable prong » events. If one assumes, therefore, that the true asymmetry in such events should be 1.4, *i.e.*, the same value observed when the proton emitted has an energy above 30 MeV, the number of hyperons missed becomes 35.

The number of negative Σ-hyperons can be estimated if it is required that the true sign ratio of « π+1 stable prong » events in which the energy of the proton lies between 10 and 30 MeV, is the same as for events in which the energy of the proton is larger. The number of Σ^--hyperons in the $(10 \div 30)$ MeV group becomes 27 if this sign ratio is taken as 4, and 22 if it is taken as 3. Corresponding to this sample of events there were 12 cases

---

[19] W. ALLES, N. N. BISWAS, M. CECCARELLI and J. CRUSSARD: *Nuovo Cimento*, **6**, 517 (1957).

of « $R\Sigma_\sigma^- + \pi$ » so that the ratio (Total no. Σ^-)/(Observed no. Σ^-) lies between 34/12 and 39/12, *i.e.*, between 2.7 and 3.2 which is consistent with the value obtained from collinear events.

A rough estimate can also be made of the Σ^+ observational loss in this same sample. Taking the π-meson sign ratio to be 4, there must be 8 missed Σ^+ hyperons in the sample with energy between 10 and 30 MeV and dip angle less than 45°. In this same sample there are 23 $R\Sigma_\pi^-$, 8 $F\Sigma_p^+$, and 14 $F\Sigma_\pi^\pm$ identified hyperons. The assumed observation loss factor of 1.2 (see Sect. 3) for $R\Sigma_\pi^+$ and $F\Sigma_\pi^\pm$ decays from « $\pi + \Sigma$ » type events would indicate a loss of between 7 and 8 hyperons in the sample, which is entirely consistent with the conclusions reached by this method of analysis that about 8 Σ^+-hyperons have escaped detection.

Appendix III

Calculation of the correction for the loss of high energy hyperons that escape from the stack.

A number of energetic particles, which could be classed as baryons, escaped from the stack without having been brought to rest. The emission energy and the observation time were determined from ionization wherever possible. The total numbers (including some with tracks going to cut edges of the emulsion that were not followed) are given in Table XV below.

Table XV. – *Energetic protons and unidentified baryons.*

		Emission energy (MeV)		
		60÷90	90÷120	120÷180
(*a*)	Total number of baryons coming to rest without producing observable decay or interaction	165	47	13
(*b*)	Total number of baryons not followed to rest	26	30	20
(*c*)	Proportion of Σ-hyperons $q(E)_1$ amongst emitted baryons. (Calculated for all charged Σ)	0.19	0.26	0.46

The total numbers of lost Σ-hyperons were determined as follows: the proportion of Σ-hyperons amongst all emitted baryons was first estimated using the numbers from the corrected Σ spectrum together with the knowledge of the total number of baryons which stop in the stack without producing any observable decay or interaction, as listed opposite (*a*) Table XV. The

hyperon proportion $q(E)$ amongst the baryons of different energies is shown in (*c*). About equal numbers of fast hyperons of either sign are known to be emitted.

The loss of hyperons was then estimated from a consideration of the emission energy (E_i) and observation time (t_i) for each of the escaping particles. The expectation of the loss will be the quantity $P_i\, q(E_i)$ summed for all the trajectories concerned, where P_i is the usual survival probability, $\exp[-(t_i/\tau)]$, for a hyperon of lifetime τ to the boundaries of the stack.

By calculating the escape for $F\Sigma_{\pi}^{-}$, $F\Sigma_{\pi}^{+}$, $F\Sigma_{p}^{-}$, separately the total loss of fast Σ-hyperons (over 60 MeV) is estimated to be:

For all Σ^+	1.7 events
For all Σ^-	6.0 events

Appendix IV

The transition amplitudes for two-nucleon events (assuming charge independence).

The two nucleon interactions may take place through states of total isotopic spin $\frac{3}{2}$, $\frac{1}{2}$. There are three independent (complex) transition amplitudes, $a_{\frac{3}{2}}$, $a_{\frac{1}{2}}^{(1)}$ and $a_{\frac{1}{2}}^{(0)}$ where $a_{\frac{1}{2}}^{(1)}$ corresponds to the case where the K-meson ($T_K = \frac{1}{2}$) is combined with the two nucleon system having $T_N = 1$ to produce a resultant $T = \frac{1}{2}$, while $a_{\frac{1}{2}}^{(0)}$ corresponds to the two nucleon system having $T_N = 0$. Then the following transition amplitudes are obtained

(1) Σ + nucleon:

$K^- + p + p \to \Sigma^0 + p$, $\frac{\sqrt{2}}{3}(a_{\frac{3}{2}} - a_{\frac{1}{2}}^{(1)})$; $K^- + (p+n)_{T=0} \to \Sigma^- + p$, $-\sqrt{\frac{2}{3}}\, a_{\frac{1}{2}}^{0}$,

$K^- + p + p \to \Sigma^+ + n$, $\frac{1}{3}(a_{\frac{3}{2}} + 2a_{\frac{1}{2}}^{(1)})$; $K^- + (p+n)_{T=1} \to \Sigma^- + p$, $\frac{\sqrt{2}}{3}(a_{\frac{3}{2}} - a_{\frac{1}{2}}^{(1)})$,

$K^- + (p+n)_{T=0} \to \Sigma^0 + n$, $\frac{1}{\sqrt{3}}\, a_{\frac{1}{2}}^{0}$; $K^- + (n+n) \to \Sigma^- + n$, $t_{\frac{3}{2}}$

$K^- + (p+n)_{T=1} \to \Sigma^0 + n$, $\frac{1}{3}(2a_{\frac{3}{2}} + a_{\frac{1}{2}}^{(1)})$.

(2) Λ + nucleon:

$K^- + p + p \to \Lambda^0 + p$, $\sqrt{\frac{2}{3}}\, {}_{\Lambda}a_{\frac{1}{2}}^{1}$,

$K^- + (p+n)_{T=0} \to \Lambda^0 + n$, ${}_{\Lambda}a_{\frac{1}{2}}^{0}$,

$K^- + (p+n)_{T=1} \to \Lambda^0 + n$, $-\frac{1}{\sqrt{3}}\, {}_{\Lambda}a_{\frac{1}{2}}^{1}$.

3263

The experimental results appear to indicate that $K^- + n + n \rightarrow \Sigma^- + n$ is a very weak process, *i.e.*, $a_{\frac{1}{2}} \simeq 0$.

If this can be assumed a number of simple relations follow, *viz.*:

$$N_{\Sigma^0 p} = \tfrac{1}{2} N_{\Sigma^+ n},$$

$$N_{\Sigma^0 n} = \tfrac{1}{2} N_{\Sigma^- p}.$$

Also

$$N^{T=1}_{\Lambda^0 n} = \tfrac{1}{2} N_{\Lambda^0 p}.$$

Appendix V

Effect of Σ^+ absorption on the measured π^- absorption probability.

If $\lambda_{\Sigma^+}(r)$ is the mean free path for Σ^+-hyperon absorption at a radius r in the nucleus, then neglecting the Fermi motion of the nucleons, so that the π-meson and Σ-hyperon can be assumed to be moving in opposite directions after production, the measured π^- absorption probability is

$$p(\pi^-) = 1 - \frac{\int_0^{\pi} \sin\theta \left(\exp\left[-\int_0^{\infty} dl \left(\frac{1}{\lambda_\pi(r')} + \frac{1}{\lambda_\Sigma(r)} \right) \right] \right) d\theta}{\int_0^{\pi} \sin\theta \left(\exp\left[-\int_0^{\infty} \frac{dl}{\lambda_\Sigma(r')} \right] \right) d\theta}, \tag{6}$$

where $r^2 = a^2 + l^2 - 2al\cos\theta$; $r'^2 = a^2 + 2al\cos\theta$. A similar expression can be written for $p(\pi^+)$.

Formally it is convenient to express $\lambda_\Sigma(r)$ in the same form as (5), the strength factor Γ_π being replaced by another, Γ_Σ. Calculations of (10) have been carried out for $\Gamma_\pi = 5.6$ and $\Gamma_\Sigma = 5.6$, 14, 28 (corresponding to mean free paths in nuclear matter of 8.5, 3.4 and 1.7 fermis respecti-

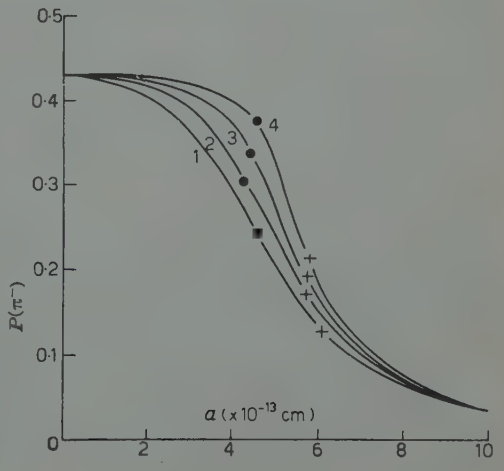

Fig. 17. – Illustrating the relation between $p_0(\pi^-)$ and $p(\pi^-)$ for various values of Γ_Σ. 1) $p_0(\pi^-)$ (no Σ absorption); 2) $p(\pi^-)$ $\Gamma_\Sigma = 5.6$; 3) $p(\pi^-)$ $\Gamma_\Sigma = 14$; 4) $p(\pi^-)$ $\Gamma_\Sigma = 28$. • Mean $p(\pi^-)$ assuming uniform production throughout nucleus. + Mean $p(\pi^-)$ assuming capture from $5g$ Coulomb state.

vely) for different values of the radius of production, a. The results are shown in Fig. 17 and illustrate the increase of $p(\pi^-)$ as Γ_Σ is increased for a given value of Γ_π. The values of $p(\pi^-)$ have also been calculated assuming both uniform production throughout the nucleus and K^- capture from the $5\,g$ Coulomb state. They are given in Table XVI.

TABLE XVI. – *Effect of Σ^+ absorption cross section on the measured values of the π^- absorption probability $p(\pi^-)$ and the Σ^+ absorption probability, $p(\Sigma^+)$ (assuming $\Gamma_{\pi^-} = 5.6$, corresponding to a mean free path in nuclear matter of 8.5 fermi).*

Γ_{Σ^+}	(1) for uniform production throughout nucleus		(2) for production following K^- capture from the $5g$ state	
	$p(\pi^-)$	$p(\Sigma^+)$	$p(\pi^-)$	$p(\Sigma^+)$
0	0.24	0	0.13	0
5.6	0.30	0.31	0.17	0.17
14	0.33	0.41	0.19	0.33
28	0.38	0.71	0.21	0.44

RIASSUNTO (*)

È stata studiata l'emissione di 3037 stelle di cattura K^- a riposo in emulsione nucleare. Si discute l'identificazione degli iperoni. Il $(17.6 \pm 1.0)\%$ di tutte le stelle K^- emette iperoni Σ carichi mentre il $(9.6 \pm 0.6)\%$ di esse emettono sia iperoni Σ che mesoni π. Il rapporto Σ^-/Σ^+ per tutte le stelle è 0.86 ± 0.12, mentre che per le stelle che emettono anche un mesone π è 0.45 ± 0.10. La differenza tra quest'ultimo valore e il valore nettamente differente (2.0) ottenuto per le interazioni K^- a riposo in una camera a bolle a idrogeno si attribuisce al moto di Fermi dei nucleoni nel nucleo ed alla dipendenza delle ampiezze relative delle transizioni K^- dall'energia del moto relativo del mesone K^- e del nucleone. Il rapporto R del numero dei decadimenti Σ^+ a quelli π^+ e protonici rispettivamente è 1.23 ± 0.27. È stata studiata la distribuzione dei rami stabili delle stelle in cui si emette un iperone, come pure la distribuzione dell'energia degli iperoni Σ all'emissione. Circa il 16% di tutti gli iperoni Σ carichi identificati avevano energia di emissione superiore a 60 MeV ed hanno dovuto essere attribuiti alle interazioni multinucleoniche del mesone K^-. Si stima che la proporzione di tutti i processi multinucleonici primari di cattura raggiunga il $(30 \div 40)\%$. L'interazione di un K^- con una coppia di neutroni sembra occorrere, se mai, raramente. Dalla frazione di stelle che emettono Σ^+ emettendo anche un mesone π^- si conclude che solo circa il 10% dei mesoni π^- non abbandonano il nucleo in cui la cattura avviene. Ciò sarebbe comprensibile se la cattura K^- avvenisse prevalentemente nelle regioni periferiche del nucleo. Da un simile studio delle stelle che emettono dei Σ^- si trova, tuttavia, che la proporzione dei mesoni π^+ o π^0, o delle due specie, assorbiti nel nucleo è molto maggiore. Si valuta il cammino libero medio degli iperoni Σ e dei mesoni π^0 nella materia nucleare. La maggior parte delle interazioni di 1 nucleone che conducono alla produzione di iperoni Σ avvengono con protoni e le ampiezze di transizione corrispondenti allo stato $T=1$ dello spin isotopico sono minori dell'ampiezza di transizione $T=0$.

(*) *Traduzione a cura della Redazione.*

IL NUOVO CIMENTO Vol. XIV, N. 2 16 Ottobre 1959

Relativistic Increase of Ionization in Xenon.

A. Rousset, A. Lagarrigue, P. Musset, P. Rançon and X. Sauteron
Ecole Polytechnique - Paris

(ricevuto il 6 Maggio 1959)

Summary. — The relativistic increase of ionization is studied in various gaseous mixtures by the method of drop-counting in a cloud chamber. If we call ϱ the relative ionization of $\beta/\sqrt{1-\beta^2}$ equal to 300, we find that in pure Xenon or mixtures of Xenon and Hydrogen, ϱ is of the order of 1.7. On the other hand the value of ϱ drops to 1.3 if Helium is mixed with Xenon.

1. – Introduction.

The initial purpose of this work was the study of a possible experimental method for identifying elementary particles of very high energies (~ 20 GeV), when $\beta = v/c$ is in the neighbourhood of 1. The relativistic increase of ionization is a sensitive function of $\gamma = 1/\sqrt{1-\beta^2}$. An apparatus sensitive to this parameter γ has a chance to be suitable. We have hence studied this phenomenon for Xenon which has a theoretical large relativistic increase of ionization.

Our technique is based on the use of a cloud chamber with simultaneous measurement of ionization by drop counting and of momentum by curvature in a magnetic field (1). We use μ-mesons and electrons from local cosmic-ray showers to establish the ionization curves.

(1) W. B. Fretter and E. W. Friesen: *Rev. Sc. Inst.*, **26**, 703 (1955); W. B. Fretter, E. W. Friesen and A. Lagarrigue: *Suppl. Nuovo Cimento*, **4**, 569 (1956).

3269

2. – Experimental set-up.

The intensity of the magnetic field is 6200 gauss; the uniformity is better than 2% in the useful region of the chamber ($45 \times 25 \times 12$ cm).

Optics: 2 apochromatic Boyer lenses, focal length $f = 24$ cm, aperture $\sigma = 20$; magnification $M = 9.5$; stereoscopic angle: 10°. French emulsion Kodak Plus X.

Lighting: 2 flashes of 800 joule each. Every flash-tube is placed on the axis of a cylindrical mirror and at the focus of a double series of square-shaped spherical lenses. Each lens is separated from the next one by a little plate intended to eliminate light rays spreading too much from the horizontal.

Triggering of the chamber is ensured by two counter trays above and below the chamber. A μ-meson is identified as a single particle of cosmic rays (double coincidence). Quadruple coincidences give us showers in which we easily identify electrons. These particles enable us to explore the relativistic range

$$3 < \beta\gamma < 2000 .$$

3. – Momentum measurement.

Accurate momentum measurement involves two difficulties:

1) Tracks are wide: in order to separate the droplets, ions are allowed to spread for 40 ms before the expansion of the chamber. One could think that microscope reading on such broad tracks would introduce large errors. Statistics of second differences in consecutive readings prove that the r.m.s. sagitta due to the setting on the track is about 0.045 mm (corresponding to a radius of curvature $R \simeq 500$ m).

2) In order to have enough light scattered by the droplets, lightning delay is set at as much as 150 ms (even 200 ms in pure Xenon). Turbulence has to be avoided during these delays for it could distort the tracks. Great care is therefore taken to keep constant temperature equilibrium in the chamber.

In order to determine directly the error on the curvature measurement, we have studied the spurious curvatures of energetic μ-meson tracks without magnetic field. The r.m.s. sagitta is 0.21 mm, corresponding to a radius of curvature of 100 m. Such a curvature corresponds to momenta of 18 GeV

Plate 1.

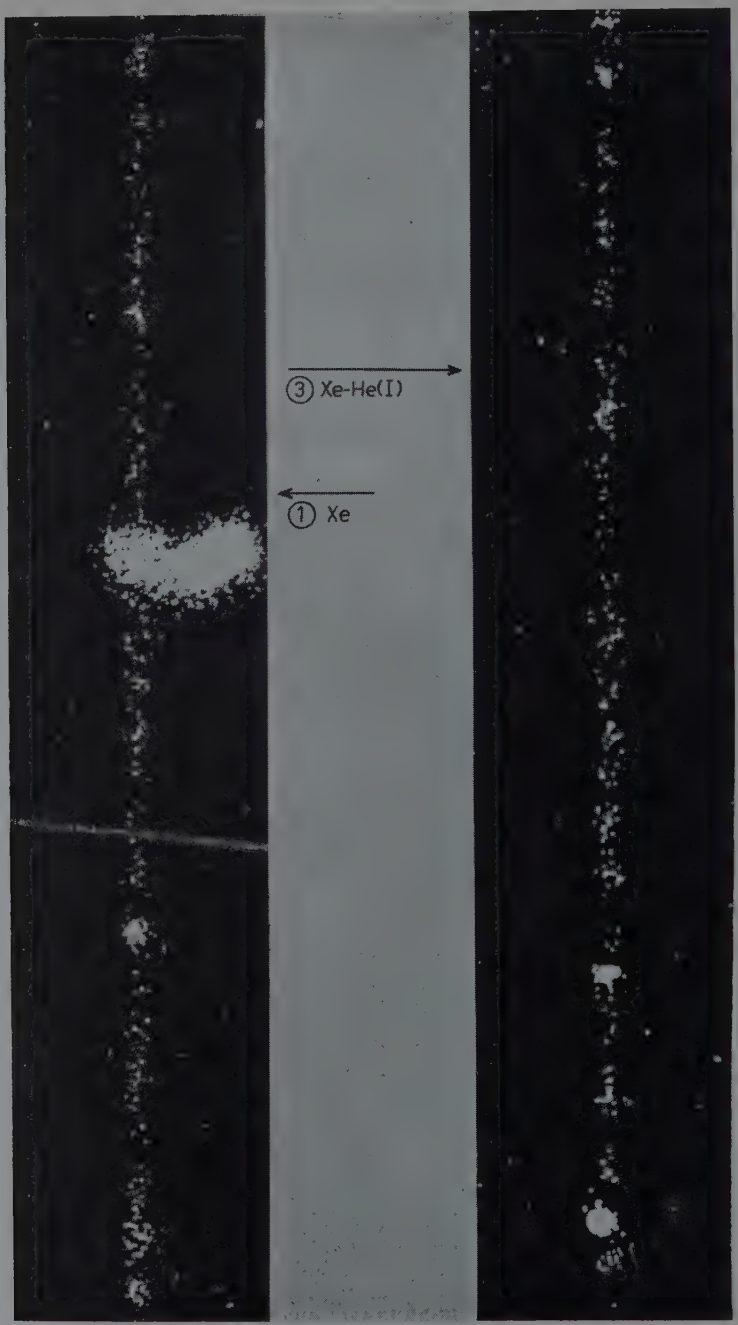

Plate 2.

in our magnetic field. It can therefore be seen that the distortion error, and not the width of the tracks, limits the accuracy in curvature measurement. On the other hand it can be seen that this error is of the same order of magnitude as that obtained in most of the classical cloud chambers (1).

This value of 18 GeV limits the use of μ-mesons at a momentum of 8 GeV ($\beta\gamma = 80$). To study values of $\beta\gamma$ larger than this limit, we use electrons from local cosmic-ray showers. In most cases the uncertainty introduced by this error in momentum is not larger than 10% of the ionization error.

4. – Ionization measurement.

We use a stereoscopic microscope for droplet counting following the method elaborated by W. B. Fretter and E. W. Friesen.

In order to obtain optimum accuracy in the ionization measurement, we operated in the neighbourhood of a droplet density of about 30 drops/cm: higher densities lead to a rapidly increasing error and lower densities to an important fluctuation error. For the use of Xenon we have built a low pressure chamber (19 cm Hg).

For droplet densities less than 50 drops/cm the overlapping correction is small ($\leqslant 2\%$). This correction was calculated using the results of the Berkeley group and fitting them to the conditions of our experiment (1).

Ionization fluctuations σ_i. – We can determine the ionization fluctuations directly from the dispersion, within the same track of the number of droplets N_i per cell. In order to ensure the independence of elementary cells from each other, we have chosen an elementary cell sufficiently large (2 cm) with respect to the mean width of the track (0.2 cm). In practice we have used cells composed of 4 adiacent counting cells (0.5 cm). (The ionization fluctuation for a full 35 cm long track is $\sigma_i = 9.0\%$).

Ionization fluctuation can also be determine by the study of the dispersion on the counting of several electrons belonging to the same electron shower. A statistics of 109 tracks gives us $\sigma_i = 9.4\%$.

Counting error σ_c. — We can estimate the personal error by comparing the counting of a same track by several people. We estimate that 5% is certainly an upper limit for this error σ_c.

Total error on ionization measurements. – We have studied external dispersion of our measurements *i.e.* dispersions of experimental points around the experimental curve. This dispersion is $\sigma_e = 12.5\%$.

Comparison between σ_i and σ_e leads us to think that one has to take into account an additional error of the order of 8% due to the fluctuations of the minimum from picture to picture.

3271

The best extimate of the total error of ionization measurements is given by the value of external dispersion σ_e, *viz.*

$$\sigma_e = 12.5\ \%$$

for one track.

However, in the cases where the number of tracks in one picture is large enough to make comparison measurements, it is possible to reduce the error to

$$\sigma_i = 9.4\ \%\ .$$

5. – Experimental results.

Four experiments have been performed with different gas mixtures:

Experiment (1)	Pure Xenon
Experiment (2)	Xenon and Hydrogen
Experiment (3)	Xenon and Helium
Experiment (4)	Xenon and Helium (with higher pressure).

The operation of the chamber required the addition of alcool (4 cm Hg) as an additional constituent to each mixture.

For each of the four experiments we have measured 200 couples of values (N, x):

N= number of droplets per centimeter,

$x = \beta\gamma\ .$

With these results we have to draw the curve $N = f(x)$ in the range of relativistic velocities.

To a first approximation the ionization increase is a linear function of $\log x$. On the other side, a law in $1/x^2$ holds before the minimum. For our calculations we choose an *a priori* expression enabling us to fit easily our results:

$$N = \alpha \frac{x^2 + 1}{x^2} \log kx\ .$$

This expression contains only the two parameters α and k. It does not take into account the density effect. Applying the least square method to all

measurements of $\beta\gamma < 500$ we can easily determine the two parameters α and k and then deduce the two other interesting physical parameters: N_0 and α/N_0.

$N_0 =$ number of drops per cm at minimum,

$\alpha/N_0 =$ slope of the logarithmic relativistic increase.

The solid curve (experimental) is the best fit of all the experimental data below $\beta\gamma = 500$ to the form:

$$\frac{N}{N_0} = (\alpha/N_0)\frac{x^2+1}{x^2}\log kx\,.$$

For all experiments most of the points beyond $x = 500$ are below this curve. We can study the deviations of these points from the straight line

$$\frac{N}{N_0} = (\alpha/N_0)\log kx$$

for judging to what extent the density effect is significant.

In a more elaborate fitting method account was taken of a possible curvature in the upper part of the curve, and all points were included. In the figure this curve is drawn in dotted lines.

We have chosen a more striking parameter than k for comparing the different curves. We adopted $\varrho = N/N_0$ for $x = 300$.

It can indeed be seen that the density effect for this value of x is small enough to let its indetermination have no influence on ϱ.

We have calculated in each case the ion proportions of each constituent. This calculation is an approximation because it does not account for the complexity of secondary ions. It was done only to show that in these four experiments we measure essentially the Xenon ionization.

We have determined in each experiment the mean-square dispersion σ_e for a track with respect to the experimental curve:

$$\sigma_e^2 = \frac{1}{n-2}\sum_i \frac{(N_i - N_{ci})^2}{N_{ci}}\,,$$

N number of drops/cm for the i-th track,

$N_{ci} =$ number of drops/cm taken on the experimental curve at the point $x = x_i$.

n = total number of tracks counted in the experiment.

This experiment involved a rather important difficulty. Xenon has bad thermal conductivity. Droplets grow slowly. In order to increase the scattered light we were obliged to adopt a longer lighting delay (≈ 200 ms) and to open the objectives at $\sigma = 16$ and reduce the depth of the illuminated region to 8 cm.

Experiment (1) - *Xenon.*

Mixture composition	Partial pressures	Ion percentage
Xenon	19 cm Hg	90%
Alcohol	4 cm Hg	10%

194 tracks investigated; 250 000 droplets counted.
$N_0 = 32.3$ drops/cm;
$\sigma_e = 12.2\%$;
$\varrho = 1.69 \pm 0.05$: important relativistic increase.
The density effect is not significant (one standard deviation).

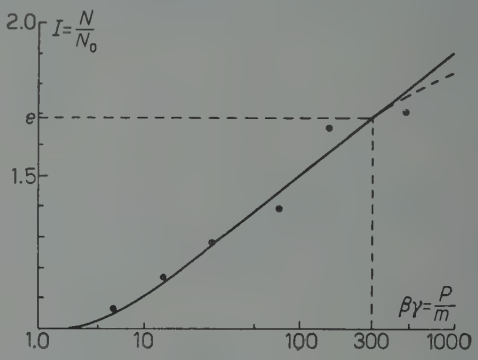

Fig. 1.

The interesting result of this experiment is to show that in a heavy gas like Xenon the relativistic increase is really important. Unfortunately the photography conditions are very difficult and this is why we performed the next experiment.

The hydrogen molecule has only two electrons and in spite of its high proportion in the mixture it contributes only very little to ionization. Hydrogen

Experiment (2) - *Xenon Hydrogen.*

Mixture composition	Partial pressures	Ion percentage
Xenon	15 cm Hg	84%
Hydrogen	25 cm Hg	6%
Alcohol	4 cm Hg	10%

201 tracks investigated; 250 000 droplets counted.
$N_0 = 27.8$ drops/cm;
$\sigma = 12.5\%$;
$\varrho = 1.72 \pm 0.05$: important relativistic increase.
A possible density effect (2 standard deviations).

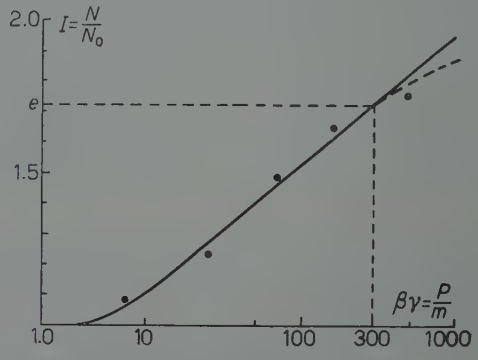

Fig. 2.

3274

being diatomic ($\gamma = 1.4$), the expansion ratio of the chamber must be higher than that for a pure noble gas. This is a further difficulty for the operation of the chamber but the droplets are of a good quality due to the good thermal conductivity of hydrogen which makes these droplets grow fast enough. Flash delay can be 150 ms and the objective aperture $\sigma = 20$.

The interesting result is the following: hydrogen does not change the relativistic increase of ionization of Xenon and it has two elements favouring these experiments.

1) Improvement of photography conditions.

2) Possibility to work with a chamber at the atmospheric pressure by increasing the proportion of hydrogen.

In order to attain a low expansion ratio we have done the following experiment, in which helium is used instead of hydrogen.

Experiment (3) - *Xenon Helium.*

Mixture composition	Partial pressures	Ion percentage
Xenon	15 cm Hg	84%
Helium	25 cm Hg	6%
Alcohol	4 cm Hg	10%

280 tracks investigated; 340 000 droplets counted.
$N_0 = 30.8$ drops/cm;
$\sigma = 13.9\,\%$;
$\varrho = 1.33 \pm 0.04$: weak relativistic increase.
Significant density effect (2.5 standard deviations).

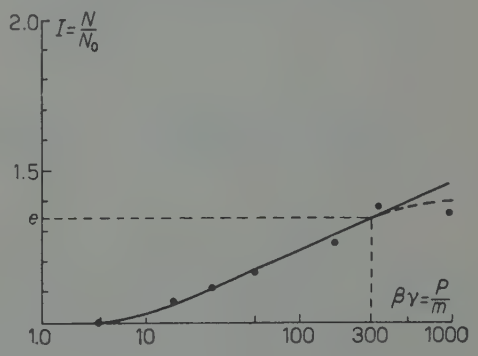

Fig. 3.

The operating conditions of the chamber and the droplet pictures were excellent.

It can be seen that in this mixture one helium atom replaces exactly one hydrogen molecule. An electron from a helium atom is little different from an electron belonging to a hydrogen molecule; we have therefore thought that the relativistic increase would be of the same order as that in the previous experiment. The present case proves that it is weaker. A similar experiment (2),

(2) R. C. Kepler, C. A. d'Andlau, W. B. Fretter and L. H. Hansen: *Nuovo Cimento*, **7**, 71 (1958); R. C. Kepler: *Thesis-Berkeley* (1957).

for lower pressure of Xenon and Helium, has given a result intermediate between the last one and that of the experiment with pure Xenon.

To check the effect of partial pressure of helium we performed the following experiment

Experiment (4) - *Xenon Helium.*

Mixture composition	Partial pressures	Ion percentage
Xenon	14 cm Hg	78%
Helium	50 cm Hg	12%
Alcohol	4 cm Hg	6%

190 tracks investigated; 240 000 droplets counted.
$N_0 = 32.0$ drops/cm;
$\sigma = 11.5\,\%$;
$\varrho = 1.25 \pm 0.05$: weak relativistic increase.
Significant density effect (3 standard deviations).

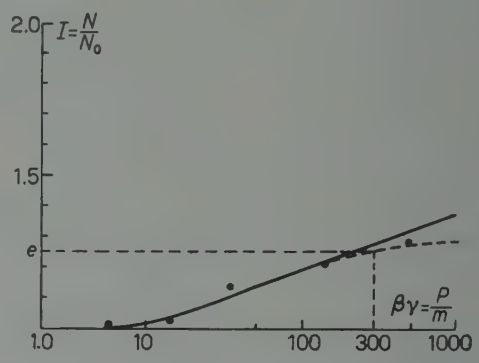

Fig. 4.

The relativistic increase is in fact less than that in the previous experiment but the difference is perhaps not significant.

6. – Interpretation of results.

We summarize our experimental results in the following way:

1) The relativistic increase in Xenon is important. This effect is certainly due to the high atomic number of Xenon.

2) Hydrogen mixed with Xenon does not significantly change the relativistic increase of Xenon. This result is not surprising, for hydrogen does not contribute appreciably to the ionization.

3) On the contrary, if Helium is mixed with Xenon, under the same conditions, the ionization increases drops considerably. This result shows that, in the velocity range investigated, ionization has no additive character as far as the constituents of the mixture are concerned.

4) The disturbing effect of helium seems to increase in the same way as the partial pressure of helium.

3276

Theoretical interpretation. – There are no theoretical calculations available for exactly fitting the phenomena under discussion. However, experiments have been done at low energies showing that ionization is proportional to the total energy loss by collisions (3). If we suppose that this proportionality is still true at relativistic energies, we can use the Bloch formula (4):

$$\left(\frac{\mathrm{d}E}{\mathrm{d}x}\right)_{<\eta} = \frac{2\pi ne^4}{mc^2\beta^2}\left[\log\frac{2mc^2\beta^2\eta}{(1-\beta^2)I_0^2} - \beta^2\right],$$

giving the total energy loss for elementary transfers less than η. In our experiment η corresponds to the energy to be given to the surrounding medium to form a blob of 40 droplets. Results of JESSE and SADAUSKIS (3) enable us to determine the energy loss necessary to form an ion pair $\eta = 700$ eV.

The slope of the relativistic increase depends on η/I_0^2 only.

The determination of I_0 can be done with the STERNHEIMER (5) data following CALDWELL's (6) calculations and the esperiments of SACKS and RICHARDSON (7).

$I_0 =$	19 eV	for H_2
$=$	44 »	He
$=$	78 »	C
$=$	90 »	O_2
$=$	755 »	Xe

We can hence calculate I_0 for each mixture.

However, in order to interpret our experiment, it seems that we should choose a different value of I_0 for Xenon. Let us consider the binding energies of the different electron shells: 34 500 eV, 5 050 eV, 830 eV, 170 eV, 64 eV and 12 eV. We can see that electrons with binding energy of 34 500 eV, 5 050 eV and 830 eV contribute very little to the studied phenomena. When a strongly bound electron is being removed a great number of ions is probably produced by secondary ionization and thus the blob will not be counted since we chose a cut-off value $\eta = 700$ eV.

---

(3) W. P. JESSE and J. SADAUSKIS: *Phys. Rev.*, **88**, 417 (1952); **94**, 764 (1954); **100**, 1755 (1955); **97**, 1668 (1954); J. WEISS and W. BERNSTEIN: *Phys. Rev.*, **103**, 1253 (1956); C. J. BAKKER and E. SEGRÈ: *Phys. Rev.*, **81**, 489 (1951).

(4) B. ROSSI: « *High Energy Particles* ».

(5) R. M. STERNHEIMER: *Phys. Rev.*, **103**, 511 (1956).

(6) D. O. CALDWELL: *Phys. Rev.*, **100**, 201 (1955).

(7) D. C. SACHS and R. J. RICHARDSON: *Phys. Rev.*, **83**, 834 (1951); **89**, 1163 (1953).

3277

Therefore we suppose that K and L electrons play no role and we use the value $I_0 = 400$ eV.

With these values we can calculate ϱ_{cal} for each experiment after bringing some slight corrections to these values for the density effect calculated following Sternheimer's theory ([5]). We take into account the uncertainties on η and I_0 to calculate the errors of ϱ_{cal}:

Experiment	I_0	Density effect	ϱ calculated	ϱ experimental
(1) Xenon	320 eV	— 0.01	1.69 ± 0.03	1.69 ± 0.05
(2) Xe + H_2	260 eV	— 0.03	1.65 ± 0.03	1.72 ± 0.05
(3) Xe + He	270 eV	— 0.025	1.66 ± 0.03	1.33 ± 0.04
(4) Xe + He	220 eV	— 0.04	1.60 ± 0.03	1.25 ± 0.05

We see that our experiment agrees with theory for the first two experiments, whereas the discrepancy is 5 standard deviations for the two other experiments.

We can question two assumptions used in the above theory in order to explain the particular property of helium.

1) The proportionality between ionization and energy loss by collision. This might not be verified at high energies, because of the complexity of secondary ionization in the case of mixtures.

2) The additive property of energy loss when polarization effects occur. Indeed the ionization potential of the six $5p$-electrons of Xenon is only 12 eV. Helium, on the other hand, has an ionization potential of 24.5 eV and therefore has absorption lines in the region of ionization frequencies of Xenon. To this absorption may correspond a strong resonance polarization preventing $5p$ electrons of Xenon to participate in the ionization increase ([8]).

This effect would not be expected to occur for hydrogen for which the ionization potential is 13 eV.

* * *

The authors wish to express their gratitude to Professor L. LEPRINCE-RINGUET for numerous discussions and encouragements. They would also

([8]) A. ROUSSET: *Thèse Paris*, Séries A, n. 3214 (1958).

like to thank all the technicians for their help during the experiment and particularly Monsieur M. REPOSEUR.

RIASSUNTO (*)

Si studia con il metodo del conteggio delle gocce in una camera a nebbia, l'aumento relativistico di ionizzazione di vari miscugli gassosi. Se indichiamo con ϱ la ionizzazione relativa di $\beta/\sqrt{1-\beta^2}$ uguale a 300, si trova che nello xenon puro e nei miscugli di xenon e idrogeno, ϱ è dell'ordine di 1.7. D'altra parte il valore di ϱ discende bruscamente a 1.3 se si mescola elio con lo xenon.

(*) *Traduzione a cura della Redazione.*

IL NUOVO CIMENTO Vol. XIV, N. 2 16 Ottobre 1959

The Proton-Neutron Mass-Difference According to Meson-Theory.

L. O'Raifeartaigh (*), B. Średniawa (**) and Ch. Terreaux (***)

Seminar für Theoretische Physik der Universität - Zürich

(ricevuto il 30 Maggio 1959)

Summary. — The proton-neutron mass difference is calculated assuming that it is due to a mixed mesic-electromagnetic self-energy. The self-energies of the proton and neutron are calculated in the e^2f^2 approximation on grounds of meson theory both for ps and pv coupling. To make these finite the form factor suggested by Arnous and Heitler is applied to all three (nucleon-meson, nucleon-photon, and meson-photon) interactions. It corresponds to a cut-off of the virtual momenta at K (of order M=nucleon mass), when the particle is at rest and is therefore a generalization of the extended source model. To carry through the otherwise extremely complicated calculation a further crude approximation is made, namely an expansion $\sim 1/M$. For both couplings the correct sign is obtained but in the ps case the result is too small by a factor 100. In the pv case the correct order of magnitude is obtained but the numerical value is still too small (by a factor of at least 5 or so) to overcompensate the purely electromagnetic self-energy of the proton. A comparison with the earlier work of Feynman and Speisman shows that the latter is not in agreement with the results of meson theory.

1. – Introduction.

In recent years some attempts have been made to calculate the proton-neutron mass-difference using semi-phenomenological methods ([1,2]). As these

(*) On leave of absence from Dublin Institute of Advanced Studies and University College, Dublin.

(**) On leave of absence from the Physical Institute of the Jagiellonian University, Cracow.

(***) Present address: Department of Theoretical Physics, the University, Liverpool.

([1]) P. Feynmann and G. Speismann: *Phys. Rev.*, **94**, 500 (1954).

([2]) M. Cini, E. Ferrari and R. Gatto: *Phys. Rev. Lett.*, **2**, 7 (1959); A. Petermann: *Helv. Phys. Acta*, **27**, 441 (1954); K. Huang: *Phys. Rev.*, **101**, 1173 (1956).

3280

attempts are, by their nature, open to some doubt, we have attempted in this paper to calculate the mass-difference consistently from ordinary electromagnetic and meson theory.

This means, of course, that we regard the mass-difference as a mixed electromagnetic-mesic self-energy effect, a viewpoint in sharp disagreement with the earlier « renormalization philosophy » ([3]) which declares that such self-energy effects are unobservable in principle. However, this latter philosophy can hardly be maintained, particularly in view of the fact that the $\pi^{\pm}$-π^0 mass-difference, which is almost certainly an electromagnetic self-energy, *is* observed. In agreement with our viewpoint, it has been shown ([4]), that in a convergent theory, the use of renormalization is purely a matter of convenience; care must only be taken to use the theory chosen (renormalized or otherwise) consistently.

We note that the mass-difference will be explainable at any rate only as mixed electromagnetic-mesic effect—as is well known, the pure electromagnetic field of the proton leads to a mass-difference of the wrong sign, while a pure mesic effect, an account of charge independence, leads to no mass-difference at all. We calculate, therefore, the lowest order in the mixed electromagnetic-mesic nucleon self-energy (ps and pv), namely the e^2g^2 and e^2f^2 terms in the perturbation-theory expansion. Even in this low order we are forced to make a further simplification in order to avoid immensely lengthy and unmanageable calculations. This is a non-relativistic (N.R.) approximation. It is, of course, of doubtful validity, as virtual-energies as high or nearly as high as the rest-mass of the nucleon take part in the process considered. Our results, therefore, can only be regarded as a crude approximation to the correct theoretical mass-difference.

A cut-off must be introduced into the theory as otherwise the integrals corresponding to an ordinary Feynman calculation are divergent. We introduce therefore a form-factor of the type advocated by ARNOUS and HEITLER ([5]), and we construct it as follows: In any Interaction-Hamiltonian corresponding to a particle (meson *or* nucleon) emitting or absorbing a single Boson we introduce a factor (in momentum space)

$$\varrho(\mathbf{p}, \mathbf{q}) = \frac{m^2K^2}{m^2K^2 + (\mathbf{p}\cdot\mathbf{q})^2 - \mathbf{p}^2\mathbf{q}^2}, \tag{1.1}$$

where $\mathbf{p}$ and $\mathbf{q}$ are the four-momenta of the emitting (absorbing) particle before and after emission (absorption), m is its mass, and K an assumed universal

([3]) S. S. SCHWEBER, H. A. BETHE and F. DE HOFFMANN: *Mesons and Fields*, vol. **1** (London, 1955), p. 273.

([4]) A. THELLUNG: *Helv. Phys. Acta*, **25**, 307 (1952).

([5]) E. ARNOUS and W. HEITLER: *Nuovo Cimento*, **11**, 443 (1959).

3281

cut-off parameter ([5]). Other experimental evidence points to a value of K in the region of the nucleon mass M_{exp}. We take $K = \frac{2}{3} M_{\text{exp}}$ and $K = M_{\text{exp}}$.

This cut-off is a generalization into the relativistic region of the « extended source » model used successfully by CHEW ([6]). For $\vec{p} = 0$, $p_0 = m$ (1.1) cuts off the virtual momentum $\vec{k}\,(= \vec{p} - \vec{q})$ at $|\vec{k}| \simeq K$. (1.1) is C, P, T invariant (separately). In our case, the form-factor of (1.1) corresponds exactly to the extended source model for all interactions in which the *nucleons* take part, because we work in the rest system of the nucleons and the nucleon is at rest or nearly at rest in *all* parts of each Feynman diagram. For the meson-photon interactions, on the other hand, the energies are large compared with the rest mass of the meson. For these interactions the influence of ϱ on the S-matrix has been derived. The latter is found to be quite convergent, but is in general not relativistically invariant, in spite of the fact that ϱ is an invariant. However, the meson-photon interaction appears in only two of the Feynman graphs, and these are already made convergent by the cut-off applied to the nucleon-meson and photon interaction (extended source). The form factor applied to the relativistic meson-photon interaction merely modifies the numerical results—as will be seen—not to a very large extent. While, admittedly our treatment of the meson-photon interaction can only be regarded as an indication, the results are not too much affected by this uncertainty, in particular in view of the crude approximations made elsewhere.

In turns out that the ps and pv theories lead to a correct sign for the mass-difference. In the ps case the order of magnitude is too small by a factor of about 100. In the pv case the order of magnitude is correct, but the result is still too small, by a factor of about 5 at least, to overcompensate the purely electromagnetic self energy of the proton. In view of the approximations involved we regard this result as not too unsatisfactory for the pv case. The result is, of course, strongly cut-off dependent. The result lends some further support in favour of pv rather than ps coupling.

2. – Notation.

The wave-function of the nucleon is represented by ψ, $(\overline{\psi} = \psi^{\dagger}\gamma^0)$. ψ includes the two isotopic-spin states ψ_{p} (proton) and ψ_{n} (neutron). The charge operator τ, acting on these two states has the following properties:

$$
\left\{
\begin{array}{ll}
\tau\psi_{\text{n}} = \psi_{\text{p}} & \tau^{\dagger}\psi_{\text{n}} = 0 \\
\tau\psi_{\text{p}} = 0 & \tau^{\dagger}\psi_{\text{p}} = \psi_{\text{n}} \\
 & \\
\tau_{\text{p}}\psi_{\text{p}} = \psi_{\text{p}} & \tau_3\psi_{\text{p}} = \psi_{\text{p}} \\
\tau_{\text{p}}\psi_{\text{n}} = 0 & \tau_3\psi_{\text{n}} = -\psi_{\text{n}} .
\end{array}
\right. \tag{2.1}
$$

([6]) G. F. CHEW: *Phys. Rev.*, **94**, 1748, 1755 (1954) and subsequent papers.

3232

The pseudo-scalar wave function of the π-meson is represented by φ, (φ_3 represents the neutral π^0 and the complex φ, φ^* represent the charged $\pi^{\pm}$). We take $e^2 = 4\pi/137$.

g = coupling constant in the pseudo-scalar (ps) meson-theory.
f = coupling constant in the pseudo-vector (pv) meson-theory.

A four vector is written as $\mathbf{x} = (x_0, \vec{x})$. The metric used is $g_{\mu\nu}$, where

$$g_{00} = -g_{ii} = 1\,, \qquad i = 1, 2, 3 \qquad g_{\mu\nu} = 0 \quad \text{for } \mu \neq \nu.$$

This means that a vector product $\mathbf{A}\cdot\mathbf{B}$ is

$$\mathbf{A}\cdot\mathbf{B} = A_0 B_0 - \vec{A}\cdot\vec{B}\,.$$

In the interaction representation the Hamiltonian-density operator describing the interaction between the nucleon, meson, and electromagnetic fields is (for the local theory)

$$\begin{aligned}(2.2)\qquad \mathbf{H}_{\text{int}}(\mathbf{x}) = {} & e\bar{\psi}(\boldsymbol{\gamma}\cdot\mathbf{A})\tau_p\psi + ie[\varphi^*\partial_\mu\varphi - (\partial_\mu\varphi^*)\varphi]A_\mu - e^2\varphi^*\varphi\mathbf{A}\cdot\mathbf{A} + \\ & + g\bar{\psi}\gamma^5\tau_3\varphi_3\psi + g\sqrt{2}\,\bar{\psi}\gamma^5(\tau\varphi + \tau^\dagger\varphi^*)\psi + \\ & + \frac{if}{\mu}\bar{\psi}\gamma^5\gamma^\mu\tau_3(\partial_\mu\varphi_3)\psi + \frac{if}{\mu}\sqrt{2}\,\bar{\psi}\gamma^5\gamma^\mu(\tau\partial_\mu\varphi + \tau^\dagger\partial_\mu\varphi^*)\psi - \\ & - \frac{ef}{\mu}\sqrt{2}\,\bar{\psi}\gamma^5\,(\boldsymbol{\gamma}\cdot\mathbf{A})\,(\tau\varphi - \tau^\dagger\varphi^*)\psi\,.\end{aligned}$$

where ψ, φ, A_μ are understood to mean $\psi(\mathbf{x})$, $\varphi(\mathbf{x})$, $A_\mu(\mathbf{x})$ respectively. In $\mathbf{H}_{\text{int}}$ the « normal-dependent » terms have already been dismissed, since according to MATHEWS (7) and RÖHRLICH (8) these play no rôle in the calculation of the S-matrix, provided that at the same time $[\dot{\varphi}_\mu\dot{\varphi}_\nu]$ is replaced by $\partial_\mu\partial_\nu[\dot{\varphi}\,\dot{\varphi}]$. Naturally this procedure, which is consistent for a local theory may be open to some doubt when a form-factor is present. The best justification for its use (in the absence of a consistent form-factor theory) is that with this procedure we obtain as close a correspondence as possible with the local case.

It is assumed that the reader is acquainted with the techniques of perturbation theory, Feynman diagrams, etc., and we use the language usually associated with them.

---

(7) P. T. MATTHEWS: *Phys. Rev.*, **76**, 684, 1419 (1949).
(8) F. ROHRLICH: *Phys. Rev.*, **80**, 666 (1950).

3283

Generally g^2 refers to ps and f^2 to pv meson-theory, but sometimes when we are concerned with meson theory as such without distinguishing between the two couplings, we use f^2 to denote both g^2 and f^2.

m_e = mass of electron.

μ = mass of π-meson, $\mu \simeq 270\ m_e$.

M_{exp} = experimental mass of the nucleon, $M_{exp} \simeq 1836\ m_e$.

δM_{exp} = $M_{exp\,p} - M_{exp\,n}$, $\delta M_{exp} \simeq -2.5\ m_e$.

M_0 = theoretical mass of the nucleon, *i.e.* the mass in the absence of electromagnetic or mesic interactions, $M_{0n} = M_{0p}$.

M = theoretical mass of the nucleon, calculated in the presence of both interactions.

$\delta M_{e_p^2}$ = electromagnetic self-energy of the proton, calculated in the order e^2.

$\delta M_{e^2 f^2_{p,n}}$ = self energy of the proton, neutron, calculated in the order $e^2 f^2$.

$\mathcal{M}$ denotes an element of the S-matrix, S. The $\mathcal{M}$ corresponding to a Feynman diagram is given the same label as that diagram. The relation between $\mathcal{M}$ and the corresponding δM is ([9])

$$\delta M = \frac{i}{(2\pi)^4}\mathcal{M}\,. \tag{2.3}$$

With this convention we do *not* attach a factor $(2\pi)^{-\frac{3}{2}}$ to the external lines of the Feynman graphs.

3. – Electromagnetic self-energy of the proton.

The purpose of the present paper is to calculate $\delta M_{e^2 f^2_{p-n}}$. As, however, the electromagnetic field alone has an appreciable contribution to the mass-difference $M_p - M_n$, we first consider $\delta M_{e^2_{p-n}} = \delta M_{e^2_p}$. (Note that due to charge independence $\delta M_{f^2_{p-n}} = 0$.)

In order to be consistent, we must cut-off $\delta M_{e^2_p}$ (which diverges logarithmically) in the same way as $\delta M_{e^2 f^2_{p-n}}$ namely, by the use of a form-factor as explained in Section 1. Now $\delta M_{e^2_p}$ is given by the well known expression derived by using the Pauli-Rose variable z (an invariant) ([10]) defined by

$$(E + |\vec{q}\,|)^2 - \vec{p}^{\,2} = M_p^2 z^2\,, \tag{3.1}$$

([9]) S. S. SCHWEBER, H. A. BETHE and F. DE HOFFMANN: l. c., p. 257.

([10]) W. HEITLER: *The Quantum Theory of Radiation* (Oxford, 1954), p. 297.

3284

($\vec{q}$ = momentum of virtual photon, E = energy of nucleon in dissociated state). $\delta M_{e_p^2}$ is an integral over z alone. It can be shown that cutting off with a form-factor as in Section **1** is much the same as cutting off z, at z_0 say, where z_0 is so chosen that it corresponds to $|\vec{q}| < K$ in the rest-system ($\vec{p} = 0$) of the proton. On calculation it turns out that

$$\delta M_{e_p^2} = \frac{e^2 M_p}{8\pi^2}\left(3 \log z_0 + \frac{1}{2z_0^2} - \frac{1}{2}\right) \tag{3.2}$$

so that, numerically

$$\delta M_{e_p^2 - n} = \begin{cases} 3.25\ m_e & \text{for } K = \frac{2}{3} M_{exp}, \\ 4.75\ m_e & \text{for } K = 1\, M_{exp}. \end{cases} \tag{3.3}$$

As is well known the sign of $\delta M_{e_p^2}$ is the opposite to that required experimentally. We remark, that if we calculate $\delta M_{e_p^2}$ using the same cut-offs, but with a N.R. approximation we obtain almost the same results. (We get those of (3.3) reduced by about 15 %). This is an indication that the N.R. approximation may not be too inaccurate.

4. – Mass renormalization.

It has already been mentioned in Section **1** that it is immaterial whether one uses a renormalized theory or not, provided only that the theory chosen is convergent and is used consistently.

In our case we *choose* to renormalize the theory with respect to its purely mesonic self-energy (which is symmetrical with respect to proton and neutron). This choice is made for two reasons: 1) It simplifies the calculation. 2) Although all self-energy effects are probably small in comparison with M_{exp}, the assumption that they *are* small seems to be much more justified in the electromagnetic and mixed electromagnetic-mesic effects (on account of the smallness of e) than in the case of pure mesic effects. We, therefore, take

$$M_{exp} \simeq M_0 + \delta M_{mes.c}\,, \tag{4.1}$$

and insert in the later formulae for $M_0 + \delta M_{n.es.c}$ the experimental nucleon mass. We do not renormalize with respect to the electromagnetic self-energy, as this contributes to the mass-difference in question.

In the $e^2 f^2$ approximation there is no point in renormalizing f^2, but the question then arises whether we should use the renormalized or unrenormalized value for numerical purposes. The former is probably of the order 0.1 but

the latter is larger and may be considerably larger. We shall, therefore, use values $0.1 \sim 0.2$ but f^2 may be still larger than the latter figure.

The renormalization with respect to δM_{mesic} is carried out as follows. Working with M_0 (*i.e.* in the completely unrenormalized theory) we would find for the mass M of a nucleon

$$M = M_0 + \delta M_{f^2}(M_0) + \delta M_{e^2}(M_0) + \delta M_{e^2 f^2}(M_0) + \dots , \tag{4.2}$$

where, for example,

$$\delta M_{e^2 f^2}(M_0) = \langle M_0 | \mathfrak{S}(H_{\text{int}}) | M_0 \rangle_{e^2 f^2} , \tag{4.3}$$

$\langle M_0|$ and $|M_0\rangle$ being free-particle states of the nucleon with the theoretical mass M_0. We now define the operator H^s_{mesic} by

$$H^s_{\text{mesic}} = \bar{\psi}\, \delta M_{\text{mesic}} \psi , \tag{4.4}$$

and then to renormalize we make the following changes ([11]),

$$H_{\text{int}} \to H_{\text{int}} - H^s_{\text{mesic}} , \tag{4,5}$$

$$M_0 \to M_0 + \delta M_{\text{mesic}}(M_0) . \tag{4,6}$$

As mentioned above, $M_0 + \delta M_{\text{mesic}}$ is to be put equal to M_{exp}.

Let us now neglect terms of order higher than e^2, f^2, $e^2 f^2$. Corresponding to (4.2) we now have

$$M = [M_0 + \delta M_{f^2}(M_0)] + \delta \widetilde{M}_{e^2}(M_0 + \delta M_{f^2}(M_0)) + \\ + \delta \widetilde{M}_{e^2 f^2}(M_0 + \delta M_{f^2}(M_0)) + \dots \tag{4.7}$$

where

$$\delta \widetilde{M}_{e^2}\,(M_0 + \delta M_{f^2}(M_0)) = \langle M_0 + \delta M_{f^2}(M_0)) \,|\, \mathfrak{S}(H_{\text{int}} - H^s_{f^2}) \,|\, M_0 + \delta M_{f^2}(M_0) \rangle_{e^2} , \tag{4.8}$$

$$\delta \widetilde{M}_{e^2 f^2}(M_0 + \delta M_{f^2}(M_0)) = \langle M_0 + \delta M_{f^2}(M_0)) \,|\, \mathfrak{S}(H_{\text{int}} - H^s_{f^2}) \,|\, M_0 + \delta M_{f^2}(M_0) \rangle_{e^2 f^2} . \tag{4.9}$$

$\langle M_0 + \delta M_{f^2}(M_0)|$ and $|M_0 + \delta M_{f^2}(M_0)\rangle$ meaning a free-particle state of the nucleon with the renormalized mass $M_0 + \delta M_{f^2}(M_0)$. Note that

$$\delta \widetilde{M}_{e^2}(M_0 + \delta M_{f^2}(M_0)) = \delta M_{e^2}(M_0 + \delta M_{f^2}(M_0)) , \tag{4.10}$$

since $H^s_{f^2}$ plays no part in a purely electromagnetic effect.

([11]) W. HEITLER: l. c., § 15.

3286

The equivalence of (4.7) and (4.2) will be shown in the appendix in order to emphasize the earlier remark that the renormalization is no more than a change of representation and leaves the relations between physical effects unchanged.

From now on, we shall be working with $H_{\text{int}} - H^s_{\text{mesic}}$ instead of H_{int}, and $M_0 + \delta M_{\text{mesic}}(M_0) \simeq M_{\text{exp}}$ instead of M_0.

5. – Feynman graphs.

We proceed now to the calculation of $\delta M_{e^2 f^2_{p-n}}$. The Feynman graphs contributing to $\delta M_{e^2 f^2_p}$ and $\delta M_{e^2 f^2_n}$ for $H_{\text{int}} - H^s_{f^2}$, are shown in Tables *A*, *B*, *C* and *D*. We consider first the graphs which on calculation give a non-zero contribution to the mass-difference. These are shown in Table *A* for the proton and Table *B* for the neutron.

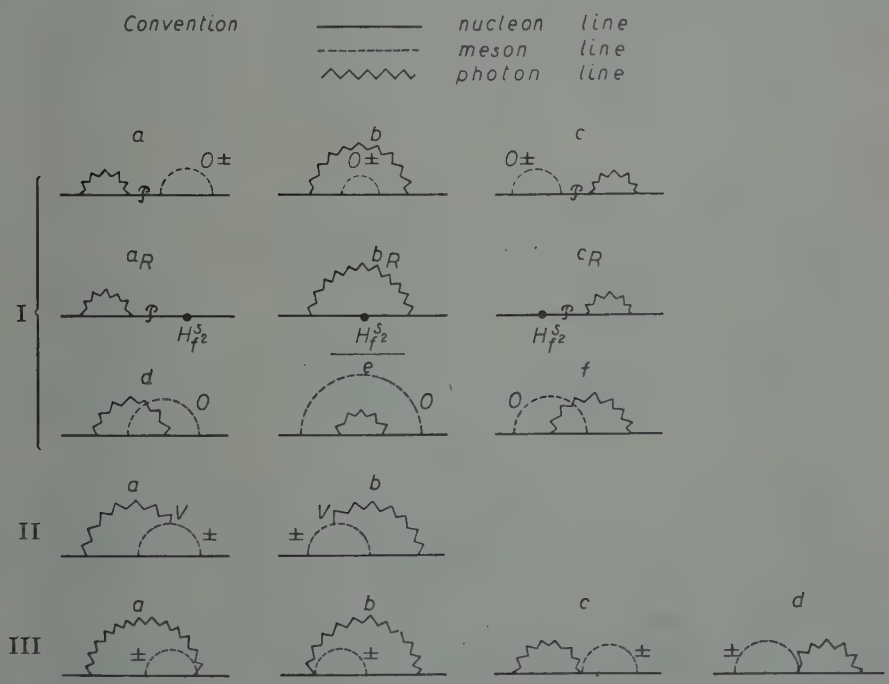

Table *A*.

The graphs labelled I_R are due to the renormalization. The dots in them correspond to the term $-H^s_{f^2}$ of (4.5). Note that $\mathcal{M}_{Ic_n} = 2\mathcal{M}_{Ie_p}$ and $\mathcal{M}_{IIa_p} = \mathcal{M}_{IIb_p}$. Some ambiguity arises in the case of the nucleon propagators labelled $\mathcal{P}$

because the values to be inserted in them are free-particle values. These ambiguities are handled by the method of HEITLER [12].

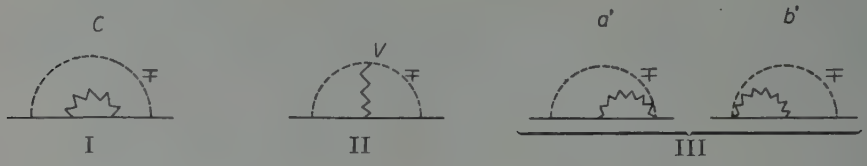

Table *B*.

In Table *C* are given the graphs for which

$$\mathcal{M}_{e^2 f_p^2} = \mathcal{M}_{e^2 f_n^2} .$$

These obviously give no contribution to the mass-difference.

Table *C*.

A further category of graphs is given in Table *D*.

Table *D*.

These occur only in the case of the proton. They are not trivially zero, but it can be shown that they do not contribute (for $\mathcal{M}_a$ and $\mathcal{M}_b$ because the spurs corresponding to the closed loops are zero, for $\mathcal{M}_c$ and $\mathcal{M}_d$, because of symmetry properties of the integrands).

It might not be out of place to discuss the consequence of adding a « contact » term to the interaction $\mathbf{H}_{\text{int}}$. Such a contact term will be given by

$$(\mathbf{H}_{\text{int}})_{\text{contact}} = k\left(\frac{g}{\mu}\psi^{+}\gamma^{5}\tau_{.}\psi\right)^{2} + k'\left(\frac{1}{\mu}\psi^{+}\gamma^{5}\gamma_{\mu}\tau_{.}\psi\right)^{2} \tag{5.1}$$

---

[12] W. HEITLER: l. c., pp. 308-309.

3288

where k and k' are constant. However, as we have renormalized our theory in δM_{f^2}, we must renormalize $(\mathbf{H}_{\text{int}})_{\text{contact}}$ in the same way. When this is done, all the graphs resulting from the addition of $(\mathbf{H}_{\text{int}})_{\text{contact}}$ are as shown in Table E.

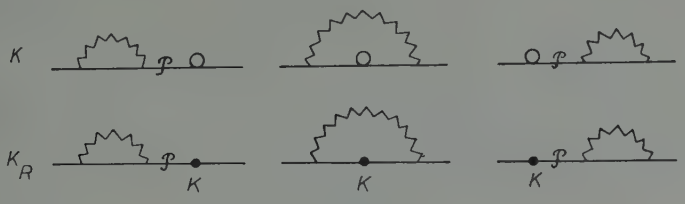

Table E.

The small circle corresponds to $(\mathbf{H}_{\text{int}})_{\text{contact}}$ itself, and the dot to the corresponding renormalization term. On evaluating the corresponding matrix elements (*e.g.* by the method of HEITLER [12]) mentioned above) it turns out that the renormalized terms exactly cancel the unrenormalized. Thus the total contribution of the contact terms is zero.

6. – Method of calculation.

The integrals corresponding to the Feynmann graphs of Sect. **5** are divergent. In order to make them convergent we introduce a form-factor as mentioned in Sect. **1**. Such a form factor appears at each corner of the graphs. In general, the presence of the form-factors will make the calculation of matrix elements extremely complicated. In the non-relativistic approximation, however, the situation is not so bad because, *in this approximation* the *nucleon* can be considered as almost at rest in any part of the graph. (Owing to the cut-off, the virtual momenta emitted by the nucleon have values $\leqslant M_{\text{exp}}$).

In this case, the form-factor at any corner involving a *nucleon line* is nothing more than an ordinary symmetrical cut-off K on the 3-momenta of the virtual Bosons (extended source model).

Now in Tables A and B almost all the corners involve nucleon lines. The only exceptions are the corners marked V in Π_a, Π_b and Π_c (one in each graph) where the interactions involve mesons and photons only and are thus relativistic. For these reasons our simple cut-off procedure, consistent with Sect. **1**, will be: All the integrals of tables A and B are to be cut off symmetrically in the 3-momenta of the Bosons (with the sharp cut-off K). In addition, for the graphs $\Pi_{a,b,c}$ the integrand is to be multiplied with the form-factors ϱ corresponding to the vertices V.

We turn now to the actual calculation. As it is not practical to show explicitly the calculation corresponding to all the graphs of Tables A and B, we choose a typical graph, II_{a_p} in the pv-case (see accompanying diagram)

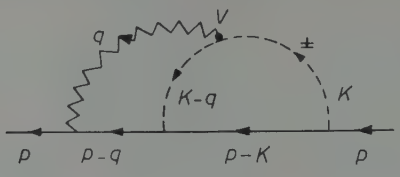

II_{a_p}.

and indicate how its matrix element has been calculated. The matrix element of $\mathrm{II}_{a_p}^{(pv)}$ is

$$\mathscr{M}_{\mathrm{II}a_p}^{(pv)} = \frac{2i}{(2\pi)^4}\left(\frac{ef}{\mu}\right)^2 \int\int^{K} \mathrm{d}^4(kq)(2\mathbf{k}-\mathbf{q},\gamma)\,\frac{1}{(\mathbf{p}-\mathbf{q},\gamma)-M_{\exp}}\cdot \tag{6.1}$$

$$\cdot\gamma^5(\mathbf{k}-\mathbf{q},\gamma)\,\frac{1}{(\mathbf{p}-\mathbf{k},\gamma)-M_{\exp}}\,\gamma^5(\mathbf{k}\cdot\gamma)\,\frac{1}{\mathbf{q}^2}\,\frac{1}{\mathbf{k}^2-\mu^2}\,\frac{1}{(\mathbf{k}-\mathbf{q})^2-\mu^2}\,\varrho_v\,,$$

where $\mathbf{p}=(p_0,\vec{p})$ is the 4-momentum of the free nucleon.

K indicates the sharp cut-off on $|\vec{q}\,|$, $|\vec{k}\,|$ and ϱ_V is the relativistic form-factor of the vertex V mentioned above. In this section ϱ_V in these vertices will be neglected. Its effect will be taken into account in the next section. An alternative form for (6.1) is

$$\mathscr{M}_{\mathrm{II}a_p}^{(pv)} = \frac{2i}{(2\pi)^4}\left(\frac{ef}{\mu}\right)^2 \int\int^{K} \mathrm{d}^4(qk)(2\mathbf{k}-\mathbf{q},\gamma)\,\frac{(\mathbf{p}-\mathbf{q},\gamma)+M_{\exp}}{(q_0-p_0)^2-\Omega_q^2}\,\gamma^5\,(\mathbf{k}-\mathbf{q},\gamma)\cdot \tag{6.2}$$

$$\cdot\frac{(\mathbf{p}-\mathbf{k},\gamma)+M_{\exp}}{(k_0-p_0)^2-\Omega_k^2}\,\gamma^5\,(\mathbf{k}\cdot\gamma)\,\frac{1}{q_0^2-q^2}\,\frac{1}{k_0^2-\omega^2}\,\frac{1}{(k_0-q_0)^2-\overline{\omega}^2}\,,$$

where

$$\Omega_q^2=(\vec{p}-\vec{q}\,)^2+M_{\exp}^2\,,\qquad \Omega_k^2=(\vec{p}-\vec{k}\,)^2+M_{\exp}^2\,,\qquad q^2=\vec{q}^{\,2},\qquad \omega^2=\vec{k}^{\,2}+\mu^2\,,$$

$$\overline{\omega}^2=(\vec{k}-\vec{q}\,)^2+\mu^2\,.$$

$\mathscr{M}_{\mathrm{II}a_p}^{(pv)}$, like all the elements of Tables A and B, has two integration variables. We first carry out the integrations over k_0 and q_0 by the method of residues. In doing this some care must be taken. In the five propagators of (6.1) it is, as usual, assumed that each of the five masses m_i has a small negative imaginary part $-i\sigma_i$, which is to be put equal to zero after integration. Now it turns out that, to avoid ambiguity, no σ_i should be put equal to zero until *both* the k_0 and q_0 integrations have been performed. Moreover, it is necessary to adopt a convention of sign for some of the differences $\sigma_i-\sigma_j$. The result

0662

is (as it must be) independent of the convention chosen. In practice, however, a suitable convention shortens the calculations.

In the case of $\mathcal{M}_{\mathrm{IIa_p}}^{(\mathrm{pv})}$ there are eight propagator poles (listed below) which contribute. The further integration of $\mathcal{M}_{\mathrm{IIa_p}}^{\mathrm{pv}}$ (over $\mathrm{d}^3k\,\mathrm{d}^3q$) is very difficult. Moreover, the terms from the eight residues mentioned contain, separately, singularities. These singularities disappear on combining the terms but the combination is very awkward. At this stage, therefore, we are forced to make the non-relativistic approximation. It consists in expanding the integrand of (6.2) after k_0, q_0-integration, in terms of $1/M_{\mathrm{exp}}$ and taking only the first term in the expansion. (For simplicity we also put $\vec{p}=0$, which is always allowed). For example, in (6.2), after k_0, q_0-integration we have

$$\Omega_q = M_{\mathrm{exp}} + \frac{\vec{q}^2}{2M_{\mathrm{exp}}},$$

$$\Omega_k = M_{\mathrm{exp}} + \frac{\vec{k}^2}{2M_{\mathrm{exp}}},$$

while ω, q, $\bar{\omega}$ remain unchanged. Note that for $\vec{p}=0$ we have the additional simplification that the denominator is invariant under the simultaneous transformations $k_i \to -k_i$, $q_i \to -q_i$ ($i=1$ or 2 or 3). Using these simplifications (6.2) reduces to

$$\mathcal{M}_{\mathrm{IIa_p}}^{(\mathrm{pv})} = \frac{2i}{(2\pi)^4}(2\pi i)^2\left(\frac{ef}{\mu}\right)^2\int\int_K \mathrm{d}^3k\,\mathrm{d}^3q\,[\vec{k}^2 - \vec{k}\cdot\vec{q}]\,\Phi, \tag{6.3}$$

where

$$\Phi = \frac{-1}{\omega q^2(\omega^2-\bar{\omega}^2)} \quad \text{from the pole} \quad \begin{matrix} q_0 = p_0 - \Omega_q \\ k_0 = -\omega \end{matrix}$$

$$+\frac{-1}{\bar{\omega}q^2(\bar{\omega}^2-\omega^2)} \quad \text{»} \quad \begin{matrix} q_0 = p_0 - \Omega_q \\ k_0 = p_0 - \Omega_q - \bar{\omega} \end{matrix}$$

$$+\frac{1}{2q\omega^2(q^2-\bar{\omega}^2)} \quad \text{»} \quad \begin{matrix} q_0 = -q \\ k_0 = p_0 - \Omega_k \end{matrix}$$

$$+\frac{2\omega - q}{4\omega^2 q^2[(q-\omega)^2-\bar{\omega}^2]} \quad \text{»} \quad \begin{matrix} q_0 = -q \\ k_0 = -\omega \end{matrix}$$

$$+\frac{2\bar{\omega}+q}{4\bar{\omega}q^2(q+\bar{\omega})[(q+\bar{\omega})^2-\omega^2]} \quad \text{»} \quad \begin{matrix} q_0 = -q \\ k_0 = -q-\bar{\omega} \end{matrix}$$

$$+\frac{1}{2\bar{\omega}\omega^2(\bar{\omega}^2-q^2)} \quad \text{»} \quad \begin{matrix} q_0 = p_0 - \Omega_k - \bar{\omega} \\ k_0 = p_0 - \Omega_k \end{matrix}$$

$$+\frac{\bar{\omega}-\omega}{4\omega^2\bar{\omega}(\omega+\bar{\omega})[q^2-(\omega+\bar{\omega})^2]} \quad \text{»} \quad \begin{matrix} q_0 = -\omega-\bar{\omega} \\ k_0 = -\omega \end{matrix}$$

$$+O\left(\frac{1}{M_{\mathrm{exp}}}\right) \quad \text{»} \quad \begin{matrix} q_0 = p_0 - \Omega_q \\ q_0 = p_0 - \Omega_k \end{matrix}$$

The singularities in the separate terms are here quite evident. However, they disappear when the terms are suitably grouped and added, the result being

$$\Phi = \frac{2\omega\bar{\omega} + q(\omega - \bar{\omega})}{4\omega^2 q^2 \bar{\omega}(\omega + \bar{\omega})(q + \bar{\omega})} \,. \tag{6.4}$$

It should, perhaps, be mentioned that $\mathscr{M}^{\mathrm{pv}}_{\mathrm{II}a_{\mathrm{p}}}$ contains no infra-red catastrophe.

Note that the N.R. approximation can be made only *after* the k_0, q_0-integration. In practice, however, it simplifies the calculation to make the approximation in the *numerator* before the k_0, q_0-integration, using in anticipation the fact that only poles for which k_0 and q_0 are of order 1 or $1/M_{\mathrm{exp}}$ will play a rôle. It might also be mentioned that in some graphs (in pv-coupling) it appears at first sight that the k_0-integration will diverge. It can be shown that this is not the case, but as this difficulty does not affect any of the terms playing a part in the N.R. approximation we shall not discuss it in this paper.

The final result is, therefore

$$\mathscr{M}^{(\mathrm{pv})}_{\mathrm{II}a_{\mathrm{p}}} = \frac{2i}{(2\pi)^4}\,(2\pi i)^2 \left(\frac{ef}{\mu}\right)^2 \iint^{K} \mathrm{d}^3k\,\mathrm{d}^3q\,(\vec{k}^2 - \vec{k}\cdot\vec{q})\,\frac{2\omega\bar{\omega} + q(\omega - \bar{\omega})}{4\omega^2 q^2 \bar{\omega}(\omega + \bar{\omega})(q + \bar{\omega})} \,. \tag{6.5}$$

This integral, like all the corresponding integrals of Tables *A* and *B*, can be integrated out over d^3k and d^3q, if we take the reasonable approximation $\mu = 0$. The calculation is extremely lengthy, however, and we shall not present it here.

7. – Effect of the cut-off in the relativistic vertex.

We now take into account the effect of the form-factor ϱ at the vertices V of graphs II_a, II_b and II_c, which was neglected in the last section. The form factor at V is, according to Sect. **1**

$$\varrho_V = \frac{\mu^2 K^2}{\mu^2 K^2 + (k_0 k_0' - \vec{k}\cdot\vec{k}')^2 - (k_0^2 - \vec{k}^2)(k_0'^2 - \vec{k}'^2)} \,, \tag{7.1}$$

where $\mathbf{k}'$ is the 4-momentum of the meson-line labelled $\mathbf{k} - \mathbf{q}$, *before* the application of the δ^4-function at V, μ is the meson-mass, and K the universal cut-off. At the other vertices we have similar nucleon-nucleon form-factors.

A treatment of the *S*-matrix theory in the presence of these form-factors would be too lengthy for the present paper, so we shall merely state that a

3292

derivation (*) of the S-matrix, according to the non-local theory (5) embodying these form factors, leads to the following result. In the N.R. approximation considered

$$(7.2)\qquad \mathcal{M}^{(\mathrm{pv})}_{\mathrm{II}a_p} = \frac{2i}{(2\pi)^4}\left(\frac{ef}{\mu}\right)^2 \iint \mathrm{d}^4(kq)[-\vec{k}^2 + \vec{k}\cdot\vec{q}]\cdot$$

$$\cdot\frac{4M^2_{\mathrm{exp}}(2k_0 - q_0)\,\frac{\varrho(+)+\varrho(-)}{2} + \left[4M^2_{\mathrm{exp}}(k_0 - q_0)\frac{\omega}{\bar{\omega}} + 4M^2_{\mathrm{exp}}k_0\frac{\bar{\omega}}{\omega}\right]\frac{\varrho(-)-\varrho(+)}{2}}{[(\mathbf{p}-\mathbf{q},\,\boldsymbol{\gamma}) - M_{\mathrm{exp}}][(\mathbf{p}-\mathbf{k},\,\boldsymbol{\gamma}) - M_{\mathrm{exp}}]\,\mathbf{q}^2(\mathbf{k}^2-\mu^2)[(\mathbf{k}-\mathbf{q})^2-\mu^2]}\,,$$

where

$$\varrho(+) = \frac{\mu^2K^2}{\mu^2K^2 + [\omega\bar{\omega} + \vec{k}\cdot(\vec{k}-\vec{q})]^2 - \mu^4}\cdot$$

and

$$\varrho(-) = \frac{\mu^2K^2}{\mu^2K^2 + [\omega\bar{\omega} - \vec{k}\cdot(\vec{k}-\vec{q})]^2 - \mu^4}\,.$$

Here, the d^3k, d^3q integration is to be taken, as we had anticipated, over all $|\vec{k}|, |\vec{q}| \leqslant K$, and $\varrho(-)$ and $\varrho(+)$ express the effect of ϱ_V. Note that $\varrho(\pm)$ contain no space-like vectors and have no poles of k_0, q_0. The integral (7.2) is perfectly convergent, but the corresponding matrix element is not invariant.

The integral (7.2) can be integrated immediately over k_0 and q_0. The remaining integral over d^3k, d^3q cannot be calculated rigorously, however, on account of the form of ϱ_V and we are forced to make (as well as the N.R. approx.) the approximation $\omega = \bar{\omega}$ (whose validity is discussed below). In this approximation, we find

$$(7.3)\qquad \mathcal{M}^{(\mathrm{pv})}_{\mathrm{II}a_p(\omega=\bar{\omega})} = (2\pi i)^2\frac{2i}{(2\pi)^4}\left(\frac{ef}{\mu}\right)^2\iint^K \mathrm{d}^3(kq)\,\frac{\vec{k}^2 - \vec{k}\cdot\vec{q}}{2\omega^3q^2}[\varrho(-)]_{\omega=\bar{\omega}}\,.$$

In the *absence* of ϱ_V the same approximation would give us, from (6.5)

$$(7.4)\qquad \mathcal{M}^{(\mathrm{pv})}_{\mathrm{II}a_p(\omega=\bar{\omega})} = (2\pi i)^2\frac{2i}{(2\pi)^4}\left(\frac{ef}{\mu}\right)^2\iint^K \mathrm{d}^3(kq)\,\frac{\vec{k}^2 - \vec{k}\cdot\vec{q}}{2\omega^3q^2}\,.$$

Thus, for $\omega = \bar{\omega}$, the effect of ϱ_V is to multiply the previous result (6.5) by a factor $\bar{\varrho}$ where

$$(7.5)\qquad \bar{\varrho} = \frac{\iint^K \mathrm{d}^3(kq)\,\frac{\vec{k}^2 - \vec{k}\cdot\vec{q}}{2\omega^3q^2}[\varrho(-)]_{\omega=\bar{\omega}}}{\iint \mathrm{d}^3(kq)\,\frac{\vec{k}^2 - \vec{k}\cdot\vec{q}}{2\omega^3q^2}}\,.$$

(*) To be published later.

On calculation

$$\bar{\varrho} \simeq \begin{cases} 0{,}7 & \text{for } K = \frac{2}{3} M_{\text{exp}}, \\ 0{,}6 & \text{for } K = M_{\text{exp}}. \end{cases} \tag{7.6}$$

We take the effect of ϱ_r (7.1) into account, therefore, by multiplying (6.5), which is calculated rigorously ($\omega \neq \bar{\omega}$), by $\bar{\varrho}$.

This replacement seems to be a good enough approximation, especially in view of the uncertainty involved in the application of ϱ to the relativistic case under discussion.

8. – Results.

Carrying out the integrations corresponding to all graphs in tables *A* and *B*, according to the methods described in the two previous sections, we have the following results (for notation, see Sect. **6** and Sect. **7**).

— ps-*Coupling*:

$$\delta M^{(\text{ps})}_{e^2 g^2 (\text{p}-\text{n})} = -\frac{(eg)^2}{(2\pi)^6} \bar{\varrho} \int\int^K \mathrm{d}^3(kq) \frac{\omega - \bar{\omega}}{2 M_{\text{exp}} q \omega \bar{\omega} (\omega + \bar{\omega})(q + \omega + \bar{\omega})}. \tag{8.1}$$

This integral corresponds actually only to graphs II_{a_p} and II_{b_p}. All other graphs are of order $1/M^2_{\text{exp}}$ and are neglected.

— pv-*Coupling*:

$$\delta M^{(\text{pv})}_{e^2 f^2 (\text{p}-\text{n})} = \left(\frac{ef}{\mu}\right)^2 \frac{1}{(2\pi)^6} \int\int^K \mathrm{d}^3(kq) \left\{ -\frac{3}{4} \frac{\vec{k}^2}{\omega^3 q^2} + \frac{\vec{k}^2}{2\omega^2 q^2 (\omega + q)} - \frac{\vec{k}^2}{4\omega^3 q (\omega + q)} - \right.$$
$$\left. - \frac{3}{4} \frac{\vec{k}^2}{\omega^2 q^2 (\omega + q)} + \bar{\varrho} (\vec{k}^2 - \vec{k} \cdot \vec{q}) \left[\frac{2\omega\bar{\omega} + q(\omega - \bar{\omega})}{\omega^2 q^2 \bar{\omega} (\omega + \bar{\omega})(q + \bar{\omega})} + \frac{2\omega\bar{\omega} + q(\omega + \bar{\omega})}{2 q \bar{\omega}^2 \omega^2 (q + \bar{\omega})(q + \bar{\omega})} \right] \right\}. \tag{8.2}$$

The first four terms of (8.2) correspond respectively to graphs $(\text{I}_a + \text{I}_{a_R} + \text{I}_c + \text{I}_{cR})_\text{p}$, $(\text{I}_d + \text{I}_f)_\text{p}$, $\text{I}_{e_{(\text{p}-\text{n})}}$, $(\text{I}_b + \text{I}_{bR})_\text{p}$. The first term of the square bracket corresponds to II_{a_p} and II_{b_p}, and the second corresponds to II_{c_n}. All graphs III are of order $1/M_{\text{exp}}$ and are neglected. Combining the terms of (8.2) we get

$$\delta M^{(\text{pv})}_{e^2 f^2 (\text{p}-\text{n})} = \left(\frac{ef}{\mu}\right)^2 \frac{1}{(2\pi)^6} \int\int^K \mathrm{d}^3(kq) \left\{ -\frac{\vec{k}^2}{\omega^3 q^2} + \bar{\varrho} (\vec{k}^2 - \vec{k} \cdot \vec{q}) \cdot \right.$$
$$\left. \cdot \left[\frac{2\omega\bar{\omega} + q(\omega - \bar{\omega})}{\omega^2 q^2 \bar{\omega} (\omega + \bar{\omega})(q + \bar{\omega})} + \frac{2\omega\bar{\omega} + q(\omega + \bar{\omega})}{2 q \bar{\omega}^2 \omega^2 (q + \bar{\omega})(q + \omega)} \right] \right\}.$$

3294

In the approximation $\mu = 0$, the respective numerical results are

$$\delta M^{(ps)}_{e^2g^2(p-n)} = -\frac{(fe)^2}{8\pi^4}\cdot(0.01)M_{exp}\left(\frac{K}{M_{exp}}\right)^2\bar{\varrho} \tag{8.4}$$

and

$$\delta M^{(pv)}_{e^2f^2(p-n)} = \left(\frac{ef\,M_{exp}}{\mu}\right)^2\frac{1}{8\pi^4}M_{exp}\left(\frac{K}{M_{exp}}\right)^3[-1+0.65\,\bar{\varrho}]\,. \tag{8.5}$$

With the values $g^2 = 15 \sim 30$ and $f^2 = 0{,}1 \sim 0{,}2$ (cf. Sect. **4**) and $\bar{\varrho}$ given by (7.6), viz $0{,}6 \div 0{,}7$, we express (8.4) and (8.5) in electron masses (m_e) and tabulate the result as shown.

Cut off	δM_{e^2}	$\delta M_{e^2q^2}$	$\delta M_{e^2g^2}$	δM_{exp}
$K = \frac{2}{3}M_{exp}$	3.25 m_e	-0.01 m_e -0.02 m_e	-0.16 m_e -0.32 m_e	-2.5 m_e
$K = M_{exp}$	4.75 m_e	-0.02 m_e -0.04 m_e	-0.60 m_e -1.2 m_e	-2.5 m_e

The two values given in each box correspond to the two different values taken for the coupling constant.

9. – Discussion.

In discussing the results of Section **8**, we note first that $\delta M_{e^2g^2}$ and $\delta M_{e^2f^2}$ are both negative (as required by experiment) and are proportional to $(K/M_{exp})^2$ and $(K/M_{exp})^3$ respectively. However, for the probable values of (K/M_{exp}) as shown in the table (cf. also Section **1**), it is seen that $\delta M_{e^2g^2}$ is too small by a factor of about a hundred and $\delta M_{e^2f^2}$ is too small by a factor of about five or more. Although $\delta M_{e^2f^2}$ is not yet large enough to overcompensate the purely electromagnetic δM_{e^2}, we regard this result as fairly satisfactory for $\delta M_{e^2f^2}$ on account of the crude approximations made: i) the expansion in $1/M_{exp}$ and ii) the expansion in f^2 (from the theory of the magnetic moments it is well known that the first term of the f^2-expansion is insufficient but that one or two more terms are likely to improve the result. The same might be expected here). In particular $\delta M_{e^2f^2}$ is sizeable only for values of $(K/M_{exp}) \to 1$ and it is precisely when $(K/M_{exp}) \to 1$ that the N.R. approximation becomes insuf-

ficient. A further uncertainty is due to the application of the form factor ϱ to the relativistic meson-photon interaction. We found $\bar{\varrho} \sim 0.6 \div 0.7$. It should be clear that in any case $0 < \bar{\varrho} < 1$. Even allowing for a maximum of uncertainty the bracket in (8.5) can only vary between -1 and -0.35, *i.e* within a factor 3. But the extreme values are out of the question and the error caused by a possibly relativistic cut-off cannot be too large. At any rate it is unlikely that our $\bar{\varrho}$ ($\simeq 0.6 \div 0.7$) is too large and a smaller $\bar{\varrho}$ would improve the results. Finally the value of f^2 to be used is open to question. As was mentioned in Section **4**, it is not clear whether, in this perturbation expansion, the renormalized or unrenormalized f^2 is to be used. Renormalization implies *some* of the higher orders in f and perhaps it would be more consistent to use the unrenormalized f. In the latter case (f larger) the results may yet improve. It is possible, therefore, that the insufficient value obtained is due to all these causes.

At any rate, we can say that the pv result is satisfactory only with some reservations. *With* these reservations, it can be said that the p — n mass difference is, for the first time understood on grounds of meson theory.

One can obtain a rough idea, mathematically, why the e^2f^2-effect is so much smaller than the e^2-effect (in spite of the meson coupling constant) by noting that in the latter effect the number of internal lines of the corresponding Feynman graph equals the number of corners, while in the e^2f^2-effect the number of propagators exceeds the number of corners by one. This leads to an extra factor $2\pi i/(2\pi)^4$ in the e^2f^2-effect. It so happens that the number of graphs and the values of the integrals (cf. (8.2)) do not offset this factor, particularly in the ps case.

It might be enquired why the next order in $1/M_{\text{exp}}$ is not also calculated. At first sight the work required for this extra calculation is not too large, because the *denominators* of all the integrals to be calculated are the same to a first and second approximation —only the numerators change. However, in the second approximation calculations, a further calculating difficulty arises: the arguments of Section **6** which allow the tremendous simplification of replacing all the form-factors occurring at nucleon vertices by sharp spherical cut-off is no longer valid (the nucleon can no longer be regarded as quite at rest in the virtual states).

10. – Gauge invariance.

The integrals used in the present paper have been made convergent by the use of a form-factor. Before this procedure is fully justified it is necessary to show that these integrals fulfil certain conditions which are imposed

3296

by gauge-invariance. Diagramatically the gauge-invariance conditions (in the order ef^2) are as shown in Table F.

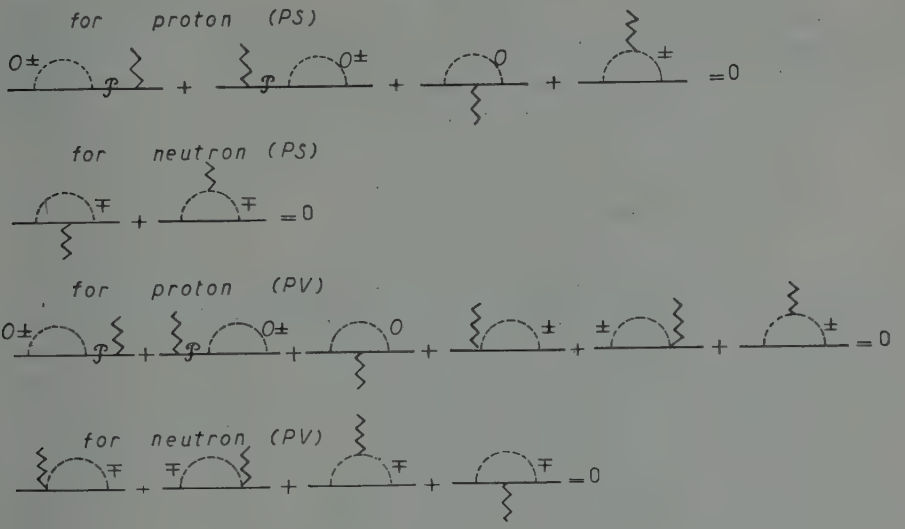

Table F.

It is understood that by each diagram is meant the corresponding matrix element, complete with free particle spinors acting to the left and right (when $\mathbf{q} = 0$ these graphs represent the effect of a *constant* electromagnetic potential on the nucleons, and this effect must, of course, be zero).

Now diagrams of the type shown in F form *parts* of the diagrams of Tables A and B. Hence, if the integrals of the A, B graphs are to be of value, the parts corresponding to the diagrams of F (complete with the free-particle spinors inserted at the relevant places — as indicated by the arrows in Table G, for example)

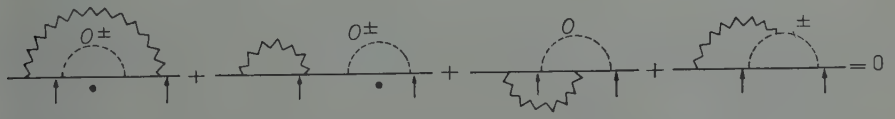

Table G.

must fulfill the relations shown in F, for $\mathbf{q} = 0$.

It is found that, in the rest system of the nucleon ($\vec{p} = 0$) and in the N.R. approximation considered, the required conditions are indeed fulfilled. Thus the convergent integrals we have used are not inconsistent with the demands of gauge-invariance.

3297

It should be mentioned, perhaps, that the presence of the free-particle spinors to the left and right in F' is responsible for the anomalous magnetic moment being a $1/M_{\text{exp}}^2$ effect ([13]). On applying the spinors the terms of order 1 and $1/M_{\text{exp}}$ vanish. In the graphs of A and B, on the other hand, there are no free-particle spinors at the corresponding places (they are inserted artificially in G only for test-purposes) and for this reason our mass-difference effect appears in the order 1 and $1/M_{\text{exp}}$.

11. – The theory of Feynman and Speisman.

FEYNMAN and SPEISMAN (referred to below as FS) have calculated $M_{\text{p}} - M_{\text{n}}$ using a semi-phenomenological approach. We discuss in this section the relation between that work and the present paper.

The FS approach is as follows. Instead of using the usual meson-theory they use only electromagnetic theory and allow for mesic interactions by adding to the usual interaction, a Pauli-term $e/4M \cdot \mu_\sigma \sigma_{\mu\nu} F^{\mu\nu}$, where μ_σ is a constant, determined phenomenologically (anomalous magnetic moment of the nucleon).

If we regard the FS Pauli-term as due principally to the order f^2 (which is not really sufficient), the effect calculated by FS corresponds graphically to our Tables A and B (three of the vertices in our graphs corresponding to a single vertex with the $\sigma_{\mu\nu} F^{\mu\nu}$ interaction in the FS graphs) but with a factor 2 for the graphs $\text{I}_{b_{\text{p}}}$, $\text{I}^R_{b_{\text{p}}}$ and with the graphs $\text{I}_{e_{\text{p}}}$, $\text{I}_{c_{\text{n}}}$ and II_{n} omitted (this is for all orders in $1/M_{\text{exp}}$, not merely the lowest). Thus the phenomenological approach does not take *all* the possible processes contributing to the mass-difference properly into account.

As well as that, by introducing the constant experimental value of μ_σ FS limit themselves to an approximation which is valid only for $\mathbf{q} \to 0$ (although their best results come from a high cut-off on $\mathbf{q}$). In our calculations the expressions used for $\mathbf{q}$ are valid (apart from the N.R. approximation) for all values of $\mathbf{q}$, and it is found that the larger values of $\mathbf{q}$ play a considerable rôle (they are partly responsible for the $(K/M_{\text{exp}})^3$ dependence of $\delta M_{e^2 f^2}$). In other words, the « magnetic moment » is strongly frequency dependent, which is ignored in FS.

Apart from the $\mathbf{q}$-dependence, there is the further question as to whether the introduction of a physical effect in place of part of a Feynman graph is valid in the first place. According to Section **10**, it is not, because the free particle spinors which are present in the calculation of the physical effect are absent in the middle of a graph, and their presence or absence has a consi

([13]) L. K. PANDIT: *Helv. Phys. Acta*, **31**, 379 (1958), Sect. **4**.

derable effect. (In our case (Section **10**) their presence changes the order in the $1/M_{\text{exp}}$ expansion, so that FS are working in the order $1/M_{\text{exp}}^2$, while we are working in the order 1 and $1/M_{\text{exp}}$. Note that for these graphs $\text{II}_{a,b}$, we obtain a different sign than FS). Further, the FS-effect contains a factor $(2\pi)^3$ more than ours, because, as in the e^2-effect, the number of propagators in FS is equal to the number of corners. This partly explains the magnitude of the FS result in comparison with ours.

It is clear, therefore, that the results of the present paper and those of FS bear very little resemblance to one other.

* * *

The authors wish to express their grateful thanks to Professor W. HEITLER for suggesting this problem and for his continued interest and help during the work. We are also deeply indebted to Dr. L. K. PANIT whose clarifications and suggestions were always more than welcome. We wish to thank also Dr. E. ARNOUS, Professor Y. TAKAHASHI, and M.lle Y. HÉNO for many very useful discussions, and to Professor A. THELLUNG we are indebted for much help in discussing the renormalization problem.

One of us (O'R.) wishes to express his gratitude to the Dublin Institute of Advanced Studies for the award of a Travelling Studentship, and one of us (S.) wishes to thank the Polish Ministry of Higher Education (Warsaw) for a grant covering the first stages of the work. All three of the authors owe sincere thanks for financial aid to the Schweizerischer Nationalfonds zur Förderung der wissenschaftlichen Forschung, Kommission für Atomwissenschaft.

APPENDIX

We wish to establish the identity of (4.7) and (4.2). The difference between these two expressions, is

$$\text{(A.1)} \qquad \delta M_{f^2}(M_0)\frac{\partial}{\partial M_0}\delta M_{e^2}(M_0)+[\delta\widetilde{M}_{e^2f^2}(M_0)-\delta M_{e^2f^2}(M_0)]\,,$$

neglecting terms of order f^4, and using (4.10). The second term in this expression is (by definition (4.9) and (4.3)) the difference between the $\delta M_{e^2f^2}$'s of the renormalized and unrenormalized theories. It is therefore represented by the graphs $\text{I}a_R$, $\text{I}b_R$ and $\text{I}c_R$

$$\text{(A.2)} \qquad \delta M_{e^2f^2}(M_0)-\delta M_{e^2f^2}(M_0)=\frac{-i}{(2\pi)^4}\bar{u}(M_0)\left\{\delta M_{f^2}\frac{\mathscr{P}}{\boldsymbol{\gamma}\cdot\mathbf{p}-M_0}H_{e^2}+\right.$$

$$\left.+H_{e^2}\frac{\mathscr{P}}{\boldsymbol{\gamma}\cdot\mathbf{p}-M_0}\delta M_{f^2}+e^2\int\gamma^\mu\frac{\mathrm{d}^4q}{q^2}\frac{1}{\boldsymbol{\gamma}\cdot(\mathbf{p}-\mathbf{q})-M_0}\delta M_{f^2}\frac{1}{\boldsymbol{\gamma}\cdot(\mathbf{p}-\mathbf{q})-M_0}\cdot\gamma_\mu\right\}u(M_0)\,,$$

3290

using the definition of H^s_{mesfe} in (4.4). H_{e^2} is defined by

$$\text{(A.3)}\quad \delta M_{e^2} = \bar{u}(M_0)\, H_{e^2} u(M_0) = \frac{i}{(2\pi)^4}\, \bar{u}(M_0) \left\{ \int \gamma^\mu \frac{1}{\boldsymbol{\gamma}\cdot(\mathbf{p}-\mathbf{q}) - M_0} \gamma_\mu \frac{\mathrm{d}^4 q}{q^2} \right\} u(M_0)\,.$$

On the other hand, by differentiating (A.3) we find

$$\text{(A.4)}\quad \delta M_{f^2} \frac{\partial}{\partial M_0} \delta M_{e^2} = \frac{i}{(2\pi)^4} \left\{ \frac{\partial \bar{u}(M_0)}{\partial M_0} H_{e^2} u(M_0) + \bar{u}(M_0) H_{e^2} \frac{\partial u(M_0)}{\partial M_0} + \right.$$
$$\left. + \bar{u}(M_0) \int \gamma^\mu \frac{1}{\boldsymbol{\gamma}\cdot(\mathbf{p}-\mathbf{q}) - M_0} \frac{1}{\boldsymbol{\gamma}\cdot(\mathbf{p}-\mathbf{q}) - M_0} \gamma_\mu \frac{\mathrm{d}^4 q}{q^2} u(M_0) \right\} \delta M_{f^2}\,.$$

The relations

$$\text{(A.5)}\quad \begin{cases} \dfrac{\partial \bar{u}(M_0)}{\partial M_0} = \bar{u}(M_0) \dfrac{\mathscr{P}}{\boldsymbol{\gamma}\cdot\mathbf{p} - M_0}\,, \\ \dfrac{\partial u(M_0)}{\partial M_0} = \dfrac{\mathscr{P}}{\boldsymbol{\gamma}\cdot\mathbf{p} - M_0}\, u(M_0)\,, \end{cases}$$

obtained by differentiation of the Dirac equation (for M_0), with respect to M_0 establish the identity of (A.4) and (A.2), apart from a minus sign. Thus (A.1) which is the sum of these two expressions, is zero, as required.

RIASSUNTO (*)

Si calcola la differenza di massa tra protone e neutrone assumendola dovuta a una autoenergia mista mesico-elettromagnetica. Le autoenergie del protone e del neutrone si calcolano nell'approssimazione $e^2 f^2$ in base alla teoria mesonica sia per l'accoppiamento ps che per l'accoppiamento pv. Per renderne le espressioni finite si applica alle tre interazioni (nucleone-mesone, nucleone-fotone e mesone-fotone) il fattore di forma proposto da Arnous e Heitler. Questo corrisponde a un taglio dei momenti virtuali a un valore K (di ordine M = massa nucleonica), quando la particella è a riposo e rappresenta pertanto una generalizzazione del modello di sorgente estesa. Per poter eseguire il calcolo, altrimenti estremamente complicato, si ricorre ad un'ulteriore grossolana approssimazione, cioè ad uno sviluppo in serie di $1/M$. Si ottiene il segno corretto per ambi gli accoppiamenti, ma nel caso ps il risultato è troppo piccolo per un fattore 100. Nel caso pv si ottiene il corretto ordine di grandezza ma il valore numerico risulta anche già troppo piccolo (per un fattore di almeno 5) per sovracompensare la pura energia elettromagnetica del protone. Il confronto coi precedenti lavori di Feynman e di Speisman fa vedere come questi non concordino coi risultati della teoria mesonica.

(*) *Traduzione a cura della Redazione.*

IL NUOVO CIMENTO Vol. XIV, N. 2 16 Ottobre 1959

Distribution Correlations in Sb (n, p) Sn (*).

R. A. Peck jr., H. P. Eubank and R. M. Howard (**)

Brown University - Providence, R. I.

(ricevuto il 15 Giugno 1959)

Summary. — The title reaction was studied at 14 MeV neutron energy and over the ranges 0 to 3 MeV excitation and 0 to 60°. It is demonstrated that the forward-peaked contribution is relatively concentrated at high proton energy and gives rise to most of the spectral group structure, and that the angle-insensitive portion has a smooth spectrum rising with decreasing proton energy. The isotropic portion does not fit the theoretical compound nucleus spectrum but is consistent with a process of incomplete compound nucleus formation. Total cross-section for the ranges of energy and angle studied is (22 ± 4) mb, of which 20% is the anisotropic contribution.

1. – Introduction.

In a survey of differential (n, p) cross-sections for elements in the vicinity of atomic number 50 ([1]) it was found that the cross-section for ^{51}Sb was at least 40 times that for ^{50}Sn. That this abrupt change cannot be attributed solely to the favorable proton configuration of ^{52}Sb, a single proton outside the closed shell, is indicated by the cross-section for ^{52}Te which is also much smaller than that of ^{51}Sb. Moreover, a similar situation is not found ([2]) at proton numbers 20 and 28, at which anomalously high cross-sections occur when the proton-magic nuclei are targets rather than products.

(*) Supported in part by the U. S. Atomic Energy Commission.

(**) Now at Corning Glass Works, Corning, N.Y. A portion of the work was submitted in partial fulfillment of the requirements for the degree of Master of Science at Brown University (June 1959).

(1) H. P. Eubank, R. A. Peck Jr. and M. R. Zatzick: *Nucl. Phys.*, **10**, 418 (1959).

(2) H. P. Eubank, M. R. Zatzick and F. L. Hassler: *Bull. Amer. Phys. Soc.*, (II) **4**, 141, 287 (1959).

3301

It thus appears that the high cross-section of Sb is specific to that nucleus rather than a simple result of shell systematics, and it is desirable to obtain further information on the mechanisms operating in this reaction. The data presented are not sufficient in resolution to identify groups in the proton spectrum. However, they do permit separation of the cross-section into major components, isotropic and forward-peaked, as in the method of Allan [3]. The range of angles observed precludes separation of a 90° symmetric part, and for the same reason the contribution identified as « isotropic » can only be an upper bound to any truly isotropic component.

Marked qualitative differences are to be expected between their separate energy distributions if, as frequently assumed, anisotropic and isotropic yields reflect direct interaction and compound nucleus formation, respectively. The isotropic protons should have an unstructured spectrum rising smoothly with decreasing proton energy (the energy resolution precluding the appearance of groups representing individual nuclear levels), and the forward-peaked yield should be concentrated at relatively high energies with a strong likelihood of group structure reflecting selective excitation of individual particle states [4]. The same qualitative correlation between spectrum form and angular distribution is to be expected even if a more cautious view is adopted, *viz.*, that the forward-peaked and angle-insensitive components are associated with few- and many-particle interactions, respectively.

We confine our report to the foremost π steradians (laboratory angles up to 60°) and the top quarter of the proton energy spectrum (residual excitations up to 4 MeV). In this energy range the forward peaking of a direct interaction contribution is a safe assumption, all protons emerge above the Coulomb barrier and (n, d) and (n, np) processes are energetically forbidden. A more detailed study over a wider energy range and with better resolution, both in energy and in angle, is being carried out by the emulsion method.

2. – Experimental.

The apparatus has been described elsewhere [5]. An evaporated film (7 mg/cm^2) of natural antimony on a thick lead support was bombarded with the 14.1 MeV D+T neutrons produced in a Cockcroft-Walton deuteron accelerator. The neutron source and a CsI(Tl) crystal 2.5 cm diameter × 2 mm thick were on opposite sides of the target film at distances of 6.4 cm and 12.7 cm, respectively. A pair of gas proportional counters fixed between the

---

[3] D. L. Allan: *Nucl. Phys.*, **10**, 348 (1958).
[4] D. L. Allan: *Proc. Phys. Soc.*, A **70**, 195 (1957), Fig. 6.
[5] H. P. Eubank, R. A. Peck Jr. and F. L. Hassler: *Nucl. Phys.*, **9**, 273 (1958).

3302

target film and crystal operated in coincidence to gate a 20 channel pulse height analyzer sorting the crystal pulses. The crystal defines an acceptance angle of $\pm 6°$ and with the width of the neutron source allows a maximum spread of recorded angles at given orientation of $\pm 17°$.

The spectrum determination at each angle was accompanied by a background spectrum and by an observation of a polyethylene recoil group at 0°. The latter served both as an intensity reference for absolute cross-sections and as an energy calibration, providing compensation for any variations in photomultiplier gain or in proton counting efficiency. Observations were made at laboratory angles of 0°, 15°, 30° and 60°.

3. – Results.

The shape of the proton spectrum up to 9 MeV excitation is shown in Fig. 1; the first 4 MeV of excitation, with which this report deals, appear again in the top of Fig. 3. Angular distributions of successive 0.5 MeV portions of the spectrum are displayed in Fig. 2, which illustrates the direct method employed in the separation of « isotropic » and anisotropic contributions in each energy interval. Integration of each component with respect to solid angle gives the integrated cross-sections as functions of energy for the separate components, which are displayed in the central and lower graphs of Fig. 3. The two dotted curves accompanying the isotropic spectrum are calculated for a compound nucleus process, using for level density the semi-empirical formula of NEWTON (6) which incorporates effects of shell structure. Only the intensity normalization constant is adjustable; the parameters determining slope and curvature are explicit in the formula.

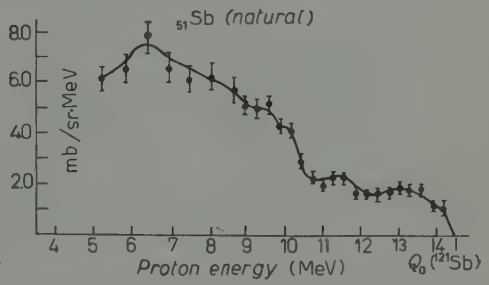

Fig. 1. – Sb(n, p)Sn differential spectrum at 0° over wide excitation range.

It is clear that the anticipated correlation is found between angular and energy distributions of the separate components. The spectrum of the forward-peaked yield (center, Fig. 3) contains virtually all of the irregularity of the unseparated spectrum and shows no tendency to rise with decreasing energy.

(6) T. D. NEWTON: *Can. Journ. Phys.*, **34**, 804 (1956).

The « isotropic » contribution, in contrast, shows a regular rise in cross-section with decreasing energy and no statistically significant fluctuations.

The fraction of the total yeld which is in the forward peak is shown in Table I, for the various excitations ranges. The tendency of the anisotropic

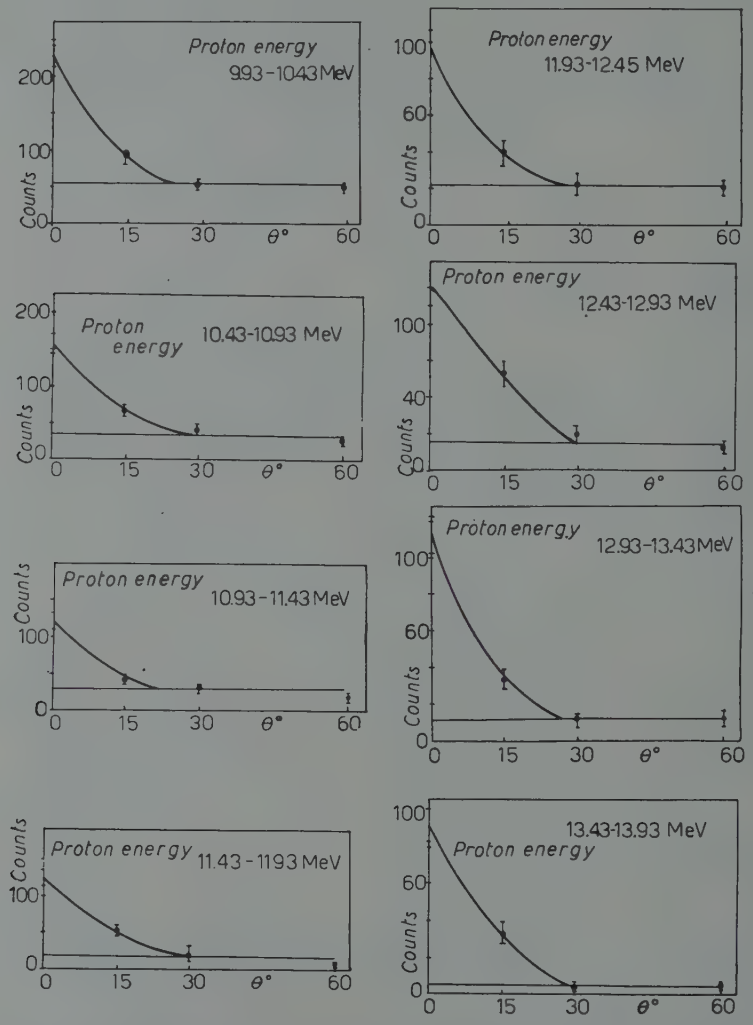

Fig. 2. - Angular distributions for successive 0.5 MeV intervals of observed spectrum.

component to concentrate at the lowest excitations is evident, in spite of irregularities introduced by the gross groups associated with this component. Both the high energy concentration and the association of gross fluctuations have been observed for the anisotropic yields from Cu and Fe, by ALLAN [3].

Over comparable energy ranges, the anisotropic fractions of Table I are substantially the same as those for Fe and smaller than for Cu.

TABLE I. – *Anisotropic fraction* (*) *as a function of excitation.*

Residual excitation (MeV)	$\frac{A}{A+I}$ (%)	Residual excitation (MeV)	$\frac{A}{A+I}$ (%)
0.0÷0.5	49	2.0÷2.5	22
0.5÷1.0	25	2.5÷3.0	10
1.0÷1.5	28	3.0÷3.5	14
1.5÷2.0	12	3.5÷4.0	11

(*) A = forward-peaked yield, I = « isotropic », each integrated over the range 0° to 60°.

It is evident in Fig. 3 that the « isotropic » spectrum does not fit the theoretical form for compound nucleus formation, for any normalization constant. The experimental curve rises more slowly than the theoretical, *i.e.*, corresponds to a much higher equivalent temperature. This suggests that the contribution identified as « isotropic » may represent incomplete compound nucleus formation, *i.e.*, a local excitation of a portion of the nucleus prior to proton emission (many-particle interaction). Such a contribution should vary slowly with angle but need not be symmetric about 90°.

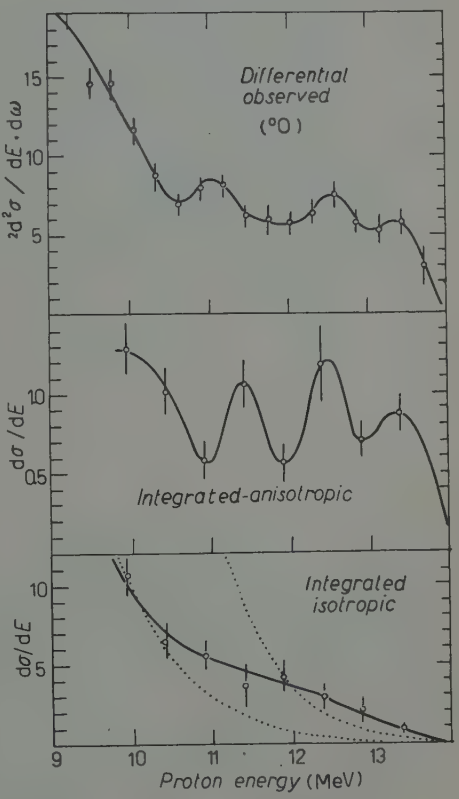

Fig. 3. – Low excitation spectra. (Top) Differential spectrum at 0°. (Center) Forward-peaked contribution integrated over angle. (Bottom) « Isotropic » contribution integrated over angles up to 60° (π steradians). Dotted curves are compound nucleus forms for two extreme normalization constants. Ordinate unit = 1 mb/sr·MeV (top) and 1 mb/MeV (center, bottom). Statistical probable errors are shown.

The total cross-section observed for all protons emitted forward of 60° (foremost π steradians) is (22.0 ± 1.5) mb,of which the forward peaked portion contributes (3.6 ± 0.2) mb and the « isotropic » portion (18.4 ± 1.4) mb. If the latter were truly isotropic, it would represent a full cross-section (for all angles) of (74 ± 6) mb. The errors cited are statistical probable errors, and all absolute cross-sections are subject to an additional systematic uncertainty of approximately 10%. Since all of these values represent only the first 4 MeV of excitation, they are relatively large cross-sections; the second 4 MeV of excitation add a cross-section (in the 0° spectrum, Fig. 1) 3.4 times as large as the first 4 MeV.

RIASSUNTO (*)

È stata studiata la reazione di cui al titolo ad una energia neutronica di 14 MeV, con eccitazioni variabili fra 0 e 3 MeV sotto angoli da 0 a 60°. Si dimostra che il contributo diretto in avanti è comparativamente più concentrato per le alte energie protoniche e dà origine alla maggior parte della struttura spettrale del gruppo; si prova inoltre che la porzione non influenzata dall'angolo ha uno spettro regolarmente crescente col decrescere dell'energia protonica. La porzione isotropica non si accorda con lo spettro teorico del nucleo composto, ma è coerente con un processo di formazione incompleta del nucleo composto stesso. Per gli intervalli di energia e angolari studiati la sezione trasversale efficace è di (22 ± 4) mb, di cui il 20% è costituito dal contributo anisotropico.

(*) *Traduzione a cura della Redazione.*

3306

IL NUOVO CIMENTO Vol. XIV, N. 2 16 Ottobre 1959

On the Analytic Properties of Partial Wave Scattering Amplitudes obtained from the Schrödinger Equation.

A. Martin

Theoretical Study Division, CERN - Geneva

(ricevuto il 1° Luglio 1959)

Summary. — On étudie les propriétés analytiques de l'amplitude de diffusion pour une onde partielle donnée à partir des propriétés de la solution radiale de l'équation de Schrödinger pour une énergie complexe. Les résultats connus dans le cas des potentiels à portée finie sont rétablis par cette méthode. On examine ensuite, en se limitant à l'onde S, les propriétés analytiques pour des potentiels décroissant exponentiellement. On retrouve ainsi une bande d'analyticité commune à tous ces potentiels. Deux exemples sont traités complètement: le cas d'un potentiel produit d'une exponentielle par une fonction sinusoïdale, le cas d'une famille assez générale de potentiels comprenant en particulier le potentiel de Yukawa et une somme de potentiels de Yukawa. Le comportement à l'infini de l'amplitude de diffusion est obtenu et il est possible d'écrire une relation de dispersion pour cette quantité. Sous des conditions plus restrictives, on peut écrire une relation de dispersion pour une quantité reliée à la fonction d'onde à une distance r de l'origine. La méthode employée pour évaluer l'amplitude de diffusion semble être, en outre, une méthode pratique d'approximation valable.

1. – Introduction.

The analytic properties of the partial wave amplitudes have been already established for finite range interactions vanishing rigorously outside a finite region. On the other hand, interesting results have been obtained by Jost who showed the existence of an analyticity strip for interactions decreasing as fast as $\exp[-\mu r]$ at infinity (1), and by Bowcock and Walecka (2) for a

(1) Private communication from H. Lehmann.

(2) J. Bowcock and D. Walecka: preprint CERN 6636/Th. 26, to be published in *Nucl. Phys.*

3307

sum of Yukawa potentials; they showed that for a fixed physical angle the scattering amplitude is analytic in the whole complex k^2 plane, except on known cuts and poles, and except perhaps at infinity, provided the interaction is sufficiently weak to make the Born series convergent; from these results at fixed angle one can obviously get information on partial waves.

The method we propose here consists in studying the behaviour of the radial reduced wave function for complex values of the energy or rather of the momentum k; this has already been done, in the past by KAPUR and PEIERLS in their study of nuclear reactions ([3]) and, more recently, by JOST ([9]). The results we have obtained by this method overlap with those obtained by the above-mentioned authors, but, in the case of infinite range potentials we can get some additional information, irrespective of the strength of the interaction, on the behaviour of the scattering amplitude for $|k| \to \infty$, which enables one to write dispersion relations. It is possible to treat the case of oscillating potentials, as was suggested by JOST ([4]), and to show in this case the existence of positive extra poles outside the imaginary axis for complex k. We should also mention that in the case of finite range potentials we get some additional information on the scattering amplitude in the lower half complex k plane, *i.e.*, in the second Riemann sheet in the k^2 plane, for instance on decaying states.

2. – Finite range potentials.

2·1. *S wave.* – The Schrödinger equation for the reduced wave function can be written

$$\text{(1)} \qquad \begin{cases} u'' + k^2 u = V(r) u \,, \\ V(r) = 0 \,, \qquad \text{for } r > r_0 \end{cases}$$

the results we derive are also valid for a non-local interaction:

$$\text{(1')} \qquad u'' + k^2 u = \int V(r, r')\, u(r')\, \mathrm{d}r' \,,$$

where

$$V(r, r') = 0 \qquad \text{for } r \text{ or } r' > r_0$$

and

$$V(r, r') = V^*(r', r) \,.$$

([3]) P. KAPUR and R. E. PEIERLS: *Proc. Roy. Soc.*, A **166**, 277 (1938).
([4]) R. JOST: private communication to D. WALECKA.

3308

Equations (1) or (1′) can be solved for complex k; the solution of equation (1) is unique up to a multiplying factor; the solution of equation (1′) is unique outside the interaction region ([5]). Outside the interaction region the solution can be written explicitly

$$u = -f(k)\exp[ikr] + g(k)\exp[-ikr] \tag{2}$$

one has to define the S matrix as

$$S(k) = \frac{f(k)}{g(k)} = \frac{(u' + iku)\exp[-ikr]}{(u' - iku)\exp[ikr]}, \tag{3}$$

for any r larger than r_0. In the case of real k this quantity is just $\exp[2i\delta(k)]$. What we have to do is to find when the right hand side of (3) is well defined for complex k and to show that it is an analytic function. The numerator and the denominator of (3) are well defined finite quantities so that all we have to do to study the existence of $S(k)$ is to study the zeros of the denominator. Combining equation (1) with its complex conjugate, and making use of the *reality* of the potential, one can derive the following relation:

$$(u^*u' - u^*u')_r + (k^2 - k^{*2})\int_0^r |u(r')|^2 \mathrm{d}r' = 0\,. \tag{4}$$

This relation holds for any value of r. For the non-local case it holds only for $r > r_0$. Equation (4) enables us to write the modulus of the denominator of (3) in the following way

$$|u' - iku|_r^2 = |u' + \operatorname{Im} k\, u|_r^2 + (\operatorname{Re} k)^2 |u|_r^2 + 4(\operatorname{Re} k)^2 \operatorname{Im} k \int_0^r |u(r')|^2 \mathrm{d}r'\,. \tag{5}$$

This equation shows that the denominator of S cannot vanish in the upper half complex k plane except perhaps on the imaginary axis. When $g(i\varkappa) = 0$ $\varkappa > 0$ this means that $u = ct \times \exp[-\varkappa r]$ outside the interaction region; the zeros of $g(k)$ in the upper half plane correspond to bound states. The vanishing of the right hand side of (5), for $(\operatorname{Re} k) \neq 0$ gives a necessary and sufficient condition for the existence of a pole in the lower half complex k plane; this will be explored in Section 2·3.

([5]) A. MARTIN: *Nuovo Cimento*, **7**, 607 (1957).

The holomorphy in the upper half plane will be proven if we shown that $S(k)$ as defined by (3) has a derivative. This can be done in the same way as on the real axis ([6,7]); the starting equation is obtained by comparing the Schrödinger equations for two neighbouring energies:

$$\left[\frac{\partial u}{\partial r}\frac{\partial u}{\partial k} - u\frac{\partial^2 u}{\partial r\,\partial k}\right]_r = 2k\int_0^r u^2(r')\,\mathrm{d}r'. \tag{6}$$

Assuming $r > r_0$ one can replace u by its asymptotic form (2) and get after some algebraic manipulations:

$$\frac{\mathrm{d}S}{\mathrm{d}k} = \frac{1}{2ik}\frac{[S - \exp[-ikr_0]]^2}{u^2(r_0)\exp[-ikr_0]}\left[2k\int_0^{r_0} u^2\,\mathrm{d}r + \frac{u(r_0)\,u'(r_0)}{k}\right] - 2ir_0S, \tag{7}$$

where $u' \equiv \partial u/\partial r$. From (7), we see that S has a well defined derivative whenever it exists. This equation gives also the residue of the poles, especially on the positive imaginary axis: in this case the asymptotic wave function can be taken as $\exp[-\varkappa r]$ $(k = i\varkappa)$, which fixes the normalization. It is easily seen that near such a pole

$$\frac{\mathrm{d}S}{\mathrm{d}k} = -iS^2\int_0^\infty u^2\,\mathrm{d}r\,. \tag{8}$$

Therefore the residue of the pole is $-i\Big/\int_0^\infty u^2\,\mathrm{d}r$.

Equation (7) makes apparent also the essential singularity at infinity $\exp[-ikr_0]$, coming from the last term of the right hand side, but it has to be proven that the first term does not contribute. This is easier to do by looking at an alternative expression of $S(k)$; use of the Schrödinger equation leads to the following equalities.

$$\begin{cases} (u' + iku)_r \exp[-ikr] = u'(0) + \displaystyle\int_0^r u(r')\exp[-ikr']\,V(r')\,\mathrm{d}r'\,, \\ (u' - iku)_r \exp[ikr] \quad\; = u'(0) + \displaystyle\int_0^r u(r')\exp[ikr']V(r')\,\mathrm{d}r'\,, \end{cases} \tag{9}$$

$S(k)$ is just the ratio of the two right hand sides. For sufficiently large $|k|$ u

---

([6]) E. P. Wigner: *Phys. Rev.*, **98**, 145 (1955).
([7]) A. Martin: *Compt. Rend.*, **243**, 22 (1956).

3310

can be replaced by Sin (kr) and it can be shown that if $V(r_1) \neq 0$ $(r_1 < r_0)$

$$|S(k) \exp[2ikr_1]| \to \infty \qquad \text{for } |k| \to \infty, \ \operatorname{Im} k > 0;$$

$$\text{if } r_2 > r_0 , \qquad S(k) \exp[2ikr_2] \to 0 ,$$

the precise nature of the essential singularity depending on the way $V(r)$ goes to zero for $r \to r_0$.

The symmetries of the function $S(k)$ come from the symmetries of the solution of the Schrödinger equation:

$$u(k, r) = C(k)\, u(-k, r) ,$$

$$u(k^*, r) = C'(k)\, u^*(k, r) .$$

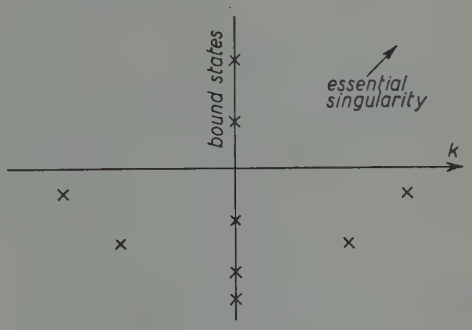

Fig. 1.

Inserting in the equation (3) we get

$$\text{(10)} \qquad \begin{cases} S(-k) = [S(k)]^{-1} , \\ S(k^*) = S^*(-k) . \end{cases}$$

This shows that the singularities in the lower half plane are necessarily isolated poles corresponding to zeros in the upper half plane. The complete structure in the complex k plane is given by Fig. 1.

2·2. *Extension to* $l \neq 0$. – One has to define solutions of the free Schrödinger equation:

$$\text{(11)} \qquad \begin{cases} O_l = kr\, h_l^{(1)}(kr) \sim \exp\left[i\left(kr - \frac{l\pi}{2}\right)\right] & \text{at infinity} , \\ I_l = kr\, h_l^{(2)}(kr) \sim \exp\left[-i\left(kr - \frac{l\pi}{2}\right)\right] & \text{at infinity} . \end{cases}$$

Notice that for k complex $O^* \neq I$. The S matrix will be defined by

$$\text{(12)} \qquad S_l(k) = \left(\frac{I_l\, u' - I_l'\, u}{O_l\, u' - O_l'\, u}\right)_{r \geqslant r_0} .$$

The singularities of S at finite distance are given by

$$O_l u' - O_l' u = 0 \qquad \text{for } r \geqslant r_0 .$$

Equation (4) still holds:

$$\left[\frac{u}{u'} - \left(\frac{u}{u'}\right)^*\right]_r + \frac{k^2 - k^{*2}}{|u_r|^2} \int_0^r |u(r')|^2 \, dr' = 0 ,$$

so that a necessary condition for the existence of a pole is

$$\left[\frac{O'}{O}-\left(\frac{O'}{O}\right)^*\right]_{r_0}+\frac{k^2-k^{*2}}{|u_r|^2}\int_0^r|u(r')|^2\,\mathrm{d}r'=0\,. \tag{13}$$

Now we can apply the trick used to get equation (4) to the free Schrödinger equation, and *assuming* $\operatorname{Im} k>0$, we obtain

$$\left[\frac{O'}{O}-\left(\frac{O'}{O}\right)^*\right]_{r_0}=\frac{k^2-k^{*2}}{|O|^2_{r_0}}\int_{r_0}^{\infty}|O|^2\,\mathrm{d}r\,,$$

because $O(\infty)=0$.

Therefore condition (13) becomes:

$$(k^2-k^{*2})\left[\frac{\int_0^{r_0}|u|^2\,\mathrm{d}r}{|u|^2_{r_0}}+\frac{\int_{r_0}^{\infty}|O|^2\,\mathrm{d}r}{|O|^2_{r_0}}\right]=0\,. \tag{14}$$

So that there cannot be any singularity in the upper half plane except for $\operatorname{Re} k=0$. It seems unnecessary to go into the details as was done in Sect. 2·1.

2·3. *Lower half plane. Poles near the real axis.* – In what follows r_0 is *fixed* and chosen as small as possible, outside the interaction region. Equation (5) shows that a pole given by

$$f(\operatorname{Re} k,\operatorname{Im} k)\equiv|u'-iku|^2_{r_0}=0\,, \tag{15}$$

cannot be infinitely near the real axis because $u(k, r_0)$ and $u'(k, r_0)$ are smooth functions of k. This qualitative statement can be put in a more quantitative way, when the pole is very close to the real axis, which corresponds to a metastable state (*e.g.*, an α particle in a nuclear potential); assume that such a pole k_p exists. Since the function $f(\operatorname{Re} k, \operatorname{Im} k)$ is everywhere $\geqslant 0$ it will have a minimum on the real axis, for variable $\operatorname{Re} k$ in the neighbourhood of k_p (see Fig. 2).

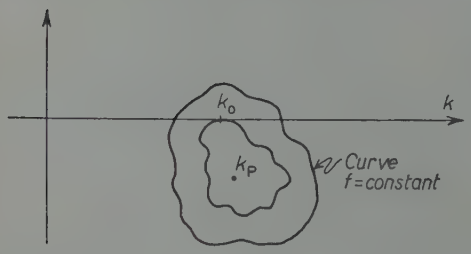

Fig. 2.

From the definition of k_0 it follows that

$$\frac{\partial f}{\partial\operatorname{Re} k}=2\operatorname{Re}\left[(u'+iku)\frac{\partial}{\partial k}(u'-iku)\right]=0\,. \tag{16}$$

Let us try to expand $u' - iku$ in the neighbourhood of k_0:

$$\frac{\partial}{\partial k}(u' - iku)_{k=k_0} = \frac{i}{u' + iku} \operatorname{Im}\left[(u' + iku)\frac{\partial}{\partial k}(u' - iku)\right], \tag{16'}$$

using (16) and, using equation (6) ($u' \equiv \partial u/\partial r$),

$$\frac{\partial}{\partial k}(u' - iku)_{k=k_0} = \frac{-i}{u'_{k_0} + ik_0 u_{k_0}}\left[2k_0^2 \int_0^{r_0} u_{k_0}^2(r)\,\mathrm{d}r + u'_{k_0} u_{k_0}\right], \tag{17}$$

so that in the neighbourhood of $k = k_0$

$$(u' - iku) = (u'_{k_0} - ik_0 u_{k_0})\left[1 - i(k - k_0)\frac{2k_0^2 \int_0^{r_0} u_{k_0}^2(r)\,\mathrm{d}r + u'_{k_0} u_{k_0}}{u'^2_{k_0} + k_0^2 u_{k_0}^2}\right]. \tag{18}$$

The assumption that k_P is very near the real axis means that

$$k_P - k_0 \simeq -i\,\frac{u'^2_{k_0} + k_0^2 u'_{k_0} u_{k_0}}{2k_0^2 \int_0^{r_0} u_{k_0}^2(r)\,\mathrm{d}r + u'_{k_0} u_{k_0}}, \tag{19}$$

the expansion (18) is valid provided the modulus of (19) is very small, *i.e.*,

$$2k_0^2 \int_0^{r_0} u^2(r)\,\mathrm{d}r \gg (u'^2_{k_0} + k_0^2 u_{k_0}^2) r_0 .$$

This condition is just the condition for the existence of the decaying state ([8]), which says that the external wave function must be as small as possible as compared to the internal wave function. We recognize on (19) the expression for the lifetime of the decaying state (up to trivial factors).

Conversely, setting $\int_0^{r_0} u^2(r)\,\mathrm{d}r = ct$, one might ask if a pole corresponds to a minimum of

$$\frac{(u'^2 + k^2 u^2)}{\int_0^{r_0} u^2(r)\,\mathrm{d}r},$$

for real k. If the value of the minimum happens to be very small, the zero of the expansion (18) lies very near k_0 so that the use of the Taylor expansion

([8]) E. FERMI: *Nuclear Physics* (Chicago, 1950), p. 59.

is *a posteriori* justified and it appears very likely that a pole given by (19) exists.

3. – Potentials decreasing faster than an exponential.

In what follows we consider local potentials such that there exists a μ giving

$$\lim_{r\to\infty} V(r)\exp[+\mu r] = 0$$

and we restrict ourselves to S waves.

3·1. *The analyticity strip.* – One can try to define the S matrix for complex k by generalizing (3)

$$S(k) = \frac{\lim_{r\to\infty}[(u' + iku)\exp[-ikr]]}{\lim_{r\to\infty}[(u' - iku)\exp[ikr]]}. \tag{20}$$

The problem is to find when these limits exist and when the denominator is different from zero. According to equation (9) these limits, if they exist, are respectively

$$\begin{cases} N(k) = u'(0) + \int_0^\infty u(r)V(r)\exp[-ikr]\,dr\,, \\ D(k) = u'(0) + \int_0^\infty u(r)V(r)\exp[+ikr]\,dr\,, \end{cases} \tag{21}$$

and

$$S(k) = \frac{N(k)}{D(k)}.$$

Now the arguments given to show that the Schrödinger equation admits two independent solutions

$$f(r, k)\exp[-ikr]\,, \qquad g(r, k)\exp[+ikr] \tag{22}$$

such that

$$f(\infty, k) = g(\infty, k) = 1$$

provided $V(r)$ decreases at least as fast as $\frac{1}{2}$ are still valid [9] for complex k.

---

[9] R. Jost: *Helv. Phys. Acta*, **19**, 256 (1946).

For $\operatorname{Im} k > 0$ the solution which blows up at infinity is the first one. $u(r)$ is a combination of the two. So we are certain that $u(r) \exp[ikr]$ tends to a finite limit (which may be zero) at infinity, for $\operatorname{Im} k > 0$. This means that the quantity $D(k)$ exists. On the other hand, $N(k)$ may be written

$$N(k) = u'(0) + \int_0^\infty u(r) \exp[ikr] \, [V(r) \exp[-2ikr]] \, dr .$$

So $N(k)$ is a well defined quantity for

$$2 \operatorname{Im} k < \mu . \tag{23}$$

We still have to study the zeros of $D(k)$ by looking at the two independent solutions (22). One is led to the following alternative: for $\operatorname{Im} k > 0$, either u behaves like $\exp[ikr]$ for $r \to \infty$ or u behaves like $\exp[-ikr]$. So to prove that $D(k) = \lim_{r\to\infty} (u' - iku) \exp[ikr] \neq 0$ it is sufficient to prove that $\lim_{r\to\infty} |u' - iku| \neq 0$. Now equation (5), established inside the range of the potential is still valid in the present case. It shows that

$$\lim_{r\to\infty} |u' - iku|^2 > 4 (\operatorname{Re} k)^2 \operatorname{Im} k \int_0^\infty |u(r')|^2 \, dr' ; \tag{24}$$

the right hand side is certainly a positive quantity for $\operatorname{Im} k > 0$, $\operatorname{Re} k \neq 0$. This means that $D(k)$ is a well defined quantity in the upper half plane, certainly different from zero outside the imaginary axis. When $\lim (u' - iku) \cdot \exp[ikr] = 0$ this means that $u(r)$ is $\exp[ikr] = \exp[-\varkappa r]$ $(k = i\varkappa, \ \varkappa > 0)$ so that the zeros of $D(k)$ on the positive imaginary axis correspond to *true bound states*.

Therefore, we have shown that it is possible to define $S(k)$ in the strip $0 < \operatorname{Im} k < \mu/2$, with possible poles, corresponding to true bound states, on the imaginary axis.

Now it is not too difficult to convince ourselves that the functions

$$N_{r_0}(k) = u'(0) + \int_0^{r_0} u(r) V(r) \exp[-ikr] \, dr ,$$

$$D_{r_0}(k) = u'(0) + \int_0^{r_0} u(r) V(r) \exp[+ikr] \, dr ,$$

converge uniformly to $N(k)$ and $D(k)$ in the region

$$0 \leqslant \operatorname{Im} k \leqslant \frac{\mu}{2} - \varepsilon , \qquad |\operatorname{Re} k| < A$$

3315

with ε arbitrarily small and A arbitrarily large. In this region $\lim u(r) \exp[ikr] = C(k)$ (for instance with a normalization $u'(0) = ct$) and $|C(k)|$ has a maximum value M; then, for r and r' large enough

$$|N_r(k) - N_{r'}(k)| < |\exp[-\varepsilon r] - \exp[-\varepsilon r']| \times \text{const}$$

and

$$|D_r(k) - D_{r'}(k)| < |\exp[-\mu r] - \exp[-\mu r']| \times \text{const}\,.$$

Excluding now a small region around the zeros of $D(k)$ on the imaginary axis, one can also show that $S_{r_0}(k) = N_{r_0}(k)/D_{r_0}(k)$ converges uniformly to $S(k)$.

It happens that $S_{r_0}(k)$ is the S matrix for the finite range potential

$$\begin{cases} V(r) & \text{for } r < r_0 \\ 0 & \text{for } r > r_0 \end{cases}$$

for which analytic properties are known. From known theorems it follows that $S(k)$ is holomorphic in the strip $0 \leqslant \operatorname{Im} k < \mu/2$ except for possible singularities on the line $\operatorname{Im} k = \mu/2$ and at infinity, and poles due to bound states on the imaginary axis.

3·2. *Analytic properties in the whole upper half complex plane.* – When the potential is precisely known, it is possible to get more than an analyticity strip for the S matrix, in spite of the breakdown of equation (20) for $\operatorname{Im} k \geqslant \mu/2$. Assume that the two independent solutions (22) are known. Then one can write the solution of the Schrödinger equation as

$$u(r) = f(r, k) \exp[-ikr] - g(r, k) \frac{f(0, k)}{g(0, k)} \exp[ikr]\,, \tag{25}$$

provided

$$g(0, k) \neq 0; \qquad \text{if} \quad g(0, k) = 0\,,$$

$$u(r) = g(r, k) \exp[ikr]\,. \tag{25'}$$

It is natural to define the S matrix for complex k as

$$S(k) = \frac{f(0, k)}{g(0, k)} \tag{26}$$

since this definition holds for real k.

One can immediately show that the zeros of $g(0, k)$ correspond to bound states and lie on the imaginary axis: these zeros, according to (25'), are such

that $\lim_{r\to\infty}(u' - iku) = 0$, which as already shown in the preceding section can only occur for $\mathrm{Re}\, k = 0$; the asymptotic form is then

$$u(r) \simeq \exp[-\varkappa r] \qquad \varkappa > 0.$$

By inserting in the Schrödinger equation, one obtains for $f(r, k)$ and $g(r, k)$ the following equations

$$(27) \qquad \begin{cases} f'' - ikf' = V(r)f\,, & \text{with } \lim_{r\to\infty} f(r, k) = 1\,, \\ g'' + ikg' = V(r)g\,, & \text{with } \lim_{r\to\infty} g(r, k) = 1\,. \end{cases}$$

Assuming provisionally, existence and unicity of these functions, we readily get the following symmetries:

$$f(r, -k) = g(r, k)\,,$$

$$f^*(r, k^*) = g(r, k)\,.$$

from which follows

$$S(k) = S^{-1}(-k)\,, \qquad S(-k^*) = S^*(k)\,.$$

Following the classical procedure of neglecting first the second order derivatives, we get the behaviour of the k functions for $r \to \infty$:

$$f(r, k) = 1 + \frac{1}{2ik}\int_r^\infty V(r')\,\mathrm{d}r' + \dots\,,$$

$$g(r, k) = 1 - \frac{1}{2ik}\int_r^\infty V(r')\,\mathrm{d}r' + \dots\,.$$

This is all we can say without more detailed information on the shape of the potentials. We shall now thoroughly treat examples, some of which are quite general. Our study will be limited to upper half k plane or first Riemann sheet of the energy plane.

3·3. *Examples.*

3·3.1. Exponential potential, sum of exponential potentials, oscillating potential. – The first case admits an exact solution [10,11] and, on the other hand, has been treated by Jost [9] using an expansion of the

---

[10] H. A. Bethe and R. Bacher: *Rev. Mod. Phys.*, **8**, 111 (1936).
[11] S. T. Ma: *Phys. Rev.*, **69**, 668 (1946).

functions $f(r, k)$, $g(r, k)$ of the type:

$$1 + \sum_{1}^{\infty} C_n \exp[-n\mu r].$$

In this way one shows that $f(0, k)/(g(0, k) = S(k)$ is holomorphic in the upper complex plane except for poles at $2ik + n\mu = 0$, and that $\lim_{|k|\to\infty} S(k) = 1$ in any direction, provided $\mathrm{Re}\, k \neq 0$. JOST also applied his treatment to a sum of exponential potentials

$$V = A \exp[-pr] + B \exp[-qr]$$

then

$$f = \sum_{mn} C_{mn}(k) \exp[-(mp + nq)r],$$

$$g = \sum_{mn} D_{mn}(k) \exp[-(mp + nq)r].$$

The coefficients C_{mn} and D_{mn} are obtained by recursion formulas.

One can notice that this treatment can be extended without trouble to the case

$$A = B = \frac{V_0}{2},$$

$$p = q^* = \mu + i\alpha,$$

i.e., (30)

$$V(r) = V_0 \cos(\alpha r) \exp[-\mu r].$$

Then the possible redundant poles (besides the bound states) are given by

$$k = \frac{(n - m)\alpha}{2} + i\frac{(m + n)\mu}{2},$$

some of which lie outside the imaginary axis. It is important to evaluate the residues of these poles to see if they really exist, since from general arguments ([12]) one would not expect them. When $2ik + Pp + Nq = 0$ all the $C_{M+m\,N+n}$'s ($m \geqslant 0$, $n \geqslant 0$) are singular. In the neighbourhood of such a singularity, the recursion formula reads:

$$C_{M+m,\,N+n}[mp + nq - 2ik][mp + nq] = \frac{V_0}{2}[C_{M+m-1,\,N+n} + C_{M+m,\,N+n-1}].$$

The $C_{M+m,\,N+n}$ are determined in terms of C_{MN} which is singular and

([12]) E. CORINALDESI: *Nucl. Phys.*, **2**, 420 (1956).

$C_{M-1,\,N+1+\lambda}\,C_{M+1+\lambda,\,N-1}$ $(\lambda \geqslant 0)$ which are not singular. So, to get the singular part of $C_{M+m,\,N+n}$ one can take the $C_{M-1,\,N+1+\lambda}$'s and the $C_{M+1+\lambda,\,N-1}$ equal to zero Then by comparison with the recursion formula for the D it can be seen that

$$\frac{\text{singular part of } C_{M+m,\,N+n}}{C_{MN}} = D_{mn}\,.$$

So $f(r, k)$, near $2ik + Mp + Nq = 0$ behaves like $C_{MN}g(r, k)$. In the special case $2ik + Mp \equiv 2ik + M(\mu + i\alpha) = 0$,

$$C_{M0} \cong \frac{V_0^M}{2^M(Mp + 2ik)[(M-1)!]^2 M\mu^{2M-1}}\,.$$

Therefore the residues of

$$S(k) = \frac{f(0, k)}{g(0, k)}\,,$$

at the poles

$$k = \frac{M(i\mu \pm \alpha)}{2}\,,$$

are certainly different from zero because $g(0, k)$ is, from general arguments different from zero, so that there is no indetermination in the ratio defining $S(k)$. We have also shown by direct calculation that the first poles corresponding to $MN \neq 0$ exist. One gets the picture given in Fig. 3. The problem is now to understand why the arguments against the existence of such poles, based on conservation of probability, fail in the present case. These arguments require that the asymptotic behaviour of the wave function be:

$$\exp[-ikr] - S(k)\exp[ikr]\,.$$

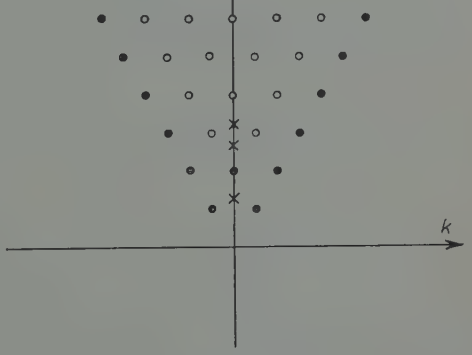

Fig. 3. – ● redundant poles; ○ probable redundant poles; × bound states.

Here the wave function is

$$[1 + C_{10}\exp[-(\mu + i\alpha)r] + C_{01}\exp[-(\mu - i\alpha)r] + \ldots]\exp[-ikr] - \\ - [1 + \ldots]S(k)\exp[ikr]\,.$$

To identify this expression with the preceding one, it is necessary that

$\exp[-\mu r]\exp[-ikr]$ be negligible as compared to $\exp[ikr]$. This means that k must be in the analyticity strip $0 \leqslant \operatorname{Im} k < \mu/2$. Outside this strip these arguments are no longer valid.

3·3.2. Yukawa potential and generalizations. – It is quite clear that example one could be generalized to any finite sum of real exponential potentials, $\sum A_{p_0} \exp -[p_i r]$; then the expected redundant poles are given by $\sum n_i p_i + 2ik = 0$, on the imaginary axis. So, above the pole given by the minimum p_i, $k = ip_{\min}/2$, the poles will become more and more dense as the number of p_i's increases. This enables us to guess what will happen for a potential

$$V(r) = V_0 \exp[-\mu r] \int_0^\infty C(\alpha) \exp[-\alpha r]\, \mathrm{d}\alpha\,, \qquad \text{with} \qquad |C(\alpha)| < M\,. \tag{31}$$

One expects a cut on the imaginary axis starting at $k = i(\mu/2)$. This family of potentials contains as a special case, the Yukawa potential for $C(\alpha) = ct$ and sums of Yukawa potentials when $C(\alpha)$ is made of a sum of step functions. It is equivalent to the family

$$\frac{\exp[-\mu r]}{r} \int_0^\infty C'(\alpha) \exp[-\alpha r]\, \mathrm{d}\alpha\,.$$

where $C'(\alpha)$ may now be a distribution, with the restriction that $\int_0^\infty C'(\alpha)\, \mathrm{d}\alpha$ is finite (this excludes potentials behaving as $1/r^{1+\varepsilon}$ at the origin).

Here the natural « ansatz » for the functions f and g is:

$$\begin{cases} f(r,k) = 1 + \exp[-\mu r] \int_0^\infty \varrho_k(\alpha) \exp[-\alpha r]\, \mathrm{d}\alpha\,, \\ g(r,k) = 1 + \exp[-\mu r] \int_0^\infty \sigma_k(\alpha) \exp[-\alpha r]\, \mathrm{d}\alpha\,. \end{cases} \tag{32}$$

Inserting in equations (27) with potential (31), we get, making use of the known properties of products of Laplace transforms, and equating the coefficients of $\exp[-\alpha r]$ in both sides of the equation thus obtained

$$\begin{cases} \varrho_k(\alpha)[\alpha+\mu][\alpha+\mu+2ik] = V_0 \left[C(\alpha) + \int_0^{\alpha-\mu} C(\alpha-\mu-\beta)\, \varrho_k(\beta)\, \mathrm{d}\beta \right], \\ \sigma_k(\alpha)[\alpha+\mu][\alpha+\mu-2ik] = V_0 \left[C(\alpha) + \int_0^{\alpha-\mu} C(\alpha-\mu-\beta)\, \sigma_k(\beta)\, \mathrm{d}\beta \right], \end{cases} \tag{33}$$

3320

where one should keep in mind that

$$\varrho(\lambda) = \sigma(\lambda) = C(\lambda) = 0 \qquad \text{for } \lambda < 0 \text{ (*)}.$$

These equations are not true integral equations. Assume $0 < \alpha < \mu$ then the integrals do not contribute and

$$\varrho(\alpha) = V_0 C(\alpha)(\alpha+\mu)^{-1}(\alpha+\mu+2ik)^{-1}, \qquad (0 \leqslant \alpha \leqslant \mu)$$

$$\sigma(\alpha) = V_0 C(\alpha)(\alpha+\mu)^{-1}(\alpha+\mu-2ik)^{-1}.$$

The functions $\varrho(\alpha)$ and $\sigma(\alpha)$ can be determined by recursion. Assume $\varrho(\alpha)$ and $\sigma(\alpha)$ are known for $0 \leqslant \alpha \leqslant n\mu$. Then the right hand sides of equations (33) are known for $0 \leqslant \alpha \leqslant (n+1)\mu$. It is clear that $\sigma_k(\alpha)$ is everywhere a well defined quantity when k is in the upper half plane. $\varrho_k(\alpha)$ is well defined when $\alpha+\mu+2ik$ cannot vanish, *i.e.*, outside a cut along the imaginary axis starting at $k = i(\mu/2)$. The problem is now to study the convergence of the integrals

$$1 + \exp[-\mu r]\int_0^\infty \varrho_k(\alpha)\exp[-\alpha r]\,\mathrm{d}\alpha\,, \qquad 1 + \exp[-\mu r]\int_0^\infty \sigma_k(\alpha)\exp[-\alpha r]\,\mathrm{d}\alpha\,.$$

This is possible because equations (33) are very suitable to get upper bounds of $|\varrho_k(\alpha)|$ and $|\sigma_k(\alpha)|$. The following results are demonstrated in Appendix I:

— $g(r, k)$ is a holomorphic function in the whole upper complex plane and $\lim_{|k|\to\infty}(g(r, k)-1)\,|k|^{1-n} = 0$ (n arbitrarily small);

— $f(r, k)$ is a holomorphic function such that $\lim_{|k|\to\infty}(f(r, k)-1)\,|k|^{1-n} = 0$ in the union of the domains:

$$0 \leqslant \operatorname{Im} k \leqslant \frac{\mu}{2} - \varepsilon\,, \qquad 0 \leqslant \operatorname{Arg} k \leqslant \frac{\pi}{2} - \varepsilon\,, \qquad 0 \leqslant \pi - \operatorname{Arg} k \leqslant \frac{\pi}{2} - \varepsilon\,,$$

(ε arbitrarily small)

Moreover $\lim_{\operatorname{Im} k\to+\infty} f(r, k) = 1$ provided

$$\operatorname{Re} k > C[\operatorname{Im} k]^{-N},$$

(*) One can check that if the functions defined by (32) and (33) exist they satisfy the Schrödinger equation with the right potential.

where N is an arbitrary positive number, so that the limit of $f(r, k)$ as $|k| \to \infty$ is unity even if one asymptotically approaches the imaginary axis at infinity.

Concerning the existence of the limiting function

$$\lim_{\substack{\mathrm{Re}\, k \to 0 \\ \mathrm{Re}\, k > 0}} f(r, k),$$

we have only considered two particular cases, but it is clear that much more general cases could be solved:

— if the weight function in the integral representation of the potential is such that

$$|C(\alpha) - C(\beta)| < B|\alpha - \beta| \tag{34}$$

in addition to $|C| < M$, where B is independent of α and β, the weight function $\varrho_k(\alpha)$ has a pole at $\alpha + \mu + 2ik = 0$, but the limit of $f(r, k)$ exists everywhere along the cut, except at $2ik + \mu = 0$, where there is a logarithmic singularity. This case does not contain the Yukawa potential because then $C(\alpha)$ has a discontinuity at $\alpha = 0$;

— for the Yukawa potential $C(\alpha) = 1$ for $\alpha > 0$. The weight function $\varrho_k(\alpha)$ has a pole at $\alpha + \mu + 2ik = 0$ and a logarithmic singularity at $\alpha + 2ik = 0$. For $\mu + 2ik \neq 0$ the limit of $f(r, k)$ exists along the cut, but for $\mu + 2ik = 0$ the limit of $f(r, k)$ has a logarithmic singularity. This singularity is harmless when one writes dispersion relations.

These properties are sufficient to give a dispersion relation for the quantity

$$A(E) = \frac{1}{2i}\left[\frac{f(0, k)}{g(0, k)} - 1\right], \qquad (E = k^2)$$

if one remembers that the zeros of $g(0, k)$ lie on the positive k imaginary axis (or E real, negative) and correspond to bound states:

$$\mathrm{Re}\, A(E_0) = \text{bound states} + \frac{P}{\pi}\int_0^{\infty} \frac{\mathrm{Im}\, A(E + i\varepsilon)\, \mathrm{d}E}{E - E_0},$$

$$- \frac{1}{\pi}\int_{(\mu/2)^2}^{\infty} \frac{\mathrm{Im}\, A(-E + i\varepsilon)\, \mathrm{d}E}{E + E_0}.$$

This relation is not very useful from a practical point of view, because one has a very large unphysical range. If we assume that the n-p potential belongs to the above considered family, we see that the pole corresponding to the deuteron lies at $E = -0.105\,\mu^2$, while the cut begins at $-0.25\,\mu^2$.

3322

The quantity $S(r, k) = f(r, k)/g(r, k)$ has the same analytic properties as $S(k)$. However, there is no general argument to guarantee that $g(r, k)$ has no zeros outside the imaginary axis. We have shown that a *sufficient* condition to avoid zeros in the upper half plane is that $|V_0| M < \frac{2}{3}\mu$ (Appendix II). This is certainly far from being necessary. Under this condition one can write a dispersion relation for

$$A(r, E) = \frac{1}{2i}(S(r, k) - 1),$$

which can be considered as a dispersion relation for the wave function. This problem is being studied for finite range potentials by Bosco and Fubini [13]. For real k or $E > 0$, $|S(r, k)| = 1$, so that there is an obvious connection between the real and imaginary parts of $A(r, E)$. This would permit to transform the dispersion relation for $A(r, E)$ into a Low integral equation, but the presence of the unphysical range makes it rather useless.

A by-product of equations (33) is a new practical method of computation of the scattering matrix and of the bound states. Some work has already been done in that direction by Koppe [14]. In Appendix III, we show that one can very quickly get an accurate value of the Yukawa well depth parameter.

4. – Concluding remarks.

In the case of finite potentials, our method is straightforward but does not bring anything really new. Its use is rather to guide us in the case of infinite range potentials. In the case of infinite range potentials, we restricted ourselves to the S wave; we hope to be able to extend this method to higher waves soon. The main results we get are, first, the anomalous poles in the upper half plane outside the imaginary axis for the oscillating potential, second, the complete analytic behaviour for Yukawa potential and generalization, including the behaviour at infinity, third, analytic properties of a quantity related to the wave function at a point r fixed, giving rise to generalized dispersion relations at least if the potential is not too strong. Except for the last result, all the other results are derived without any assumption on the strength of the potential. This is due to the fact that we have separated the spurious poles or cuts arising in the complex plane, which appear in the numerator of the S matrix, from the poles due to bound states which appear as zeros of the denominator.

---

[13] S. Fubini: private communication.

[14] A. Koppe: *Zeits. f. Naturfor.*, A **6**, 229 (1951).

* * *

The author wishes to thank Professors FIERZ, FUBINI and GLASER, Drs. BOWCOCK and WALECKA, for useful comments and suggestions.

Note: While this paper was mimeographed, we received a preprint by R. E. PEIERLS, in which some of the results presented here are derived under more restrictive assumptions. The behaviour at infinity is not studied.

APPENDIX I

In the upper half plane $|\alpha+\mu-2ik|>|\alpha+\mu|$. From the inequality

$$|\sigma_k(\alpha)|<\frac{|V_0|M}{(\alpha+\mu)^2}\left[1+\int_0^{\alpha-\mu}|\sigma_k(\beta)|\,\mathrm{d}\beta\right], \tag{I.1}$$

one sees that an upper bound of $\sigma_k(\alpha)$ is $\sum(\alpha)$ given by

$$\sum(\alpha)=\frac{|V_0|M}{(\alpha+\mu)^2}\left[1+\int_0^{\alpha-\mu}\sum(\beta)\,\mathrm{d}\beta\right], \tag{I.2}$$

where $\sum(\alpha)=0$ for $\alpha<0$. From (I.2) one can easily get

$$1+\int_0^{\infty}\sum(\alpha)\,\mathrm{d}\alpha<\frac{1+\int_0^{\alpha_1}\sum(\alpha)\,\mathrm{d}\alpha}{1-\dfrac{|V_0|M}{\alpha_1+\mu}}, \tag{I.3}$$

provided $\alpha_1+\mu>M|V_0|$ and also with (I.1):

$$\int_A^{\infty}|\sigma_k(\alpha)|\,\mathrm{d}\alpha<\frac{|V_0|M}{A+\mu}\left(1+\int_0^{\infty}\sum(\alpha)\,\mathrm{d}\alpha\right).$$

This establishes the *uniform* and *absolute* convergence of the integral defining $g(r,k)$ in the whole upper half plane. Since one can see by recursion that $1+\exp[-\mu r]\int_0^A\exp[-\alpha r]\sigma_k(\alpha)\,\mathrm{d}\alpha$ is a holomorphic function, the same is true for $g(r,k)$ [15].

---

[15] C. CARATHEODORY: *Theory of Functions of a Complex Variable*, 2nd english ed. (Chelsea, 1958), pp. 180-197.

3324

Since $\lim_{|k|\to\infty}\left[1+\int_0^A|\sigma_k(\alpha)|\,\mathrm{d}\alpha\right]=1$, the same is true for $g(r,k)$, more precisely using equations (33) and (I.3):

$$\int_0^\infty|\sigma_k(\alpha)|\,\mathrm{d}\alpha<\frac{C_1}{|k|}\int_0^A\frac{\mathrm{d}\alpha}{\alpha+\mu}+\frac{C_2}{A+\mu},$$

taking $A=|k|$ we see that this goes to zero as fast as $\log|k|/|k|$.

With some precautions, one can extend this treatment to $\varrho_k(\alpha)$: if

$$0\leqslant\operatorname{Im}k\leqslant\frac{\mu}{2}-\varepsilon\,,\qquad|\alpha+\mu+2ik|\,|\alpha+\mu|>(\alpha+\varepsilon)^2\,.$$

In this domain the existence and analyticity of $f(r,k)$ are established in the same way as for $g(r,k)$.

If

$$\varepsilon\leqslant|\operatorname{Arg}-ik|\leqslant\frac{\pi}{2}\,,$$

$$|(\alpha+\mu)(\alpha+\mu+2ik)|\geqslant|\alpha+\mu|^2\,|\sin\varepsilon|\,.$$

So we have only to replace in inequality (I.1) $|V_0|$ by $|V_0/\sin\varepsilon|$ and the holomorphy of $f(r,k)$ is established. In the same way, one can also, using

$$|(\alpha+\mu)(\alpha+\mu+2ik)|>2\,|\alpha+\mu|\,|k|\,|\sin\varepsilon|\,,$$

show that

$$\int_0^\infty|\varrho_k(\alpha)|\,\mathrm{d}\alpha\to0\,,$$

as fast as $\log|k|/|k|$ when $|k|\to\infty$.

The above conditions define a domain which does not contain the cut, and does not give the behaviour of $f(r,k)$ for $\operatorname{Im}k\to+\infty$, $\operatorname{Re}k$ finite. One has to be more careful:

$$|\varrho_k(\alpha)|<\frac{2\,|V_0|\,M}{(\alpha+\mu)\,[\,|\alpha+\mu-2\operatorname{Im}k|+2\,|\operatorname{Re}k|\,]}\left[1+\int_0^\alpha|\varrho_k(\gamma)|\,\mathrm{d}\gamma\right].$$

From this one can show that

$$[1-\psi(\alpha_1,k)]\leqslant\frac{1+\int_0^{\alpha_1}|\varrho_k(\alpha)|\,\mathrm{d}\alpha}{1+\int_0^\infty|\varrho_k(\alpha)|\,\mathrm{d}\alpha}\,,$$

with $\alpha_1 < 2 \operatorname{Im} k - \mu$ and

$$\psi(\alpha_1 k) = |V_0| M \left(\frac{1}{\operatorname{Im} k + \operatorname{Re} k} \log \frac{\operatorname{Re} k}{\operatorname{Im} k} \frac{2(\operatorname{Re} k + \operatorname{Im} k) - \alpha_1 - \mu}{\alpha_1 + \mu} + \right.$$

$$\left. + \frac{1}{\operatorname{Im} k - \operatorname{Re} k} \log \frac{\operatorname{Im} k}{\operatorname{Re} k} \right) .$$

For fixed α_1, provided $\operatorname{Re} k > C [\operatorname{Im} k]^{-n}$ (n arbitrary), one can make $|\psi(\alpha_1, k)|$ arbitrarily small by taking $\operatorname{Im} k$ large enough. Since

$$\lim_{\operatorname{Im} k \to +\infty} \int_0^{\alpha_1} \varrho_k(\alpha) \, \mathrm{d}\alpha = 0 ,$$

the only possibility is

$$\lim_{\operatorname{Im} k \to +\infty} \int_0^{\infty} |\varrho_k(\alpha)| \, \mathrm{d}\alpha = 0 .$$

Existence of a limit of $f(r, k)$ along the cut.

Assume first

$$|C(\alpha) - C(\beta)| < B(\alpha - \beta); \tag{34}$$

take first

$$\alpha_0 = 2 \operatorname{Im} k - \mu > 0 ,$$

$$\varrho_k(\alpha)[\alpha + \mu][\alpha - \alpha_0 + 2i \operatorname{Re} k] = V_0 [C(\alpha) + \int_0^{\alpha - \mu} C(\alpha - \mu - \beta) \, \varrho_k(\alpha) \, \mathrm{d}\alpha ;$$

$\lim \varrho_k(\alpha)$ exists for $\alpha < \alpha_0$. Near $\alpha = \alpha_0$

$$\varrho_k(\alpha) \simeq \varphi(\alpha_0)[\alpha - \alpha_0 + 2i \operatorname{Re} k]^{-1} ,$$

with

$$\varphi(\alpha) = \frac{V_0 [C(\alpha) + \int_0^{\alpha - \mu} C(\alpha - \mu - \beta) \, \varrho_k(\beta) \, \mathrm{d}\beta]}{\alpha + \mu} .$$

If $C(\alpha)$ satisfies condition (34), which contains $C(0) = 0$, $\lim \varrho_k(\alpha)$ is well defined for $\alpha > \alpha_0$ because the limit of the integral is well defined. We have now to investigate the convergence for large α:

3326

for $\alpha > \alpha_0 + \mu$

$$|\varrho_k(\alpha)| < \frac{1}{|\alpha - \alpha_0|^2} V_0 \Big[M + M \int_0^{\alpha_0 - \Delta} |\varrho_k(\beta)|\,\mathrm{d}\beta + M \int_{\alpha_0 + \Delta}^{\alpha - \mu} |\varrho_k(\beta)\mathrm{d}\beta + M \int_{\alpha_0 - \Delta}^{\alpha_0 + \mu} \varrho_k(\beta)\,\mathrm{d}\beta + 2\Delta \cdot B \cdot \max_{\alpha_0 - \Delta}^{\alpha_0 + \Delta} |\varphi(\beta)| \Big] = \frac{1}{|\alpha - \alpha_0|^2} \Big[C_1 + C_2 \int_{\alpha_0 + \Delta}^{\alpha - \Delta} |\varrho_k(\beta)|\,\mathrm{d}\beta \Big] .$$

Then one can easily establish the convergence of

$$\int_{\alpha_0 + \Delta}^{\infty} |\varrho_k(\alpha)|\,\mathrm{d}\alpha ,$$

as was done outside the cut. If $\alpha_0 = 0$, *i.e.* $2 \operatorname{Im} k = \mu$, we get a logarithmic singularity in

$$\int_{\blacksquare}^{\infty} |\varrho_k(\alpha)|\,\mathrm{d}\alpha ,$$

when $\operatorname{Re} k \to 0$.

We now treat the Yukawa case ($C(\alpha) = 1$ for $\alpha > 0$). We have the same logarithmic singularity at $\alpha_0 = 0$, $2 \operatorname{Im} k = \mu$. The trouble is now that in addition to the pole $\alpha = \alpha_0$, we have a new singularity when the singularity of $\varrho(\beta)$ happens to be at the upper limit of the integral defining $\varrho(\alpha)$ for $\alpha > \alpha_0$:

$$\varrho_k(\alpha)[\alpha + \mu][\alpha - \alpha_0 + 2i \operatorname{Re} k] = V_0 \Big[1 + \int_0^{\alpha - \mu} \varrho_k(\beta)\,\mathrm{d}\beta \Big] .$$

This happens for $\alpha = \alpha_0 + \mu$. Fortunately this new singularity is a logarithmic singularity, so that the integral

$$\int_{\blacksquare}^{\alpha - \mu} \varrho_k(\beta)\,\mathrm{d}\beta ,$$

is still well defined for $\alpha \geqslant \alpha_0 + 2\mu$. Then, using the inequality

$$|\varrho_k(\alpha)| < \frac{V_0}{|\alpha - \alpha_0|^2} \Big[1 + \Big| \int_0^{\alpha_0 + 2\mu} \varrho_k(\beta)\,\mathrm{d}\beta \Big| + \int_{\alpha_0 + 2\mu}^{\alpha - \mu} |\varrho_k(\beta)|\,\mathrm{d}\beta \Big] ,$$

one can prove the existence of $\lim_{\operatorname{Re} k \to 0} f(r, k)$.

Appendix II

Sufficient condition for the absence of zeros of g in the upper half plane.

A sufficient condition for this is

$$\int_0^\infty \sum(\alpha)\,\mathrm{d}\alpha < 1\,.$$

Then

$$1 + \exp[-\mu r]\int_0^\infty \sigma_k(\alpha)\exp[-\alpha r]\,\mathrm{d}\alpha\,,$$

can never vanish. From (I.2) one can show that

$$1+\int_0^\infty \sum(\alpha)\,\mathrm{d}\alpha < \frac{1+\int_0^{n\mu}\sum(\alpha)\,\mathrm{d}\alpha}{1-\dfrac{|V_0|\,M}{(n+1)\mu}}\,.$$

$\int_0^{n\mu}\sum(\alpha)\,\mathrm{d}\alpha$ can be computed exactly. With $n=0$ we get

$$|V_0|\,M < \frac{\mu}{2}\,;$$

$n=1$ gives

$$|V_0|\,M < \frac{2\mu}{3}\,.$$

This could be still slightly improved, but not much because $M|V_0| = \mu$ gives

$$\int_0^\infty \sum(\alpha)\,\mathrm{d}\alpha > 1\,.$$

Appendix III

Numerical use of equations (33).

We look on equations (33) at the bound state at zero energy. This gives

$$1+\int_0^\infty \sigma_0(\alpha)\,\mathrm{d}\alpha = 0\,,$$

with

$$\sigma_0(\alpha)[\alpha+\mu]^2 = -V_0\left[1+\int_0^{\alpha-\mu}\sigma_0(\gamma)\,\mathrm{d}\gamma\right].$$

3328

If we take as a first approximation

$$1+\int_0^{\infty}\sigma_0(\alpha)\,\mathrm{d}\alpha \simeq 1+\int_0^{\mu}\sigma_0(\alpha)\,\mathrm{d}\alpha\,,$$

we get

$$1-\frac{|V_0|}{2\mu}=0\,, \qquad \frac{\mu}{|V_0|}=0.5\,.$$

The second approximation

$$1+\int_0^{2\mu}\sigma_0(\alpha)\,\mathrm{d}\alpha=0\,,$$

gives

$$1-\frac{V_0}{2\mu}-\frac{V_0}{6\mu}+\left|\frac{V_0}{\mu}\right|^2\left[\frac{1}{3}-\log\frac{4}{3}\right]=0\,,$$

and

$$\frac{\mu}{|V_0|}=0.595.$$

The exact result ([16]) is 0.5953.

([16]) J. Blatt and V. Weisskopf: *Theoretical Nuclear Physics* (London, 1952), p. 56.

RIASSUNTO (*)

Prendendo le mosse dalle proprietà della soluzione radiale dell'equazione di Schrödinger per una energia complessa, si studiano le proprietà analitiche dell'ampiezza di diffusione per una data onda parziale. Si ristabiliscono con questo metodo i risultati conosciuti nel caso dei potenziali a portata finita. Si esaminano quindi, limitandosi all'onda S, le proprietà analitiche di potenziali esponenzialmente decrescenti. Si ritrova in tal modo una banda di analiticità comune a tutti questi potenziali. Si prendono in esame, in maniera completa, due esempi: il caso di un potenziale prodotto di una funzione esponenziale per una funzione sinusoidale, ed il caso di una famiglia abbastanza generale di potenziali comprendenti, in particolare, il potenziale di Yukawa e una somma di potenziali di Yukawa. Si ottiene il comportamento all'infinito dell'ampiezza di diffusione, ed è possibile scrivere una relazione di dispersione per questa quantità. Sotto condizioni più restrittive si può scrivere una relazione di dispersione per una quantità connessa alla funzione d'onda ad una distanza r dall'origine. Il metodo impiegato per valutare l'ampiezza di diffusione sembra costituire, oltretutto, un metodo pratico di valida approssimazione.

(*) *Traduzione a cura della Redazione.*

IL NUOVO CIMENTO Vol. XIV, N. 2 16 Ottobre 1959

On the Existence of the Hypernucleus $^6He_\Lambda$.

L. H. Schick

University of Colorado - Boulder, Colo.

(ricevuto il 2 Luglio 1959)

Summary. — Hypernuclei have been observed for all $2 < A \leqslant 9$ with the exception of $A = 6$. The lack of observation of both $^6He_\Lambda$ and $^6Li_\Lambda$ implies that the binding energies of these hypernuclei either are negative, or are positive but less than that of $^5He_\Lambda$ so that if formed they decay immediately into $^5He_\Lambda$+nucleon, or are greater than that of $^5He_\Lambda$ in which case their ultimate observation would be expected. The $^6He_\Lambda$ hypernucleus is analyzed to determine in which of these three regions its binding energy lies. This analysis is carried out under the assumption that $^6He_\Lambda$ is a bound system, Λ+(neutron+α). A variation calculation using phenomenological potentials yields a lower bound of (2.00±0.60) MeV for the total binding energy of $^6He_\Lambda$. This indicates that both $^6He_\Lambda$ and $^6Li_\Lambda$ are unstable against decay into $^5He_\Lambda$+nucleon and are therefore not expected to be observed.

1. – Introduction.

Observations of hypernuclei have been reported for all mass numbers A up to and including $A = 9$ with the exceptions of $A = 2$ and $A = 6$ (1). Theoretically there is reason to believe that the hypernucleus with $A = 2$ (hyperdeuteron) is not bound (2). For $A = 6$ neither member of the $^6He_\Lambda$-$^6Li_\Lambda$ isospin

(1) R. Levi Setti, W. E. Slater and V. L. Telegdi: *Proc. of the Seventh Annual Rochester Conference on High-Energy Physics*, vol. **7** (New York, 1957), Sect. **8**, p. 6. Recently, F. Breivik, O. Skjeggestad and S. O. Sorensen (*Nuovo Cimento*, to be published) have observed an event which they interpret as a mesonic decay, possibly of $^6He_\Lambda$.

(2) B. W. Downs and R. H. Dalitz: *Phys. Rev.*: to be published. (See also R. H. Dalitz and B. W. Downs: *Phys. Rev.*, **110**, 958 (1958) and other references) cited there.

doublet has been observed so that the binding energies for these two hypernuclei are missing from the data. For either member of this doublet there are three possible explanations for this lack of observation: The hypernucleus in question 1) is not bound; 2) is bound but with a binding energy less than that of the relatively high binding energy of the $^5He_\Lambda$ hypernucleus ([3]) and hence decays immediately into $^5He_\Lambda$ + a nucleon; 3) has a binding energy greater than that of $^5He_\Lambda$, but so far it has escaped detection. A theoretical analysis of at least one member of this doublet to determine which of the above three statements is true seems altogether worthwhile. Because of the complication arising from the additional Coulomb interaction which is present in $^6Li_\Lambda$, it is more favorable to perform such an analysis for $^6He_\Lambda$. It is the purpose of this paper then to analyze the $^6He_\Lambda$ hypernucleus with the aim of determining in which of the above mentioned regions its binding energy lies and infer from this the corresponding information for $^6Li_\Lambda$.

To this end it is assumed that the interaction of the Λ-particle with the five nucleons is strong enough to allow the $^6He_\Lambda$ system to form a bound state. Furthermore this system will be treated as a two-body system. From a physical standpoint the most reasonable two-body approach would be to consider $^6He_\Lambda$ as $^5He_\Lambda$+neutron. In this case, however, it is not at all clear what the form of the odd-neutron wave function should be. Thus the two-body approach taken here will be that of « ^{5}He »+Λ. (In this analysis the notation « ^{5}He » is used to denote tha α-particle—odd neutron part of the system with a bound state trial function, rather than a scattering state function, for the odd neutron.) Since in $^5He_\Lambda$ the presence of the Λ does not appreciably distort the α-particle—at least as far as a radial compression is concerned ([3])—it is assumed that in $^6He_\Lambda$ the presence of the Λ does not alter the neutron—α-particle potential. Hence it is not unreasonable to take the odd neutron in a $p_{\frac{3}{2}}$ state with respect to the center of mass of the neutron—α-particle part of the system. Further, since the state of the Λ is not restricted by the Pauli principle, the Λ is taken to be in an s state with respect to the center of mass of ^{5}He. Because of calculational difficulties which would arise from the use of direct Λ-neutron and Λ-α particle correlations, no such correlations were included in the wave function for the system.

This treatment of $^6He_\Lambda$ is similar to SUH's ([4]) work on $^9Be_\Lambda$ in that both deal with a hypernucleus which has the form Λ+(unbound system). In the case of $^9Be_\Lambda$ the relatively large binding energy of the Λ to each of the α-particles in ^{8}Be easily overcomes the weak ($\sim$ 100 keV resonance) α-α instability. For $^6He_\Lambda$ however, it is not at all certain that the Λ-α binding will compen-

([3]) R. H. DALITZ and B. W. DOWNS: *Phys. Rev.*, **111**, 967 (1958).
([4]) K. S. SUH: *Phys. Rev.*, **111**, 941 (1958).

3331

sate for the α-neutron (~ 1 MeV $p_{\frac{3}{2}}$ resonance) and the Λ-neutron instabilities so as to bind the odd neutron. On the other hand, on the basis of the work of FESHBACH and RUBINOW [5] it can be expected that the binding energy of ${}^6\mathrm{He}_\Lambda$ should be greater than the sum of the α-neutron, α-Λ, and Λ-neutron binding energies. Thus, the stability of ${}^6\mathrm{He}_\Lambda$ against decay into neutron$+{}^5\mathrm{He}_\Lambda$ depends on the relative importance of the two above effects.

The two-body problem $\Lambda+{}^5\mathrm{He}$ will be solved by a variation calculation. The results of the numerical integration needed in this calculation are taken over directly from those of DALITZ and DOWNS [3] as are the form and shape of the Λ-nucleon potential. This spin-dependent potential has the form [6]

$$V_{\Lambda-n}=\frac{3+\boldsymbol{\sigma}_\Lambda\cdot\boldsymbol{\sigma}}{4}V_p+\frac{1-\boldsymbol{\sigma}_\Lambda\cdot\boldsymbol{\sigma}}{4}V_a\,, \tag{1}$$

where $\boldsymbol{\sigma}_\Lambda$ and $\boldsymbol{\sigma}$ are the Pauli spin matrices for the Λ and the nucleon respectively, and V_a and V_p denote the singlet and triplet interactions respectively. The shape $v(r)$ of the V_p and V_a—taken to be Gaussian for calculational convenience [7]—is given by

$$v(r)=\left(\frac{1.4354}{\pi^{\frac{1}{2}}b}\right)^3\exp\left[-r^2\right]\left(\frac{1.4354}{b}\right)^2, \tag{2}$$

where b, the intrinsic range of the potential, is taken here to correspond to one-half the π-meson Compton wavelength [8].

2. – Details of the calculation.

The Hamiltonian for the system is taken to include only two potentials: $V_{n\ \alpha}(\boldsymbol{r}')$, the potential between the odd neutron and the α-particle, and $V_{\Lambda-{}^5\mathrm{He}}(\boldsymbol{r})$, the average potential that the Λ moves in due to its interaction with the five nucleons. The vectors $\boldsymbol{r}'$ and $\boldsymbol{r}$ extend from the α-particle to the odd neutron and from the Λ to the ${}^5\mathrm{He}$ center of mass, respectively. The

---

[5] H. FESHBACH and S. I. RUBINOW: *Phys. Rev.*, **98**, 188 (1955).

[6] The spin of the Λ is generally accepted to be $\frac{1}{2}$ and it is taken to be so here.

[7] In reference [3] it is pointed out that the details of the shape of the potential are relatively unimportant and that it is the R.M.S. radius which is the determining feature so far as the Λ binding energy is concerned.

[8] See Sect. **1** of reference [3] for a discussion of the possible ranges — and their interpretations — of the Λ-nucleon interaction.

333

trial wave function for the system is taken to be of the form [9] $\psi = \varphi_\Lambda(\boldsymbol{r})\,\varphi_n(\boldsymbol{r}')$ where $\varphi_\Lambda(\boldsymbol{r})$ is the wave function for the Λ and $\varphi_n(\boldsymbol{r}')$ is the wave function for the odd neutron (which is taken to include the coupled spins of the $p_{\frac{3}{2}}$ neutron and the s-state Λ). With this Hamiltonian and trial wave function the Schrödinger equation for the system separates into the two equations

$$\left\{-\frac{\hbar^2}{2\mu_\Lambda}\nabla_r^2 + V_{\Lambda-^5He}(\boldsymbol{r}) + B_{\Lambda-^5He}\right\}\varphi_\Lambda(r) = 0\,, \tag{3}$$

$$\left\{-\frac{\hbar^2}{2\mu_n}\nabla_{r'}^2 + V_{n-\alpha}(\boldsymbol{r}') + B_{n-\alpha}\right\}\varphi_n(\boldsymbol{r}') = 0\,. \tag{4}$$

Here $B_{\Lambda-^5He}$ and $B_{n-\alpha}$ can be considered to be the respective binding energies of the Λ-^{5}He and neutron-α particle parts of the system. The two corresponding reduced masses are $\mu_\Lambda = M_\Lambda(M_\alpha+M_n)/(M_\Lambda+M_\alpha+M_n)$ and $\mu_n = M_n M_\alpha/(M_n+M_\alpha)$, where M_n, M_α, and M_Λ are the neutron, α-particle, and Λ masses, respectively. A variation treatment of Eqs. (3) and (4) gives $B_{\Lambda-^5He}$ and $B_{n-\alpha}$ as functions of the variation parameter. By construction, the result of adding these two functions and maximizing the sum with respect to the variation parameter gives a lower bound for the total binding energy B of $^6He_\Lambda$,

$$B \geqslant [B_{\Lambda-^5He} + B_{n-\alpha}]_{Max}\,. \tag{5}$$

To solve Eq. (3) it is first necessary to choose a potential $V_{\Lambda-^5He}(\boldsymbol{r})$. With the use of Eqs. (1) and (2) this potential can be written [10]

$$V_{\Lambda-^5He}(\boldsymbol{r}) = -U_5\int v(|\boldsymbol{r}-\boldsymbol{r}'|)\,\varrho(r'/R_5)\,d\boldsymbol{r}'\,, \tag{6}$$

where $\varrho(r'/R_5)$ is the nucleon distribution in the ^{5}He « core » and R_5 is the R.M.S. radius of the distribution. With $v(|\boldsymbol{r}-\boldsymbol{r}'|)$ normalized to unity, U_5 is the volume integral of all the Λ-nucleon interactions of the spin state of the system.

In order to choose the nucleon distribution, the four nucleons in the α-particle are taken to be in s states, the odd neutron in a $p_{\frac{3}{2}}$ state, and the Λ in an s state, all with respect to the center of mass of ^{5}He. Furthermore, the Λ-nucleon singlet interaction is taken to be more attractive than the corres-

---

[9] The motion of the $^6He_\Lambda$ c.m. is of no interest. Hence it has been separated out of the calculation at the start.

[10] See reference [3], Sect. 2.

ponding triplet interaction ([11]) so that the odd nucleon couples to the Λ to form a total angular momentum state $J=1$. Under these assumptions the nucleon distribution about the ^{5}He center of mass—normalized to unity and again with Gaussian shapes for convenience—is given by

$$\varrho(\boldsymbol{r}') = \frac{4}{5}\left(\frac{\alpha}{\pi^{\frac{1}{2}}}\right)^3 \exp\left[-(\alpha r')^2\right] + \frac{2}{15}\left(\frac{\beta}{\pi^{\frac{1}{2}}}\right)^3 (\beta r')^2 \exp\left[-(\beta r')^2\right], \tag{7}$$

where the term on the left corresponds to the s state nucleons, the term on the right corresponds to the p state nucleon ([12]), and α and β are parameters to be determined. It is easily seen that this expression along with Eqs. (2) and (6) leads to a non-Gaussian form for $V_{\Lambda-^5\mathrm{He}}(\boldsymbol{r})$. In order to utilize the results of DALITZ and DOWNS ([3]) for the numerical integration of Eq. (3), the nucleon distribution given by Eq. (7) is replaced by a Gaussian distribution, $\varrho(r'/R_5)$, of the same R.M.S. radius, R_5 ([7]),

$$\varrho(r'/R_5) = \left(\frac{3}{2\pi R_5^2}\right)^{\frac{3}{2}} \exp\left[-3r'^2/2R_5^2\right], \tag{8}$$

with

$$R_5^2 = \frac{6}{5\alpha^2} + \frac{1}{2\beta^2}. \tag{9}$$

At this point the parameter α can be evaluated. From Eq. (7) the mean square radius of the α-particle is given by $R_4^2 = 3/2\alpha^2$. Hence from Eq. (9)

$$R_5^2 = \frac{4}{5}R_4^2 + \frac{1}{2\beta^2}. \tag{10}$$

With a Gaussian shape for the nucleon distribution $\varrho(r/R_4)$ for an α-particle the results of the Stanford experiments can be well fit with $R_4 = (1.44 \pm 0.07)$ fermi, ([3]) (1 fermi (f) $= 10^{-13}$ cm).

([11]) R. H. DALITZ: *Phys. Rev.*, **112**, 605 (1958). See also reference ([3]) and M. LEON: *Phys. Rev.*, **113**, 1604 (1959). R. H. DALITZ and L. LIU: *Phys. Rev.* (to be published) have recently shown that the conclusion that the singlet interaction is more attractive than the triplet is not so strong as the preceeding references indicate.

([12]) The $p_{\frac{3}{2}}$ neutron and the s-state Λ are coupled to form the state $\Phi^m_{J=1}$. However, the quantum number m plays no role in this problem. Thus to simplify the integrations later on in the calculations the factor $|\Phi^m_{J=1}|^2$ which should appear in the right-hand term of Eq. (7) was replaced by $\frac{1}{3}\sum_{m=-1}^{1} |\Phi^m_{J=1}|^2$ which is spherically symmetric. This substitution was made throughout the calculation.

Equations (2), (6), and (8) now yield

$$V_{\Lambda-^5He}(r) = -U_5\left(\frac{1.4354}{\pi^{\frac{1}{2}}b'}\right)^3 \exp\left[-\left(\frac{1.4354}{b'}r\right)^2\right], \tag{11}$$

where

$$b' = [b^2 + (1.373\,6)R_5^2]^{\frac{1}{2}}. \tag{12}$$

The volume integral U_5 can be evaluated in a straightforward manner to give

$$\begin{cases} U_5 = (3U_p + U_a) + \frac{1}{3}(2U_a + U_p) \\ \quad = \frac{5}{3}(2U_p + U_a), \end{cases} \tag{13}$$

where the parenthesis on the left in the first line contains just the Λ-α particle volume integral while the second term is the volume integral for the Λ interacting with the $p_{\frac{3}{2}}$-state neutron ([3]), with U_p and U_a being the Λ-nucleon volume integrals for the triplet and singlet states, respectively. The numerical values of U_p and U_a have been calculated by DALITZ and DOWNS ([2,3]) from U_4 and U_2 the volume integrals for $^5He_\Lambda$ and $^3H_\Lambda$. These in turn were derived from the experimental values for the binding energies of $^5He_\Lambda$ and $^3H_\Lambda$ respectively ([13]). These values are

$$B_{^5He_\Lambda} = (2.9 \pm 0.3)\ \text{MeV}, \qquad B_{^3H_\Lambda} = (0.6 \pm 0.4)\ \text{MeV},$$

$$U_4 = 3U_p + U_a = 925(\pm 22)\ \text{MeV f}^3, \tag{14a}$$

$$U_2 = \tfrac{3}{2}U_a + \tfrac{1}{2}U_p = 667(\pm 52)\ \text{MeV f}^3, \tag{14b}$$

where the error in U_4 is just that due to the statistical error in $B_{^5He_\Lambda}$. Although U_4 is sensitive to the uncertainty in R_4, the results of this paper are not. The uncertainty in U_2 is arrived at as described in reference ([2]).

With the Λ in an s state the numerical integration of Eq. (3) yields $B_{\Lambda-^5He}$ as a function of β.

([13]) The value of U_4 given above is for an undistorted α-particle. Although DALITZ and DOWNS ([3]) have calculated that U_4 is optimum for a 3% radial compression of the α-particle, an undistorted α-particle was considered here since it was not known how this distortion would affect the α-neutron potential.

3335

Eq. (4) is solved by a straightforward variation calculation. The wave function $\varphi_n(\boldsymbol{r}')$ is chosen so as to yield the same distribution as the term on the extreme right of Eq. (7). The neutron-α particle potential, $V_{n-\alpha}(r')$, is taken to be that given by SACK, BIEDENHARN, and BREIT [14] for the $p_{\frac{3}{2}}$ neutron on the basis of a best fit to the proton-α particle low energy resonance scattering data.

$$V_{n-\alpha}(r') = -A\left(1+\frac{2\beta'}{a^2}\right)\exp[-r'^2/a^2], \tag{15}$$

where the first term is a central potential only and the second is the $\boldsymbol{L}\cdot\boldsymbol{\sigma}$ term for a $p_{\frac{3}{2}}$ state; $A = 47.32$ MeV, $a = 2.30$ fermi, and $\beta' = 7.40(\hbar/M_n c)^2$. The variation calculation then yields

$$B_{n-\alpha} \geqslant -64.90\beta^{*2} + \frac{53.16\beta^{*5}}{[\beta^{*2}+1/a^2]^{\frac{5}{2}}}, \tag{16}$$

where $\beta^* = [M_\alpha/(M_\alpha + M_n)]\beta$, the mass factor arising from the choice of the neutron being in a p state with respect to the ^{5}He center of mass. Eq. (16) is the desired relation between $B_{n-\alpha}$ and β.

3. – Results.

Addition of the two curves $B_{\Lambda-{}^5\mathrm{He}}(\beta)$ given by the results of the numerical integration of Eq. (3), and $B_{n-\alpha}(\beta)$, given by Eq. (16), and maximization of the sum with respect to the variation parameter β yields (*)

$$B \geqslant (2.00 \pm 0.60)\ \mathrm{MeV} \quad \text{for} \quad \beta^{-1} = (1.50 \pm 0.02)\ \mathrm{f}, \tag{17}$$

where the upper and lower bounds here correspond to the upper and lower bounds, respectively, for U_4 and U_2 in Eq. (14). Since the limits on U_4 are based upon $B_{{}^5\mathrm{He}\Lambda} = (2.90 \pm 0.3)$ MeV, it follows from Eq. (17) that $B_n \equiv B -$

---

(14) S. SACK, L. C. BIEDERNHARN and G. BREIT: *Phys. Rev.*, **93**, 321 (1954).

(*) *Note added in proof.* - If in contrast to what was assumed, the Λ-nucleon interaction is such that $U_p > U_a$, U_5 would be given by $U_5 = U_4 + (U_2/2)$. This value of U_5 is only 1.5% larger than that used above; too small a change to alter the result $B < 2.9$ MeV.

$-B_{^5He_\Lambda}$ is given by [15]

$$B_n \geqslant (-0.90 \pm 0{,}30)\ \text{MeV}\,. \tag{18}$$

Therefore, since the $p_{\frac{3}{2}}$ resonance level of ^5He is 0.95 MeV [16], so far as the neutron is concerned, the presence of the Λ provides (0.05 ± 0.30) MeV more binding than the α-particle alone would provide. On the basis of a simple model (square well plus rectangular barrier) and the most probable value of B, the mean lifetime of $^6He_\Lambda$ (assuming it was somehow formed in the first place) before decay into $^5He_\Lambda$+neutron was estimated to be less than 10^{-19} s, far too short to be observed.

One defect of the above calculation is its sensitivity to the parameters in the α-neutron potential. For example, a change of only 6.2% in the depth parameter A would make the most probable value of B just equal to $B_{^5He_\Lambda}$. This is not too serious a fault however, since on the basis of a square well model a 6% change in the depth would lower the $p_{\frac{3}{2}}$ resonance level to less than 0.6 MeV. This is in marked disagreement with the observed value of 0.95 MeV [16].

A greater defect is the lack of direct Λ-neutron and Λ-α particle correlations in the trial wave function. Only indirect correlations appear in the trial function through the dependence of the distance between the Λ and the ^5He center of mass on the Λ-α and Λ-neutron interparticle distances. This is analogous to Dalitz and Downs' treatment of $^5He_\Lambda$ with the odd neutron-α particle binding energy here being the counterpart of the α-particle compression energy used in their work. Thus the present work yields the $^6He_\Lambda$ binding energy in comparison to that of $^5He_\Lambda$ only to the accuracy of the value for the volume integral U_4 as derived in reference [3]. It is hoped that the treatment of $^6He_\Lambda$ given here has the same order of accuracy as the treatment of $^5He_\Lambda$ to which it is compared.

Within the limitations of the calculation described above, it is concluded that the binding energy of $^6He_\Lambda$ is positive but not large enough to prevent

---

[15] A 3-body approach in which $^6He_\Lambda$ was considered as $\alpha+\Lambda+n$ was also tried. In this case a variation calculation was performed using $V_{n-\alpha}$ and $V_{n-\Lambda}$ as given above with $V_{\Lambda-\alpha}$ taken from reference [3]. Because wave functions involving direct correlations between the Λ and the neutron proved not amenable to analytic treatment, the wave function used for the variation calculation was

$$\psi = \Phi_1^m(1 + \alpha r_n^2)(\beta r_n)^2 \exp\left[-\tfrac{1}{2}\beta^2 r_n^2\right] \exp\left[-\tfrac{1}{2}\gamma^2 r_\Lambda^2\right],$$

where r_n and r_Λ were the α-n and α-Λ interparticle distances and α, β, γ were the variation parameters. This calculation gave $B_n \geqslant -1.95$ MeV. Hence the 2-body calculation was much the preferred one.

[16] F. AJZENBERG and T. LAURITSEN: *Rev. Mod. Phys.*, **27**, 77 (1955).

its immediate decay (assuming it was somehow formed in the first place) into ${}^5\mathrm{He}_\Lambda +$ a neutron. Since the binding energy of ${}^6\mathrm{Li}_\Lambda$ should have a value less by ~ 1 MeV ([3]) than that of ${}^6\mathrm{He}_\Lambda$, an analogous statement can be made for ${}^6\mathrm{Li}_\Lambda$. If the estimate of the goodness ot the trial wave function is correct it is expected that neither member of the ${}^6\mathrm{He}_\Lambda$-${}^6\mathrm{Li}_\Lambda$ isospin doublet should be experimentally observed.

* * *

We wish to thank Dr. B. W. Downs for suggesting this problem and for many enlightening discussions throughout the work.

RIASSUNTO (*)

Sono stati osservati ipernuclei per tutti i $2 < A \leqslant 9$ ad eccezione di $A = 6$. Il non aver osservato ne ${}^6\mathrm{He}_\Lambda$ ne ${}^6\mathrm{Li}_\Lambda$ implica che le energie di legame di questi ipernuclei sono negative o positive ma minori di quella del ${}^5\mathrm{He}_\Lambda$, cosicchè se quegli ipernuclei si formano decadono immediatamente in ${}^5\mathrm{He}_\Lambda +$ nucleone, oppure sono maggiori di quella del ${}^5\mathrm{He}_\Lambda$ nel qual caso ci si aspetterebbe di poterli osservare. Si analizza l'ipernucleo ${}^6\mathrm{He}_\Lambda$ per determinare in quale di queste tre regioni giaccia la sua energia di legame. Tale analisi è condotta nell'ipotesi che il ${}^6\mathrm{He}_\Lambda$ sia un sistema legato $\Lambda +$ (neutrone $+ \alpha$). Un calcolo variazionale usufruendo di potenziali fenomenologici fornisce un limite inferiore di (2 ± 0.60) MeV per l'energia di legame totale del ${}^6\mathrm{He}_\Lambda$. Ciò indica che sia il ${}^6\mathrm{He}_\Lambda$ che il ${}^6\mathrm{Li}_\Lambda$ sono instabili rispetto al decadimento in ${}^5\mathrm{He}_\Lambda +$ nucleone e quindi non ci si può attendere di osservarli.

(*) *Traduzione a cura della Redazione.*

3338

IL NUOVO CIMENTO Vol. XIV, N. 2 16 Ottobre 1959

Adiabatic Passages in Nuclear Magnetic Resonance with the Rotating Co-ordinate Method.

G. Bonera and L. Giulotto

Istituto di Fisica dell'Università - Pavia

(ricevuto il 10 Luglio 1959)

Summary. — The cases of adiabatic passages in nuclear magnetic resonance are studied with the rotating coordinate method. The expressions for the corresponding nuclear signals, already found by Bloch, are rederived by this method. In addition a simple geometrical model, which describes the movement of the nuclear magnetization during a slow passage, is derived.

1. – Introduction.

It is known that by using the rotating co-ordinate system introduced by Rabi, Ramsey and Schwinger [1] it is possible to solve more easily some problems of nuclear magnetic resonance; indeed the movement of the nuclear magnetization is in general more simple with respect to this co-ordinate system than with respect to the laboratory system.

Nevertheless only some particular cases, where the oscillating magnetic field effect and the relaxation effect can be considered separately, have been treated by means of the rotating co-ordinate method.

Cases of this type are that of rapid adiabatic passages [2,1,3] and that of spin echoes [4-6].

---

[1] I. I. Raby, N. F. Ramsey and J. Schwinger: *Rev. Mod. Phys.*, **26**, 167 (1954).
[2] L. Giulotto: *Rend. Semin. Mat. Fis. Milano*, **24**, 41 (1953).
[3] J. G. Powles: *Proc. Phys. Soc.*, **71**, 497 (1958).
[4] E. L. Hahn: *Phys. Rev.*, **80**, 580 (1950).
[5] H. Y. Carr and E. M. Purcell: *Phys. Rev.*, **94**, 630 (1954).
[6] S. Meiboom and D. Gill: *Rev. Sci. Instr.*, **29**, 688 (1958).

3339

In this work we will show that it is possible to apply the rotating co-ordinate method in order to treat easily also the cases where the oscillating magnetic field effect and the relaxation effect are to be considered simultaneously. More precisely we will reconsider the cases analyzed by BLOCH in his first paper on nuclear induction ([7]), and we will show that they are in general resolvable in a simple manner by using rotating co-ordinates without starting from his famous equations which are related to the laboratory system.

This manner of treating the problem presents the advantage of giving a modellistic picture of the behavior of the nuclear magnetization during an adiabatic passage through resonance.

2. – The slow adiabatic passage with the rotating coordinate method.

Let us consider an assembly of identical atomic nuclei having gyromagnetic ratio γ, and let us submit them to a constant magnetic field $\boldsymbol{H}_0$ directed along the z axis, and to a small magnetic field $\boldsymbol{H}_1$ rotating in the xy plane with angular speed $\boldsymbol{\omega}$ in the same sense of the Larmor precession.

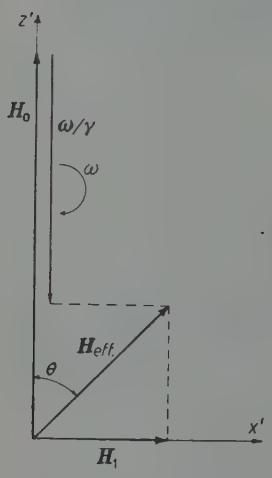

Fig. 1. – The effective magnetic field in the rotating co-ordinate system.

Let us refer to the rotating system, that is to a system of cartesian axes x', y', z' ($z' \equiv z$) rotating with the same angular speed as the rotating field $\boldsymbol{H}_1$. With respect to this reference system the field $\boldsymbol{H}_1$ has a fixed direction, perpendicular to z'; we take this direction as the x' axis.

If the relaxation phenomena are negligible and if $\boldsymbol{H}_0$ and $\boldsymbol{\omega}$ are not varying, simple kinematic considerations, which can be justified from a quantum mechanical point of view, show that the movement of the nuclear magnetization $\boldsymbol{M}$ relative to the rotating co-ordinates is the same as we would obtain if there existed only a steady effective magnetic field (see Fig. 1):

$$\boldsymbol{H}_{\text{eff}} = \boldsymbol{H}_0 + \boldsymbol{H}_1 + \boldsymbol{\omega}/\gamma \,, \tag{1}$$

$\boldsymbol{H}_{\text{eff}}$ forms therefore with the z' axis an angle θ given by:

$$\operatorname{tg}\theta = \frac{\gamma H_1}{\Delta\omega} \,, \tag{2}$$

being $\Delta\omega = \gamma H_0 - \omega$.

([7]) F. BLOCH: *Phys. Rev.*, **70**, 470 (1946).

3340

The modulus of $\boldsymbol{H}_{\text{eff}}$ is:

$$H_{\text{eff}} = [H_1^2 + (\Delta\omega/\gamma)^2]^{\frac{1}{2}} . \tag{3}$$

In the aforesaid hypothesis the nuclear magnetization $\boldsymbol{M}$ precesses, with respect to the rotating co-ordinates, around $\boldsymbol{H}_{\text{eff}}$ with the angular speed

$$\omega_r = \gamma H_{\text{eff}} = [(\gamma H_1)^2 + \Delta\omega^2]^{\frac{1}{2}} . \tag{4}$$

If we now also consider the relaxation effect, the precessional motion of $\boldsymbol{M}$ around $\boldsymbol{H}_{\text{eff}}$ should be perturbed until an equilibrium situation is reached characterized by the condition that during a small interval of time dt a small rotation of $\boldsymbol{M}$ around $\boldsymbol{H}_{\text{eff}}$ is compensated by a small variation in the opposite sense due to the relaxation effect. Thus in the steady state one would have in the rotating co-ordinate reference:

$$\frac{d\boldsymbol{M}}{dt} = \left(\frac{d\boldsymbol{M}}{dt}\right)_{\text{rot}} + \left(\frac{d\boldsymbol{M}}{dt}\right)_{\text{relax}} = 0 , \tag{5}$$

where $(d\boldsymbol{M}/dt)_{\text{rot}}$ and $(d\boldsymbol{M}/dt)_{\text{relax}}$ represent respectively the variation speeds of the vector $\boldsymbol{M}$ due to the precession around $\boldsymbol{H}_{\text{eff}}$ and due to the relaxation.

Resolving this equation we should find the equilibrium value of the magnetization.

The adiabatic case of slow passage considered by BLOCH is then easily obtained as a succession of equilibrium values.

The vector equation (5) gives the three scalar equations:

$$\begin{cases} \left(\dfrac{dM_{x'}}{dt}\right)_{\text{rot}} - \dfrac{M_{x'}}{T_2} = 0 , \\ \left(\dfrac{dM_{y'}}{dt}\right)_{\text{rot}} - \dfrac{M_{y'}}{T_2} = 0 , \\ \left(\dfrac{dM_{z'}}{dt}\right)_{\text{rot}} + \dfrac{M_0 - M_z}{T_1} = 0 , \end{cases} \tag{6}$$

being M_0 the equilibrium value of the magnetization in absence of the rotating field, T_1 and T_2 respectively the longitudinal and the transversal relaxation time.

In order to find the expressions of $(dM_{x'}/dt)_{\text{rot}}$, $(dM_{y'}/dt)_{\text{rot}}$ and $(dM_{z'}/dt)_{\text{rot}}$ we consider a vector $\boldsymbol{M}$ of constant modulus M which precesses around $\boldsymbol{H}_{\text{eff}}$ with angular speed ω_r. Let us indicate with α the angle formed by $\boldsymbol{M}$ with

$\boldsymbol{H}_{\text{eff}}$; with $\omega_r t$ the angle that the plane determined by $\boldsymbol{H}_{\text{eff}}$ and by $\boldsymbol{M}$ forms with the $x'z'$ plane; with β the angle that $\boldsymbol{M}$ forms with z' and with φ the angle that the plane $\boldsymbol{M}z'$ forms with the plane $x'z'$ (see Fig. 2).

Using some relations of spherical trigonometry, the components of $\boldsymbol{M}$ relative to the axes are then given by:

$$(7)\qquad \begin{cases} M_{x'} = M \sin\beta \cos\varphi = M[\cos\alpha \sin\theta - \cos\theta \sin\alpha \cos\omega_r t], \\ M_{y'} = M \sin\beta \sin\varphi = M \sin\alpha \sin\omega_r t, \\ M_{z'} = M \cos\beta = M[\cos\theta \cos\alpha + \sin\theta \sin\alpha \cos\omega_r t]. \end{cases}$$

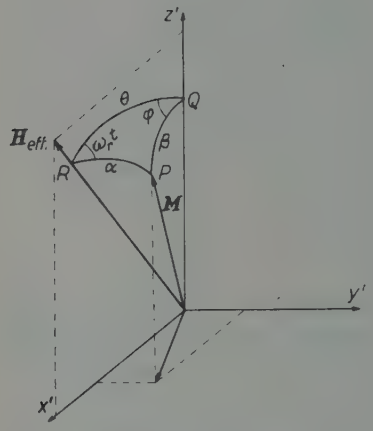

Fig. 2. – The nuclear magnetization $\boldsymbol{M}$ in the rotating co-ordinate system.

From these equations we obtain:

$$(8)\qquad \begin{cases} \left(\dfrac{\mathrm{d}M_{x'}}{\mathrm{d}t}\right)_{\text{rot}} = \omega_r M \cos\theta \sin\alpha \sin\omega_r t, \\ \left(\dfrac{\mathrm{d}M_{y'}}{\mathrm{d}t}\right)_{\text{rot}} = \omega_r M \sin\alpha \cos\omega_r t, \\ \left(\dfrac{\mathrm{d}M_{z'}}{\mathrm{d}t}\right)_{\text{rot}} = -\omega_r M \sin\alpha \sin\theta \sin\omega_r t. \end{cases}$$

Substituting in (6) the values of $M_{x'}$, $M_{y'}$, $M_{z'}$ and of $(\mathrm{d}M_{x'}/\mathrm{d}t)_{\text{rot}}$, $(\mathrm{d}M_{y'}/\mathrm{d}t)_{\text{rot}}$ and $(\mathrm{d}M_{z'}/\mathrm{d}t)_{\text{r.t}}$ given by (7) and (8) and indicating with Ω the equilibrium value of $\omega_r t$ we obtain immediately:

$$(9a)\qquad \operatorname{tg}\Omega = T_2[(\gamma H_1)^2 + \Delta\omega^2]^{\frac{1}{2}},$$

$$(9b)\qquad \operatorname{tg}\alpha = \operatorname{tg}\theta \cos\Omega,$$

$$(9c)\qquad M = M_0 \frac{\cos\Omega}{[(T_1/T_2)\sin^2\Omega + \cos^2\Omega]\sin\alpha \sin\theta + \cos\alpha \cos\theta \cos\Omega}.$$

When the value of $\boldsymbol{H}_{\text{eff}}$ is known, equations (9) yield the three quantities M, α, Ω which characterize the equilibrium value of $\boldsymbol{M}$.

In order to obtain the equations of slow adiabatic passage, it is then sufficient to vary $\Delta\omega$ from great positive values to great negative values.

If we want now to obtain from (9) the equations describing the signals for slow adiabatic passage, it is enough to observe that the components of $\boldsymbol{M}$ in phase and out of phase with respect to the field $\boldsymbol{H}_1$ are respectively $M_{x'}$ and $M_{y'}$. From (7) and (9) and from (2) we obtain for the in phase signal u

3342

and for the out of phase signal v the following expressions:

$$(10a) \qquad u = M_{x'} = M[\cos\alpha \sin\theta - \cos\theta \sin\alpha \cos\Omega] = M_0 \frac{\gamma H_1 T_2^2 \Delta\omega}{1 + (T_2\Delta\omega)^2 + (\gamma H_1)^2 T_1 T_2},$$

$$(10b) \qquad v = M_{y'} = M \sin\alpha \sin\Omega = M_0 \frac{\gamma H_1 T_2}{1 + (T_2\Delta\omega)^2 + (\gamma H_1)^2 T_1 T_2},$$

which are coincident with those found by Bloch.

3. – Geometrical picture of the nuclear magnetization motion.

It is now interesting to study the motion of the nuclear magnetization during a slow passage by using equations (9).

From (9*b*) it appears immediately (*) that the spherical triangle PQR (see Fig. 2) determined by $\boldsymbol{M}$, $\boldsymbol{H}_{\text{eff}}$ and the z' axis is right-angled at P.

Multiplying numerator and denominator of (9*c*) by $\cos\theta/\cos\alpha\cos\Omega$ and using (9*a*) and (9*b*) we have:

$$(11) \qquad M = M_0 \frac{\cos\theta/\cos\alpha}{[(T_1/T_2)\sin^2\Omega + \cos^2\Omega]\sin^2\theta + \cos^2\theta}.$$

Since the spherical triangle is right-angled we also have

$$(12a) \qquad \cos\beta = \frac{\cos\theta}{\cos\alpha},$$

$$(12b) \qquad \sin\beta = \sin\theta \sin\Omega.$$

Equation (11) thus becomes:

$$(13) \qquad M = M_0 \frac{\cos\beta}{(T_1/T_2)\sin^2\beta + \cos^2\beta}.$$

Since β is the angle formed by $\boldsymbol{M}$ with the z' axis, (13) is the equation in polar co-ordinates of a rotational ellipsoid. This ellipsoid is tangent to the $x'y'$ plane at the origin, and is obtained by rotating around the z' axis an ellipse

---

(*) It is rather evident also from a physical point of view that the spherical triangle PQR should be right-angled at P. In fact only in this case a small variation of $\boldsymbol{M}$ due to a precession around $\boldsymbol{H}_{\text{eff}}$ can be opposite to a small variation due to relaxation effects.

whose major semiaxis, directed along z', is $M_0/2$ and whose minor semiaxis is $(T_2/T_1)^{\frac{1}{2}}M_0/2$ (see Fig. 3).

Equation (13) shows that the extremity of the vector $\boldsymbol{M}$, which represents the nuclear magnetization, always remains on this ellipsoid during a slow passage. We call therefore this ellipsoid the « equilibrium ellipsoid ».

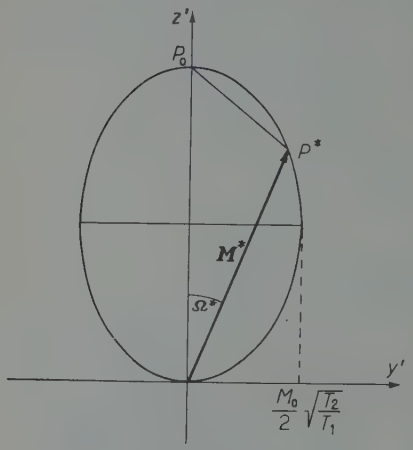

Fig. 3. – Equilibrium ellipsoid intersection with the $y'z'$ plane.

In the case that $T_1 = T_2$ the equilibrium ellipsoid becomes a sphere of diameter M_0 (see Fig. 4).

Let us consider now a particular slow passage, one in which the following conditions are satisfied:

$$\gamma H_1 T_1 \gg 1 \quad \text{and} \quad \gamma H_1 T_2 \gg 1 .$$

From (9*a*) we have then $\Omega = \pi/2$ and from (9*b*) $\alpha = 0$. In such a case during a slow passage the nuclear magnetization is always directed along $\boldsymbol{H}_{\text{eff}}$; it remains therefore always in the $x'z'$ plane and it thus describes during the passage the ellipse given by intersection of the equilibrium ellipsoid with the $x'z'$ plane. In the case $T_1 = T_2$ this ellipse becomes the circle c of Fig. 4.

In order to find the curve that the nuclear magnetization describes on the ellipsoid in the general case of slow passage let us find the position of $\boldsymbol{M}$ in resonance.

In resonance we have $\boldsymbol{H}_{\text{eff}} = \boldsymbol{H}_1$, $\theta = \pi/2$. From (9*b*) one obtains

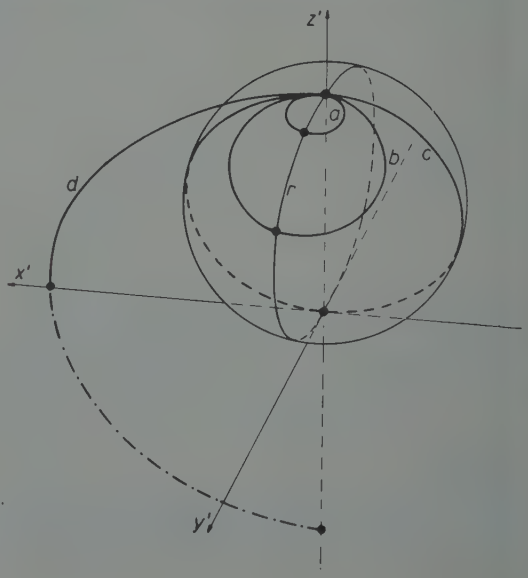

Fig. 4. – In the case $T_1 = T_2$ the equilibrium ellipsoid becomes the sphere shown in the figure. The circles a and b represent two possible paths for the nuclear magnetization during a slow passage through resonance; the circle c is the path described by the nuclear magnetization for $H_1 \gg 1/\gamma T_2$. During a rapid adiabatic passage the nuclear magnetization goes out of the equilibrium sphere and reverses itself describing the semicircle d.

3844

$\alpha = \pi/2$. This means that M lies in the $y'z'$ plane. If we label M^* the equilibrium value of the nuclear magnetization in resonance we have from (9*c*):

$$M^* = M_0 \frac{\cos \Omega^*}{(T_1/T_2) \sin^2 \Omega^* + \cos^2 \Omega^*}, \tag{14}$$

where Ω^* is the value assumed by the angle Ω in resonance. From (12*b*) it results that Ω^* is the angle that $\boldsymbol{M}$ forms with the z' axis in resonance. From (9*a*) we have:

$$\operatorname{tg} \Omega^* = \gamma H_1 T_2 . \tag{15}$$

The direction and the modulus of $\boldsymbol{M}$ in resonance thus depend on the experimental conditions.

By passing from small to large values of $\gamma H_1 T_2$ the angle Ω^* varies from 0 to $\pi/2$ and the extremity P^* of M^* describes in the $y'z'$ plane just half of the ellipse which is the intersection of this plane with the equilibrium ellipsoid (see Fig. 3). In the case $T_1 = T_2$ this ellipse becomes the circle r of Fig. 4.

Let us consider the ellipse we obtain by the intersection of the equilibrium ellipsoid with a plane passing through P_0P^* and perpendicular to the plane of the Fig. 3. During a slow passage the nuclear magnetization describes this ellipse. This is easily seen in the case $T_1 = T_2$. Let us consider indeed the position of the vector $\boldsymbol{M}$ at an arbitrary moment during a slow passage. The extremity P of $\boldsymbol{M}$ should have then the co-ordinates $M \sin\beta \cos\varphi$, $M \sin\beta \sin\varphi$, $M \cos\beta$. With a simple calculation from (12*a*) and (12*b*) one finds:

$$\overline{P_0P}^2 + \overline{PP^*}^2 = \overline{P^*P_0}^2 .$$

This means that during a slow passage the nuclear magnetization describes on the equilibrium sphere a circle of diameter $\overline{P^*P_0}$. The circles a and b of Fig. 4 represent two possible paths of the magnetization during a slow passage in the case $T_1 = T_2$.

With a little more complicated calculation one can show that in the general case $T_1 \neq T_2$ the nuclear magnetization describes on the equilibrium ellipsoid an ellipse of major axis $\overline{P_0P^*}$.

The equilibrium ellipsoid model makes evident some conclusions already found in the first work of BLOCH or easily deducible from it; namely:

1) The symmetry of the dispersion and absorption signals.

2) For very small values of $\boldsymbol{H}_1$ the amplitudes of the absorption signal is twice that of the disperstion signal.

3) For very large values of $\boldsymbol{H}_1$ one has only the dispersion signal.

4) The maximum amplitude of the absorption signal which one can obtain for an appropriate value of H_1 is equal to the maximum amplitude of the dispersion signal that one obtains for very high values of H_1 ($u_{\max\max} = v_{\max\max} = (T_2/T_1)^{\frac{1}{2}} \cdot M_0/2$).

In Fig. 4 is also shown the path of the nuclear magnetization during a rapid adiabatic passage.

As is known, during such a passage the magnetization completely reverses itself, maintaining its modulus unchanged.

Fig. 4 gives therefore a geometrical picture of the cases of the adiabatic passages in nuclear magnetic resonance relative to the rotating frame of reference.

* * *

The authors wish to express their gratefulness to the Office, Chief of Research and Development, U.S. Department of Army, who has sponsored in part this work through its European Office.

RIASSUNTO

I casi dei passaggi adiabatici nella risonanza magnetica nucleare vengono studiati col metodo delle coordinate rotanti. Si trovano così facilmente le espressioni dei corrispondenti segnali nucleari già trovate da Bloch. Inoltre si ricava un semplice modello geometrico che descrive il moto della magnetizzazione nucleare durante un passaggio lento.

LETTERE ALLA REDAZIONE

(La responsabilità scientifica degli scritti inseriti in questa rubrica è completamente lasciata dalla Direzione del periodico ai singoli autori)

Remarks on the Covariant Hamiltonian Formalism for Vectorial Fields.

R. S. Liotta

Istituto di Fisica dell'Università - Roma
Istituto Nazionale di Fisica Nucleare - Sezione di Roma

(ricevuto il 20 Luglio 1959)

In three preceeding papers (1) we have developed a covariant hamiltonian formalism for neutral and charged scalar fields, for spinor fields, and for the electromagnetic field based on the lagrangian

$$L = \frac{1}{2} \frac{\partial A_\mu}{\partial x_\nu} \frac{\partial A_\mu}{\partial x_\nu} .$$

We want now, for the sake of completeness, to apply this formalism to the vectorial meson field and to the electromagnetic field based on the lagrangian

$$L = -\frac{1}{4}\left(\frac{\partial A_\nu}{\partial x_\mu} - \frac{\partial A_\mu}{\partial x_\nu}\right)^2 - \frac{1}{2}\left(\frac{\partial A_\mu}{\partial x_\mu}\right)^2 .$$

It is worth noting that the covariant hamiltonian formalism, which we have developed, is strongly connected to the possibility of reducing the system of equations of motion to the normal form.

On the basis of this remark, it is not essential that the invariant hamiltonian function H be the spur of the canonical tensor, as will be shown below. It must only be such an invariant as to give the equations of motion, of the dynamical system reduced to the normal form, as Hamilton's equations.

(1) R. S. Liotta: *Nuovo Cimento*, **3**, 438 (1956) (in the following referred to as I); *Nuovo Cimento*, **8**, 798 (1958) (referred to as II); *Nuovo Cimento*, **13**, 921 (1959); see references in the above mentioned papers.

1. – Charged vectorial meson field.

Consider the lagrangian [2]

$$L = -\frac{1}{2}\left(\frac{\partial \varphi_\nu^*}{\partial x_\mu} - \frac{\partial \varphi_\mu^*}{\partial x_\nu}\right)\left(\frac{\partial \varphi_\nu}{\partial x_\mu} - \frac{\partial x_\mu}{\partial \varphi_\nu}\right) - \mu^2 \varphi_\nu^* \varphi_\nu \,. \tag{1}$$

From (I, 3), we get for the canonical conjugate momenta to the lagrangian variables φ_μ and φ_μ^*,

$$\varphi_{\mu\nu} = 4\left(\frac{\partial \varphi_\nu^*}{\partial x_\mu} - \frac{\partial \varphi_\mu^*}{\partial x_\nu}\right), \qquad \varphi_{\mu\nu}^* = 4\left(\frac{\partial \varphi_\nu}{\partial x_\mu} - \frac{\partial \varphi_\mu}{\partial x_\nu}\right). \tag{2}$$

From these relations it can be seen that one cannot deduce the $\partial \varphi_\mu / \partial x_\nu$ by means of the $\varphi_{\mu\nu}$: hence one cannot define the spur of the canonical tensor as a function of this type

$$H = H(\varphi_\mu, \varphi_\mu^*, \varphi_{\mu\nu}, \varphi_{\mu\nu}^*) \,,$$

(that is to say, the system cannot be reduced to a normal form). Accordingly one cannot develop the covariant hamiltonian formalism by means of this procedure.

We can however still put the system of equations of motion in a normal form, by letting the scheme remain covariant.

The equations of motion are given by

$$\left.\begin{aligned} &\Box \varphi_\nu - \mu^2 \varphi_\nu = 0 \,, && (3)\\ &\frac{\partial \varphi_\nu}{\partial x_\nu} = 0 \,. && (4) \end{aligned}\right\} \quad \text{and c.c.} \,,$$

When the antisymmetrical tensors

$$f_{\mu\nu} = \frac{\partial \varphi_\nu}{\partial x_\mu} - \frac{\partial \varphi_\mu}{\partial x_\mu} = -f_{\nu\mu} \,, \tag{5}$$ and c.c.,

are introduced, the equations of motion (1), when taking into account the Lorentz condition (2), are written

$$\left.\begin{aligned} &\frac{\partial f_{\mu\nu}}{\partial x_\nu} = -\mu^2 \varphi_\mu \,, && (6)\\ &\frac{\partial \varphi_\mu}{\partial x_\nu} = \frac{\partial \varphi_\nu}{\partial x_\mu} - f_{\mu\nu} \,. && (7) \end{aligned}\right\} \quad \text{and c.c.} \,.$$

If one introduces the invariant

$$H = -\mu^2 \varphi_\mu \varphi_\mu^* + \pi_{\mu\nu}^* \pi_{\mu\nu} \,, \tag{8}$$

---

[2] G. WENTZEL: *Quantum Theory of Fields* (1953).

3348

with

$$\pi_{\mu\nu} = \frac{\partial \varphi_\mu}{\partial x_\nu}, \qquad \pi^*_{\mu\nu} = \frac{\partial \varphi^*_\mu}{\partial x_\nu}, \tag{9}$$

one has:

$$f_{\mu\nu} = \pi_{\nu\mu} - \pi_{\mu\nu}, \qquad \text{and c.c.}, \tag{10}$$

and therefore, taking into account (2), also

$$\frac{\partial f_{\mu\nu}}{\partial x_\nu} = -\frac{\partial \pi_{\mu\nu}}{\partial x_\nu}. \qquad \text{and c.c.}. \tag{11}$$

The equations (6) and (7) can be written

$$\left.\begin{aligned} \frac{\partial \pi_{\mu\nu}}{\partial x_\nu} &= -\frac{\partial H}{\partial \varphi^*_\mu}, \quad (12) \\ \frac{\partial \varphi_\mu}{\partial x_\nu} &= \frac{\partial H}{\partial \pi^*_{\mu\nu}}, \quad (13) \end{aligned}\right\} \qquad \text{and c.c.},$$

where the hamiltonian H is given by (6), and the Lorentz condition is introduced separately.

The equations (10) and (11) are the equations of motion for the vectorial field, in a covariant hamiltonian form such that the lagrangian variables φ^*_λ, φ_μ have as conjugate momenta $\pi_{\lambda\mu}$, and $\pi^*_{\mu\nu}$, respectively.

In this case there exists a Jacobi equation, so that one can make the transformation into the Tomonaga-Schwinger equation following the procedure indicated in I and II.

It is worth noting that according to the definitions (9), we get from (1)

$$4L = -2(\pi^*_{\nu\mu} - \pi^*_{\mu\nu})(\pi_{\nu\mu} - \pi_{\mu\nu}) - 4\mu^2 \varphi^*_\nu \varphi_\nu, \tag{14}$$

and

$$T_{\mu\mu} = \pi_{\mu\nu} \frac{\partial \varphi^*_\mu}{\partial x_\nu} + \pi^*_{\mu\nu} \frac{\partial \varphi_\mu}{\partial x_\nu} - 4L \neq H. \tag{15}$$

2. – Vectorial meson field in presence of a given electromagnetic field.

It is known that one can deduce from the equations of the free vectorial field the equations for the meson field in the external electromagnetic fields by substituting in the lagrangian (1)

$$\frac{\partial \varphi_\mu}{\partial x_\nu} \to \left(\frac{\partial}{\partial x_\nu} - ieA_\nu\right)\varphi_\mu \equiv \partial_\nu \varphi_\mu, \tag{16}$$

$$\frac{\partial \varphi^*_\mu}{\partial x_\nu} \to \left(\frac{\partial}{\partial x_\nu} + ieA_\nu\right)\varphi^*_\mu \equiv \partial^*_\nu \varphi_\mu. \tag{17}$$

In this case the equations of motion are

$$\partial_\mu f_{\mu\nu} = \mu^2 \varphi_\nu \,, \qquad \text{and c.c.}, \tag{18}$$

where $f_{\mu\nu}$ is an antisymmetrical tensor defined by

$$f_{\mu\nu} = \partial_\mu \varphi_\nu - \partial_\nu \varphi_\mu \,. \tag{19}$$

If by using the lagrangian (1), and by making the substitutions (16), (17), one intends to arrive at an hamiltonian formulation according to the method indicated in I, one finds the same difficulties as pointed out in Sect. 1 of the present paper.

On the contrary, if one follows the procedure in which an invariant is found such that Hamilton's equations are the equations of motion, one has to follow the same procedure as for the free field case. Putting

$$\partial_\nu \varphi_\mu = P_{\mu\nu} \,, \qquad \partial^*_\nu \varphi_\mu = P^*_{\mu\nu} \,, \tag{20}$$

one has

$$f_{\mu\nu} = P_{\nu\mu} - P_{\mu\nu} \,, \qquad \text{and c.c.}, \tag{21}$$

and moreover

$$\partial_\nu f_{\mu\nu} = \partial_\nu (P_{\nu\mu} - P_{\mu\nu}) = \partial_\nu \partial_\mu \varphi_\nu - \partial_\nu P_{\mu\nu} \,, \qquad \text{and c.c.}. \tag{22}$$

Since

$$[\partial_\nu \partial_\mu]_- = ie F_{\mu\nu} \,, \tag{23}$$

where $F_{\mu\nu}$ is the electromagnetic tensor, one has definitively for the equations of motion:

$$\left.\begin{aligned} &\partial_\nu P_{\mu\nu} = \mu^2 \varphi_\mu + ie F_{\mu\nu} \varphi_\nu + \frac{ie}{2\mu^2} \partial_\mu (F_{\alpha\nu} f_{\alpha\nu}) \,, && (24) \\ &\partial_\nu \varphi_\mu = P_{\mu\nu} \,, && (25) \end{aligned}\right\} \qquad \text{and c.c.}.$$

From (21), the last term of (24) contains the gradient

$$\frac{\partial}{\partial x_\mu} (P_{\nu\alpha} - P_{\alpha\nu}) \,, \tag{26}$$

so that, the system (24), (25) cannot be reduced to a normal form. Hence one cannot develop a covariant hamiltonian formalism even by this way.

However, we do not go deep into this problem since we are interested only in that part which was developed for the considerations concerning the electromagnetic field.

3350

3. – Electromagnetic field.

From the lagrangian

$$L = -\frac{1}{4}\left(\frac{\partial A_\nu}{\partial x_\mu} - \frac{\partial A_\mu}{\partial x_\nu}\right)^2 - \frac{1}{2}\left(\frac{\partial A_\mu}{\partial x_\mu}\right)^2, \tag{27}$$

we get, according to (I, 3)

$$\pi_{\mu\nu} = 4\left(\frac{\partial A_\nu}{\partial x_\mu} - \frac{\partial A_\mu}{\partial x_\nu}\right) - 4\delta_{\mu\nu}\frac{\partial A_\alpha}{\partial x_\alpha}, \tag{28}$$

and thus it is impossible to solve (28) with respect to $\partial A_\mu/\partial x_\nu$, as for the case of the meson vectorial field of Sect. **1**.

We can, on the contrary, do so by following the other procedure, indicated in Sect. **1**. Thus we get an invariant H such as to give the equations of motion as Hamilton's equations. In this case we easily see that we obtain again the formalism given in I and II, and the Lorentz condition must be introduced separately, as in III.

3:51

IL NUOVO CIMENTO Vol. XIV, N. 2 16 Ottobre 1959

Charge Distribution of the Nucleon.

V. De Alfaro and E. Predazzi

Istituto di Fisica dell'Università - Torino
Istituto Nazionale di Fisica Nucleare - Sezione di Torino

(ricevuto il 24 Luglio 1959)

In the recent years the experimental knowledge of the nucleon form factors has been greatly enhanced, by the high energy electron experiments performed at Stanford [1].

In comparison to this rather good experimental situation, the theoretical one is still quite obscure in spite of the most recent theoretical approaches by means of the dispersive techniques. Indeed Federbush, Goldberger and Treiman [2], and Chew, Karplus, Gasiorowicz and Zachariasen [3] in this way obtained results not completely satisfying for the understanding of the electromagnetic structure of the nucleon.

Recently a threshold theorem has been derived [4] which connects (in the case of no pion-pion interaction) the behaviour of the spectral functions of charge and magnetic moment form factors at the threshold with the behaviour for large r of charge and magnetic moment densities (respectively $\varrho(r)$ and $\mu(r)$) in the configuration space. In this way a necessary condition was deduced for the behaviour of $\varrho(r)$ and $\mu(r)$, in order to give a theoretical basis to the phenomenological models which have been used to describe the nucleon structure [5]. In fact in I it has been shown that the isovector part of $\varrho(r)$ asymptotically behaves as:

$$\varrho_v(r) \underset{r\to\infty}{\approx} \frac{C_v}{\sqrt{\mu}} \frac{\exp[-2\mu r]}{r^{7/2}}, \tag{1}$$

where μ is the π-meson mass.

---

[1] R. Hofstadter, F. Bumiller and M. R. Yearian: *Rev. Mod. Phys.*, **30**, 482 (1958).
[2] P. Federbush, M. L. Goldberger and S. B. Treiman: *Phys. Rev.*, **112**, 642 (1958).
[3] G. F. Chew, R. Karplus, S. Gasiorowicz and F. Zachariasen: *Phys. Rev.*, **110**, 265 (1958).
[4] B. Bosco and V. De Alfaro: *Nuovo Cimento*, **13**, 154 (1959), hereafter referred to as I.
[5] R. Hofstadter: *Nuovo Cimento*, **12**, 63 (1959); L. Schiff: *Rev. Mod. Phys.*, **30**, 462 (1958).

3352

C_v is connected to the pion-nucleon charge exchange scattering amplitudes by [6]:

$$C_v = \frac{e}{24\pi^3}\,\mu\,\mathrm{Re}\left\{B_2(0,-4\mu^2) + A_2'(0,-4\mu^2)\right\}. \tag{2}$$

Here $A_2(\nu, \Delta^2)$ and $B_2(\nu, \Delta^2)$ are defined as in CHEW, LOW, GOLDBERGER and NAMBU [7]. From this it appears that it is possible to connect quantities related to the nucleon structure with the pion nucleon charge exchange scattering amplitudes for non physical values of the parameters, and so obtain a check of the hypothesis under which the asymptotical behaviour is derived.

Therefore our aim has been to see whether the experimental data about the charge distribution in the nucleon can be fitted with such an asymptotical behaviour of $\varrho(r)$ in analogy with what has been done recently [5] and to compare the value of C_v obtained in this way with that derived by continuation of $A_2(\nu, \Delta^2)$ and $B_2(\nu, \Delta^2)$ in the point $\nu = 0$ and $\Delta^2 = -4\mu^2$.

In order to describe both the proton and the neutron we need besides the behaviour of the vector part of $\varrho(r)$, also the behaviour of the isoscalar charge distribution $\varrho_s(r)$ for large r. We have derived under suitable conditions of regularity for the amplitudes α, β, H^* [8], the power law according to which the scalar charge spectral function vanishes when the dispersion variable goes to $(3\mu)^2$. In an analogous way to I one then obtains:

$$\varrho_s(r) \underset{r\to\infty}{\approx} \frac{C_s}{\mu^2}\,\frac{\exp[-3\mu r]}{r^5}. \tag{3}$$

A similar result holds also for $\mu_s(r)$ which we don't consider here. We have used the following density distributions:

$$\begin{cases} \varrho_s(r) = \varrho_{0s}\mu^3, & 0 \leqslant r \leqslant a, \\ \varrho_s(r) = \dfrac{C_s}{\mu^2}\,\dfrac{\exp[-3\mu r]}{r^5}, & r \geqslant a, \end{cases} \tag{4}$$

$$\begin{cases} \varrho_v(r) = \varrho_{0v}\mu^3, & 0 \leqslant r \leqslant a, \\ \varrho_v(r) = \dfrac{C_v}{\sqrt{\mu}}\,\dfrac{\exp[-2\mu r]}{r^{7/2}}, & r > a. \end{cases} \tag{4'}$$

The density distributions given in eqs. (4), (4'), have been chosen so as to fulfil the asymptotical behaviour as deduced from the field theory, joining them to a constant density core of radius a. In this way we have only one arbitrary parameter, the radius of the core. The two constants C_s and C_v are determined by imposing that both the scalar and the vector total charge should be $e/2$.

---

(6) In the right hand side of this formula a factor $\frac{1}{2}$ is missing in I.
(7) G. F. CHEW, M. L. GOLDBERGER, F. E. LOW and Y. NAMBU: *Phys. Rev.*, **106**, 1337 (1957).
(8) See (2), p. 655.

The choice of the form for the core is of no practical significance since for the experimentally known range of momentum transfers almost everything is governed by the asymptotical tail of $\varrho(r)$.

The previously mentioned distributions correspond to the form factors:

$$F_s(q^2)=\frac{4\pi C_s}{\mu^2 qa^3}\left\{\frac{\exp[-3\mu a]\sin qa - qa\cos qa}{(qa)^2}+\frac{1}{6}\operatorname{Im}\left(\exp[-\lambda](2-\lambda+\lambda^2)+\lambda^3 Ei(-\lambda)\right)\right\},$$

$$F_v(q^2)=\frac{4\pi C_v}{qa\sqrt{\mu a}}\left\{\frac{\exp[-2\mu a]\sin qa - qa\cos qa}{(qa)^2}+\frac{2}{3}\operatorname{Im}\left(\exp[-\xi](1-2\xi)+2\xi^{\frac{3}{2}}\Gamma(\tfrac{1}{2},\xi)\right)\right\},$$

where q is the usual four momentum transfer, and $\lambda = 3\mu a - iqa$, $\xi = 2\mu a - iqa$. $Ei(-\lambda)$ is the exponential integral for complex argument, and $\Gamma(\frac{1}{2},\xi)$ is the incomplete Euler function of order $\frac{1}{2}$ for complex argument.

The best fit for the proton form factor is for $a=0.6$ fermi. The values of F_p^2 and F_n are given in Figs. 1 and 2. The corresponding charge distributions are shown in Figs. 3 and 4.

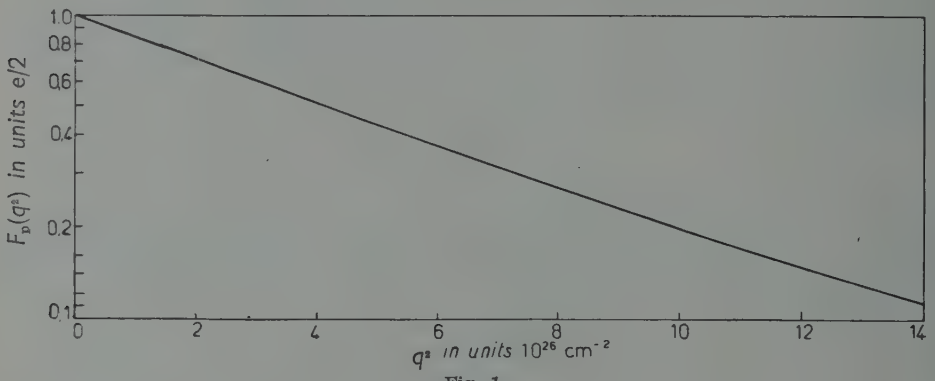

Fig. 1.

The mean square radius $\langle r^2\rangle$ for the proton is $\langle r_p^2\rangle = 0.76$ (fermi)^2 which is a somewhat high value in comparison to the present experimental data. The neutron mean square radius is zero. As one can see, the fit of F_p^2 is quite good. On the

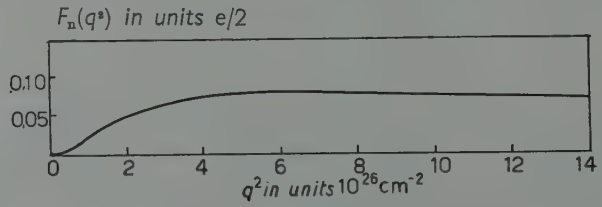

Fig. 2.

contrary the neutron form factor comes out to be wrong even in sign. The experiments about the neutron show in fact that the neutron form factor is negative, and has to be very small ($\langle r_n^4\rangle$ is practically zero). With no reasonable value of the core radius a is possible to obtain a good picture of the neutron.

3354

The value obtained for C_v in this way is $C_v = .070$ in units e. In order to compare this value with the theoretical one obtained from (2), we have used for $A_2(\nu, \Delta^2)$ and $B_2(\nu, \Delta^2)$ their values given by the dispersion relations retaining only the inhomogeneous term. So obviously $A_2(0, -4\mu^2) = 0$, and $B_2(0, -4\mu^2) = 2g^2/\mu^2$.

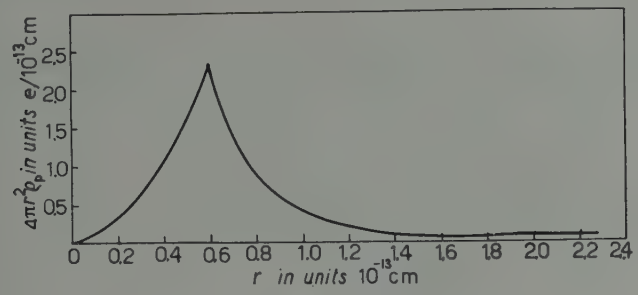

Fig. 3.

In this way we obtain for the theoretical C_v the value 0.63. We calculated also the $\frac{3}{2}, \frac{3}{2}$ resonance contribution to the dispersive integrals. The Born approximation is then not substantially modified. In fact the $\frac{3}{2}, \frac{3}{2}$ contributions to $A_2(0, -4\mu^2)$ and $B_2(0, -4\mu^2)$ are of the same order of magnitude (small with respect to the Born approximation) and of the opposite sign.

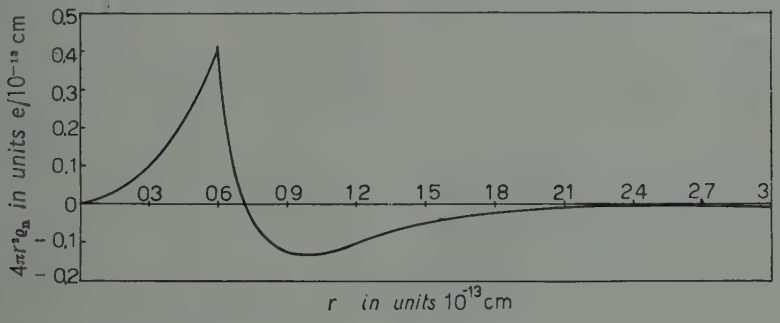

Fig. 4.

Even if this is an approximate result, the agreement with the previously obtained C_v is bad. We conclude that the picture of the nucleon given by the distributions (4) and (4′) is not completely satisfying.

In spite of the good fit for the proton form factor, the neutron form factor seems to be not correct. The neutron mean square radius, as expected, is zero, but the proton mean square radius is slightly high. From these considerations and the disagreement about C_v we believe that either the threshold limit is not representative of the low intermediate mass states in the spectral function (due to the anomalous behaviour of this function at the threshold), or that something as two pion interaction plays a rather important role in the nucleon structure.

* * *

We are greatly indebted to Professors S. Fubini and B. Bosco for their kind interest and for many helpful discussions.

Annealing of Electron Irradiated Germanium.

G. Airoldi, Z. Fuhrman and E. Germagnoli (*)

Laboratori C.I.S.E. - Milano

(ricevuto il 5 Settembre 1959)

The annealing kinetics of isolated Frenkel defects produced by electron irradiation in germanium has been shown to be complex (1): this fact has been interpreted by taking into account both preferential recombination of close interstitial-vacancy pairs and the recombination controlled by thermally induced diffusion of mobile defects (2). Some further evidence that this picture is consistent with experimental results is presented.

n-type germanium single crystals, whose initial resistivities ranged between 0.01 and 1 Ω cm, were uniformly irradiated with 1.3 MeV electrons from a Van de Graaff accelerator. Irradiations were performed at room temperature and the total integrated flux was about 10^{16} electrons cm^{-2}. The changes of carrier concentration during isothermal annealings were deduced from conductivity and Hall effect measurements and assumed to be proportional to the actual concentration of defects, which is reasonable, because during the whole irradiation the conductivity of specimens depended linearly upon the total flux.

The density of dislocation lines within the specimens being about $5 \cdot 10^4$ cm^{-2} (3), the equations given by Waite (2) should hold. In the fast initial recovery, the percentage of residual defects n/n_0 is linearly dependent on $t^{\frac{1}{2}}$, as predicted by Waite; the percentage of radiation-induced Frenkel pairs disappearing in this early stage ranges between 15% and 40% in the investigated interval of temperature ((190 ÷ 270) °C). This is probably correlated with a preferential recombination mechanism.

After long annealing intervals, bimolecular recombination, controlled by thermally induced diffusion, is expected (2):

$$\frac{\mathrm{d}n}{\mathrm{d}t} = -4\pi r_0 D n^2 ,$$

r_0 being the capture radius defined by Waite and D the diffusion coefficient of defects. Linear dependence of $n_0/n - 1$ on annealing time is deduced: this fact is apparent from Fig. 1 where the initial annealing stage is not shown. From the slopes of the straight lines in Fig. 1,

(*) Laboratori C.I.S.E. and Istituto di Fisica del Politecnico, Milan.

(1) W. L. Brown, R. C. Fletcher and K. A. Wright: *Phys. Rev.*, **92**, 591 (1953).

(2) T. R. Waite: *Phys. Rev.*, **107**, 471 (1957).

(3) S. Granata and G. Schiavini: *Energia Nucleare*, **6**, 267 (1959).

3356

D is $\simeq 10 \exp[-1.4\ \mathrm{eV}/kT]\ \mathrm{cm^2\ s^{-1}}$, if r_0 is assumed equal to $5 \cdot 10^{-8}$ cm.

the related hypotheses, namely the distribution function of initial interstitial-

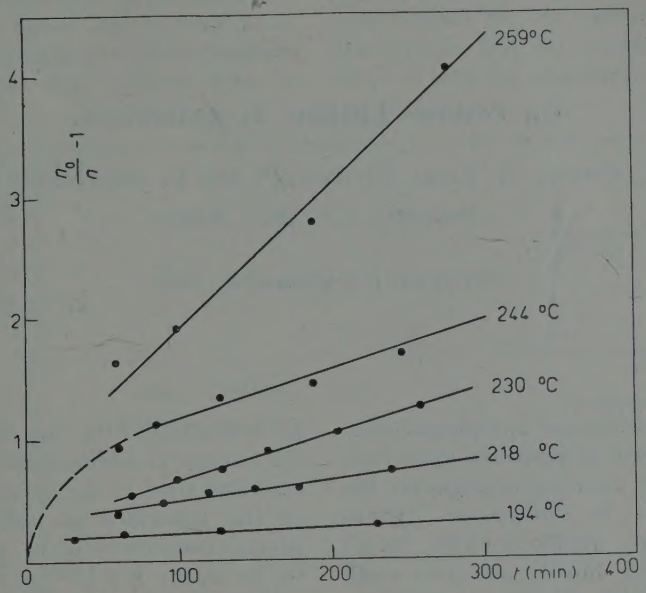

Fig. 1. – Evidence for second order recombination of defects for long annealing intervals.

Nearly the same value of the migration energy is deduced from an analysis of the initial annealing stage in terms of direct recombination: in this case a much smaller D is deduced. It must be pointed out, however, that in this case D depends critically on the chosen values for the parameters involved in the equation given by Waite and on vacancy distances and the use of Fick's law.

* * *

The help by Soc. Pirelli, whose Van de Graaff accelerator was used, is gratefully acknowledged. Thanks are also due to Eng. G. Trogu, of the same firm, for his kind assistance during the irradiations.

2357

IL NUOVO CIMENTO Vol. XIV, N. 2 16 Ottobre 1959

On Positron Lifetime in Anthracene.

C. Cottini, G. Fabri, E. Gatti (*) and E. Germagnoli (*)
Laboratori C.I.S.E. - Milano

(ricevuto il 5 Settembre 1959)

The dependence of two-photon annihilation lifetime of positrons upon temperature and state of aggregation has been studied in anthracene. About 60 μC of high specific activity ^{22}NaCl were deposited directly into two small anthracene single crystals, so that the positron source was sandwiched between the two crystals. The positron decay times were measured in the range of temperature between -200 and $+295$ °C. Near the melting point of anthracene (217 °C) the temperature was stabilized within ± 0.1 °C by means of a boiling naphthalene bath with a carefully controlled argon pressure above it.

The delay spectra of annihilation γ-rays with respect to 1.28 MeV γ-rays from ^{22}Na were studied by means of two plastic scintillators optically coupled with RCA 6342 phototubes. Pulses were fed into a vernier time-sorter [1] working in connection with two slow channels for energy discrimination. The overall resolving time of the apparatus, defined as the full-width at half-height of a prompt coincidence curve, was estimated to be about $6.5 \cdot 10^{-10}$ s, from prompt curves obtained with a ^{60}Co γ source.

In solid anthracene positrons showed only a short lifetime which is fairly independent of temperature and equal to $(3.7 \pm 0.2) \cdot 10^{-10}$ s. A few degrees below the melting point a longer life-

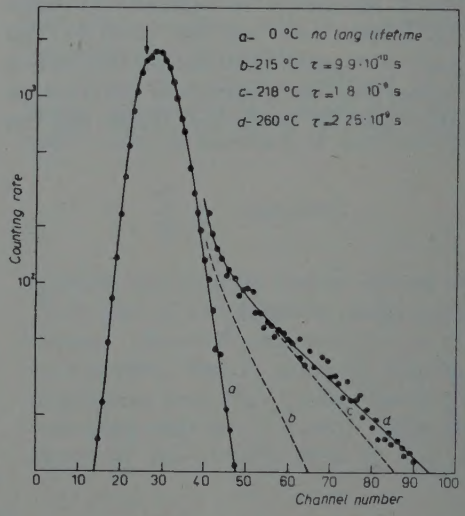

Fig. 1. – Typical decay curves of positrons in anthracene. 1 channel $= 1.15 \cdot 10^{-10}$ s. Curves are normalized to equal number of counts

(*) Laboratori C.I.S.E. and Istituto di Fisica del Politecnico, Milan.

(1) C. Cottini and E. Gatti: *Nuovo Cimento*, **4**, 1550 (1956); C. Cottini and E. Gatti: *Rev. Nucl. Instr.*, **2**, 88 (1958); C. Cottini, E. Gatti and F. Vaghi: *Nanosecond Vernier Time-Analyzer* (*Proc. of Colloque International sur l'électronique nucléaire*, Paris, Sept. 1958); C. Cottini, E. Gatti, V. Svelto and F. Vaghi: *Time Sorting of Nanosecond Pulses* (*Proc. of the Second Symposium on advances in fast pulse techniques for nuclear counting*. Lawrence Radiation Laboratory, Berkeley Cal., February 1959).

3358

time was observed which sharply increases with increasing temperature; its final value is equal to about $2.3 \cdot 10^{-9}$ s some degrees above the melting point and does not change with further increase of temperature. Fig. 1 shows a set of measurements with the specimens which were single crystals before having been melted. A slight increase in lifetime was noticed at low temperature with polycrystals but the evidence for this effect is still not conclusive.

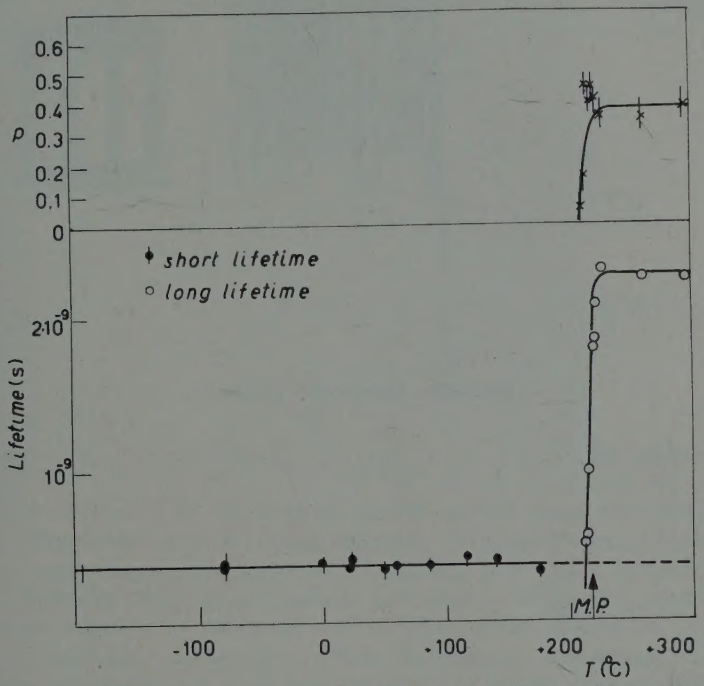

Fig. 2. – Positron lifetime and percentage p of positrons annihilating with a long lifetime as functions of temperature.

typical experimental decay curves of positrons. Eight of them were taken in the range between 211 and 226 °C. The percentage of positrons annihilating with a long lifetime appears to increase from zero to (35÷40)% near the melting point of anthracene. The results are summarized in Fig. 2.

A few attempts to investigate the influence of crystallinity on the positron decay were made. Results which were almost the same as described above were obtained both with polycrystalline anthracene and in a second run of

The similarity between the present results and the ones which have been described in the case of naphthalene [2] is evident with respect to the absolute values of both short and long lifetime and the behaviour near the melting point; however no evidence of a long lifetime was found in solid anthracene, while it was reported for solid naphthalene [2].

---

[2] H. S. LANDES, S. BERKO and A. J. ZUCHELLI: *Phys. Rev.*, **103**, 828 (1956).

3359

PROPRIETÀ LETTERARIA RISERVATA

Direttore responsabile: G. POLVANI

Tipografia Compositori - Bologna

Questo fascicolo è stato licenziato dai torchi il 10-XI-1959

3360